UC Berkeley
UC Berkeley Electronic Theses and Dissertations

Title

Electronic and Optical Properties of Materials for Energy-Related Applications

Permalink

https://escholarship.org/uc/item/6ww8t49b

Author

Ong, Chin Shen

Publication Date

2019

Peer reviewed|Thesis/dissertation

eScholarship.org Powered by the California Digital Library
University of California

Electronic and Optical Properties of Materials for Energy-Related Applications

by

Chin Shen Ong

A dissertation submitted in partial satisfaction of the

requirements for the degree of

Doctor of Philosophy

in

Physics

in the

Graduate Division

of the

University of California, Berkeley

Committee in charge:

Professor Steven G. Louie, Chair
Professor Alex Zettl
Professor Mark Asta

Fall 2019

Electronic and Optical Properties of Materials for Energy-Related Applications

Copyright 2019
by
Chin Shen Ong

Abstract

Electronic and Optical Properties of Materials for Energy-Related Applications

by

Chin Shen Ong

Doctor of Philosophy in Physics

University of California, Berkeley

Professor Steven G. Louie, Chair

In this dissertation, I discuss the electronic and optical properties of materials for energy-related applications, with a focus on silicon (Si), gallium arsenide (GaAs) and the transition metal dichalcogenides (TMDs) in particular.

Si is the most widely used photovoltaic material today, dominating the photovoltaic industry by more than 90%. This is because Si is non-toxic, abundant and benefits from technologies developed over the years in the microelectronics industry. Despite its widespread usage as a photovoltaic material, Si does not efficiently absorb most of the light in the solar spectrum because it has an indirect bandgap. On the other hand, GaAs has a direct bandgap that is optimal for solar energy conversion, even though it is more expensive than Si and is also toxic due to the presence of arsenide. Nonetheless, in the atomically-thin film limit, both cannot be compared with the TMDs, absorbing significantly less light than the TMDs in the solar spectrum. This optical property of the TMDs makes them a very appealing class of candidate materials for flexible ultra-thin solar cells.

In Chapter 1, I give an overview of the different approaches that we use to address different problems in this dissertation. In Chapter 2, I discuss our work [157] that aims to understand how the structure of an alternative Si phase can lead to an improved calculated absorption relative to diamond-Si. In Chapter 3, I discuss how we [17] can use first-principles to calculate the hot carrier dynamics in GaAs, such as by calculating its electron-phonon relaxation times. In the Chapters 4, 5, 6, I discuss the electronic and optical properties of mono- to few-layer TMDs. Not only are their quasiparticle bandgap and exciton energy levels affected by dielectric screening due to substrates [158], the dielectric screening environment can also be modified to engineer an intrinsic lateral heterojunction within a homogeneous TMD monolayer [212]. In Chapter 7, we [240] report the first observation and control of the Berry-phase induced splitting of the 2p-exciton states in monolayer $MoSe_2$, and in Chapter 8, we [236] study that the dynamics of atomically-sharp lateral heterojunctions between differently-stacked TMD domains.

To my parents, Hua Hui Ong and Sok Kheng Er,
for your endless love and support.

Contents

Contents ii

List of Figures iv

List of Tables xii

1 Introduction 1

2 Real-Space Study of the Optical Absorption in Alternative Phases of Silicon 6
2.1 Introduction 6
2.2 Method 8
2.3 Results and discussion 12
2.4 Conclusion 20

3 *Ab initio* Study of Hot Electrons in GaAs 21
3.1 Introduction 21
3.2 Results and Discussion 23
3.3 Conclusion 29
3.4 Methods 30

4 Substrate-Induced Dynamical Anti-Screening of Excitons in Quasi-2D Materials 33
4.1 Introduction 33
4.2 Theoretical and Computational Approaches 35
4.3 Results 40
4.4 Conclusion 47

5 Theoretical Concepts and Methods for Screening in Quasi-2D Materials 52
5.1 DFT Calculations 52
5.2 GW-BSE Calculations 53
5.3 Derivation of the Ideal-Metal Substrate Model 55
5.4 Singularity in Electron-Hole Continuum of a 2D metal 64

5.5 QP Bandgap Renormalization due to Substrate and Encapsulation 66
5.6 Wavefunction Hybridization between the Substrate and Quasi-2D Material . 68
5.7 Conventions for Fourier Series Expansion 68

6 A Dielectric-Defined Lateral Heterojunction in a Monolayer Semiconductor 71
6.1 Introduction 71
6.2 Heterojunction device design and electrical measurement 72
6.3 KPFM characterization 74
6.4 Energy band modelling 76
6.5 Conclusions 78
6.6 Methods 79
6.7 GW_0 calculations for the CBM offsets and change in bandgap of MoS_2 due to dielectric screening from the substrates 80

7 Valley-dependent Exciton Fine Structure and Autler-Townes Doublets from Berry Phases in Monolayer $MoSe_2$ 83
7.1 Introduction 83
7.2 Results and Discussion 84
7.3 Materials and Methods 87
7.4 GW-BSE calculations of $MoSe_2$ 88
7.5 Convention Used for Circularly-Polarized Light 91
7.6 Convention Used to Define the Angular Momentum of Exciton Wavefunction 93

8 Dynamics of Symmetry-breaking Stacking Boundaries in Bilayer MoS_2 102
8.1 Introduction 102
8.2 Results and Discussion 104
8.3 Conclusion 108
8.4 First-principle calculations 108

Bibliography 118

List of Figures

1.1 The GW-BSE optical spectrum of diamond-Si (black) and GaAs (red) and the measured solar spectrum (gray). 1
1.2 (a) The solar spectrum (gray) and the absorbance of 5-Å-thick diamond-Si (black) and 5-Å-thick GaAs (red). (b) A zoom-in of the energy range (shaded yellow) from 1.3 to 3.0 eV of (a), superposed with absorbance of a MoS_2 monolayer. . . 2
1.3 A schematic diagram of the field lines between two charges inside (a) 2D, (b) quasi-2D and (c) 3D materials. 3
1.4 Dielectric screening of a charge. Charge is (a) completely unscreened, (b) partially screened by substrate and (c) completely screened by substrate. 4

2.1 The absorption of diamond-Si (black) and Si_{20} (red) calculated with the DFT (a) and BSE (b) approaches. 9
2.2 The isosurface of calculated bonding (a) and anti-bonding (b) Wannier functions in diamond-Si. Gray spheres are silicon atoms forming the bond. Isosurface in (a) is 1.4 and 1.0 in (b). Red and blue colors indicate parts of the Wannier function with opposite signs. 12
2.3 Conventional unit cell of diamond-Si containing eight silicon atoms. Its primitive unit cell contains only two silicon atoms. 13
2.4 Conventional unit cell of Si_{20} containing 20 silicon atoms. Its primitive unit cell is the same as the conventional unit cell. Four distinct Si-Si bonds are indicated with labels a, b, c, and d. Bonds forming a triangle are labelled with letter a. . 13
2.5 On-site energy of bonding (e_i, lower value) and anti-bonding ($\bar{e}_i$, higher value) Wannier function in diamond-Si (left, black) and Si_{20} (right, red). Numbers indicate $\bar{e}_i - e_i$ in eV. In the case of Si_{20} we show $\bar{e}_i - e_i$ for all four types of bonds. (The origin of the energy scale is arbitrary.) 15
2.6 Hopping integrals between bonding Wannier functions, as a function of hopping distance for diamond-Si (black) and Si_{20} (red). 16
2.7 Hopping integrals between anti-bonding Wannier functions, as a function of hopping distance for diamond-Si (black) and Si_{20} (red). 17
2.8 Optical absorption of diamond-Si (black), Si_{20} (solid red), and two hybrid cases (dashed, dotted, see text for details). Absorption curves are scissor shifted by 0.6 eV in all four cases based on our GW-BSE calculation. 18

3.1 e-ph scattering in GaAs. (A) e-ph scattering rates for hot electrons in GaAs shown together with the electronic DOS. The zero of the energy axis is the CBM. The contributions to the total e-ph scattering rate in A from the acoustic and optical phonons are shown in B and C, respectively. LA, TA, LO, and TO label e-ph scattering induced by LA, TA, LO, and TO phonons in B and C. The sum of the scattering rates in B and C equals the total scattering rate in A. 23
3.2 Comparison of *ab initio* and semiempirical calculations. (A) e-ph scattering rates from all modes in our work vs. those in Ref. [56]. (B) Contributions of individual phononmodes to the e-ph scattering rate for *ab initio* calculations (solid lines) carried out in this work and semiempirical calculations (dashed lines) that we reproduce using the parameters in Ref. [56]. The curves shown are the **k**-averaged scattering rates for (Left) acoustic modes and (Right) optical modes. 24
3.3 e-ph relaxation times in GaAs. (A) e-ph relaxation times of hot electrons in GaAs. Up to E_X, data points shown in yellow originate from electronic states in the Γ valley, and data points shown in green originate from states at the bottom of the L valley. At energies above E_X, states in red and blue are located near the X and L valleys, respectively. (B) Schematic of the states and valleys giving rise to the e-ph scattering rates in A. 26
3.4 II rates in GaAs. II rates computed with the GW method shown together with the Keldysh fit. The energies are referenced to the CBM and extend to $\sim$5 eV above the II threshold. 28
3.5 Comparison between the GW II rates in this work (black curve) and those in Ref. [56] (red curve). Shown are the Keldysh fits of the two datasets. 29

4.1 Diagonal elements of the inverse dielectric matrices of doped monolayer graphene, ideal-metal (surface-charge) model and image-charge model. Here, a is the lattice constant of graphene, the out-of-plane components are set to $G_\perp = G'_\perp = 0$. . . 49
4.2 Calculated GW_0 QP bandgaps of monolayer WSe_2 on different substrates (●) and encapsulations (✖). The substrates are plotted along the horizontal axis using their experimental dielectric constants. The experimental dielectric constants used for PTFE [18, 51], SiO_2 [159], hBN [47], n-layered graphene [176] are 2.1, 4.6, 6.1 and 15, respectively. Also plotted using a dashed line is the calculated QP bandgap of monolayer WSe_2 when substrate screening is included using the substrate dielectric constant as in the conventional model (i.e., homogeneous local screening). 50

4.3 (a) Calculated GW-BSE exciton excitation energies of the four lowest-lying excitons (■) and GW QP bandgaps (●) of WSe_2 on different substrates. The substrates are plotted along the horizontal axis using their experimental dielectric constants as in Fig. 4.2. Also plotted using dashed lines are the excitation energies when substrate screening is included using the substrate dielectric constant as in the conventional model (i.e., homogeneous local screening). For ideal metal model as the substrate, excitation energies are calculated using dynamical and static screening. (b) Exciton envelope functions of the three lowest-lying bright excitons of freestanding monolayer WSe_2. (c) Effective 2D dielectric function of monolayer WSe_2 when screened by an ideal-metal model substrate at static frequency (dark blue) and 0.3 eV (red). 51

5.1 Image-point-charge model in a periodic supercell. In this model, the point charge ρ_{ext} induces an image charge ρ_{ind}. In the limit where $\mathcal{V} \to \infty$, there will be no periodic images. In practical calculations, the periodic supercell has a finite volume. To avoid interactions between the periodic images, the Coulomb potential $v_c(\mathbf{q}+\mathbf{G})$ used to calculate the response function $\chi_{\mathbf{G}\mathbf{G}',\text{static}}(\mathbf{q})$ is appropriately truncated in the out-of-plane direction [85]. 57

5.2 Surface-charge-inducing ideal metal model (IMM) in a periodic supercell of height L. In this model, the point charge ρ_{ext} induces a quasi-2D surface charge ρ_{ind}. In the limit where $\mathcal{V} \to \infty$, there will be no periodic images. In practical calculations, the periodic supercell has a finite volume. To avoid interaction between the periodic images, the Coulomb potential $v_c(\mathbf{q}+\mathbf{G})$ used to calculate the response function $\chi_{\mathbf{G}\mathbf{G}',\text{static}}(\mathbf{q})$ is appropriately truncated in the out-of-plane direction [85]. 59

5.3 Perfect screening by a surface-charge-inducing quasi-2D ideal-metal model (IMM) (a) is equivalent to screening by a semi-infinite metal (b) according to the Uniqueness Theorem. 62

5.4 The right panel show the plot of $\text{Re}[\chi^0(q+G,\omega)]$ for a 2D electron gas in color scale. The region of the $(q+G,\omega)$-plane in which $\text{Im}[\chi^0(q+G,\omega)]$ differs from zero is known as the electron-hole continuum. The left panel shows the zoomed-in region for small-q and small-ω, which is the relevant length and energy scales of a Wannier exciton. Here, q is the momentum wavevector restricted to the First Brillouin Zone. 65

5.5 Calculated binding energies E_b at different screening frequencies ω. 66

5.6 Image charges due to substrate (a) and encapsulation (b) 67

5.7 DFT bandstructures of monolayer MoS_2 (a,c,e) and MoS_2 on monolayer undoped graphene (b), bilayer hBN (d) and three layers of (001)-terminated gold (e). . . 69

6.1 Engineering 2D heterojunctions through dielectric-dependent bandgap renormalization. a, Schematic illustration of the heterostructure. Two substrates with different dielectric constant ($\epsilon_{\text{low}} < \epsilon_{\text{high}}$) are used to locally vary the MoS_2 electronic bandgap. b, The expected band alignment of isolated monolayer MoS_2 situated on the low-ϵ substrate (Cytop) and on the high-ϵ substrate (hBN), respectively. The segments of MoS_2 monolayers on Cytop and on hBN are assumed to have the same electron doping density from the electrostatic gating. c, The band alignment from b if the MoS_2 segments on the two substrates are in contact and reach equilibrium following Anderson's rule. A type-I lateral heterojunction forms with an energy barrier for electron transport in the conduction band. . . . 73

6.2 Current-voltage characteristics of a MoS_2 heterojunction device. a, Optical micrograph of a MoS_2 monolayer that is partially situated on Cytop and on hBN substrates. The white dashed line denotes the location of the monolayer that acts as the device channel. The MoS_2 segment on hBN received the high bias potential (drain). Scale bar: 2 μm. b, The output characteristics of the device with various back gating at a temperature of 200 K. c, The output characteristics of a reference MoS_2 monolayer device on a uniform Cytop substrate measured at 200 K. Inset: The micrograph of the reference device. Scale bar: 2 μm. d, The output characteristics of the heterojunction device at 17 K on a log-log scale. The forward bias current is fitted with a straight line that extrapolates to a turn-on voltage of 90 mV. Inset: the same data on a linear scale. 74

6.3 KPFM characterization of the MoS_2 heterojunction formation from differences in the degree of local dielectric screening. a, Schematic of the KPFM set-up with V_{bias} applied to the sample. For the measurements herein, the device is back gated to $V_{\text{gs}} = 50$ V and the lift height of the tip is set to h = 30 nm. b, The topography image recorded in tapping mode AFM. c, The height profile, averaged from the area inside the white dashed rectangle in b. d, The spatially mapped V_{bias} from the same area as in b. e, The V_{bias} profile from d, also averaged similarly from the same area as in c. Given that $\Delta E_{\text{c}} = -e\Delta V_{\text{bias}}$ in the measurement configuration, the KPFM result demonstrates that the conduction band edge of MoS_2 on the Cytop substrate is higher by 90 meV than that of MoS_2 on hBN. f, Results from GW calculations of the bandgap and band alignment of monolayer MoS_2 that is freestanding without a substrate screening effect (left), placed on a surface of a fluoropolymer (middle), and placed on a hBN substrate (right). Scale bars in b and d correspond to 500 nm. 75

6.4 Simulation results of the energy band bending at the 2D heterojunction. a-c, The conduction band edges and Fermi levels are calculated at zero bias (a), forward bias (current: 80 nA μm^{-1}) (b) and reverse bias (current: -6 nA μm^{-1}) (c) conditions. In the three cases, the MoS_2 segment on Cytop is assigned to be electrically grounded. Under a small forward bias ($V_{ch} = V_1 + V_2$), an electron traversing the heterojunction from the segment on Cytop to that on hBN experiences an energy barrier due to the built-in voltage. However, for large enough bias beyond the turn-on voltage ($V_{ch} > V_t$), electrons traversing the heterojunction (blue circle) do not experience a significant energy barrier and the current-voltage characteristic is determined by the resistance of the channel instead of the junction. Inset in b, a schematic of the diode modelling according to piecewise linear model. d, Carrier density distribution across the junction under different bias conditions. e, Simulated current-voltage characteristics with a carrier-density-dependent mobility. All calculations are performed using a carrier density of 2.0×10^{12} cm^{-2} at 140 K. 78

6.5 AFM height profile of a typical Cytop surface. a, AFM image. b, Height profile along the white dashed line in a 82

7.1 Schematics of exciton spectrum and optical transition in $MoSe_2$ monolayer. a. Diagram illustrating the effects of Berry curvature Ω_e and Ω_h on the energy of exciton. The electron and hole acquire an anomalous velocity $\nabla \times \Omega$ in a central potential V(r), resulting in a lift of the degeneracy between the exciton states with opposite angular momentum. b. Illustration of the optical transition and selection rules for one-photon and two-photon excitations in the K and K' valleys of $MoSe_2$ monolayer. $|g\rangle$, $|1s\rangle$, $|2p_-\rangle$, and $|2p_+\rangle$ denote the ground state, 1s, 2p$_-$, and 2p$_+$-exciton states, respectively. The symbol σ^+ and σ^- denotes left and right circular polarization state, respectively. c. Optical micrograph of monolayer $MoSe_2$ encapsulated by hBN layers on alumina coated silver substrate. The scale bar corresponds to 50 μm. d. The reflection contrast of hBN encapsulated $MoSe_2$ monolayer on alumina coated silver surface at 77 K. It shows prominent A-exciton resonance at 1.627 eV with a FWHM of $\approx$9 meV. e. Schematic diagram illustrating the avoided-crossing behavior due to quantum-mechanical coupling between the infrared photons field and the 1s-2p$_+$ electronic transition. The dashed lines show the energy difference between the $|g, n\hbar\omega\rangle$ and the unperturbed $|1s, n\hbar\omega\rangle$ and $|2p_+, (n-1)\hbar\omega\rangle$ states as a function of the infrared pump photon energy. The bare $|2p_+, (n-1)\hbar\omega\rangle$ state has one fewer pump photon than the bare $|1s, n\hbar\omega\rangle$ state, and will have a total energy decreasing linearly with the pump photon energy. The blue and red solid lines show the dressed exciton states from quantum hybridization. The arrows show the optical transitions from the ground state to the dressed 1s exciton state. 96

7.2 Transient reflection spectra of K-valley exciton transitions. a-c. Two-dimensional plot of transient reflection spectra of the K-valley 1s-exciton resonance of $MoSe_2$ at 77 K following photoexcitation with σ^+-polarized infrared pump at photon energy of (a) 120 meV, (b) 142 meV and (c) 170 meV. The color scale, vertical axis and horizontal axis represent the relative reflectivity change ΔR /R, the pump-probe time delay τ, and the probe photon energy, respectively. The positive (negative) ΔR /R represents decrease (increase) of absorption. The photoinduced absorption in the K-valley 1s-exciton is monitored by σ^+-polarized probes. The signals are finite only when the pump and probe pulses overlap in time, indicating an instantaneous coherent response and negligible excitation of real exciton population. d-f. At $\tau = 0$ ps, the coherent signals for σ^+-probes exhibit spectral responses that are characteristic of (d) energy redshift to (e) splitting and then to (f) energy blueshift as the driving photon energy is increased from 120 meV to 170 meV. 97

7.3 Valley-dependent intraexciton optical Stark effect. a-b. Experimentally observed (a) and calculated (b) photoinduced absorption spectra of $MoSe_2$ monolayer at $\tau = 0$ ps under various σ^+- pump excitation energy for the K and K' valleys. The dashed-lines indicate the peak position of unperturbed A-exciton. The dotted lines are guides to the eyes for the peak position at different driving energies. The spectra are offset for clarity and labelled according to the excitation energy (meV). The spectra evolve from energy redshift to splitting and then to blueshift, as the driving energy is increased. The calculation is based on the Hamiltonian shown in Eq. 7.2. Exciton-photon coupling leads to avoided-crossing and the observed peak splitting at resonant coupling. This resonant coupling occurs at driving photon energy of 142 meV and 128 meV in the K and K' valleys, respectively. It corresponds to a Berry-phase induced 1s-$2p_+$ intraexciton transition energy difference of 14 meV. c. Measured 1s exciton peak position (circles) in the K and K' valleys as a function of σ^+-infrared pump photon energy for an effective driving intensity is 7±1 MW/cm^2. The greyscale shows the relative strength of optical transition. The solid lines show the calculated dressed-exciton states based on the Hamiltonian shown in Eq. 7.2. 98

7.4 Valley-dependent Autler-Townes splitting. a-b. Photoinduced absorption spectra of $MoSe_2$ monolayer on ZnS substrate at $\tau = 0$ ps for a series of σ^+-pump intensity at driving energy of (a) 150 meV and (b) 138 meV for K and K'-valley. The dashed-lines indicate peak position of undriven A-exciton. The spectra are offset and labelled according to the effective driving intensity (MW/cm^2). c-d. The dependence of Autler-Townes splitting energy in K and K'-valley on the squared root of effective pump intensity ($\sqrt{I_{\text{eff}}}$) for driving photon energy of (c) 150 meV and (d) 138 meV, respectively. The top axis shows the corresponding effective local optical field strength (E_{eff}). The splitting energies are obtained from fitting the photoinduced absorption lines with two Lorentzian lines. The dashed lines are fitting obtained from the Hamiltonian shown in Eq. 7.2. 99

7.5 Plots of the exciton energy levels and their envelope functions in real and reciprocal space using a hydrogenic gauge. 100
7.6 Angular momentum of circularly-polarized light. 101

8.1 Ball-and-stick models for monolayer H-phase MoS_2, and AB (R phase) and AA' (2H-phase) stacked bilayer MoS_2, viewed from the top and the side, with red balls representing Mo atoms and blue balls representing S atoms. The lattice constant ($\mathbf{a}$) for monolayer H phase MoS_2 is 3.16 Å, and the Mo lattice distance in one layer MoS_2 ($\mathbf{a_1}$) is 2.74 Å, as indicated by red shadings in the schematics for both AB and AA' bilayers. 103
8.2 Stitching of AB and AA' stacked regions with sharp stacking boundaries in bilayer MoS_2. (a) High-resolution STEM ADF image taken at time 0s, showing AB stacked bilayer MoS_2. (b) After 14 s of scanning in the same area, rearrangement of atoms occurred, as highlighted by the orange ellipse. at the center of this AB stacked region, (c) High-resolution STEM ADF image showing a triangular AA' stacked region (highlighted by an orange circle) surrounded by AB stacked region. This image was taken 14 seconds after (b) and is from the same area as (b). (d) (e), STEM ADF images from AB stacked region in (a) and AA' stacked region in (c), respectively, with the intensity averaged over more than 10 unit cells of the same stacking sequence. The experimental results are compared to the multislice simulation [102] of STEM ADF images of AB and AA' stacked bilayer MoS_2 under the same experimental imaging condition in (d) and (e), respectively. All images in (d) and (e) are plotted on the same absolute scale. Scale bars in (a) (b) and (c) are 1 nm. 111
8.3 Nucleation and motion of the stacking boundaries in bilayer MoS_2 at 400°C. (a)-(d), STEM ADF image series of structural change in bilayer MoS_2 from the same area as time evolves from left to right. Red circles and triangles in these images highlight the same atoms and lattice points in this area. e-h, enlarged images of the area highlighted with purple squares in a-d respectively. e, At $t = 0$ s, AB stacked bilayer MoS_2 with the lattice points connected by blue lines. The S-S columns from the top layer occupy the hollow centers of the hexagonal lattices in this image. f, At $t = 7$ s, local atomic rearrangement starts to occur, which triggers the nucleation of AA' stacked domain. Large-area linear features with spacing 2.74 Å (orange lines) are due to the interlayer lateral shift between the top and bottom MoS_2 layers. Other structural changes are also observed, such as extra atoms (white arrowheads) and local shrinkage of projected Mo-Mo distance (green lines). g, At $t = 14$ s, AA' stacked region grows to $\sim$2.88 nm^2. h, At $t = 21$ s, AA' stacked region grows to 4.75 nm^2 as outlined by the blue hexagons. The angle between the two straight stacking boundaries is 60°. The growth direction for the AA' stacked region is now along vector $\mathbf{W}$. Scale bars in (e)-(h) are 5 Å. 112

8.4 Atomic structure at the stacking boundaries. (a) A typical triangular AA' stacked domain is connected to the AB stacked domain by atomically sharp boundaries. At the three boundaries (labelled B_1, B_2, B_3), Mo lattices from the top layer are outlined by solid lines, and those from the bottom layer are outlined by dashed lines. Scale bar is 5 Å. (b) Summary of Mo lattice distances measured at six boundaries of two cases where AA' and AB domains are stitched together. Blue triangles represent the Mo lattice distances from the top layer, and red dots represent the Mo lattice distances from the bottom layer. The Mo lattice distances in the top layer at these boundaries shrink more than those in the bottom layer, indicating more severe structural change thus more energy injection from the electron beam into the top layer. (c) Schematic of the boundary structure obtained from DFT calculations. The dimensions of this boundary structure agree with the experimentally observed most dominant boundary structure. This boundary structure features a T-phase-like structure. (d) Experimental STEM ADF image at a typical stacking boundary, with the intensity averaged over 5 unit cells across the boundary, compared to the simulated STEM ADF image based on the atomic model in (c). The experimental and simulated STEM ADF images are plotted on the same color scale. (e) Energy barrier per atom as S migrates during domain wall propagation. (f) Schematic diagram of domain wall nucleation ($r = 0.0$) and domain growth ($r > 0.0$), starting from a pristine, strained AB-stacked bilayer. . 113
8.5 First-principles modelling of domain walls. (a) Atomic structure of the domain wall. The left side shows the AB domain while the right side shows the AA' domain, separated by the domain wall. The top half of the figure shows both the top and bottom layers of the bilayer, superposed with the 15% isosurface of the charge densities of the boundary states. The bottom half of the figure shows only the top layer, superposed with the contour lines of the same charge densities on a two-dimensional cut of the Mo plane. (b) Band structure of the domain wall within DFT in the local density approximation (LDA). 114
8.6 (a) Atomic structure of the domain wall separating AB and AA' domains. (b) shows the calculated change in the Mo-Mo distance of the top (red) and bottom (black) layers close to the domain wall in (a). In the top layer, S deficiency at the domain wall causes the Mo-Mo distance to narrow. 115
8.7 The $13 \times 1 \times 1$ supercell used for band structure calculation 116
8.8 (a) and (b), Atomic structures of domain walls 1 and 3, respectively. Band structures of domain walls 1 and 3, without H passivation (c and d) and with H passivation (e and f). 117

List of Tables

4.1 Calculated exciton binding energies E_b, exciton excitation energies E_{xct} and QP bandgap $E_{\mathrm{gap}}^{\mathrm{QP}}$ of bilayer WSe_2, for which the closest Se in the two layers are separated by 4 Å in the out-of-plane direction. In the first two columns, one (mono)layer is treated as an effective system embedded in the screening environment due to the second (mono)layer. In the first column, local field effects of screening due to the second layer is neglected in the in-plane directions but still explicitly included in the out-of-plane direction. In the second column, all local field effects of screening due to the second layer are included. In the third column, we report the results of exact calculations for an explicit bilayer WSe_2 system. (We use the following notations: ml for monolayer and bl for bilayer.) Precision to 1 meV obtained from *ab initio* calculations is given in parenthesis. 37

4.2 Eigenvalue-self-consistent (GW_0) QP bandgap renormalizations in meV of three different monolayer TMDs supported by different substrates, to the nearest 10 meV. "Sub" denotes substrate-only screening, while "Enc" denotes screening upon encapsulation. The GW_0 QP gaps (including spin-orbit coupling) for freestanding MoS_2, $MoSe_2$ and WSe_2 are calculated to be 2.42, 2.10 and 2.19 eV, respectively. The calculated values for monolayer WSe_2 are plotted in Fig. 4.2. . 41

4.3 Binding energies of four lowest-lying excitons at the K valley in monolayer WSe_2 when screened by different substrates and encapsulations, to the nearest 10 meV. The QP bandgap of monolayer WSe_2 when freestanding and when screened by SiO_2, hBN and graphene substrates are 2.19, 2.11, 2.06 and 1.93 eV (from Table 4.2). The excitation energies of these excitons are plotted in Fig. 4.3. Here, f denotes the oscillator strengths of the exciton and $\langle r \rangle$ denotes the root-mean-squared (rms) radius of its envelope function. 44

Acknowledgments

If there is a singular life-defining moment of my life, it has to be the time when I joined the Louie group as a graduate student. Six years since, words alone cannot describe the gratitude and indebtedness that I have towards my Ph.D. advisor, Professor Steven G. Louie, whose scientific rigor and intellect has led me far beyond my initial horizons of a dewy-eyed just-out-of-college graduate gazing wistfully into the allure of scientific research. I am forever grateful for your kindness, advices and the patience you have afforded me over the years, that I know are extremely valuable and can be hard to come by in an alternate universe.

I am also very grateful to Professor Marvin L. Cohen, with whom I have the privilege to collaborate. You have shown me what it is like to be extremely kind and knowledgeable at the same time, and that it is not only humanly attainable, but should also be the epitome of scientific excellence that one should strive for.

During my time in the Louie group, I benefitted immensely from its vibrant research environment. I have the great fortune of being able to work with incredibly talented and highly motivated individuals. My heartfelt gratitude goes out to Sinisa Coh, Marco Bernardi, Felipe H. da Jornada, Diana Y. Qiu and Ting Cao, with whom I am so privileged to have worked together very closely. Thank you for putting up with me all the time, for being so patient with me always and for unreservedly sharing your knowledge with me. We may or may not have the chance to work together again. Even as we will eventually part ways and move on to different pastures, I treasure the time we have spent working together, which will always remain etched as an indelible part of my living memory.

Just as importantly, I thank all former and current members of the Louie group with whom I have the privilege to interact, namely, Gabriel Antonius, Omar Ashour, Bradford A. Barker, Andrea Cepellotti, Yang-Hao Chan, Hyoung Joon Choi, Sangkook Choi, Jingwei Jiang, Sheng Ju, Yea-Lee Lee, Zhenglu Li, Johannes Lischner, Jamal I. Mustafa, Liang Z. Tan, Derek Vigil-Fowler, Meng Wu and Fangzhou Zhao. Thank you all for your friendship. You are great scientists and make incredible friends. Even though we may not have worked very closely together due to physical constraints, I have benefitted greatly from your counsels and scientific insights. I wish that one day I will have another chance at working with you again, even more closely this time.

Next, I want to express my immense gratitude to my experimental collaborators: Prof. Feng Wang, Prof. Alex Zettl, Aiming Yan, M. Iqbal Bakti Utama and Chaw Keong Yong. Thank you for being so supportive of my work. Experiment and theory are two sides of the same coin. I am a better scientist because of my collaborations with you. Given your world-class expertise, intellect and drive, I could not have asked for more.

I am also very grateful to Prof. Jun Ding and Prof. Yuan Ping Feng from the National University of Singapore and Mrs Joan Fong Fui Fong from the Raffles Junior College of Singapore for your invaluable tutelage and for setting me on this path of scientific research. The road has been long and winding, but it has been absolutely rewarding and is totally worth the ride. I also acknowledge the financial support from the Singapore National Research Foundation (Clean Energy) Ph.D. Scholarship for the majority of my Ph.D. studies.

To everyone I have mentioned above, my countless teachers, family, friends and colleagues, I am but a derivative of your collective wisdom, as it has always been and as it always will be. I love you all and thank you.

Chapter 1

Introduction

In terms of solar applications, silicon is the most widely used photovoltaic material today, dominating the photovoltaic industry by more than 90%. This is because silicon is non-toxic, abundant and benefits from technologies developed over the years in the microelectronics industry. Despite its widespread usage as a photovoltaic material, silicon does not efficiently absorb most of the light in the solar spectrum (Fig. 1.1) [7]. The solar spectrum that is

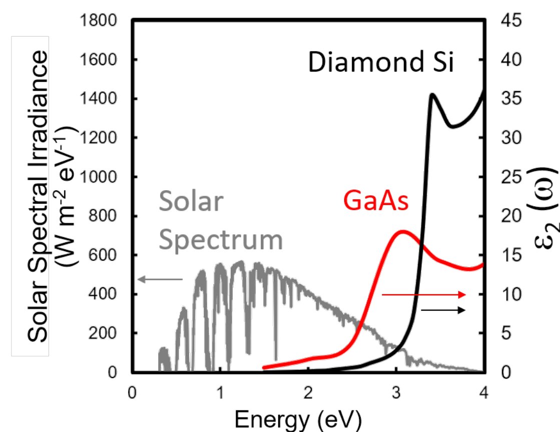

Figure 1.1: The GW-BSE optical spectrum of diamond-Si (black) and GaAs (red) and the measured solar spectrum (gray).

received on the Earth's surface [1] ranges from 0.3 to 4.4 eV and is the strongest around 1.2 eV (Fig. 1.1). According to the Shockley-Quiesser model [191], the optimal direct band gap for solar energy conversion lies within the range of 1.1 to 1.4 eV [191, 179, 170]. One approach [37] to increasing the absorption range of silicon is to find a crystal phase of silicon that has a smaller direct band gap than that of diamond-Si using first-principles computational techniques [220, 28, 163, 108]. In Chapter 2, we [157] aim to understand how the structure of an alternative silicon phase can lead to an improved calculated absorption

relative to diamond-Si. A real-space approach is introduced to understand the relationship between optical absorption and crystal structure, which is then used to study alternative phases of silicon, with a focus on the Si_{20} crystal phase [228]. We find that about 83% of the changes in the calculated low-energy absorption in Si_{20} as compared to Si in the diamond structure can be attributed to reducing the differences between the on-site energies of the bonding and anti-bonding orbitals as well as increasing the hopping integrals for specific Si-Si bonds.

On the other hand, gallium arsenide (GaAs) has advantages over silicon for solar applications because it has a direct band gap (Fig. 1.1) [7], its band gap of 1.4 eV is optimal for solar energy conversion according to the Shockley-Quiesser model [191, 179, 170] and its conduction electrons have very small effective masses, which are indicative of high carrier mobilities. This is despite the fact that GaAs is more expensive than Si and is also toxic due to the presence of arsenide. In energy applications, hot carriers lose energy over nanometer lengths and picosecond timescales, critically impacting the performance of electronic, optoelectronic, photovoltaic, and plasmonic devices. In Chapter 3, we [17] compute electron-phonon relaxation times at the onset of the Γ, L, and X valleys from first-principles and found them to be in excellent agreement with ultrafast optical experiments. We are able to show that the ultrafast (tens of femtoseconds) hot electron decay times observed experimentally arise from electron–phonon scattering. The work provides definitive microscopic insight into hot electrons in GaAs and accurate *ab initio* computation of hot carriers in advanced materials.

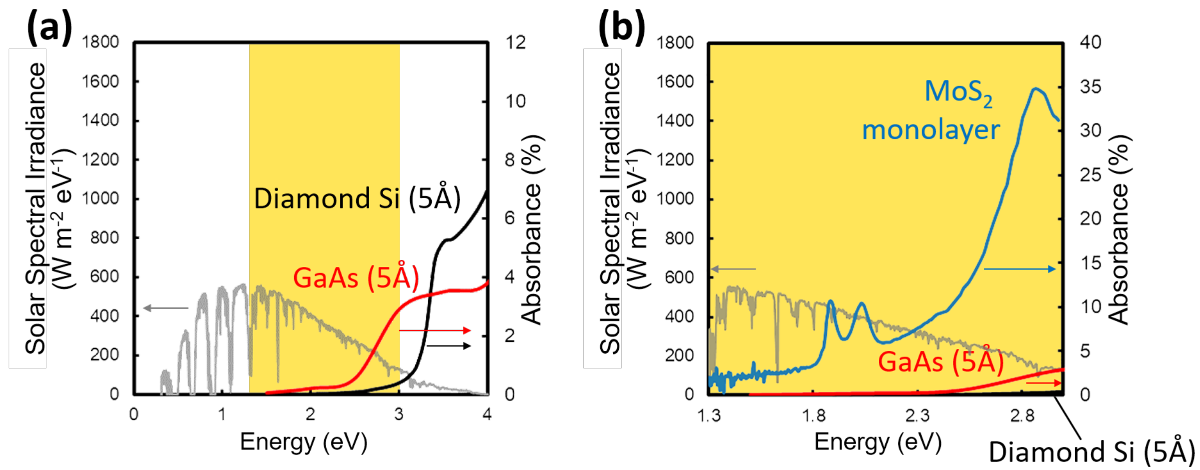

Figure 1.2: (a) The solar spectrum (gray) and the absorbance of 5-Å-thick diamond-Si (black) and 5-Å-thick GaAs (red). (b) A zoom-in of the energy range (shaded yellow) from 1.3 to 3.0 eV of (a), superposed with absorbance of a MoS_2 monolayer.

In the remaining chapters, I discuss excited states in mono- and few-layer transition metal dichalcogenides (TMDs), which are semiconducting quasi-2D materials. Due to their

reduced dimensions, atomically thin TMDs are candidate materials for flexible ultra-thin solar cells. Moreover, MoS_2, $MoSe_2$, and WS_2 also undergo a crossover from indirect to direct gap semiconductors when going from bilayer to monolayer [132], resulting in enhanced monolayer photoluminescence. Compared to the equivalent absorbance of Si and GaAs of similar thickness (~ 5 Å) (Fig. 1.2), we see that TMDs has significantly larger optical absorbance within the solar spectrum, making them appealing for solar energy conversion [7, 132, 16]. We use the term "quasi-2D" to describe the dimension of TMD to emphasize the fact that a monolayer TMD is a two-dimensional material embedded in a three-dimensional space. "Quasi-2D" is distinct from a purely two-dimensional model (Fig. 1.3a), which is in flatland and does not have an out-of-plane direction.

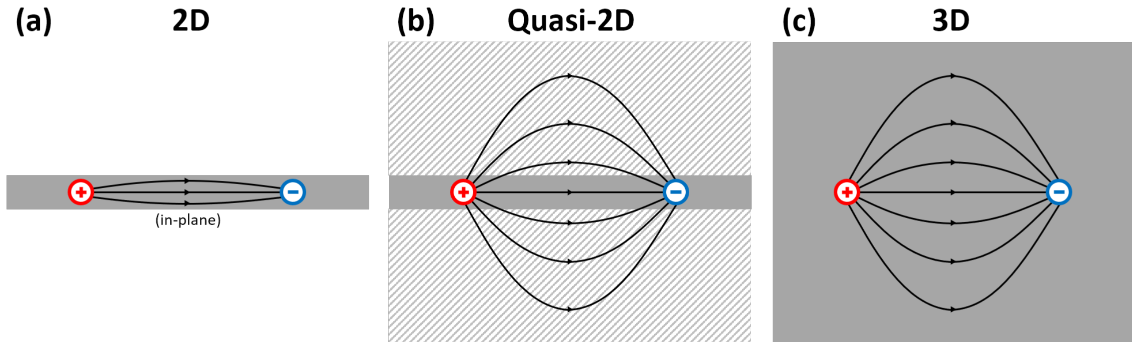

Figure 1.3: A schematic diagram of the field lines between two charges inside (a) 2D, (b) quasi-2D and (c) 3D materials.

In Chapter 4, I discuss how the electronic and optical properties of monolayer TMDs are affected by dielectric screening (Fig. 1.4) due to its environment. Unlike in a three-dimensional (Fig. 1.3c) material such as bulk silicon, electrons in an atomically-thin quasi-2D (Fig. 1.3b), like a TMD monolayer, are confined in their motions and experience reduced intrinsic dielectric screening. As a result, electron-electron and electron-hole interactions within the material are enhanced, leading to large bandgap renormalization due to self-energy effects and tightly-bound excitons [132, 33, 211, 168, 169]. In the non-periodic out-of-plane direction, the Coulomb field of the electrons extends outside of the quasi-2D material (Fig. 1.3b), and hence, unlike in a bulk 3D material (Fig. 1.3c), electrons in a quasi-2D material are sensitive to the screening environment due to its substrate and encapsulating material, which can drastically modify optical and electronic measurements and can also be exploited to bring about new applications [117, 211, 20, 167, 173, 199, 212, 215, 174].

It is now well-established [132, 168, 33, 211, 169] that the screening from substrates can strongly reduce many-electron interactions in quasi-2D materials and renormalize both the quasiparticle bandgap and the exciton binding energy. However, for metallic substrates, the frequency dependence of the screening plays a paramount role that is often ignored. In Chapter 4, we [158] predict that the frequency dependence of the substrate screening can

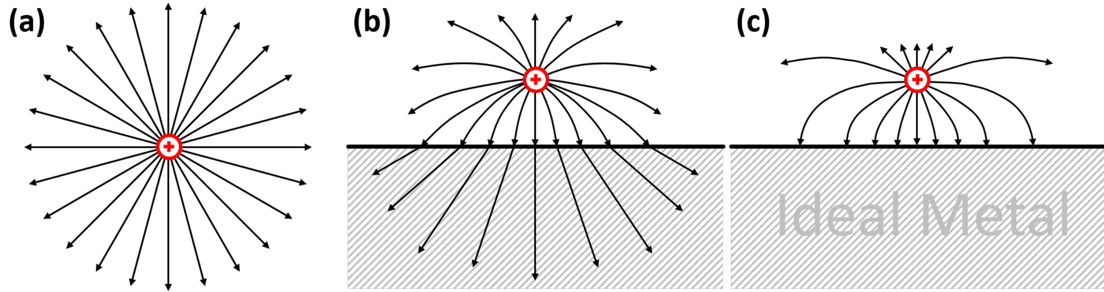

Figure 1.4: Dielectric screening of a charge. Charge is (a) completely unscreened, (b) partially screened by substrate and (c) completely screened by substrate.

induce a strong anti-screening effect within the quasi-2D material and lead to anomalously non-hydrogenic exciton energy levels. A systematic study of renormalizations by a wide range of experimentally-motivated substrates is also carried out and our calculated results show very good agreement with experiments. Computational details and the our derivation of the the frequency-dependent ideal-metal substrate (Fig. 1.4c) are elaborated in Chapter 5. In Chapter 6, we [212] show that this dielectric-dependent electronic bandgap can be used to engineer a lateral heterojunction within a homogeneous MoS_2 monolayer. We examine its electrical transport experimentally and theoretically. The heterostructure is visualized using a Kelvin probe force microscopy. We observe a lateral heterojunction with $\sim$90 meV band offset due to different bandgap renormalization of monolayer MoS_2 when it is on a substrate in which one segment is made from an amorphous fluoropolymer (Cytop) and another segment from hexagonal boron nitride. This heterostructure leads to a diode-like electrical transport with a strong asymmetric behavior.

Moreover, it was recently predicted that Berry phase effect can also modify the exciton states in transition metal dichalcogenide monolayers, and lift the energy degeneracy of exciton states with opposite angular momentum through an effective valley-orbital coupling [230, 251, 198, 210, 15, 224]. In Chapter 7, we [240] report the first observation and control of the Berry-phase induced splitting of the 2p-exciton states in monolayer $MoSe_2$ using the intraexciton optical Stark spectroscopy. We observe the time-reversal-symmetric analog of the orbital Zeeman effect resulting from the valley-dependent Berry phase, which leads to energy difference of +14 (-14) meV between the $2p_+$ and $2p_-$ exciton states in the K (K') valley, consistent with the ordering from our *ab initio* GW-BSE results. In addition, we show that the light-matter coupling between intraexciton states are remarkably strong, leading to prominent valley-dependent Autler-Townes doublet under resonant driving. This study opens up new pathways to coherently manipulate the quantum states and excitonic excitation with infrared radiation in two-dimensional semiconductors.

Lastly, in Chapter 8, we [236] study that metallic boundary states at the atomically-sharp lateral heterojunction between differently-stacked TMDs domains. In quasi-2D materials, the

ability to engineer its crystal symmetry has emerged as a promising way to achieve novel properties and functions. The non-centrosymmetric structure of monolayer TMDs, such as MoS_2, has allowed for valley control of optical excitations via circularly polarized optical excitation. In bilayer TMDs, inversion symmetry can be controlled by varying the stacking sequence, providing a pathway to engineer valley selectivity. With the *in situ* integration of AA' and AB stacked bilayer MoS_2 with different inversion-symmetries, we create atomically sharp stacking boundaries between the differently stacked domains. In this setup, we track the formation and atomic motion of the stacking boundaries, and in conjunction with density functional theory calculations, we establish the dynamics of the boundary nucleation and expansion, and identify the metallic boundary states. This approach provides a means to synthesize domain boundaries with intriguing transport properties, and opens up a new avenue for controlling valleytronics in nanoscale domains via real-time patterning of domains with different symmetry properties.

Chapter 2

Real-Space Study of the Optical Absorption in Alternative Phases of Silicon

2.1 Introduction

In order to reduce the cost of solar-cell energy generation, a great deal of effort has been put into attempts to increase the number of charge carriers collected by the solar cell relative to the number of incident photons (quantum efficiency). Silicon is the most widely used photovoltaic material. In terms of global annual power production, a recent market survey shows that crystalline silicon dominates the photovoltaic industry by more than 90%. One of the major reasons for its popularity is that silicon is non-toxic and abundant. There are also benefits from technologies developed over the years in the microelectronics industry.

Despite its widespread usage as a photovoltaic material, silicon does not efficiently absorb most of the light in the solar spectrum. The solar spectrum that is received at the Earth's surface (under the so-called air mass of 1.5 or AM 1.5 for short [1]) ranges from 0.3 to 4.4 eV and is the strongest around 1.2 eV. According to the Shockley-Quiesser model [191], the optimal direct band gap for solar energy conversion lies within the range of 1.1 to 1.4 eV [191, 179, 170]. Since silicon has a direct band gap of 3.3 eV, optical absorption due to direct transitions can only take place at the high-energy end of the solar spectrum between 3.3 and 4.4 eV. Phonon-assisted indirect transitions[150, 125] lower the onset of optical absorption to 1.2 eV. Even then, absorption coefficients due to indirect transitions alone are smaller and require the solar cell to be thick in order to amplify the phonon contributions. With a thicker absorber layer, the solar cell has to have high purity to prolong its carriers lifetime. Together, the increased thickness and need for material purity add to the cost of production.

Under ambient conditions, the diamond cubic phase (diamond-Si) is the most stable crystal phase of silicon, and this is also the crystal phase of silicon most commonly used to make solar cells today. However, silicon is known to exist in other crystal phases as

well. For instance, with increase in pressure, silicon undergoes phase transitions from the diamond-Si phase to the β-Sn phase [89], *Imma* phase [140], simple hexagonal phase [155, 80, 30, 31] and *Cmca* phase [75]. Pressure release from the β-Sn phase does not recover the diamond-Si phase. Instead, a slow pressure release produces the metastable R8 phase [165] which subsequently transforms into the BC8 phase [143, 98, 221, 135], while a very rapid pressure release leads to two other tetragonal phases [250]. Many of these phases are not suitable to make solar cells. For example, the first four phases mentioned above only exist under high pressure. The β-Sn and simple hexagonal phases are also metallic [30, 31] while the BC8 phase [135] is semi-metallic. On the other hand, phases like the R8 [134] and body-centered tetragonal [133] phases are semiconducting, and since they have direct band gaps smaller than diamond-Si's, they in principle can also absorb light over a wider energy range [37] than diamond-Si. Recently, a low-density silicon allotrope with an open silicon framework consisting of large empty channels, Si_{24}, has reportedly [100] been synthesized. It has a direct calculated G_0W_0 band gap of 1.34 eV, which is smaller than that of diamond-Si.

One approach [37] to increasing the absorption range of silicon is then to find a crystal phase of silicon that has a smaller direct band gap than that of diamond-Si. With the advent of first-principles computational techniques, it has become possible to search[220, 28, 163, 108] for crystal phases that have not been previously discovered. Botti *et al.* [19] found several crystal phases of silicon that have lower energies than the R8 and BC8 phases and have quasiparticle band gaps ranging from 0.8 to 1.5 eV from GW calculations. Wang *et al.* [218] proposed phases of silicon that have band gaps from 0.39 to 1.25 eV obtained within density functional theory (DFT) using the hybrid HSE functional. Lee *et al.* [109] used the conformational space annealing (CSA) approach and presented several other direct-gap silicon phases. Using the same CSA approach, Oh *et al.* [154] subsequently proposed a series of direct-gap silicon superlattices composed of bulk-like Si layers intercalated by defective layers made of Seiwatz chains [187]. Depending on the thicknesses of the bulk-like layers, these superlattices can have calculated G_0W_0 band gaps that fall within the optimal range for solar conversion.

In Ref. [228], Xiang *et al.* found the structure of Si_{20} (also called Si_{20}-T) using the particle swarm optimization (PSO) [220] approach. The calculated DFT-HSE band gap of Si_{20} is 1.55 eV. One of the structural features of Si_{20}, which is not found in diamond-Si, is that some of the bonds form equilateral triangles. In Ref. [228], it was suggested that these bonds might be related to its improved optical absorption. Nevertheless, the microscopic reason for the increase in the calculated absorption in Si_{20} remained unknown. In a related work, Guo *et al.* [72] proposed an alternative ground state of silicon with a band gap of 0.61 eV from DFT-HSE that also contains triangular bonds.

The purpose of this work is to understand how the structure of an alternative silicon phase may lead to an improved calculated absorption relative to diamond-Si. While there are many proposed metastable phases of silicon with improved absorption, we focus here in detail on Si_{20} as a case study for our approach since it has a very desirable calculated optical absorption. (We note that Si_{20} has a somewhat high formation energy [109, 5, 229], which may make it harder to access experimentally.) To demonstrate the generality of our

approach, near the end of this chapter, we also study two other silicon phases (SC5 and Si_{24}) that have drastically different structures from that of Si_{20}.

One of the obstacles in establishing the relationship between the crystal structure and optical absorption is the fact that the crystal structures of alternative phases of silicon like Si_{20} and diamond-Si are very different. For example, one cannot be related to the other by the removal or addition of a single atom, or by a small structural distortion that will not drastically disturb the bonding network of the silicon atoms. Moreover, the primitive unit cell of diamond-Si contains two atoms whereas that of Si_{20} contains 20 atoms. Therefore, a conventional analysis of optical absorption in the reciprocal space is non-trivial as each k-point in Si_{20} contains 40 valence and 40 conduction sp^3-like bands (unlike diamond-Si, which only has four of each).

To overcome this difficulty, we study the optical absorption in a real space representation using Wannier functions. Our analysis reveals that about 33% of the enhanced optical absorption of Si_{20} can be attributed to the decreased differences of the on-site energies between the bonding and anti-bonding orbitals. Roughly 50% is due to the increased hopping integrals between the bonding and anti-bonding orbitals. The remaining 17% is due to a variety of other contributions.

2.2 Method

In this section, we will first describe the conventional density functional theory (DFT) interband-transition approach and the GW plus Bethe-Salpeter equation (GW-BSE) approach for computing optical absorption in reciprocal space. The latter approach is more accurate and includes electron self-energy and electron-hole (excitonic) effects. Next we briefly introduce a real-space representation of the electronic structure in terms of Wannier functions. Finally, we transform the expression for the optical absorption from the reciprocal space representation into the real space representation.

Optical absorption

Optical absorption can be expressed through $\epsilon_2(\omega)$, the imaginary part of the dielectric function. Within the independent-particle DFT approach and neglecting the photon momentum, the diagonal elements of $\epsilon_2(\omega)$ can be computed using the random-phase approximation for a specific light polarization,

$$\begin{aligned}\epsilon_2(\omega) =& 8\pi^2 e^2 \hbar^2 \sum_{\mathbf{k}} \sum_{n\in\{C\}} \sum_{m\in\{V\}} |\mathbf{e}\cdot\langle n\mathbf{k}|\mathbf{r}|m\mathbf{k}\rangle|^2 \\ & \times \delta(\hbar\omega - E_{n\mathbf{k}} + E_{m\mathbf{k}}).\end{aligned} \tag{2.1}$$

Here $\mathbf{k}$ is the wave vector, $\mathbf{e}$ is the polarization direction, $\mathbf{r}$ is the position operator, ω is the frequency of absorbed photon, $E_{n\mathbf{k}}$ and $E_{m\mathbf{k}}$ are the DFT eigenvalues, $|n\mathbf{k}\rangle$ and $|m\mathbf{k}\rangle$ are

the DFT Bloch eigenstates and $\{V\}$ and $\{C\}$ are the valence and conduction bands. The matrix element $\langle n\mathbf{k}|\mathbf{r}|m\mathbf{k}\rangle$ describes a transition of an electron from state $|m\mathbf{k}\rangle$ into state $|n\mathbf{k}\rangle$ upon the absorption of a photon.

The $\epsilon_2(\omega)$ calculated within the DFT approach is shown in Fig. 2.1a for diamond-Si (black) and Si_{20} (red). In this calculation we used a norm-conserving pseudopotential and we used the local density approximation as implemented in Quantum-ESPRESSO [66]. The plane-wave cutoff for the electron wavefunction is 36 Ry. For diamond-Si, the Wannier functions are constructed from a coarse k-mesh of $16\times16\times16$ and they are used to interpolate quantities on a fine k-mesh of $30 \times 30 \times 30$ to calculate $\epsilon_2(\omega)$. For Si_{20}, the coarse k-mesh is $8 \times 8 \times 8$ and the fine k-mesh is $20 \times 20 \times 20$.

From Fig. 2.1a, it is clear that within the DFT approach, the onset of optical absorption in Si_{20} is 1.7 eV lower in energy than in diamond-Si. However, absorption of Si_{20} at the absorption edge is relatively small, and it increases significantly only at 0.8 eV above the absorption edge. Comparing the steep edges of the absorption spectra, the steep edge of Si_{20} is still about 0.9 eV lower in energy than it is for diamond-Si.

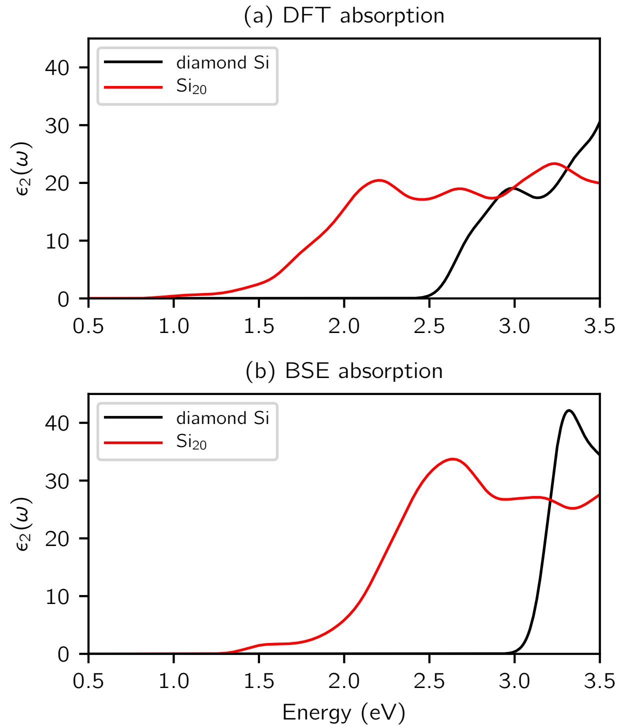

Figure 2.1: The absorption of diamond-Si (black) and Si_{20} (red) calculated with the DFT (a) and BSE (b) approaches.

In what follows, we discuss two well-known limitations of the optical absorption calculated

within the DFT-RPA approach. The first limitation is that the calculated DFT-LDA band gap is typically too small due the fact that DFT eigenvalues are not quasiparticle excitation energies. The GW approximation [83] removes this limitation by properly including the electron self energy effects. In the case of Si_{20} and diamond-Si, the inclusion of the GW correction [2] separates the DFT valence and conduction bands by 0.7–0.8 eV (depending on the k-points and electron bands) which is close to the value obtained by the hybrid-functional approach in Ref. [228].

The second limitation of the optical absorption calculated within the DFT approach is that it does not consider electron-hole interactions. Within the interacting many-electron picture, an electron is excited from a ground state $|0\rangle$ to an excited excitonic state $|S\rangle$ in which the electron interacts with the hole that it left behind. This process can be calculated [178] by solving the BSE and $\epsilon_2(\omega)$ is then expressed as,

$$\epsilon_2(\omega) = 8\pi^2 e^2 \hbar^2 \sum_S |\mathbf{e} \cdot \langle S|\mathbf{r}|0\rangle|^2 \delta(\hbar\omega - \Omega_S). \tag{2.2}$$

Here S labels the exciton states and Ω_S is the exciton eigenenergy.

The $\epsilon_2(\omega)$ spectra calculated [2] by solving the BSE for Si_{20} and diamond-Si are shown in Fig. 2.1b. Comparing the GW-BSE and DFT absorption spectra, we see two main differences. First, the absorption edge in the GW-BSE spectrum is 0.6 eV higher in energy than the edge in the DFT spectrum. This shift is close to the shift resulting from the GW correction (0.7 eV). The second difference with the GW-BSE approach is that $\epsilon_2(\omega)$ is larger in amplitude by a factor of about 1.5–2.0 near the band edge.

Therefore, while the optical absorption in absolute terms is very different between the GW-BSE and DFT approaches, the corrections made by the GW-BSE approach are nearly the same for both Si_{20} and diamond-Si. To better understand the improved absorption of Si_{20}, it is sufficient to focus on an analysis of results from the DFT-RPA approach, since the geometric effect of the crystal structure is already present at the DFT-RPA level.

Localized representation

The Bloch states appearing in the expression for $\epsilon_2(\omega)$ (in Eq. 2.1) have a well-defined crystal momentum $\mathbf{k}$. They are eigenstates of the Kohn-Sham Hamiltonian,

$$\langle n\mathbf{k}|H|m\mathbf{k}\rangle = \delta_{nm} E_{n\mathbf{k}}. \tag{2.3}$$

By superposing the Bloch states of different crystal momenta $\mathbf{k}$, one can construct a well localized Wannier state,

$$|j\mathbf{R}\rangle = \frac{1}{N_\mathbf{k}} \sum_{n\mathbf{k}} e^{-i\mathbf{k}\cdot\mathbf{R}} U_{nj}^{(\mathbf{k})} |n\mathbf{k}\rangle . \tag{2.4}$$

Here $\mathbf{R}$ is a real-space lattice vector and $U^{(\mathbf{k})}_{nj}$ is an arbitrary unitary matrix that mixes the Bloch bands at $\mathbf{k}$. In this chapter, we use indices i and j to denote individual Wannier functions and indices n and m to denote individual Bloch bands.

One often chooses the matrices $U^{(\mathbf{k})}_{nj}$ according to the scheme introduced by Marzari and Vanderbilt [139] so that $|j\mathbf{R}\rangle$ is as localized in real space around the centers of mass of the Wannier functions as possible. For this reason, $|j\mathbf{R}\rangle$ is also called the maximally localized Wannier function. The Bloch functions can be reconstructed back from the Wannier functions through an inverse transformation,

$$|n\mathbf{k}\rangle = \sum_{j\mathbf{R}} e^{i\mathbf{k}\cdot\mathbf{R}} U^{(\mathbf{k})\dagger}_{nj} |j\mathbf{R}\rangle \,. \tag{2.5}$$

Since the set of Wannier functions contains the same amount of information as the set of Bloch bands from which it is generated, it is convenient to rewrite the Hamiltonian and position operators in the Wannier basis. The Hamiltonian in the Wannier (or real space) representation is simply $\langle i\mathbf{0}|H|j\mathbf{R}\rangle$ which can be calculated by a Fourier transform of $\langle n\mathbf{k}|H|m\mathbf{k}\rangle$,

$$\langle i\mathbf{0}|H|j\mathbf{R}\rangle = \frac{1}{N_{\mathbf{k}}} \sum_{nm\mathbf{k}} e^{-i\mathbf{k}\cdot\mathbf{R}} U^{(\mathbf{k})\dagger}_{ni} \langle n\mathbf{k}|H|m\mathbf{k}\rangle\, U^{(\mathbf{k})}_{mj}. \tag{2.6}$$

There are two types of Hamiltonian matrix elements that we will focus on in this chapter. For the first type, we have $\mathbf{R} = \mathbf{0}$ and $i = j$. We will refer to this type of matrix element,

$$\langle i\mathbf{0}|H|i\mathbf{0}\rangle = e_{i,} \tag{2.7}$$

as the on-site energy of Wannier function i. The remaining matrix elements

$$\langle i\mathbf{0}|H|j\mathbf{R}\rangle = t_{ij\mathbf{R}} \tag{2.8}$$

are known as the hopping integrals. The hopping integral measures the probability amplitude for Wannier function j in cell $\mathbf{R}$ to tunnel to the Wannier function i in the unit cell at the origin.

Wannier functions are constructed from a set of Bloch bands so a different choice of Bloch bands will lead to different Wannier functions. Since the expression for optical absorption in Eq. 2.1 refers explicitly to occupied and empty Bloch states, we constructed the Wannier functions either from only empty or only occupied Bloch states. Therefore, by construction, $\langle i\mathbf{0}|H|j\mathbf{R}\rangle$ is zero unless bra and ket are either both derived from empty or occupied states.

We will refer to the Wannier functions constructed from the occupied Bloch states as bonding Wannier functions and those from the empty states of the relevant conduction bands as anti-bonding Wannier functions since they typically have real-space forms that resemble bonding and anti-bonding molecular orbitals. Since silicon bonds are highly covalent, the valence charges are localized on the bonds between these two nearest-neighboring silicon atoms. Therefore, the bonding and anti-bonding Wannier states are localized in the region

(a) Bonding Wannier function

(b) Anti-bonding Wannier function

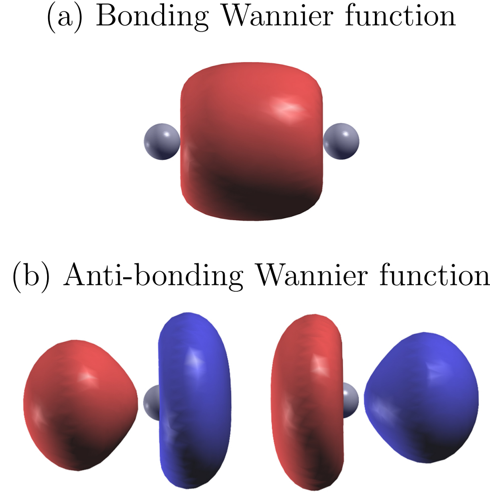

Figure 2.2: The isosurface of calculated bonding (a) and anti-bonding (b) Wannier functions in diamond-Si. Gray spheres are silicon atoms forming the bond. Isosurface in (a) is 1.4 and 1.0 in (b). Red and blue colors indicate parts of the Wannier function with opposite signs.

between these two silicon atoms, as shown in Fig. 2.2 for the case of diamond-Si. Each Si-Si bond has only one sp^3-like bonding and one sp^3-like anti-bonding Wannier function (per each spin). For convenience, we will label the on-site energy for the bonding and anti-bonding states as, e_i and $\bar{e}_i$ respectively. Similarly, we denote the hopping integral between anti-bonding states as $\bar{t}_{ij\mathbf{R}}$.

Optical absorption in the localized basis

The optical absorption calculated using $\epsilon_2(\omega)$ (Eq. 2.1) within the DFT-RPA approach depends on the energy of the Bloch states $E_{n\mathbf{k}}$, and the matrix element of the position operator. The Bloch state energies are fully determined by e_i and $t_{ij\mathbf{R}}$. Similarly, the position operator matrix element can be computed from its representation in the Wannier basis

$$\langle i\mathbf{0}|\mathbf{r}|j\mathbf{R}\rangle = \mathbf{r}_{ij\mathbf{R}}. \tag{2.9}$$

In all, optical absorption is exactly determined given the following three real-space quantities: e_i, $t_{ij\mathbf{R}}$, and $\mathbf{r}_{ij\mathbf{R}}$.

2.3 Results and discussion

In this section, we will compare e_i, $t_{ij\mathbf{R}}$, and $\mathbf{r}_{ij\mathbf{R}}$ in diamond-Si and Si_{20} and relate them to the structural differences between the two materials, as well as the differences in their optical absorption.

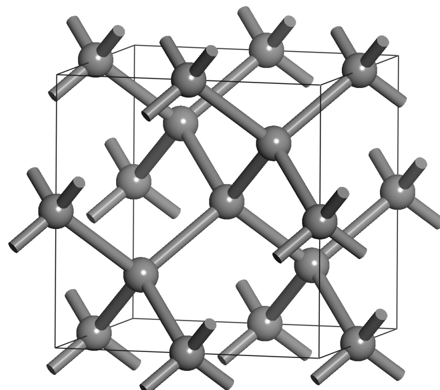

Figure 2.3: Conventional unit cell of diamond-Si containing eight silicon atoms. Its primitive unit cell contains only two silicon atoms.

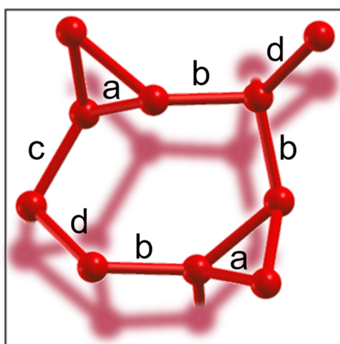

Figure 2.4: Conventional unit cell of Si_{20} containing 20 silicon atoms. Its primitive unit cell is the same as the conventional unit cell. Four distinct Si-Si bonds are indicated with labels a, b, c, and d. Bonds forming a triangle are labelled with letter a.

Comparison of structures

Figures 2.3 and 2.4 show the crystal structures of diamond-Si and Si_{20}. Both of their conventional unit cells have cubic lattices. In our calculations, we use fully relaxed structures of Si_{20} and diamond-Si. The lattice parameters of the conventional unit cells of Si_{20} and diamond-Si are 7.40 Å and 5.43 Å. On the average, Si_{20} has one Si atom every 20.2 Å^3 (2.30 g/cm^3) and diamond-Si has one atom every 20.0 Å^3 (2.33 g/cm^3).

Each Si atom in diamond-Si is tetrahedrally coordinated to four other Si atoms, such that every bond angle is exactly 109.5°. Every Si-Si bond in diamond-Si is symmetrically equivalent. The distance between the bond centers of two nearest-neighboring bonds is 1.9 Å.

For Si_{20}, every Si atom is also coordinated to four other Si, but in a distorted tetrahedron. The distortions bring some of the bond centers of Si_{20} closer together and others further apart. There are four symmetry-inequivalent groups of Si-Si bonds in Si_{20} and they are labelled from a to d in Fig. 2.4. One feature of the Si_{20} structure is the type-a bonds which form triangles. These bonds are highly strained as they are distorted from 109.5° to a narrow 60.0°. As a result, the distance between two nearest-neighboring bond centers ranges from as short as 1.2 Å (between two type-a bonds of the same triangle) to 2.1 Å. We will label this range, 1.2–2.1 Å, as the nearest-neighbor hopping regime.

On-site energy e_i

Here we compare on-site energies of diamond-Si and Si_{20}. Since we can assign a single bonding and anti-bonding Wannier function to each Si-Si bond, we will focus here on comparing the on-site energies, e_i and $\bar{e}_i$, for the same bond in the crystal.

Calculated values of e_i and $\bar{e}_i$ for diamond-Si and Si_{20} are shown in Fig. 2.5 with horizontal lines. The arrow represents the difference between e_i and $\bar{e}_i$ for a given set of symmetry-related bonds in the structure. In the case of diamond-Si, $\bar{e}_i - e_i$ for its Si-Si bond is 9.66 eV. On the other hand, $\bar{e}_i - e_i$ for Si_{20} ranges from 8.78 to 10.10 eV. The smallest value (8.78 eV) belongs to the highly strained type-a bonds. Its large deviation from diamond-Si's 9.66 eV is likely due to large strain present in these triangular bonds. Less strained type-b and type-c bonds have $\bar{e}_i - e_i$ similar to that in diamond-Si (9.64 and 9.78 eV). Finally, type-d bonds have the largest $\bar{e}_i - e_i$ (10.10 eV).

We expect that the smaller $\bar{e}_i - e_i$ of type-a bonds will lower the optical absorption edge of Si_{20} with respect to diamond-Si's. This will be analyzed in more detail in Sec. 2.3.

Hopping integral $t_{ij\mathbf{R}}$

After analyzing e_i, we now focus on the hopping integral $t_{ij\mathbf{R}}$ of diamond-Si and Si_{20}.

For the analysis of $t_{ij\mathbf{R}}$, we will define the hopping distance as the distance between the centers of mass of the Wannier functions $|i\mathbf{0}\rangle$ and $|j\mathbf{R}\rangle$, $\left| \langle i\mathbf{0}|\mathbf{r}|i\mathbf{0}\rangle - \langle j\mathbf{R}|\mathbf{r}|j\mathbf{R}\rangle \right|$. In what follows, we will relate $t_{ij\mathbf{R}}$ with its hopping distance.

Bonding states

First, we discuss the hopping integrals between bonding Wannier functions. As shown in Fig. 2.6, the hopping integrals of both diamond-Si and Si_{20} are nearly zero for hopping distances beyond 5 Å. This behavior is characteristic of the exponential localization [21] of Wannier functions for insulators.

The hopping integral $t_{ij\mathbf{R}}$ with the largest magnitude for diamond-Si is -1.23 eV. This hopping integral couples a bonding Wannier function with its nearest bonding neighbor and has a hopping distance of 1.9 Å. In Fig. 2.6, it is denoted by the leftmost black dot. For Si_{20}, hopping integrals coupling the nearest bonding neighbors are distributed over the range of

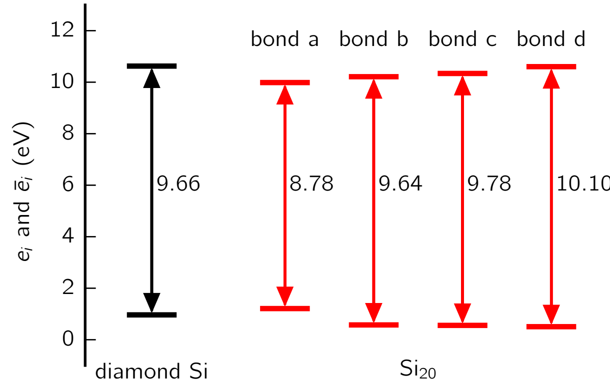

Figure 2.5: On-site energy of bonding (e_i, lower value) and anti-bonding ($\bar{e}_i$, higher value) Wannier function in diamond-Si (left, black) and Si_{20} (right, red). Numbers indicate $\bar{e}_i - e_i$ in eV. In the case of Si_{20} we show $\bar{e}_i - e_i$ for all four types of bonds. (The origin of the energy scale is arbitrary.)

1.2–2.1 Å (see Sec. 2.3). In Fig. 2.6, they are represented by the group of red dots surrounding the above-mentioned black dot.

The largest $|t_{ij\mathbf{R}}|$ for Si_{20} corresponds to the hopping integral with the shortest hopping distance of 1.2 Å. This hopping integral couples type-a bonds and is 0.70 eV larger than the largest $|t_{ij\mathbf{R}}|$ of diamond-Si. The presence of this large hopping integral in Si_{20} is due to the fact that the distance between triangular bonds is $1.9 - 1.2 = 0.7$ Å shorter than the shortest bond–bond distance in diamond-Si.

As we will analyze later in more detail, we expect the larger hopping integrals of the occupied Wannier functions to raise the valence band edge in Si_{20} as we expect the valence bands to have a larger bandwidth.

Anti-bonding states

Now, we look at the hopping integrals between the anti-bonding states. Figure 2.7 shows that the largest $|\bar{t}_{ij\mathbf{R}}|$ for diamond-Si is 0.54 eV and has a hopping distance of 5.8 Å. Unlike the bonding states, this largest $\bar{t}_{ij\mathbf{R}}$ does not couple the nearest-neighboring Wannier functions. That hopping integral is four times smaller (0.13 eV). For Si_{20}, the largest $|\bar{t}_{ij\mathbf{R}}|$ is 0.62 eV and has a hopping distance of 3.5 Å. It is somewhat larger than diamond-Si's largest $|\bar{t}_{ij\mathbf{R}}|$ and it also does not couple the nearest-neighboring Wannier functions.

Nevertheless, in the nearest-neighbor hopping regime of 1.2–2.1 Å, the largest $|\bar{t}_{ij\mathbf{R}}|$ in Si_{20} is 0.40 eV. This value is significantly larger than the corresponding $|\bar{t}_{ij\mathbf{R}}|$ for diamond-Si (0.13 eV) in the same regime.

Notably, even though $|\bar{t}_{ij\mathbf{R}}|$ for anti-bonding Wannier functions are nearly zero above

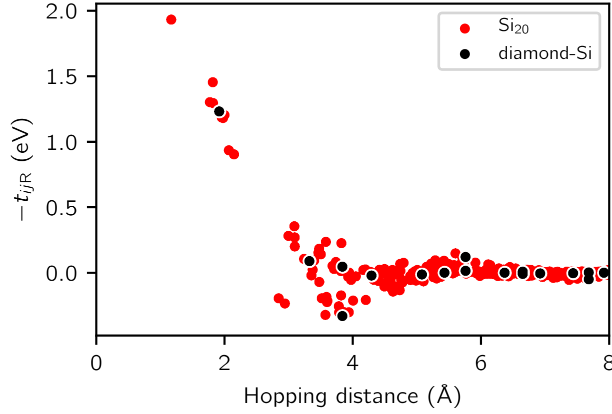

Figure 2.6: Hopping integrals between bonding Wannier functions, as a function of hopping distance for diamond-Si (black) and Si_{20} (red).

hopping distance of 9 Å, it does not increase monotonically below 9 Å as the hopping distance decreases. The distribution of $\bar{t}_{ij\mathbf{R}}$ (Fig. 2.7) is more dispersive than that of $t_{ij\mathbf{R}}$ (Fig. 2.6). This is likely related to the fact that the anti-bonding Wannier functions (Fig. 2.2b) have more nodes than the bonding Wannier functions (Fig. 2.2a). They are also more diffuse than the bonding Wannier functions. In addition, anti-bonding Wannier functions hybridize with the continuum, making them somewhat sensitive to the choice of the frozen window used in the Wannier disentanglement [195] procedure. (For consistency, we have chosen the frozen windows for both diamond-Si and Si_{20} to span the same energy range, from the conduction band minimum (CBM) to 3.5 eV above the CBM of diamond-Si.)

Hopping integrals between anti-bonding Wannier states of Si_{20} are distributed over a wider energy range than diamond-Si. We expect the larger hopping integrals between the empty Wannier functions of Si_{20} to increase the bandwidth of the conduction bands and lower its lower band edge. This will be further discussed in Sec. 2.3.

Position integral $\mathbf{r}_{ij\mathbf{R}}$

Now we discuss the third real-space object required to compute the optical absorption: position operator in the real space representation, $\mathbf{r}_{ij\mathbf{R}}$, between a bonding Wannier function and an anti-bonding Wannier function. (The matrix elements between two bonding or two anti-bonding Wannier functions do not enter into Eq. (2.1).)

For diamond-Si, $|\mathbf{r}_{ij\mathbf{R}}|^2$ is the largest when i and j are both centered on the same bond, as can be expected. Its value is $|\mathbf{r}_{ij\mathbf{R}}|^2 = 0.59$ Å^2 and it is seven times as large than that between the neighboring bonds (0.09 Å^2). For Si_{20}, the largest $|\mathbf{r}_{ij\mathbf{R}}|^2$ are also on the same bond. Their values for four types of Si_{20} bonds are nearly the same. Their average value is

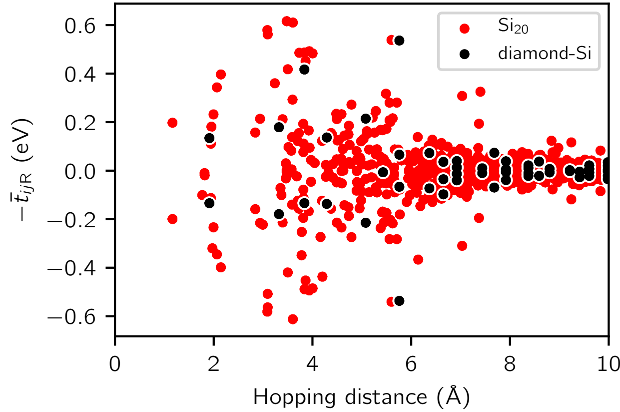

Figure 2.7: Hopping integrals between anti-bonding Wannier functions, as a function of hopping distance for diamond-Si (black) and Si_{20} (red).

0.53±0.02 Å^2. (The next largest value is only 0.15 Å^2.)

Here, two observations can be made. First, we see that in the real space representation, $|\mathbf{r}_{ij\mathbf{R}}|^2$, like the Hamiltonian, is highly localized. Second, the largest $|\mathbf{r}_{ij\mathbf{R}}|^2$ for Si_{20} and diamond-Si have nearly the same numerical value. This is likely because the Wannier functions of Si_{20} have similar real-space character as those in diamond-Si.

Relating e_i and $t_{ij\mathbf{R}}$ to the optical absorption

Now, we will relate the magnitudes of e_i and $t_{ij\mathbf{R}}$ to the optical absorption in diamond-Si and Si_{20}. For this purpose, we compute the optical absorption in three model systems, which are hybrids between diamond-Si and Si_{20}. These hybrid systems have the same Hamiltonian as Si_{20}, except for some e_i, $\bar{e}_i$, $t_{ij\mathbf{R}}$ and $\bar{t}_{ij\mathbf{R}}$ which are modified to resemble those in diamond-Si. Figure 2.8 shows the calculated optical spectra of diamond-Si (in solid black), Si_{20} (in solid red), and the hybrid systems (in dashed, dotted-and-dashed, and dotted red).

The dashed red curve in Fig. 2.8 shows the calculated optical absorption of the first hybrid system, where all on-site energies, e_i and $\bar{e}_i$, of Si_{20} are made to be equal to those of diamond-Si.

The dotted-and-dashed curve in Fig. 2.8 represents the second hybrid system where, on top of the modifications made for the first hybrid system, hopping integrals $t_{ij\mathbf{R}}$ between bonding Wannier functions are modified as well. This modification is done in the following way. First, we identify hopping integrals in Si_{20} larger than the nearest-neighbor hopping integral in diamond-Si (their values are −1.93, −1.45, −1.30, and −1.29 eV). Second, we modify these hopping integrals so that they are equal to the nearest-neighbor hopping integral in the diamond-Si (−1.23 eV).

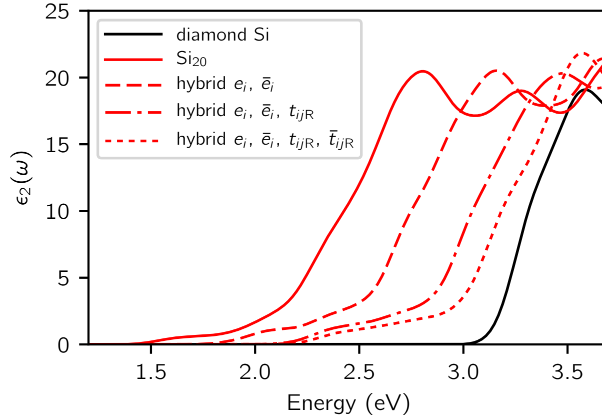

Figure 2.8: Optical absorption of diamond-Si (black), Si_{20} (solid red), and two hybrid cases (dashed, dotted, see text for details). Absorption curves are scissor shifted by 0.6 eV in all four cases based on our GW-BSE calculation.

Finally, the dotted red curve in Fig. 2.8 shows the optical absorption of the third hybrid system which, in addition to the modifications made for the first and second hybrid systems, has modified hopping integrals between the anti-bonding Wannier functions, $\bar{t}_{ij\mathbf{R}}$. Here we follow the same logic as is used for hopping integrals between the bonding Wannier functions. We first identify hopping integrals in Si_{20} in the nearest-neighbor regime that are larger than the nearest-neighbor hopping integral in diamond-Si (their magnitudes are 0.18, 0.20, 0.23, 0.32, 0.34, and 0.40 eV). Next, we modify these hopping integrals to the nearest-neighbor hopping integral between anti-bonding states in diamond-Si (0.13 eV).

As can be seen from Fig. 2.8, modifying only e_i and $\bar{e}_i$ shifts the leading edge of the absorption spectrum of Si_{20} to a higher energy by about 0.30 eV. This is about 33% of its difference with diamond-Si. Modifying e_i, $\bar{e}_i$, and $t_{ij\mathbf{R}}$ further shifts the leading edge of the absorption spectrum by another 0.30 eV. When e_i, $\bar{e}_i$, $t_{ij\mathbf{R}}$ and $\bar{t}_{ij\mathbf{R}}$ are all modified, the edge of the absorption spectrum is shifted by a total of 0.75 eV from the original calculated spectrum which accounts for approximately 83% of its difference with diamond-Si.

This behavior can be understood by considering a simple tight-binding model of a periodic one-dimensional mono-atomic chain. The band structure of such a model is given by $e + 2t\cos(ka)$ where e is the on-site energy, t is the hopping integral between the nearest-neighboring orbitals, and a is the distance between atoms. Therefore, on-site energy e can be thought of as an average energy of the band while the hopping integral t determines its bandwidth. This means that smaller $\bar{e}_i - e_i$ and larger $t_{ij\mathbf{R}}$ and $\bar{t}_{ij\mathbf{R}}$ found in Si_{20} will lower the average band gap.

The modifications that are made to the hybrid systems do not account for the remaining 17% and an absorption tail at low energy. We attribute this to the following two effects.

First, we only modified some of the larger hopping integrals in our calculations of the hybrid models. Second, even though we modified the hopping integrals in our calculations, we have always kept the crystal structure of Si_{20} the same. Therefore, relative phases of the Bloch states between neighboring silicon-bond sites will be different in Si_{20} and in diamond-Si. In other words, even if the hopping integrals were somehow made exactly the same in the two structures, their optical absorption edges may still not be the same because of this effect. Nevertheless, the total influence of these two effects on the improved optical absorption of Si_{20} is rather small (17%) and the majority of the difference can be attributed to the changes in the on-site energies and hopping integrals.

SC5 and Si_{24} silicon phases

To demonstrate the generality of our approach, we consider here two other phases of silicon that also absorb light (without phonon-assisted transitions) at photon energy lower than diamond-Si. The first phase can be described as a Si superlattice composed of alternating stacks of bulk-like Si layers intercalated by Seiwatz chains [154]. Each stack is made of five Si(111) layers of hexagonal diamond-Si. The Seiwatz chains are arranged in a configuration that results in a simple monoclinic Bravais lattice. We refer to this phase as SC5. The second phase is a low-density Si_{24} structure with an open silicon framework [100]. Unlike Si_{20} we discussed earlier, none of these two phases have Si-Si bonds in a triangular arrangement.

Repeating the analysis in the previous sections for SC5, we find that all of its bonds have $\bar{e}_i - e_i$ smaller than that in diamond-Si. In SC5, they range from 9.09 to 9.61 eV. If we change the on-site energies of SC5 to match those of diamond-Si, we find that the optical spectrum more closely resembles that of diamond-Si. This change in the on-site energies accounts for roughly 70% of the change in the optical absorption. Furthermore, if we also change the hopping integrals of SC5 to match those of diamond-Si, we find another 20% of the change in the optical absorption. Therefore, the improved calculated optical absorption edge of SC5 is mostly due to changes in the on-site energies, not hopping integrals. This is in contrast to Si_{20} where dominant effect came from the hopping integrals.

Switching now to Si_{24}, our calculation shows that most of the on-site energy differences $(\bar{e}_i - e_i)$ are larger than those in diamond-Si. Out of 24 bonds in the primitive unit cell, 18 have higher on-site energy differences while only six have smaller differences than that of diamond-Si. The range of calculated $\bar{e}_i - e_i$ in Si_{24} ranges from 9.18 to 10.69 eV. We attribute this to Si_{24}'s open silicon framework and its low density (2.17 g/cm^3) [100] as compared to that of diamond-Si (see Sec. 2.3). If we modify the on-site energies of Si_{24} so that they are equal to that of diamond-Si, we find that the onset of optical absorption shifts to a lower energy. If we also modify the hopping elements, the optical absorption more closely matches that of diamond-Si. Therefore, we conclude that in the case of Si_{24}, the effect of the on-site energies on the optical absorption is opposite to that of the hopping integrals.

2.4 Conclusion

The different structure of Si_{20}, relative to diamond-Si, leads to smaller on-site energy differences and larger hopping integrals between some of its Wannier functions. We have identified that most of these differences are due to the strained bonds forming triangles (i.e. type-a bonds) in Si_{20}. Different on-site energies and large hopping integrals are responsible for approximately 83% of the improved optical absorption in Si_{20} for photovoltaic applications relative to diamond-Si. The remaining difference is attributed to contributions from the smaller hopping integrals and the effect of the crystal structure on the relative phase of the electron wave functions.

Introducing strain to the bonds in the crystal structure turns out to be important when looking for crystal phases of silicon that have band gaps smaller than diamond-Si. However, as strain may reduce the band gap of diamond-Si, it also reduces the stability of the crystal structure. It is possible that a large band gap reduction may require a strain that is too large for the crystal structure to be thermodynamically stable. Hence, in the search for a practically viable silicon crystal phase that has a band gap smaller than that of diamond-Si, it is a balance between reducing the band gap and increasing the strain in the crystal structure.

Chapter 3

Ab initio Study of Hot Electrons in GaAs

3.1 Introduction

Hot carriers (HCs) generated by the absorption of light or injection at a contact are commonly found in many advanced technologies [56, 58, 60, 86, 206, 166, 38, 29, 145]. In electronics, the operation of high-speed devices is controlled by HC dynamics, and HC injection is a key degradation mechanism in transistors [71, 204]. In solar cells and plasmonics, recent work has focused on extracting the kinetic energy of HCs before cooling [38, 145], a process defined here as the energy loss of HCs, ultimately leading to thermal equilibrium. HC dynamics is also crucial to interpret time-resolved spectroscopy experiments used to study excited states in condensed matter [189]. This situation has sparked a renewed interest in HCs in a broad range of materials of technological relevance.

Experimental characterization of HCs is challenging because of the subpicosecond timescale associated with the electron-phonon (e-ph) and electron-electron (e-e) scattering processes regulating HC dynamics. For example, HCs can be studied using ultrafast spectroscopy, but microscopic interpretation of time-resolved spectra requires accurate theoretical models. However, modeling of HCs thus far has been dominated by empirical approaches, which do not provide atomistic details and use *ad hoc* parameters to fit experiments [56, 88]. Notwithstanding the pioneering role of these early studies, the availability of accurate *ab initio* computational methods based on density functional theory (DFT) [137] and many-body perturbation theory [83] enables studies of HCs with superior accuracy, broad applicability, and no need for fitting parameters.

Hot electrons in gallium arsenide (GaAs) are of particular interest because of the high electron mobility and multivalley character of the conduction band. Electrons excited at energies greater than ∼0.5 eV above the conduction band minimum (CBM) can transfer from the Γ to the L and X valleys, with energy minima at ∼0.25 and ∼0.45 eV above the CBM, respectively [126]. Such intervalley scattering processes play a crucial role in hot

electron cooling and transport at high electric fields.

Ample experimental data exist on hot electron transport and cooling in GaAs [189, 54, 184, 189, 241]. The interpretation of these experiments relies on Monte Carlo simulations using multiple parameters fit to experimental results. For example, Fischetti and Laux [56] used two empirical deformation potentials to model electron scattering induced by optical and acoustic phonons. Additionally, Fischetti and Laux [56] used simplified band structure and phonon dispersions. We note that, because multiple parameter sets can fit experimental results, the HC scattering rates due to different physical processes obtained empirically are not uniquely determined [56, 88].

Although heuristic approaches can provide some insight into HC dynamics of well-characterized materials (e.g., GaAs), there is a lack of generally applicable, predictive, and parameter-free approaches to study HCs.

Here, we carry out *ab initio* calculations of hot electrons in GaAs with energies up to 5 eV above the CBM. Our ability to use extremely fine grids in the Brillouin zone (BZ) allows us to resolve hot electron scattering in the conduction band with unprecedented accuracy. We focus here on three main findings. First, our overall computed e-ph scattering rates are in excellent agreement with those in previous semiempirical calculations in Ref. [56] that combine multiple empirical parameters. The advantage of our approach is the ability to compute the electronic band and momentum dependence of the e-ph scattering rates without fitting parameters. Second, we show that both optical and acoustic modes contribute substantially to e-ph scattering, with a dominant scattering from transverse acoustic (TA) modes. This result challenges the tenet that HCs lose energy mainly through longitudinal optical (LO) phonon emission. Third, our calculations provide valuable means for quantitative interpretation of experiments of hot electron cooling in GaAs. In particular, the ultrafast ($\sim$50 fs) e-ph relaxation times that we compute at the onset of the X valley are in excellent agreement with the fastest decay time observed in ultrafast optical experiments [54, 184, 241]. This signal was attributed by some [54] to e-e scattering and by others [241] to e-ph scattering. The excellent agreement with time decay signals in time-resolved experiments shows the dominant role of e-ph scattering for hot electron cooling at low carrier density.

Our approach combines electronic band structures computed *ab initio* using the GW (where G is the Green function, W is the screened Coulomb potential, and GW is the diagram employed for the electron exchange-correlation interactions) method [83] with phonon dispersions from density functional perturbation theory (DFPT) [11], and it is entirely free of empirical parameters. We compute the e-ph matrix elements using a Wannier function formalism [67] on very fine BZ grids and are able to resolve e-ph scattering for the different conduction band valleys. The e-e rates for hot electrons - also known as impact ionization (II) rates - are computed using the GW method [83, 78], and thus include dynamical screening effects. Additional details of our calculations are discussed in Sec. 3.4.

3.2 Results and Discussion

Accurate determination of e-ph scattering rates is essential to understand HC cooling with microscopic detail. Fig. 3.1A shows the computed e-ph scattering rates for hot electrons in GaAs with energies up to 5 eV above the CBM. Throughout this chapter, all energies are referenced to the CBM. The e-ph scattering rates follow trends similar to the electronic density of states (DOS), consistent with the fact that the DOS reflects the available phase space for e-ph scattering. At a fixed energy, the scattering rates are distributed over a range of values caused by the k dependence of the e-ph matrix elements (here, k is the crystal momentum of the electronic state in the BZ). We find a significant spread in the scattering rates for a fixed energy by up to ∼25% of their average value.

We carry out a quantitative analysis of the contributions from the individual phonon modes to the e-ph scattering rates. Analytical treatments of e-ph scattering in polar materials have relied extensively on the Fröhlich Hamiltonian [59, 127, 254], which couples electrons to LO phonons. This fact has often led to the assumption that e-ph scattering in polar materials is primarily caused by coupling of electrons with LO phonon modes. Fig. 3.1 B and C shows that all optical and acoustic modes contribute substantially to e-ph scattering in GaAs. Our calculations show that the TA modes provide the single largest contribution to e-ph scattering, whereas the LO modes possess the greatest scattering rates among the optical modes. The scattering rates from acoustic modes are overall roughly two times the value of the optical modes. These results highlight the limitations of previous models using LO phonon scattering alone and emphasize the need for *ab initio* calculations with fine k grids to obtain quantitative evaluations of e-ph scattering.

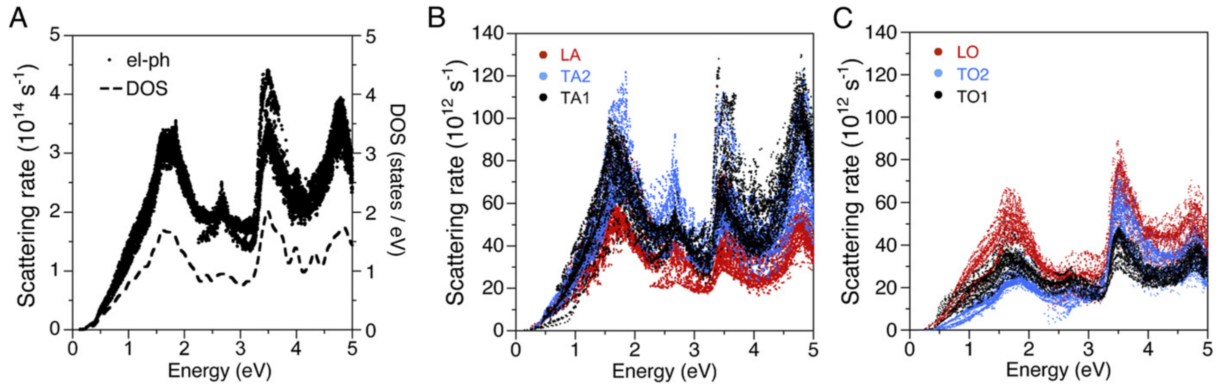

Figure 3.1: e-ph scattering in GaAs. (A) e-ph scattering rates for hot electrons in GaAs shown together with the electronic DOS. The zero of the energy axis is the CBM. The contributions to the total e-ph scattering rate in A from the acoustic and optical phonons are shown in B and C, respectively. LA, TA, LO, and TO label e-ph scattering induced by LA, TA, LO, and TO phonons in B and C. The sum of the scattering rates in B and C equals the total scattering rate in A.

The total *ab initio* e-ph scattering rates (i.e., summed over all modes) computed here are in excellent agreement with those obtained by Fischetti and Laux [56] (Fig. 3.2A), who used empirical deformation potentials to describe the coupling to optical and acoustic modes and the Fröhlich Hamiltonian to take into account the long-range effect on electrons of the LO phonons. Their empirical approach yields e-ph scattering rates able to reproduce experimental velocity-field curves in Monte Carlo calculations. The agreement with the total e-ph scattering rates fit to experiment highlights the accuracy of our *ab initio* approach and validates the Monte Carlo simulations carried out in Ref. [56]. Clearly, the additional benefit of our approach is the ability to compute e-ph scattering rates in the absence of experimental data. The agreement obtained here is striking given that multiple empirical parameters were used in Ref. [56]. We provide a detailed analysis of this result to understand the differences between previous semiempirical e-ph calculations and our *ab initio* approach.

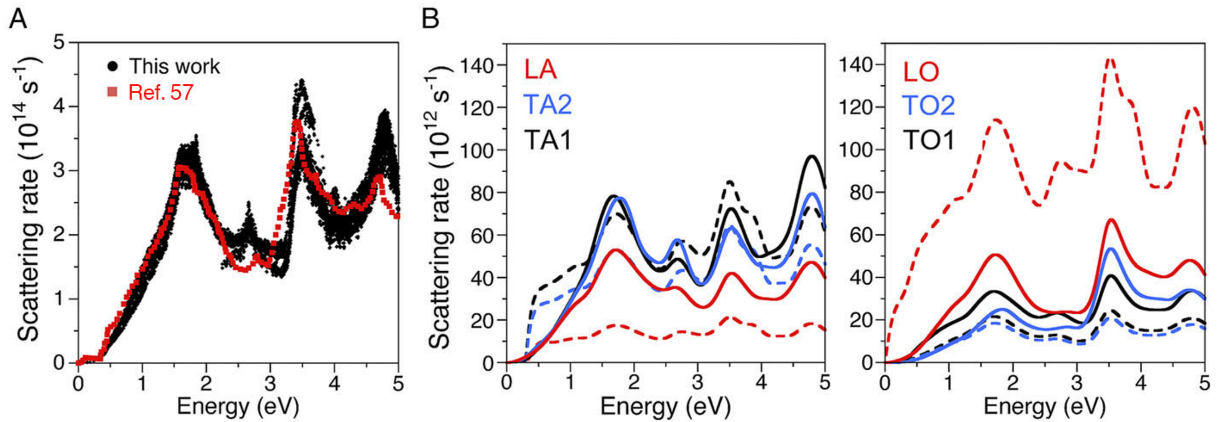

Figure 3.2: Comparison of *ab initio* and semiempirical calculations. (A) e-ph scattering rates from all modes in our work vs. those in Ref. [56]. (B) Contributions of individual phononmodes to the e-ph scattering rate for *ab initio* calculations (solid lines) carried out in this work and semiempirical calculations (dashed lines) that we reproduce using the parameters in Ref. [56]. The curves shown are the **k**-averaged scattering rates for (Left) acoustic modes and (Right) optical modes.

As noted by Ziman [254], accurate calculations of e-ph matrix elements are the nub of the e-ph interaction. For a scattering process connecting two electronic states that differ in crystal momentum by Zq, the e-ph matrix element is an integral of the initial and final Bloch states and the change in the crystal potential caused by a phonon with wavevector q (Eq. 2). Direct computation of such e-ph matrix elements within the adiabatic approximation requires knowledge of the potential acting on the electrons as well as the phonon eigenvectors and Bloch states in the entire BZ. Computation of these quantities has become possible owing to the advent of DFT and related methods [137], which were later extended to compute and interpolate e-ph matrix elements on fine reciprocal space grids [67, 59]. Such

detailed calculations were technically unfeasible in the early days of semiconductor physics and in particular, at the time of the work in Ref. [56]. The e-ph matrix elements were often approximated by mode-dependent parameters called deformation potentials [56, 88, 254] and multiplied by an overlap integral over the unit cell between the initial and final electronic states [56, 254]. In polar materials, such as GaAs, the Fröhlich Hamiltonian [59] was added explicitly to take into account the long-range electric fields generated by LO vibrations of the ions. The deformation potentials were then tuned until agreement with carrier velocity vs. electric field or other transport data was achieved in Monte Carlo calculations using the computed e-ph scattering rates. However, because multiple deformation potentials are used in such semiempirical e-ph calculations, different choices of the parameters are able to reproduce the total e-ph scattering rates and thus, the experimental data. The contributions of individual phonon modes are, thus, ambiguously determined in the semiempirical approach, because they are arbitrarily set by the particular choice of the deformation potentials. In contrast, individual phonon contributions are uniquely determined in *ab initio* calculations.

To carry out a quantitative comparison of the individual phonon mode contributions with the work by Fischetti and Laux [56], we attempted to reproduce their calculations by combining our band structures and phonon dispersions with their deformation potential parameters (Methods). The total e-ph scattering rates obtained with this approach agree well with Ref. [56], thus guaranteeing that we correctly reproduced their calculations. Fig. 3.2B shows a comparison between this work and Ref. [56] of the e-ph scattering rates from individual phonon modes. Despite the fact that the total scattering rates are in excellent agreement, we find that the scattering rates from individual phonon modes largely differ in the two approaches. Compared with our *ab initio* calculations, scattering by longitudinal acoustic (LA) phonons is largely underestimated, and scattering by LO phonons is largely overestimated in Ref. [56]. In addition, scattering by transverse optical (TO) phonons is slightly underestimated, whereas scattering by TA phonons is adequately described in Ref. [56]. The too-large LO e-ph scattering rates in Ref. [56] seem to be compensated by too-small acoustic scattering rates compared with our calculations as a consequence of the arbitrary choice of deformation potential parameters for acoustic phonons. The different LO scattering rates are caused by a key difference between the *ab initio* treatment of the e-ph interaction in polar materials and semiempirical theories. In the *ab initio* approach, explicit inclusion of the Fröhlich Hamiltonian becomes redundant, because it assumes the concept of rigid ions carrying a net charge. Inclusion of both Fröhlich and nonpolar matrix elements for LO phonons in semiempirical treatments is clearly ad hoc, because it arbitrarily separates the long- and short-range e-ph interactions, which are taken into account on the same footing in *ab initio* calculations. Future work will be necessary to more fully establish the differences between the *ab initio* approach based on DFT adopted here and semiempirical theories for a range of polar and nonpolar materials.

The main practical challenge to control HC dynamics in devices is the subpicosecond timescale for HC cooling. This situation has led to extensive studies with ultrafast pump-probe spectroscopies to understand the microscopic details of HC cooling. Fig. 3.3A shows our computed e-ph relaxation times (defined here as the inverses of the e-ph scattering rates)

for energies up to 1.5 eV. We find relaxation times of ∼1.5 ps, 200 fs, and 50 fs at energies near the bottom of the Γ, L, and X valleys, respectively. Within an optical phonon energy (∼40 meV in GaAs) of the onset energy of the valleys, the e-ph relaxation times increase rapidly as the carrier energy approaches the valley minima because of the decrease in the DOS of the given valley and the resulting decrease in the phase space for intravalley e-ph scattering.

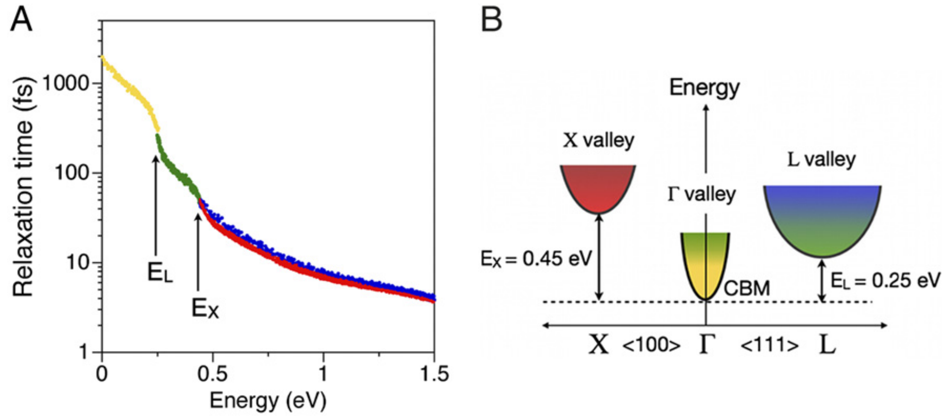

Figure 3.3: e-ph relaxation times in GaAs. (A) e-ph relaxation times of hot electrons in GaAs. Up to E_X, data points shown in yellow originate from electronic states in the Γ valley, and data points shown in green originate from states at the bottom of the L valley. At energies above E_X, states in red and blue are located near the X and L valleys, respectively. (B) Schematic of the states and valleys giving rise to the e-ph scattering rates in A.

The energy range above E_X has been studied extensively in ultrafast optical experiments because of the coexistence of the Γ, L, and X valleys. We find that the relaxation times decrease rapidly from ∼200 fs at E_L to ∼10 fs at 1.5 eV energy and remain nearly constant above 1.5 eV. At the onset of the X valley at energy E_X, the scattering rates split into two different curves, with one set of scattering rates higher than the other by ∼10%. The higher scattering rates are associated with hot electron states in the X valleys, whereas the lower scattering rates stem from hot electrons in the L valleys. The distinct behavior of the two sets of states extends up to 1.5 eV and thus, for ∼1 eV above E_X. We remark that existing models of e-ph scattering in GaAs have so far relied on energy- but not k-dependent scattering rates. Our calculations show that the scattering rates for the L and X valleys are slightly different, thus complicating the hot electron dynamics caused by intervalley scattering.

Below, we use our calculations to analyze previous experiments of hot electron cooling after excitation with ∼2 eV light [54, 184, 189, 241]. These experiments use time-resolved absorption and luminescence measurements with sub-100-fs time resolutions and report inelastic scattering of the hot electrons over tens of femtoseconds. Such ultrafast inelastic

processes were attributed by some to e-e scattering [54], even at low carrier density, where e-e scattering is typically minimal [188]. Other works attributed the fast inelastic scattering to e-ph processes. For example, Young et al. [241] have carried out transient absorption experiments at different carrier densities and found that the decay of the absorption bleaching signal shows little variation with carrier density. At low carrier density, where e-ph is typically the dominant inelastic scattering process, Young et al. [241] find that the recovery of the bleaching at 2 eV can be fit by three exponentials with decay times of 35 fs, 185 fs, and 1.4 ps and attribute these features to e-ph scattering. We find that the decay times in the work in Ref. [241] are in excellent agreement with the relaxation times presented in Fig. 3.3A, which are discussed next.

The valence band edge of GaAs is split at Γ because of the spin-orbit interaction into two valence band maximum (VBM) states (heavy- and light-hole bands) and the split-off (SO) band located 350 meV below the VBM. Given the ∼1.4-eV gap of GaAs, pumping with 2 eV light, thus, generates hot electron populations at energies of ∼0.5 eV above the CBM because of excitation from the heavy- and light-hole bands and ∼0.15 eV because of excitation from the SO band [241]. Our computed e-ph relaxation time of ∼50 fs at 0.5 eV above the CBM is in very good agreement with the 35-fs decay signal found experimentally by Young et al. [241] and attributed to intervalley scattering from the Γ to the L and X valleys. In addition, the 185-fs timescale attributed in Ref. [241] to e-ph scattering of electrons excited from the SO band agrees well with the ∼200-fs relaxation time that we predict at the bottom of the L valley. Finally, the 1.4-ps rate for the overall carrier cooling is in agreement with a fast transfer to the Γ valley followed by cooling to the CBM with ∼1.5-ps relaxation time as found in our calculations.

In comparing experimental decay times of the bleaching signal with computed e-ph relaxation times, one must keep in mind that the pump pulse has a finite energy resolution and thus, generates a pocket of carriers with a spread in energy. The probe pulse also has a finite energy resolution and captures average carrier relaxation times from several states. Given these differences and considering the rapid variation of the computed e-ph scattering rates around E_L, we believe that the attribution in Ref. [241] of the 185-fs decay signal to the electrons excited from the SO band is correct and consistent with our calculation. Although a direct comparison of state-specific e-ph relaxation times (i.e., state lifetimes) with decay times in transient absorption experiments is approximate, we believe it is justified here by the fact that the probe populates well-defined conduction band states; therefore, the bleaching decay time in Ref. [241] can be interpreted as the relaxation time or state lifetime of specific conduction band states, consistent with the interpretation given in Ref. [241]. Our data seem to confirm the interpretation in Ref. [241] that the e-ph interaction alone can account for the ultrafast inelastic scattering at low carrier density observed in several experiments [54, 184, 189, 241].

To further show that e-ph scattering dominates the cooling of low-energy hot electrons, we carry out GW calculations of the II rates (Sec. 3.4), which are shown in Fig. 3.4. The II rates are well-fit by a Keldysh formula: $\Gamma_{II} = \alpha \cdot (E - E_{th})^{\beta}$, where Γ_{II} is the II rate, E_{th} is a threshold energy for the onset of II, and α and β are fitting coefficients. Similar to

previous work [56, 164, 96], we use a threshold $E_{th} = 1.7$ eV for the onset of II and obtain fitting coefficients of $\alpha = 10^{13}$ s^{-1} and $\beta = 2.36$. The threshold is numerically close to the GW band gap of GaAs, and the value of β deviates from the parabolic trend (i.e., $\beta = 2$) found in the free electron gas [127] caused by the multiband character of GaAs. The II rates become greater than the e-ph rates at energy higher than ∼6 eV, and we, thus, predict that energy loss for hot electrons with energy higher than 6 eV is dominated by inelastic II and Auger processes. Because of the use of the random phase approximation (RPA) screening in the GW formalism, our approach can provide accurate rates for interband II processes induced by the screened Coulomb interaction. However, phonon-assisted II processes are not included in the GW formalism and may result in underestimating the experimental II rates.

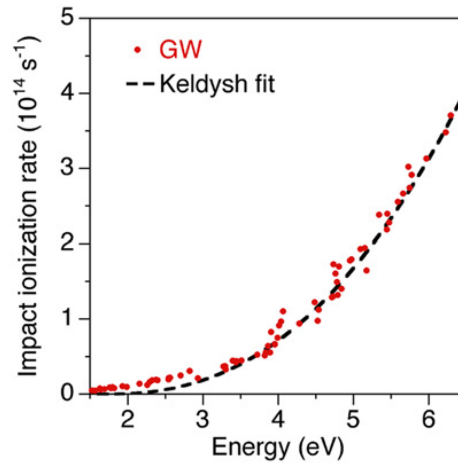

Figure 3.4: II rates in GaAs. II rates computed with the GW method shown together with the Keldysh fit. The energies are referenced to the CBM and extend to ∼5 eV above the II threshold.

In assessing the accuracy of our calculations, we note that recent *ab initio* calculations of Auger scattering (i.e., the inverse process of II) show that phonon-assisted Auger rates are at least one order of magnitude higher than the Auger rates caused by the Coulomb interaction alone [97]. This finding suggests that accurate calculations of II rates caused by the Coulomb interaction should underestimate the experimental II rates caused by the absence of phonon-assisted processes. The empirical II rates calculations in Ref. [56] should be able to yield the correct order of magnitude for the II rates because of their accurate e-ph rates and the fit to experiment data. The absence of phonon-assisted processes in our approach justifies our lower II rates compared with those in Ref. [56] (Fig. 3.5). However, even with the II rates in Ref. [56], our conclusions are unchanged regarding the dominant role of the e-ph scattering for hot electron cooling up to ∼2 eV energy as used in the experiments considered here.

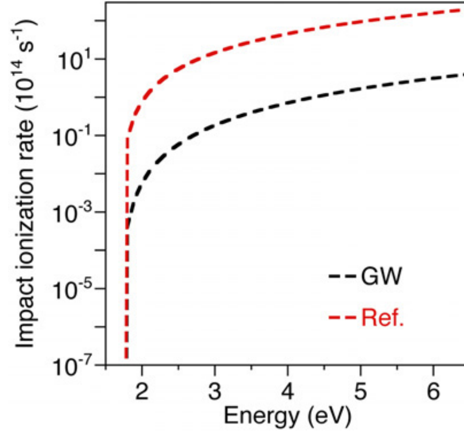

Figure 3.5: Comparison between the GW II rates in this work (black curve) and those in Ref. [56] (red curve). Shown are the Keldysh fits of the two datasets.

Finally, we note that our e-e scattering rates do not include e-e scattering among excited carriers within the conduction band, namely processes whereby a hot electron loses energy by transferring it to another conduction band electron. At high carrier density (e.g., greater than 1018 cm^{-3}), this mechanism is important to achieve equilibrium within the hot electron gas, because it leads to the establishment of a hot electron temperature and a corresponding HC Fermi-Dirac distribution. Our scattering rates are, thus, expected to be accurate only at relatively low carrier density. We note that at high carrier density the GW formalism can, in principle, account for e-e scattering within the conduction band provided that the dielectric screening and Green functions are appropriately computed with an additional assumed out-of-equilibrium initial carrier distribution or alternatively, a hot Fermi-Dirac distribution. However, one problem associated with this approach is that such e-e scattering processes are so fast that they usually take place while the pump pulse is still on; therefore, an initial carrier distribution cannot be defined for the computation of the GW self-energy. To circumvent this bottleneck, truly nonequilibrium *ab initio* theories need to be developed (for example, by evolving in time nonequilibrium Green's functions on the Keldysh contour [97]), which is beyond the scope of this study.

3.3 Conclusion

In summary, although the theoretical interpretation of HC dynamics and time-resolved spectroscopy without empirical parameters is still in its infancy, our *ab initio* calculations show excellent agreement with semiempirical e-ph scattering rates and ultrafast spectroscopy data. Taken together, these results show the dominant role of e-ph scattering in hot electron cooling in GaAs. Our work further highlights the need to treat e-ph interactions in GaAs (and more

broadly, polar semiconductors) with models going beyond the Fröhlich Hamiltonian and include all phonon modes on the same footing with *ab initio* calculations of e-ph scattering. Although such calculations are currently computationally expensive and highly specialized, our recent improvements in the algorithms (to be reported in the future) can make them more broadly accessible. The computational approach to study HCs and ultrafast electron scattering shown in this work is general and can be applied to semiconductors, insulators, metals, surfaces, and nanostructures. HCs are relevant in several branches of materials science and applied physics, including electronics, optoelectronics, semiconductor physics, solar energy, plasmonics, and spectroscopy. In several cases of practical interest (e.g., solar energy conversion, plasmonics, and photocatalysis), HCs are generated at low density, and therefore, the approach developed here can capture HC cooling processes of relevance in these applications.

3.4 Methods

We carry out *ab initio* calculations on GaAs in the diamond structure with a DFT-relaxed lattice parameter of 5.55 Å. The ground-state electronic structure is computed within the local density approximation (LDA) of DFT using the QUANTUM ESPRESSO code [27, 161, 66]. Norm-conserving pseudopotentials are used to describe the core-valence interaction [208], and a kinetic energy cutoff of 45 Ry is used for the plane-wave basis set; e-ph and II calculations are discussed below.

e-ph Scattering Calculations

Lattice dynamical properties are computed by means of DFPT [241]. We use an in-house modified version of the EPW code [149] to compute the imaginary part of the lowest order e-ph self-energy, Im $(\Sigma^{e-ph}_{n,\mathbf{k}})$, for the Bloch state of energy $\epsilon_{n,\mathbf{k}}$ at band n and $\mathbf{k}$ point in the BZ:

$$\mathrm{Im}(\Sigma^{e-ph}_{n,\mathbf{k}}) = \sum_{m,\lambda,\mathbf{q}} |g^{\lambda,\mathbf{q}}_{n,m,\mathbf{k}}|^2 \mathrm{Im}\left[\frac{N_{\lambda,\mathbf{q}} + 1 - f_{m,\mathbf{k}}}{\epsilon_{n,\mathbf{k}} - \epsilon_{m,\mathbf{k+q}} - \hbar\omega_{\lambda,\mathbf{q}} - i\eta} + \frac{N_{\lambda,\mathbf{q}} + f_{m,\mathbf{k}}}{\epsilon_{n,\mathbf{k}} - \epsilon_{m,\mathbf{k+q}} + \hbar\omega_{\lambda,\mathbf{q}} - i\eta}\right] \tag{3.1}$$

where $\epsilon_{n,\mathbf{k}}$ is the GW quasiparticle energy, $\hbar\omega_{\lambda,\mathbf{q}}$ is the energy of a phonon with polarization λ and wavevector $\mathbf{q}$ in the BZ, $f_{m,\mathbf{k}}$ and $N_{\lambda,\mathbf{q}}$ are Fermi and Bose occupation numbers, respectively (evaluated here at room temperature), and η is a small Lorentzian broadening (here, we use η = 10 meV). In Eq. 3.1, the key quantities are the e-ph matrix elements, which are defined as

$$g^{\lambda,\mathbf{q}}_{n,m,\mathbf{k}} = \sqrt{\frac{\hbar}{2M\omega_{\lambda,\mathbf{q}}}}\, \langle \Psi_{m,\mathbf{k+q}} | \partial_{\lambda,\mathbf{q}} V | \Psi_{n,\mathbf{k}} \rangle \tag{3.2}$$

where $\Psi_{n,\mathbf{k}}$ is the Kohn-Sham wave function for band n and $\mathbf{k}$ in the BZ, $\partial_{\lambda,\mathbf{q}}V$ is the variation of the Kohn-Sham potential for a unit displacement of the nuclei along the phonon mode of polarization λ and wavevector $\mathbf{q}$, and M is the mass of the unit cell. The e-ph scattering rate $\Gamma^{e-ph}_{n,\mathbf{k}}$ is computed from the imaginary part of the self-energy as $\Gamma^{e-ph}_{n,\mathbf{k}} = \frac{2}{\hbar} \cdot \mathrm{Im}(\Sigma^{e-ph}_{n,\mathbf{k}})$, and the relaxation time $\tau_{n,\mathbf{k}} = (\Gamma^{e-ph}_{n,\mathbf{k}})^{-1}$ is the inverse of the scattering rate. We remark that this procedure is equivalent to applying perturbation theory in the lowest order of the e-ph perturbation [127]. We first compute the electronic states on an $8 \times 8 \times 8$ k-point grid using DFT corrected with the GW self energies and the vibrational states on an $8 \times 8 \times 8$ q-point grid using DFPT. The e-ph matrix elements are computed using these coarse grids. We then interpolate the quantities needed to evaluate the e-ph self-energy on significantly finer grids using an interpolation procedure based on Wannier functions implemented in the EPW code [149]. Our fine grids consist in a $40 \times 40 \times 40$ k-point grid and up to 512,000 random $\mathbf{q}$ points in the BZ. Such fine grids allow us to fully converge the self-energy in Eq. 3.1. The scattering rates for the individual phonon modes shown in Fig. 3.1 are computed by restricting the summation in Eq. 3.1 to a given phonon mode (i.e., a given phonon branch and thus, a given value of λ). The e-ph relaxation times near the bottomof the valleys in Fig. 3.3 were computed separately with fine grids up to $200 \times 200 \times 200$ k points around the minimum of each valley to resolve the relaxation times. Convergence with respect to all parameters was carefully tested. The converged e-ph calculations shown in this work require computing ∼10 trillion e-ph matrix elements; these matrix elements are used on the fly to compute the e-ph self-energy, because their storage would require tens of terabytes of memory.

To reproduce the semiempirical calculations in Ref. [56], we set the square modulus of the matrix elements to $|g^{\lambda,\mathbf{q}}_{n,m,\mathbf{k}}|^2 = |\frac{\hbar}{2M\omega_{\lambda,\mathbf{q}}}| \cdot \Delta^2_\lambda(q) \cdot I^2(q)$, where $\Delta_\lambda(q)$ is the deformation potential for the phonon mode λ, and the overlap integral is computed in the rigid ion approximation [254], yielding $I(x) = 3[x\cos(x) - \sin(x)/x^3$, where $x = qr_0$ and r_0 is the Wigner-Seitz cell radius [254]. The deformation potentials are taken from Ref. [56]. (i) For optical phonons, $\Delta_{OP}(q) = b \cdot q$, where $b = 5.0$ eV for electron energy above 0.3 eV and $b = 7.0$ eV for electron energy below 0.3 eV. (ii) For acoustic phonons, $\Delta_{AC}(q) = a$, where $a = 2.1 \cdot 10^8$ eV/cm for electron energy above 0.3 eV and $a = 0$ eV for electron energy below 0.3 eV. (iii) For LO phonons, we add the Fröhlich contribution $\Delta^2_{LO,F} = [\frac{\hbar}{2M\omega_{\lambda,\mathbf{q}}}]^{-1} \cdot [\frac{\pi e^2 \hbar\omega_{LO}}{V_{uc}q^2}] \cdot (\frac{1}{\epsilon_\infty} - \frac{1}{\epsilon_0})$, where $\hbar\omega_{LO}$ is the LO phonon energy at the BZ center, V_{uc} is the volume of the unit cell, and ϵ_∞ and ϵ_0 are the high and low frequency dielectric constants of GaAs, respectively. All electron energies above are referenced to the CBM.

Impact Ionization (II) Calculations

We carry out full-frequency GW calculations [83, 78] using the BerkeleyGW code [46] to compute the imaginary part of the GW self-energy, Here, $\mathrm{Im}(\Sigma^{GW}_{n,\mathbf{k}})$ denotes the diagonal matrix element of the imaginary part of the GW self-energy for the Kohn-Sham state $|n, \mathbf{k}\rangle$, and we compute $\mathrm{Im}(\Sigma^{GW}_{n,\mathbf{k}})$ on shell (i.e., we evaluate it at the LDA eigenvalues). Kinetic

energy cutoffs of 10 and 45 Ry are used for the screened and bare Coulomb interactions, respectively, and 70 empty bands are used to compute the dielectric screening and the Green's function. For the GW calculations, the PARATEC code was used for the ground-state DFT LDA calculation, and we used the one-shot G_0W_0 approximation. Although a fine sampling of the BZ is essential to converge the e-ph self-energy, we find that an $8 \times 8 \times 8$ k-point grid is sufficient to converge the imaginary part of the GW self-energy. The data shown here are obtained with a Ga pseudopotential with the d states in the core. We have verified that including the semicore d states of Ga as valence states does not lead to significant changes in the II rates, which validates our approach, because only the imaginary part of the GW self-energy is of interest here. Details of the implementation of the imaginary part of the GW self-energy in our code can be found in Refs. [46, 196].

Chapter 4

Substrate-Induced Dynamical Anti-Screening of Excitons in Quasi-2D Materials

4.1 Introduction

Electrons in an atomically thin quasi-two-dimensional (quasi-2D) material, such as a transition metal dichalcogenide (TMD) monolayer, are confined in their motions and experience reduced intrinsic dielectric screening. As a result, electron-electron and electron-hole interactions within the material are enhanced, leading to large bandgap renormalization due to self-energy effects and tightly bound excitons [132, 168, 33, 211, 169]. In the out-of-plane direction orthogonal to the periodic crystal plane, the Coulomb field of the electrons extends outside of the quasi-2D material. Hence, unlike in a bulk three-dimensional (3D) material, electrons in a quasi-2D material are sensitive to the screening environment due to the substrate or any encapsulating material. This substrate screening effect can drastically modify the quasiparticle (QP) excitation energy and the exciton binding energy and can be exploited to bring about new applications and optoelectronic devices, such as rectifier without atomic heterostructures [117, 211, 20, 113, 199, 167, 173, 174, 212, 215].

The *ab initio* GW [83] and GW plus Bethe-Salpeter equation (GW-BSE) [178] approaches are parameters-free and based on the many-body perturbation theory. They are respectively regarded as accurate formalisms to study the quasiparticle and optical properties of quasi-2D materials and are naturally applicable for this class of systems, i.e., 2D materials in different environments. However, since such heterostructures often form incommensurate or nearly incommensurate lattices, several computationally simpler approaches have been recently proposed to deal with the structural complexity. For neutral excitonic optical excitations, which typically only involve long-wavelength electron-hole interactions, it is common to include substrate screening using an effective dielectric constant or the Rytova-Keldysh's model [181, 99]. However, these models do not contain the microscopic local field effects, and

hence, they are not suitable for the calculations of the QP bandgap within the *ab initio* GW approach, and also depend on fitting the substrate dielectric screening based on *ab initio* calculations [40].

Due to the importance of accurately capturing the screening environment and its local fields, various approaches have been employed in the past to calculate the electronic and optical properties of quasi-2D materials that also include dielectric screening due to the substrates [84, 148, 171, 62, 177, 205, 117, 197, 12, 211, 6, 20, 52, 106, 49, 48, 167, 146, 194, 222, 112, 234, 121]. Most approaches are based on the fact that when wavefunction hybridization between the quasi-2D material and the substrate is small, the noninteracting irreducible polarizability can be computed separately for the two subsystems [117]. An important simplification developed in Ref. [211] takes advantage of the fact that substrate screening is often nearly translationally invariant in the quasi-2D plane (i.e., screening within the quasi-2D material is unchanged if the substrate is displaced along its periodic direction), allowing one to circumvent calculations that explicitly depend on the geometry of a supercell that contains both the quasi-2D material and the substrate [211, 20, 113, 146, 167, 212]. Variants of this approach have also been developed: when substrate screening is not translationally invariant along the in-plane directions, such as for molecular adsorbates, a folding scheme and a real-space truncation of the polarizability have been implemented [121, 234]. For a layered substrate, a quantum electrostatic heterostructure model has been proposed that further simplifies the substrate into a composition of different layers coupled together electrostatically [6, 106, 194, 222]. Finally, using a model dielectric function, substrate screening has been included explicitly within the so-called GdW approximation [177, 48], wherein the *ab initio* calculated dielectric matrix is replaced by a model dielectric function. The metallic surface has also been modeled using a classical local function based on the Drude dielectric function [197]. The classical image-charge model has also been used to include substrate screening [84, 148, 171, 62, 205, 52], in what is often referred to as the DFT+Σ approach. In hybrid quantum-classical approaches, the GW QP self-energy of the quantum-mechanical subsystem is embedded in an environment that contributes to screening based on molecular mechanics [49, 112]. In all cases, calculations have found that the exciton binding energy of a supported quasi-2D material decreases relative to the freestanding case and that this renormalization is nearly canceled by a reduction of the QP bandgap, in such a way that the lowest exciton excitation energy barely changes.

The large binding energies of excitons and their changes by the substrate also raise the question of whether it is still appropriate to approximate the screened, time-dependent electron-hole interaction in the BSE as being instantaneous, a common practice known as the static approximation to the BSE [178, 136, 13, 61, 138], even though there are instances in which the frequency dependence has been shown to be important, such as for some noble metals [136] and doped systems of reduced dimensionality [61]. While the BSE should be rigorously solved in a fully frequency-dependent fashion, the most important energy at which screening takes place is at the exciton binding energy [178]. Consequently, the static approximation to the BSE is often reasonable: for a bulk 3D semiconductor or insulator, the dielectric function is nearly constant in the small-energy range that the exciton binding

energies fall into; for metals, even though the dielectric screening varies drastically in this energy range, screening is overall large and the exciton binding energy is typically very small, with the important exceptions mentioned above [136, 61]. The case of a quasi-2D material supported by a metallic substrate is expected to be another example for which this approximation breaks down, since a quasi-2D material has large exciton binding energies of a few hundred meV, and screening from the substrate changes considerably as a function of wavevector in this energy range.

In this work, we study the effects that the wavevector and frequency dependences of substrate screening have on the quasiparticle and excitonic properties of monolayer TMDs for a range of substrates. We show that a physical phenomenon of *antiscreening* emerges when a quasi-2D insulator is supported by a metallic substrate. This effect is due to the presence of low-energy surface plasmons in metallic substrates, which act as mediating bosons for the electron-hole interactions in the quasi-2D material. Remarkably, these retarded interactions have an attractive component (i.e., they may enhance the interactions) that is analogous to the Bardeen-Pines [10] attractive phonon-mediated electron-electron interactions. In order to observe this effect in calculations, it is necessary to perform our *ab initio* GW and GW-BSE calculations carefully and treat the wavevector and frequency dependences of substrate screening on the same footing. For example, a k-point sampling as dense as 3000×3000 is needed to capture the correct long-wavelength behavior of screening in metallic substrates.

As we show, the frequency dependence of screening by the metallic substrate is of paramount importance in this regime, and the static approximation severely overscreens the electron-hole interaction of an exciton, yielding unphysical results. Moreover, the antiscreening effect will also not be observed if the static approximation is used. We also derive a frequency-dependent polarizability of an ideal-metal model to elucidate the intricate and non-trivial coupling of the spatial-energy variations.

This Chapter is organized as follows. In Sec. 4.2, we describe how we incorporate screening from the substrate into our GW and GW-BSE calculations through the in-plane substrate average (IPSA) approximation. We then introduce the ideal-metal model (IMM) for the substrate. In Sec. 4.3, we discuss how the QP self-energy and the exciton binding energies are modified by the presence of a substrate. In Sec. 4.4, we report our conclusions.

4.2 Theoretical and Computational Approaches

In-plane Substrate Averaging (IPSA) Approximation

This class of structurally complex systems involving a quasi-2D material and a substrate can be very efficiently tackled if we make use of the fact that the van der Waals interactions between the quasi-2D layer and its supporting substrate are typically weak, leading to spatial separation between these two subsystems with minimal wavefunction hybridization. If the interface is also incommensurate, this hybridization is even weaker [123, 223] due to the lack of long-ranged periodicity.

In Ref. [211], the in-plane substrate averaging (IPSA) approximation [211, 20, 113, 167, 212] was introduced. It takes advantage of this spatial separation to efficiently compute the substrate effect on the quasiparticle and optical properties of the quasi-2D material by assuming that the noninteracting irreducible polarizability $\chi^0(\mathbf{r},\mathbf{r}')$ of the total system, which is related to the many-electron screening, is a sum of the contribution from the quasi-2D material $\chi^0_{\mathrm{TMD}}(\mathbf{r},\mathbf{r}')$, and the contribution from the substrate $\chi^0_{\mathrm{sub}}(\mathbf{r},\mathbf{r}')$. This separation becomes exact in the limit of vanishing wavefunction hybridization between these two subsystems. The main physical approximation in IPSA is then to neglect the atomistic details of the substrate screening in the in-plane directions, which is exact in the long-wavelength limit. This is equivalent to assuming that the substrate polarizability is translationally invariant in these directions and therefore the microscopic local field effects due to the substrate in the in-plane x- and y-directions (but not the out-of-plane z-direction) can be ignored,

$$\chi^0_{\mathrm{sub}}(\mathbf{r},\mathbf{r}') \approx \chi^0_{\mathrm{sub}}(x-x';y-y';z,z'). \tag{4.1}$$

The noninteracting irreducible polarizability $\chi^0(\mathbf{r},\mathbf{r}')$ is related to the random-phase approximation (RPA) of the dielectric matrix $\epsilon(\mathbf{r},\mathbf{r}')$ through $\epsilon(\mathbf{r},\mathbf{r}') = \delta(\mathbf{r}-\mathbf{r}') - \int d\mathbf{r}'' v_c(\mathbf{r}-\mathbf{r}'')\chi^0(\mathbf{r}'',\mathbf{r}')$. In this work, the substrate is not assumed to be homogeneous [211, 20, 146] (unless otherwise specified), layered [6] or have an analytic form [99, 177, 197, 48].

To verify the validity of not including local field effects due to the substrate in the in-plane directions, we carry out GW and GW-BSE calculations for a set-up consisting of an untwisted bilayer $\mathrm{WSe_2}$, for which the closest Se atoms in the two layers are separated by 4 Å in the out-of-plane direction. Even though this distance is larger than the typical distance of ∼3.1 to ∼3.4 Å between a quasi-2D material and its substrate, hybridization effects are much larger between the two layers of an untwisted bilayer $\mathrm{WSe_2}$ due to the proximity of the Se atoms and long-ranged periodicity. We, therefore, artificially increase the interlayer distance to decrease the hybridization between the two layers, to the level of hybridization that is similar to when $\mathrm{WSe_2}$ is supported by a real substrate. For such a system, we see that the IPSA approximation introduces an error of only a few meV in the QP and exciton excitation energies (see the first two columns of Table 4.1).

The major advantage of the IPSA approximation is that it avoids the need of many-body perturbation theory calculations of a very large supercell that explicitly contains both the quasi-2D material and the substrate. Hence, as opposed to an otherwise expensive calculation, the effective computational cost of a GW-BSE calculation that incorporates substrate screening using our approach is nearly the same as a GW-BSE calculation for a unit cell of the quasi-2D material only. Moreover, since substrate effects are longer-ranged effects than electron-electron interactions within the quasi-2D material, the perturbative change in the GW QP self-energy of the quasi-2D material due to the substrate, $\Delta\Sigma_{\mathrm{TMD}} \approx iG_{\mathrm{TMD}}\Delta W$ [where $\Delta W = (\epsilon^{-1}_{\mathrm{TMD+sub}} - \epsilon^{-1}_{\mathrm{TMD}})v_c$, and $\epsilon^{-1}_{\mathrm{TMD+sub}}$ and $\epsilon^{-1}_{\mathrm{TMD}}$ are respectively the inverse dielectric matrices of the combined system and the TMD-only subsystem] can be evaluated using a much smaller energy cutoff (E_s) for the number of components in the plane-wave basis set and correspondingly fewer bands (N_b) in the summation over empty states for

Table 4.1: Calculated exciton binding energies E_b, exciton excitation energies E_{xct} and QP bandgap $E_{\text{gap}}^{\text{QP}}$ of bilayer WSe_2, for which the closest Se in the two layers are separated by 4 Å in the out-of-plane direction. In the first two columns, one (mono)layer is treated as an effective system embedded in the screening environment due to the second (mono)layer. In the first column, local field effects of screening due to the second layer is neglected in the in-plane directions but still explicitly included in the out-of-plane direction. In the second column, all local field effects of screening due to the second layer are included. In the third column, we report the results of exact calculations for an explicit bilayer WSe_2 system. (We use the following notations: ml for monolayer and bl for bilayer.) Precision to 1 meV obtained from *ab initio* calculations is given in parenthesis.

	ml+ml with in-plane local field (eV)	ml+ml without in-plane local field (eV)	bl exact calc (eV)
E_b^{1s}	0.40(0)	0.39(6)	0.38(2)
E_b^{2s}	0.22(4)	0.22(1)	0.21(3)
E_{xct}^{1s}	1.65(9)	1.65(8)	1.65(4)
E_{xct}^{2s}	1.83(5)	1.83(3)	1.82(2)
$E_{\text{gap}}^{\text{QP}}$	2.06(0)	2.05(5)	2.03(6)

the computation of the noninteracting irreducible polarizability and the self-energy for this purpose. For instance, in our calculations of a pristine monolayer freestanding WSe_2, we employ a plane-wave cutoff of $E_s = 35$ Ry when calculating the dielectric matrix and the self-energy, including $N_b = 26450$ bands for both calculations. However, when calculating the perturbative change in the QP self-energy of WSe_2 due to substrate screening by hBN, a much smaller plane-wave cutoff of $E_s = 6$ Ry is used and only $N_b = 1116$ bands are included, and the result is found to already be converged to better than 5 meV. See Sec. 5.1 for more details.

Using the IPSA approach, one can calculate not only the renormalizations of the QP bandgap $E_{\text{gap}}^{\text{QP}}$ due to screening from a substrate, but also compute the changes in the absolute QP excitation energies (e.g., conduction band minimum and valence band maximum) [212], exciton excitation energies E_{xct} and exciton binding energies E_b. For this approach to be accurate, wavefunction hybridization between the quasi-2D material and the substrate in the combined system should be minimal. In Sec. 5.3, we plot the projections of the wavefunctions of the combined system onto the wavefunctions of the quasi-2D material. While the hybridization is small for a wide variety of substrates, including SiO_2, hBN, and graphene, we find that it is markedly larger for Au, making this approach less appropriate for such a substrate.

In this work, the GW QP self-energies and the GW-BSE exciton excitation energies are computed using the BerkeleyGW [83, 178, 46] package. The QP self-energies are calculated using the eigenvalue-self-consistent, fully-frequency-dependent GW_0 approximation.

The full frequency-dependent dielectric matrices for monolayer MoS_2, $MoSe_2$ and WSe_2 are calculated on effective [94] q-grids of 1143×1143, 1100×1100 and 1102×1102, respectively, using a total of 26450 bands. An energy cutoff of 35 Ry is used to calculate the dielectric matrix and the self-energy. The frequency-dependent BSE is solved self-consistently to obtain the exciton excitation energies. The electron-hole interaction kernel of the BSE Hamiltonian is interpolated from a uniform k-grid of 72×72 to a finer uniform k-grid of 1440×1440, using directly calculated matrix elements for q-points of density equivalent to 5184×5184 [178, 94]. The TMD-substrate distances are determined in separate DFT calculations that also incorporate van der Waals interactions (vdW-DF$^{\mathrm{C09x}}$) [39] and dipole corrections [14, 142] by minimizing the energies of the systems. For computational details, see Sec. 5.1.

Frequency and Wavevector Dependences

An important aspect of this work is the study of the frequency dependence of the dielectric matrix when calculating the GW self-energy and solving the BSE, without resorting to static approximations or plasmon-pole models [83, 116, 68]. This is particularly important for a metallic substrate because its dielectric screening displays coupled spatial-energy variations even at small frequencies ω. In this work, we include the frequency dependence of the dielectric matrix self-consistently when solving the BSE to obtain exciton excitation energies (see Sec. 4.3). While this is a computationally expensive step that is often neglected in *ab initio* calculations because its effects are usually minor for dielectric substrates, we find that it quantitatively and qualitatively changes the exciton energies if the substrate is metallic.

In addition to the dynamical effects, the small-q dependence of the polarizability matrix is also important and non-trivial for a quasi-2D material [168, 169] and are accurately captured using non-uniform Brillouin-zone sampling approaches [94]. In general, since Wannier excitons are low-energy and spatially extended excitations, small-ω and small-q dependences have to be calculated accurately and on equal footing (Sec. 5.1).

Screening in an Ideal-Metal Model (IMM)

To more clearly elucidate the intricate frequency and wavevector dependences of screening by metallic substrates, we derive here an expression for the irreducible polarizability of a grounded ideal-metal model substrate: a semiclassical model which at steady state completely screens any external potential above its surface by inducing a 2D surface charge like a classical ideal metal. The model also displays retardation effects based on the Lindhard theory for the 2D electron gas. For the full derivation and a more detailed discussion, see Sec. 5.2.

The associated irreducible polarizability for this surface-charge-inducing ideal-metal model (IMM), $\chi^0_{\mathbf{G}\mathbf{G}',\mathrm{IMM}}(\mathbf{q},\omega)$, is decomposed as a product of two terms using the following ansatz,

$$\chi^0_{\mathbf{G}\mathbf{G}',\mathrm{IMM}}(\mathbf{q},\omega) \equiv \chi^0_{\mathbf{G}\mathbf{G}',\mathrm{static}}(\mathbf{q}) f^0_{\mathrm{L}}(\mathbf{q}+\mathbf{G}_{\parallel},\omega)\delta_{\mathbf{G}_{\parallel},\mathbf{G}'_{\parallel}}. \tag{4.2}$$

The first term $\chi^0_{\mathbf{GG'},\mathrm{static}}(\mathbf{q})$ corresponds to the irreducible polarizability of a static classical ideal metal, which has, for instance, no retardation effects or information regarding the Fermi surface. The delta function $\delta_{\mathbf{G}_\parallel,\mathbf{G'}_\parallel}$ emphasizes the fact that $\mathbf{G}$ and $\mathbf{G'}$ components of $\chi^0_{\mathbf{GG'},\mathrm{static}}(\mathbf{q})$, $f^0_{\mathrm{L}}(\mathbf{q}+\mathbf{G}_\parallel,\omega)$ and therefore $\chi^0_{\mathbf{GG'},\mathrm{IMM}}(\mathbf{q},\omega)$ are diagonal in the in-plane directions, due to the translational invariance of this model and the homogeneous 2D electron gas in the in-plane directions. This ansatz makes the drastic but physically-motivated assumption that the frequency response in the in-plane directions is independent of the $G_\perp$ and $G'_\perp$ components. The irreducible polarizability is computed numerically from the reducible polarizability $\chi_{\mathbf{GG'},\mathrm{static}}(\mathbf{q})$, using the following matrix equation,

$$\chi^0_{\mathrm{static}}(\mathbf{q}) = [1 + v_c(\mathbf{q})\chi_{\mathrm{static}}(\mathbf{q})]^{-1}\chi_{\mathrm{static}}(\mathbf{q}), \tag{4.3}$$

where v_c is the (truncated) Coulomb potential [85]. The static reducible polarizability of a classical ideal metal, $\chi_{\mathbf{GG'},\mathrm{static}}(\mathbf{q})$, is derived by us in Sec. 5.3 to be,

$$\chi_{\mathbf{GG'},\mathrm{static}}(\mathbf{q}) = -e^{iG_\perp z}\frac{\delta_{\mathbf{G}_\parallel\mathbf{G'}_\parallel} I(\mathbf{q},\mathbf{G}_\parallel,G'_\perp)}{v_c(\mathbf{q}+\mathbf{G'})}e^{-iG_\perp z}, \tag{4.4}$$

where

$$I(\mathbf{q},\mathbf{G}_\parallel,G'_\perp) = \mathcal{V}\frac{|\mathbf{q}+\mathbf{G}_\parallel|\left[1 - e^{-\frac{L}{2}|\mathbf{q}+\mathbf{G}_\parallel|}\cos(\frac{L}{2}G'_\perp)\right]}{\frac{L}{2}(G'^2_\perp + |\mathbf{q}+\mathbf{G}_\parallel|^2)},$$

z is the position of the substrate, L is the length of the unit cell in the out-of-plane direction and $\mathcal{V}$ is the volume of the crystal. Note also that $\chi_{\mathbf{GG'},\mathrm{static}}(\mathbf{q})$, and therefore $\chi^0_{\mathbf{GG'},\mathrm{IMM}}(\mathbf{q},\omega)$, are diagonal in the in-plane directions, as should be expected, since our model is translationally invariant in the in-plane directions.

The second term $f^0_{\mathrm{L}}(\mathbf{q}+\mathbf{G}_\parallel,\omega)$ in Eq. (4.2) contains the frequency-dependent retardation effects of the screening response of the substrate. As we detail in Sec. 5.3, $f^0_{\mathrm{L}}(\mathbf{q}+\mathbf{G}_\parallel,\omega)$ is taken from the Lindhard function of a 2D metal, which is $\chi^0_{\mathrm{L}}(\mathbf{q}+\mathbf{G}_\parallel,\omega)$ through the following defining equation,

$$\chi^0_{\mathrm{L}}(\mathbf{q}+\mathbf{G}_\parallel,\omega) \equiv \chi^0_{\mathrm{L,static}}\, f^0_{\mathrm{L}}(\mathbf{q}+\mathbf{G}_\parallel,\omega), \tag{4.5}$$

where $\chi^0_{\mathrm{L,static}} = \lim_{q\to 0}\chi^0_{\mathrm{L}}(q,0)$. As our response function in Eq. (4.2) also captures the out-of-plane local field effects of screening due to the induced surface charge at the surface of an ideal-metal substrate, it is a function of $G_\perp$, is thus z-dependent and contains the distance dependence between the substrate and the quasi-2D material. In this work, the ideal-metal substrate is positioned at a distance from the quasi-2D material that is the same as the distance the charge center of the closest p_z orbital of the doped 14-layer graphene substrate is from the quasi-2D material. The charge centers are defined using the peaks in the calculated *ab initio* noninteracting irreducible polarizability $\chi^0(z = z')$ of a doped 14-layer graphene substrate for $q \to 0$. In addition, $f^0_{\mathrm{L}}(\mathbf{q}+\mathbf{G}_\parallel,\omega)$ depends on the Fermi

wavevector k_F. We set k_F to 0.72 Å^{-1} using the calculated Fermi surface of a doped 14-layer graphene substrate and can be regarded as a highly screening metallic substrate. (For the corresponding hole concentrations of the doped n-layered graphene, see Sec. 4.3.)

Together, Eqs. (4.2), (4.3) and (4.4) form a set of equations that are physically motivated, yet simple and easy to implement in first-principles calculations such as in the *ab initio* GW-BSE approach, in the physically meaningful limit that is the upper bound of saturated metallic substrate screening. Its simplicity contrasts sharply with the otherwise numerically intensive computation of the polarizability of a metallic substrate, which requires a very dense k-point sampling and can be difficult to converge.

Importantly, our surface-charge-inducing ideal-metal model is robust. It correctly reproduces the QP-bandgap renormalizations that are calculated *ab initio* in the limit of saturated metallic screening of multiple-layer graphene (Table 4.2). Additionally, it is also able to reproduce the $|\mathbf{q}+\mathbf{G}|$ dependence of $\epsilon^{-1}_{\mathbf{G}=\mathbf{G}',\text{static}}(\mathbf{q})$ of a doped monolayer graphene that has been calculated *ab initio* in the long-wavelength limit of $G_\perp = G'_\perp = 0$ (Fig. 4.1) and most features of the local field effects in the out-of-plane direction.

This is because our ideal-metal model screens by inducing a 2D surface charge that correctly reproduces the surface of an ideal-metal substrate, including the local field effects. Our model improves upon the traditional image-charge (substrate) model, which has a screening response that is not given by a surface charge, but by an image charge inside the substrate. For a given value of $\mathbf{G} = \mathbf{G}'$, the traditional image-charge model screens constantly for all q's and does not agree with the microscopic screening response of doped graphene.

4.3 Results

Quasiparticle Bandgap Renormalization

In this Section, we calculate the QP-bandgap renormalizations of three monolayer TMDs, namely MoS_2, $MoSe_2$ and WSe_2, supported by 13 selected substrates (Table 4.2), including bilayer hBN, 4.8-nm-thick (10-layer) crystalline film of polytetrafluoroethylene (PTFE), 4.5-nm-thick SiO_2, 4.3-nm-thick (14-layer) hBN, doped and undoped n-layered graphene and ideal n-layered metal (Fig. 4.2). In this work, the doped n-layered graphene is always gated at 0.3 eV [211] below the charge neutrality point, which is mimicked by rigidly lowering the Fermi level of an intrinsic undoped sample. This corresponds to hole-doping of $p = 9.6 \times 10^{12}$ cm^{-2}, 2.4×10^{13} cm^{-2} and 2.0×10^{14} cm^{-2} for the monolayer, bilayer, and 14-layer graphene samples, respectively. The selection of these substrates is experimentally motivated and covers a range of electrical conductivities, from insulators and semiconductors to semimetals and metals. In some cases, we also consider the scenario in which the monolayer TMD is not only screened from below by the substrate (i.e., substrate only), but also screened from above by a capping layer of the same material (i.e., encapsulated).

Firstly, we find, as expected, that insulators and semiconductors screen less than semimetals and metals (Table 4.2 and Fig. 4.2). The larger is the screening by the substrate, the

Table 4.2: Eigenvalue-self-consistent (GW_0) QP bandgap renormalizations in meV of three different monolayer TMDs supported by different substrates, to the nearest 10 meV. "Sub" denotes substrate-only screening, while "Enc" denotes screening upon encapsulation. The GW_0 QP gaps (including spin-orbit coupling) for freestanding MoS_2, $MoSe_2$ and WSe_2 are calculated to be 2.42, 2.10 and 2.19 eV, respectively. The calculated values for monolayer WSe_2 are plotted in Fig. 4.2.

		MoS_2			$MoSe_2$			WSe_2		
Substrate Types	Substrates	Sub	Enc	Ratio	Sub	Enc	Ratio	Sub	Enc	Ratio
semiconducting	bl-hBN	60	110	1.8	50	90	1.8	60	100	1.8
	4.8-nm-thick PTFE	60	110	1.8	50	90	1.8	60	100	1.8
	4.5-nm-thick SiO_2	80	140	1.7	70	120	1.7	80	130	1.7
	14L-hBN	130	210	1.6	110	180	1.6	120	200	1.6
semimetallic	undoped graphene	270	350	1.3	230	310	1.3	250	330	1.3
	undoped blg	330	400	1.2	290	350	1.2	310	380	1.2
	undoped 14L-graphene	330	400	1.2	300	350	1.2	320	380	1.2
metallic	doped graphene	340	400	1.2	300	350	1.2	320	380	1.2
	doped blg	350	410	1.2	310	360	1.2	330	390	1.2
	doped 14L-graphene	350	410	1.2	310	360	1.2	330	390	1.2
n-layered metals in the IMM	monolayer	350	410	1.2	310	360	1.2	330	390	1.2
	bilayer	350	410	1.2	310	360	1.2	330	390	1.2
	14-layer	350	410	1.2	310	360	1.2	330	390	1.2

larger is the bandgap renormalization of the TMD. For monolayer WSe_2, a 14-layer hBN substrate renormalizes its bandgap by 120 meV, whereas a doped 14-layer graphene substrate renormalizes its bandgap by 330 meV, which is more than twice as much.

Secondly, this renormalization is not a simple function of the macroscopic dielectric constants of the substrates (Fig. 4.2). Due to the importance of substrate screening, it is common practice [53, 193, 82, 182] to incorporate substrate screening using a momentum-independent effective dielectric constant defined as the average of the macroscopic dielectric constants of the media above and below the TMD, i.e., $\epsilon_{\text{env}} = (\epsilon_{\text{above}} + \epsilon_{\text{below}})/2$. Using this conventional model, it is equivalent to replacing the substrate by a homogeneous dielectric medium that permeates throughout space, responding locally to an external potential. This approximation always overestimates substrate screening (Fig. 4.2) because it assumes that the substrate overlaps spatially with the sample. For monolayer WSe_2, this overestimation of the QP-bandgap renormalization can exceed the upper bound of saturated metallic screening (390 meV) by more than 400 meV (Fig. 4.2). Moreover, the choice of a correct macroscopic dielectric constant for the substrate can be difficult or ill-defined for some materials, particularly if the substrate is metallic since $\epsilon(q, \omega)$ will then be strongly dependent on the screening frequency ω as $q \to 0$, or if the substrate is quasi-2D since $\epsilon(q, \omega)$ will then vary non-trivially with q [169]. In fact, $\epsilon(q, \omega)$ of a semiconducting quasi-2D material always approaches 1 as $q \to 0$, due to the lack of long-ranged electronic screening [169]. As a result, the range of experimentally measured macroscopic dielectric constants for some materials is large and can be a source of controversy (e.g., it reportedly ranges from 2 to 16 for graphene [91, 176, 193, 182]).

Thirdly, the effect of substrate screening by layered substrates saturates very quickly with (layer-)thickness for metallic and semimetallic substrates, but is saturated only at very large thickness for semiconducting and insulating substrates (Table 4.2). For monolayer WSe_2, an ideal-metal substrate leads to a bandgap renormalization of 330 meV. This is the same as the renormalization by doped bilayer graphene and doped 14-layer graphene substrates and is only 10 meV larger than the renormalization by a doped monolayer graphene substrate. Substrate screening by doped graphene layers is already saturated at two-layer thickness. For a hBN substrate, a 14-layer hBN renormalizes the bandgap by 120 meV while a bilayer hBN substrate renormalizes the bandgap by half as much (60 meV). Even with a 14-layer thickness of hBN, the renormalization of the bandgap is less than half of the renormalization in the limit of saturated metallic screening of 330 meV. This also addresses a long-standing discussion in the literature regarding the layer dependence of substrate screening by n-layered graphene [131, 173].

Fourthly, the ratio of the calculated bandgap renormalization due to substrate versus encapsulation screening ranges from 1.2 to 1.8 (Table 4.2). The classical image-charge model predicts this ratio to be 1.4. Interestingly, this may run counter to a naïve expectation that if the monolayer TMD sample is not only screened from below by a substrate, but also screened from the above by a capping layer of the same material, the bandgap renormalization due to encapsulation will be twice as large as the renormalization due to the substrate only. This is not correct, because even though the substrate alone may induce a potential of ϕ_{ind} in

the sample, the addition of a capping layer will not induce an additional potential of exactly ϕ_{ind} in the sample. The potential induced by the capping layer is now a response to not only the charges in the sample but also the induced charges in the substrate. We show in the Sec. 5.3 that the total induced potential at the center of the sample upon encapsulation is an alternating harmonic series that sums up to $2 \ln 2\phi_{\text{ind}} = 1.4\phi_{\text{ind}}$.

Fifthly, the maximum calculated renormalization of the QP bandgap of any of the three monolayer TMDs due to the selected substrates and encapsulations we have studied is 0.4 eV (Table 4.2). This is close to the largest experimental QP-gap renormalization of 0.3 eV reported in Ref. [173] when monolayer WS_2 is encapsulated by non-intrinsic monolayer graphene. In our calculations, when monolayer WSe_2 is encapsulated in doped 14-layer graphene or the ideal metal model, the QP bandgap of monolayer WSe_2 is reduced by 390 meV, which is 20% of its freestanding QP bandgap (2.19 eV). This percentage of renormalization is large, and our calculated result also serves to inform the maximum extent of bandgap renormalization that one can expect to obtain by tuning the dielectric screening environment in an experiment.

Lastly, we emphasize that substrate renormalization of the bandgap cannot be correctly calculated at the DFT level within the local-density (LDA) and generalized-gradient approximations (GGA) because under these approximations, the exchange-correlation potential $V_{\text{xc}}(\mathbf{r})$ in the DFT Hamiltonian is local by construction. Substrate screening is non-local and can be very long-ranged (e.g., for insulating substrates) [148]. In a GW calculation, screening of the Coulomb potential due to the substrate $W(\mathbf{r}, \mathbf{r}', \omega)$ is manifestly non-local. When MoS_2 is renormalized by a bilayer hBN substrate, the QP-bandgap renormalization is 60 meV (Table 4.2). When the DFT bandgap of MoS_2 is calculated in the presence of the same substrate, the change in the bandgap is negligible (5 meV).

Exciton Binding Energy Renormalization

In this section, we calculate the substrate renormalizations of the exciton energies in quasi-2D materials using the GW-BSE approach. Throughout this section, we focus on pristine monolayer WSe_2 as our prototypical quasi-2D material, as screened by three substrates with increasing dielectric constants, namely, 4.5-nm-thick SiO_2, 4.3-nm-thick (14-layer) hBN and an ideal metal.

Firstly, just as the QP bandgap decreases as screening increases (Fig. 4.2), the exciton binding energy E_b also decreases as screening increases (Fig. 4.3a and Table 4.3). When a freestanding WSe_2 is screened by SiO_2, hBN and an ideal metal, the calculated QP bandgap decreases by 80, 120 and 330 meV, respectively (Table 4.2). Meanwhile, the 1s exciton binding energy $E_b^{1\text{s}}$ of 520 meV for a freestanding monolayer WSe_2, decreases by 70, 110 and 260 meV (Table 4.3). As screening increases, the QP bandgap decreases by almost as much as the decrease in the exciton binding energy so that the 1s exciton excitation energy (and hence the optical gap) remains approximately constant, as was also observed experimentally in Ref. [173]. Between a freestanding WSe_2 and when it is screened by an ideal-metal substrate, the calculated 1s exciton excitation energy decreases by only 70 meV.

Table 4.3: Binding energies of four lowest-lying excitons at the K valley in monolayer WSe_2 when screened by different substrates and encapsulations, to the nearest 10 meV. The QP bandgap of monolayer WSe_2 when freestanding and when screened by SiO_2, hBN and graphene substrates are 2.19, 2.11, 2.06 and 1.93 eV (from Table 4.2). The excitation energies of these excitons are plotted in Fig. 4.3. Here, f denotes the oscillator strengths of the exciton and $\langle r \rangle$ denotes the root-mean-squared (rms) radius of its envelope function.

		Substrate		
	freestanding	SiO_2	hBN	ideal metal
Dynamic Screening				
Binding Energies E_b (meV)				
• 1s	520	450	410	260
• $2p_-$	360	300	270	180
• $2p_- - 2p_+$	15	11	9	2
• 2s	290	250	230	170
$\eta = E_b^{1s}/\Delta_{12}$	2.2	2.2	2.2	2.7
f_{2s}/f_{1s}	0.25	0.22	0.20	0.11
$\langle r_{1s} \rangle$ (Å^{-1})	0.079	0.076	0.073	0.062
$\langle r_{1s} \rangle$ (Å)	13.8	14.5	14.9	17.5
$\langle r_{2s} \rangle$ (Å^{-1})	0.080	0.070	0.064	0.040
$\langle r_{2s} \rangle$ (Å)	38	43	46	69
Static Screening				
Binding Energies E_b (meV)				
• 1s	520	450	410	70
• $2p_-$	360	300	270	$\sim$0
• $2p_- - 2p_+$	15	11	9	$\sim$0
• 2s	290	250	230	$\sim$0
$\eta = E_b^{1s}/\Delta_{12}$	2.2	2.2	2.2	$\sim$1.0
f_{2s}/f_{1s}	0.25	0.22	0.20	0.00
$\langle r_{1s} \rangle$ (Å^{-1})	0.079	0.076	0.073	0.062
$\langle r_{1s} \rangle$ (Å)	13.8	14.5	14.9	17.5
$\langle r_{2s} \rangle$ (Å^{-1})	0.080	0.070	0.064	0.003
$\langle r_{2s} \rangle$ (Å)	38	43	46	674

When a hBN-screened monolayer WSe_2 has its substrate replaced by SiO_2, the calculated 1s and 2s exciton excitation energies decrease by 10 and 30 meV, respectively (Table 4.3), which are the same as (and in good agreement) with the experimental measurements of Ref. [173].

Secondly, although the 1s exciton excitation energy remains almost constant across different substrates, the exciton wavefunctions have changed (Table 4.3). As substrate screening increases, the exciton wavefunctions becomes more spatially extended in real space. The root-mean-squared (rms) radius of the exciton envelope function of the 1s exciton increases from 13.8 Å for freestanding WSe_2, to 14.5 Å, 14.9 Å and 17.5 Å when screened by a 4.5-nm-thick SiO_2, a 4.3-nm-thick hBN and an ideal metal, respectively. The ratio of the oscillator strengths of the 2s to 1s excitons also decreases from 0.25 to 0.22, 0.20 and 0.11 as screening increases (Table 4.3), indicating that the 2s states become even more spatially extended and relatively less strongly bound compared to the 1s states as the screening environment becomes stronger. In general, as dielectric screening due to the substrate increases, electron-hole interactions within the exciton become weaker. The exciton wavefunctions become more spatially extended in real space, reducing the oscillator strengths of the exciton, leading to decreases in the intensity of the sharp peaks in the optical spectrum [167]. We note that in experiments, for a freestanding quasi-2D material, impurities and disorder at its surfaces can also result in the broadening of the absorption peaks in the optical spectrum [73], leading to sharper features upon encapsulation despite increased screening from the encapsulation [174].

Thirdly, when a quasi-2D material is freestanding or screened by an insulator or semiconductor, a static approximation for the dielectric screening is very good, giving exciton binding energies, E_b, that are within 10 meV of those calculated using dynamical screening (Table 4.3). This is because the dielectric function is approximately constant with respect to ω in the energy range around the exciton binding energy, E_b. However, when the quasi-2D material sits on a metallic substrate, we find that it is important to account for the frequency dependence of the dielectric matrix in solving the BSE. This is because dielectric screening of a metal changes drastically in the energy range of a few hundred meV typical of exciton binding energies in quasi-2D semiconductors (Sec. 5.3). Moreover, as the substrate screening increases, the exciton binding energy decreases and the exciton becomes more spatially extended in real space (or localized in reciprocal space), entering the regime near $q \approx 0$ where the dielectric function of the metal is a singular function, limit of which depends strongly on the direction along which the singularity is approached. For finite non-zero frequencies, in the limit of $q \to 0$ (the dynamical long-wavelength limit), the dielectric function of a metal always approaches 1. In the static limit, in which $\omega = 0$, however, the dielectric function of a 2D metal diverges like $1/q$ as $q \to 0$. Since the bound exciton should rigorously be screened at the frequency of the binding energy, this means that if a static screening is employed, the exciton will be dramatically overscreened.

Indeed, static versus dynamical screening for a metallic substrate leads to qualitatively different results. In Table 4.3 and Fig. 4.3a, we see that if static screening is employed, the electron-hole interaction is reduced to the point that the quasi-2D material only supports a single bound exciton state (within the accuracy of our calculation that has a finite k-

point sampling of up to 1440×1440), whereas multiple bound excitons remain if dynamical screening is employed. Moreover, solving the BSE using the static approximation leads to unphysical results: the 1s exciton on a metallic substrate becomes higher in energy than that in freestanding monolayer WSe_2 (Fig. 4.3a). We note, as a technical detail, that in practical calculations, if the k-point sampling of the electron wavefunction is not converged, the calculated static dielectric function of a quasi-2D metal will mimic the dielectric behavior of a small-gap semiconductor and will be finite as $q \to 0$. This leads to a fortuitous cancellation of errors in the calculation of the exciton excitation energies that, for example, will lower the calculated excitation energy of the 1s exciton. This nonetheless obscures the correct physics behind the frequency-dependent screening, e.g., a strictly positive dielectric function in this case means that, despite the cancellation of errors, the true antiscreening effects (as we discuss below) will never be correctly calculated.

Interestingly, unlike the renormalization of the exciton binding energy, the renormalization of the QP self-energy by an ideal-metal substrate is fairly insensitive to the small-q and small-ω variations in the dynamical long-wavelength limit of the dielectric function. Setting $f^0_{\mathrm{L}}(\mathbf{q} + \mathbf{G}_\parallel, \omega)$ to 1 in Eq. (4.2) gives the same QP bandgap renormalization to within 5 meV. This reflects the fact that while a Wannier-like exciton in quasi-2D materials is very extended in real space (typically spanning several nm in the quasi-2D plane) and is therefore very sensitive to screening at small q's, the QP self-energy is relatively more sensitive to the screening environment at shorter length scales on the order of the crystal lattice constant (typically spanning several Å).

Finally, we note that optical experiments [50, 132, 33, 34, 173] frequently rely on theoretical models to deduce the QP bandgap $E^{\mathrm{QP}}_{\mathrm{gap}}$ from measured exciton excitation energies, leading to uncertainty in obtaining the QP bandgap from optical experiments. For the systems we studied, the s-like excitons are the states that are optically active, even though this needs not be the case in general. The first two lowest-lying (i.e., 1s and 2s) excitonic states are also the states with the largest oscillator strengths and are thus most easily accessible experimentally using linear optics. By measuring the difference between the excitation energies of the 1s and 2s excitons Δ_{12} ($= E^{2s}_{\mathrm{xct}} - E^{1\mathrm{s}}_{\mathrm{xct}}$), the QP bandgap is usually deduced based on an assumption of the ratio η ($= E^{1\mathrm{s}}_b/\Delta_{12}$), where $E^{1\mathrm{s}}_b$ ($= E^{\mathrm{QP}}_{\mathrm{gap}} - E^{1\mathrm{s}}_{\mathrm{xct}}$) is the binding energy of the lowest-lying bright excitonic state. In Ref. [173], for instance, η is considered to be bounded between $\frac{9}{8}$ to 2, where the lower bound ($\eta = \frac{9}{8}$) was from the 2D hydrogenic model and the upper bound ($\eta = 2$) was obtained by using the experimental s-like exciton excitation energies for a monolayer of WS_2 on a SiO_2 substrate fit to results from a potential of the Rytova-Keldysh form in the long-wavelength limit [33].

It is widely hypothesized that η will approach the lower bound of the 2D hydrogenic model as the external screening increases. This is because as external screening increases, screening is expected to become a constant at the relevant length-scale of an exciton. When we approximate the effect of the substrate as a homogeneous local screening that has the magnitude of the substrate's dielectric constant (ϵ_{env}), we find that the ratio η indeed decreases as the environmental dielectric constant increases, approaching the limit of the 2D hydrogenic model for large ϵ_{env} (Fig. 4.3a). In fact, as $\epsilon_{\mathrm{env}} \to \infty$, the attractive electron-hole

interactions become so strongly screened that there are no more bound excitons. However, in our fully *ab initio* calculations with dynamical screening, the ratio η ranges from 2.2 to 2.7 (Table 4.3) with greater deviations from the 2D hydrogenic limit if the external screening is metallic. For freestanding monolayer WSe_2 and WSe_2 screened by semiconducting and insulating substrates of finite thicknesses, the calculated ratio η is consistently 2.2. Intriguingly, for an ideal-metal substrate, the calculated ratio η in the static limit is $\sim$1.0, but 2.7 when the frequency dependence of the screening is properly accounted for. This large deviation can be understood from the structure of the poles in the dielectric function at different frequencies. Following Ref. [169], we define an effective 2D dielectric function $\epsilon^{2D}_{eff}(\mathbf{q}, \omega)$, which we plot in Fig. 4.3c as a function of q for $\omega = 0$ and an exemplary finite frequency. At finite frequency, the pole moves away from $q = 0$, and the dielectric function becomes less than 1 in the small-q region.

Consequently, excitons screened by a metallic substrate experience an *antiscreening* effect as they become more extended in real space (i.e., more localized in reciprocal space), resulting in anomalously strong electron-hole interactions (and concomitant larger exciton binding energies) for excited exciton states. We emphasize that such an antiscreening is only apparent when the dynamical screening is used, as the pole in the dielectric function occurs at $q \to 0$ in the static limit. This antiscreening is also a unique property of metallic substrates as the dielectric function of insulators, semiconductors and semimetals (like intrinsic graphene) are strictly positive for all q's and relevant frequencies. Hence, we predict that, contrary to previous expectations, the excitonic Rydberg series in monolayer TMDs supported on a metallic substrate will be even more non-hydrogenic than in freestanding monolayer TMDs. Our predictions can, for example, be tested by measuring the first few excited excitonic states on a gate-tunable substrate, such as doped graphene.

4.4 Conclusion

We perform first-principles atomistic calculations to understand the effects of substrate screening on the renormalization of QP energies and exciton binding energies. By carefully treating the wavevector and frequency dependences of screening, as well as solving the dynamical BSE, we find that the QP bandgap and exciton binding energies are renormalized in a non-trivial fashion which does not depend solely on the macroscopic dielectric constant of the substrate.

We find that substrate screening is thickness-dependent and saturates at small thickness for metals but saturates at large thickness for insulators. Encapsulation increases the QP-bandgap renormalization by $\sim$0.4 times, when compared to substrate-only screening. By tuning the dielectric screening environment, it is possible to achieve QP-bandgap renormalization that is as large as 20% of the QP bandgap itself for the systems we investigated.

Finally, we find that metallic substrates can lead to the antiscreening of excitonic states. Higher-energy excitonic states, which are more localized in reciprocal space, experience a screening environment from the metallic substrate, which can be smaller than 1 and even

negative, in the small-wavevector limit as q approaches 0. This leads to the ratio of the binding energies of 2s versus 1s excitons to be larger when the monolayer TMD is screened by a metallic substrate, than when the monolayer TMD is freestanding. This can be measured in experiments with gated substrates. Our predictions open up the possibility of not only using substrate to tune the QP and optical properties of quasi-2D systems, but also couple excitations such as 2D plasmons with excitons in atomically thin materials.

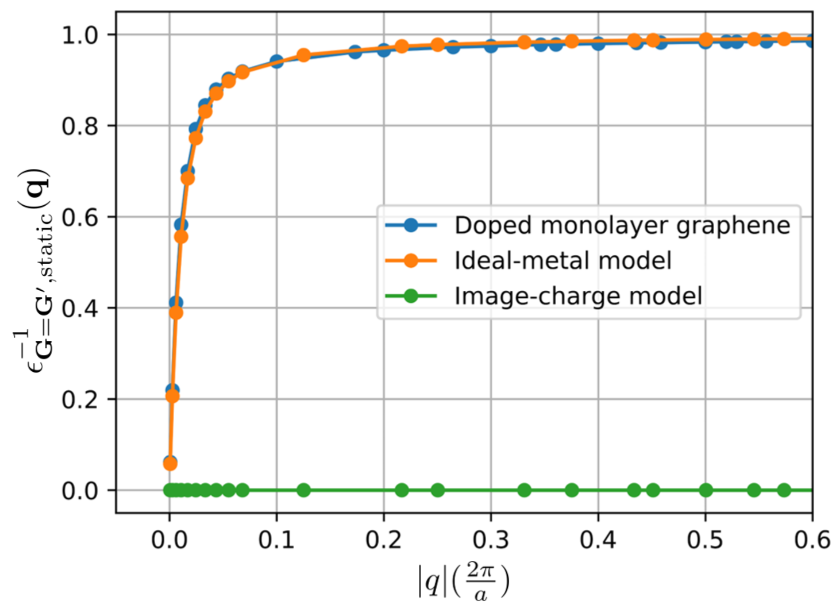

Figure 4.1: Diagonal elements of the inverse dielectric matrices of doped monolayer graphene, ideal-metal (surface-charge) model and image-charge model. Here, a is the lattice constant of graphene, the out-of-plane components are set to $G_\perp = G'_\perp = 0$.

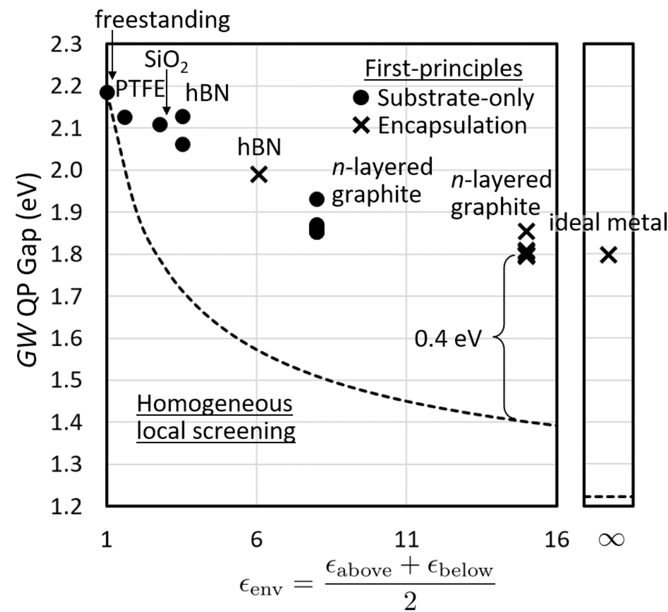

Figure 4.2: Calculated GW_0 QP bandgaps of monolayer WSe_2 on different substrates (●) and encapsulations (✕). The substrates are plotted along the horizontal axis using their experimental dielectric constants. The experimental dielectric constants used for PTFE [18, 51], SiO_2 [159], hBN [47], n-layered graphene [176] are 2.1, 4.6, 6.1 and 15, respectively. Also plotted using a dashed line is the calculated QP bandgap of monolayer WSe_2 when substrate screening is included using the substrate dielectric constant as in the conventional model (i.e., homogeneous local screening).

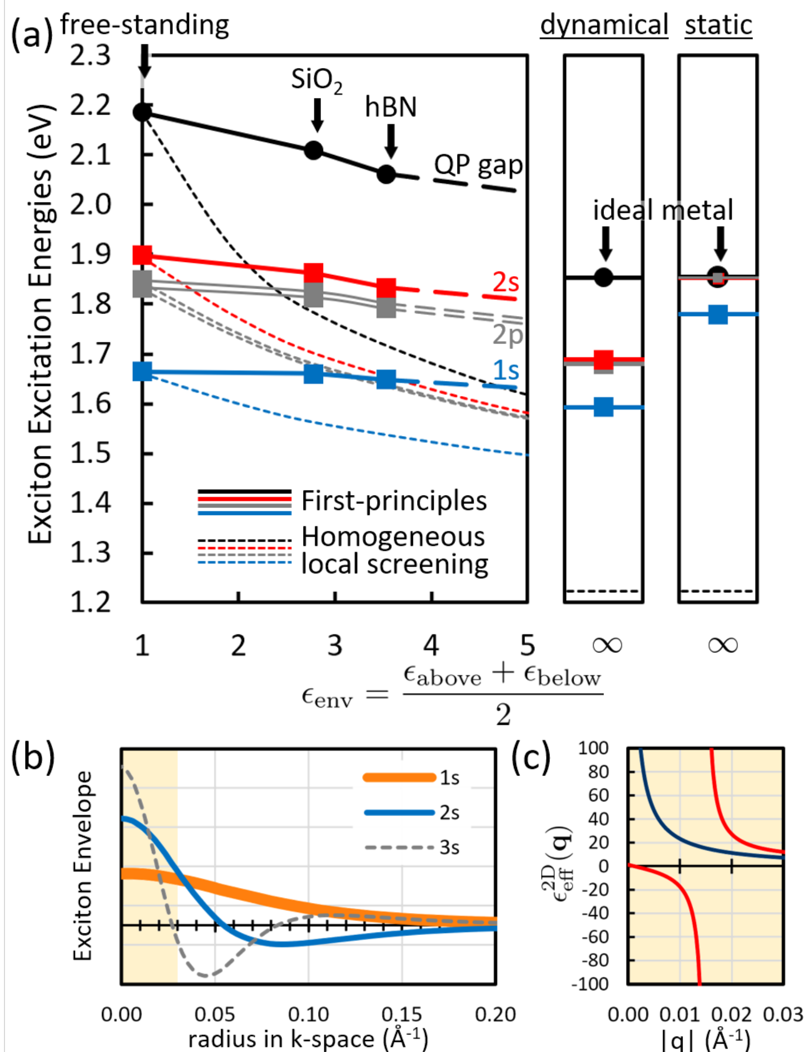

Figure 4.3: (a) Calculated GW-BSE exciton excitation energies of the four lowest-lying excitons (■) and GW QP bandgaps (●) of WSe_2 on different substrates. The substrates are plotted along the horizontal axis using their experimental dielectric constants as in Fig. 4.2. Also plotted using dashed lines are the excitation energies when substrate screening is included using the substrate dielectric constant as in the conventional model (i.e., homogeneous local screening). For ideal metal model as the substrate, excitation energies are calculated using dynamical and static screening. (b) Exciton envelope functions of the three lowest-lying bright excitons of freestanding monolayer WSe_2. (c) Effective 2D dielectric function of monolayer WSe_2 when screened by an ideal-metal model substrate at static frequency (dark blue) and 0.3 eV (red).

Chapter 5

Theoretical Concepts and Methods for Screening in Quasi-2D Materials

5.1 DFT Calculations

Density-functional theory (DFT) calculations for the monolayer TMDs (MoS_2, $MoSe_2$ and WSe_2) and the substrates (bilayer hBN, 4.8-nm-thick (10-layer) crystalline film of polytetrafluoroethylene (PTFE), 4.5-nm-thick SiO_2, 4.3-nm-thick (14-layer) hBN, doped and undoped n-layered graphene) are carried out using the Quantum ESPRESSO [66] package. We use a plane-wave basis set, norm-conserving scalar-relativistic pseudopotentials. For monolayer WSe_2, the generalized gradient approximation (GGA-PBE) [162, 183, 74] is used for electron exchange and correlation. For other monolayer TMDs and substrates, the local density approximation (LDA) [27, 161] is used. To accurately capture the exchange contribution to the GW quasiparticle (QP) self-energy of the monolayer TMDs, semi-cores states are included in the pseudopotentials for the transition metals. For Mo, 4s and 4p semi-core states and the 4d and 5s valence states are included. For W, 5s, 5p, 6s semi-core states and the 5d valence states are included. The kinetic energy cutoff for the DFT calculation is set at 80 Ry for the plane-wave expansion of the wavefunctions.

In our calculations, the length of the periodic supercell for all monolayer TMDs and substrates in the out-of-plane direction is set to be $L_z = 120$ Å. Crystal structures of monolayer MoS_2 [242], $MoSe_2$ [211] and WSe_2 [185] have in-plane lattice constants of 3.1643 Å, 3.2890 Å and 3.2820 Å and thicknesses of 3.1663 Å, 3.3374 Å and 3.3411 Å when measured from the centers of the chalcogenide (S or Se) atoms. The hBN substrate [225] has an in-plane lattice constant of 2.5040 Å, and interlayer separation of 3.3306 Å. n-layered graphene substrate [209] has an in-plane lattice constant of 2.4640 Å, and has an interlayer separation of 3.3555 Å. For the 4.5-nm-thick SiO_2 substrate, we use the α-quartz polymorph [76] that is terminated at the (001)-surface (Z-cut) and have lattice constants of $a = 4.9141$ Å and $c = 5.4061$ Å. Unsaturated Si at the surfaces are passivated using H-atoms and the positions of these Si and H at the surface are obtained by minimizing every force component to less

than 10^{-8} Ry/Bohr radius and the total energy to less than 10^{-8} Ry. For PTFE, we use a supercell with an orthorhombic crystal lattice ($a = 2.6578$ Å, $b = 5.5494$ Å). The C-C bonds of the polymer chains are oriented parallel to the in-plane directions of MoS_2. Ten layers of PTFE (4.83-nm thick) are used.

The MoS_2-substrate distances are determined in separate DFT calculations that also incorporate van der Waals interactions (vdW-DF$^{\mathrm{C09x}}$) [39] and dipole corrections [14, 142] by minimizing the energies of the systems. When the substrates are SiO_2, PTFE, n-layered graphene and hBN, these distances are found to be 2.6 Å, 2.9 Å, 3.3 Åand 3.3 Å, respectively, in the out-of-plane direction. For $MoSe_2$ and WSe_2 which are terminated by Se instead of S, these distances are found to be larger by 0.1 Å.

5.2 GW-BSE Calculations

The QP self-energies and the GW-BSE exciton energy levels are computed with the BerkeleyGW [46, 178, 83] package. In the GW and GW-BSE calculations, the Coulomb interaction beyond 60 Å in the z-direction (i.e., out-of-plane) is always truncated [85].

The QP self-energies are calculated using the eigenvalue-self-consistent, full-frequency GW_0 approximation. The full frequency-dependent dielectric matrices for monolayer MoS_2, $MoSe_2$, WSe_2 are calculated on effective [94] q-grids of 1143×1143, 1100×1100 and 1102×1102, which are expanded from a uniform q-grid of 6×6 using 10 subsampled points. When calculating the dielectric matrices for all three monolayer TMDs, a total of 26450 bands are used and the energy cutoff used to calculate the screened exchange is set at 35 Ry. The periodic supercell cells used for the GW-BSE calculations are the same as those used in Sec. 5.1 for the DFT calculations and have an $L_z = 120$ Å.

To calculate the low-lying exciton energy levels, the Bethe-Salpeter Equation (BSE) [178] is solved using the calculated QP energies. The electron-hole interaction kernel of the BSE Hamiltonian is first calculated on a uniform k-grid of 72×72, using one valence band and one conduction band and a dielectric matrix that is calculated on uniform q-grid of 72×72 using 1400 bands and a 5 Ry-energy cutoff for the screened exchange. To obtain the envelope function of the lowest four exciton wavefunctions, the BSE Hamiltonian is diagonalized iteratively using interaction kernel matrix elements that are interpolated [94, 178] from the uniform 72×72 k-grid to a finer uniform k-grid of 1440×1440, using directly-calculated matrix elements for q-points of a density equivalent to 5184×5184. Since the lowest-lying exciton wavefunctions are localized [168] in reciprocal space, the kernel matrix elements are only interpolated onto a round patch of k-points centered at the K-valley. The radius of the patch is 0.155 times the length of a reciprocal lattice vector (which is 0.181 Bohr^{-1} for WSe_2). To solve the frequency-dependent BSE self-consistently, we take advantage of the fact that the exciton is highly localized at the K-valley, such that that $E_c^{QP} - E_v^{QP}$ is approximately a constant for all k-points of the exciton wavefunction. With this approximation, we solve the BSE equation self-consistently for every exciton, using a screening frequency that corresponds to the exciton binding energy. In this work, all

oscillator strengths of the excitons are calculated for light that is polarized in the in-plane direction, in the bond-direction between a transition metal and chalcogenide.

Screening due to the substrates and encapsulations are included during the calculation of the QP energies and the energy levels of the excitons using the in-plane substrate-averaging (IPSA) approximation (see Sec. 4.2). In this approach, substrate screening is assumed to be translationally invariant. For this, we calculate the non-interacting polarizability $\chi^0_{\mathbf{GG}'}(\mathbf{q})$ of the substrates. Small q's corresponding to the subsampled q-points of the monolayer TMDs are always computed directly. Large q's for each substrate are calculated on a different uniform grid and interpolated onto $\chi^0_{\mathbf{GG}'}(\mathbf{q})$. As mentioned in Sec. 5.1, the length of the periodic supercells of all substrates in the out-of-plane direction is fixed at $L_z = 120$ Å. The dimensions of the supercells of the substrates, namely, bilayer hBN, 4.8-nm-thick PTFE, 4.5-nm-thick SiO_2, 14-layer hBN, doped and undoped n-layered graphene are also the same as those used in Sec. 5.1 for the DFT calculations. For bilayer and 14-layer hBN, the DFT wavefunctions are calculated on k-grid of 8×8 and using a kinetic energy cutoff of 60 Ry. Its $\chi^0_{\mathbf{GG}'}(\mathbf{q})$ is calculated on a uniform q-grid of 8×8, using a screened energy cutoff of 6 Ry and 1116 bands for the summation over empty states. For the 4.5-nm-thick SiO_2, the DFT wavefunctions are calculated on a uniform k-grid of 5×5 and using a kinetic energy cutoff of 60 Ry. Its $\chi^0_{\mathbf{GG}'}(\mathbf{q})$ is calculated on a uniform q-grid of 5×5, using a screened energy cutoff of 6 Ry and 4350 bands. For 4.8-nm-thick PTFE, the DFT wavefunctions are calculated on k-grid of 8×4 and using a kinetic energy cutoff of 100 Ry. Its $\chi^0_{\mathbf{GG}'}(\mathbf{q})$ is calculated on a q-grid of 8×4, a screened energy cutoff of 8 Ry and 4700 bands. When substrate screening is added using a momentum-independent effective dielectric constant, a value of 1001 is assumed to be infinite screening (Fig. 4.2).

For intrinsic (undoped) graphene, the DFT wavefunctions are calculated with a kinetic energy cutoff of 60 Ry. To calculate the small subsampled q-points of $\chi^0_{\mathbf{GG}'}(\mathbf{q})$ and in order to sample the k-points at the Dirac point accurately, wavefunctions for bands crossing the Fermi level are calculated on a fractal k-grid. Starting with a uniform k-grid of density $2^5 \times 2^5$, the k-grid is progressively subdivided by half near the K and K' valleys, up till a maximum density of $2^{12} \times 2^{12}$ at the K and K' valleys. Nonlinear broadening that corresponds to the nonlinear k-point sampling is also used to calculate $\chi^0_{\mathbf{GG}'}$. For each k-point, broadening is set to a maximum of 0.2 eV or the energy difference between each conduction band and the valence band that are being summed over, if it is smaller. This is important to ensure that the poles of $\chi^0_{\mathbf{GG}'}(\mathbf{q})$ are located at the right frequencies. For other q-points, the DFT wavefunctions are calculated on a uniform k-grid of 10×10 and $\chi^0_{\mathbf{GG}'}(\mathbf{q})$ is calculated on a uniform q-grid of 10×10, using an energy cutoff of 8 Ry and 1700 bands in the summation over empty states for the computation of the noninteracting polarizability and the self-energy.

For doped n-layered graphene, doping is achieved in the rigid band model by lowering the Fermi-level from the Dirac point by 0.3 eV (p-doped) [211]. To calculate the small subsampled q-points of $\chi^0_{\mathbf{GG}'}(\mathbf{q})$, the k-points of the wavefunctions at the Fermi surface are calculated at a density that is at least twice the density of the q-grid for intraband excitations. This corresponds to a k-point density ranging from 46×46 to 2938×2938. Nonlinear broadening that corresponds to the k-point sampling is also used to calculate $\chi^0_{\mathbf{GG}'}(\mathbf{q})$ to

ensure correct pole positions. For interband transitions of small q's and transition of all other q-points, the DFT wavefunctions are calculated on a uniform k-grid of 10×10 and $\chi^0_{\mathbf{GG'}}(\mathbf{q})$ is calculated on a uniform q-grid of 10×10, using an screened energy cutoff of 8 Ry and 1700 bands in the summation over empty states for the computation of the noninteracting polarizability and the self-energy.

With these parameters, we ensure that the calculated GW bandgaps are converged to better than 0.1 eV, and that the relative GW-bandgap renormalization across different substrates are converged to better than 0.01 eV. The exciton energy levels are also converged to better than 0.1 eV and the exciton binding energies and relative renormalization across different substrates are converged to better than 0.01 eV.

5.3 Derivation of the Ideal-Metal Substrate Model

In this work, an ideal-metal substrate model is defined as a semiclassical model which at steady state completely screens any external potential above its surface by inducing a 2D surface charge like a classical ideal metal. The model also displays retardation effects based on the Lindhard theory for the 2D electron gas. It serves as the theoretical upper bound of saturated metallic substrate screening. In this section, we first define the interacting polarizability $\chi_{\mathbf{GG'}}(\mathbf{q},\omega)$ and then use it to derive the static response function of the ideal-metal substrate model(s), before finally extending it to finite frequencies using the frequency-dependence of the Lindhard function $\chi^0_{\mathrm{L}}(q+G,\omega)$.

Interacting Polarizability

The interacting polarizability $\chi(\mathbf{r},\mathbf{r}',t-t')$ is the time-dependent linear response function of the particle density $\rho_{\text{ind}}(\mathbf{r},t)$ to an external potential $\phi_{\text{ext}}(\mathbf{r}',t')$, defined as,

$$\chi(\mathbf{r},\mathbf{r}',t-t') = \frac{\delta\rho_{\text{ind}}(\mathbf{r},t)}{\delta\phi_{\text{ext}}(\mathbf{r}',t')}, \tag{5.1}$$

such that,

$$\rho_{\text{ind}}(\mathbf{r},t) = \int_{\mathcal{V}} \mathrm{d}\mathbf{r}' \int_{-\infty}^{t} \mathrm{d}t' \chi(\mathbf{r},\mathbf{r}',t-t')\phi_{\text{ext}}(\mathbf{r}',t'). \tag{5.2}$$

Here, $\mathcal{V}$ is the large crystal volume in real space that satisfies the Born-von Karmen periodic boundary conditions. Also, due to the time translation symmetry of the response function, χ depends only on the time difference $t-t'$, making ρ_{ind} in Eq. (5.2) a convolution of χ and ϕ_{ext} in the time domain and a product in the frequency domain,

$$\rho_{\text{ind}}(\mathbf{r},\omega) = \int_{\mathcal{V}} \mathrm{d}\mathbf{r}' \chi(\mathbf{r},\mathbf{r}',\omega)\phi_{\text{ext}}(\mathbf{r}',\omega). \tag{5.3}$$

Fourier transforming Eq. (5.3) from the real-space representation to the momentum-space representation and using the conventions as defined in Sec. 5.7, we get

$$\begin{aligned}\rho_{\text{ind}}(\mathbf{q},\omega) &= \frac{1}{\mathcal{V}}\sum_{\mathbf{q}'}\chi(\mathbf{q},\mathbf{q}',\omega)\phi_{\text{ext}}(\mathbf{q}',\omega)\\ &= \frac{1}{\mathcal{V}}\sum_{\mathbf{q}'}\chi(\mathbf{q},\mathbf{q}',\omega)v_c(\mathbf{q}')\rho_{\text{ext}}(\mathbf{q}',\omega),\end{aligned} \tag{5.4}$$

where v_c is the Coulomb interaction. We will first define $\mathbf{q}$ as the momentum wavevector spanning the whole reciprocal space. Here, we used the classical electromagnetic theory relating $\phi_{\text{ext}}(\mathbf{q},\omega) = v_c(\mathbf{q})\rho_{\text{ext}}(\mathbf{q},\omega)$. For a crystal with translation vectors $\mathbf{R}$ in real space, the discrete spatial translational symmetry of the system dictates that $\chi(\mathbf{q},\mathbf{q}')$ is zero unless $\mathbf{q}-\mathbf{q}'=\mathbf{G}$. Further restricting $\mathbf{q}$ to the First Brillouin Zone, we rewrite Eq. (5.4) as,

$$\begin{aligned}\rho_{\text{ind}}(\mathbf{q}+\mathbf{G},\omega) &= \frac{1}{\mathcal{V}}\sum_{\mathbf{G}'}[\chi(\mathbf{q}+\mathbf{G},\mathbf{q}+\mathbf{G}',\omega)v_c(\mathbf{q}+\mathbf{G}')\\ &\qquad\times\rho_{\text{ext}}(\mathbf{q}+\mathbf{G}',\omega)]\\ &= \frac{1}{\mathcal{V}}\sum_{\mathbf{G}'}[\chi_{\mathbf{G}\mathbf{G}'}(\mathbf{q},\omega)v_c(\mathbf{q}+\mathbf{G}')\\ &\qquad\times\rho_{\text{ext}}(\mathbf{q}+\mathbf{G}',\omega)]\\ \rho^{\text{ind}}_{\mathbf{G}}(\mathbf{q},\omega) &= \frac{1}{\mathcal{V}}\sum_{\mathbf{G}'}\chi_{\mathbf{G}\mathbf{G}'}(\mathbf{q},\omega)v^c_{\mathbf{G}'}(\mathbf{q})\rho^{\text{ext}}_{\mathbf{G}'}(\mathbf{q},\omega),\end{aligned} \tag{5.5}$$

which will be used to derive the static response functions $\chi_{\mathbf{G}\mathbf{G}',\text{static}}(\mathbf{q})$ of the image point charge model (Sec. 5.3) and of the surface charge model (Sec. 5.3).

Classical Static Response

In this subsection, we derive the classical static response functions $\chi_{\mathbf{G}\mathbf{G}',\text{static}}(\mathbf{q})$ of two metal substrate models. The static response function $\chi_{\mathbf{G}\mathbf{G}',\text{static}}(\mathbf{q})$ is the response in the static limit, in which the substrate perfectly screens the external potential.

Image-Point-Charge Response

Classical electrostatics yields that in the presence of an external potential originating from a static external charge, a grounded ideal-metal substrate will induce a potential *above the substrate* that is identical to the potential that would have been induced by an image charge (of an opposite sign) (Fig. 5.1) in the absence of the substrate. In the simplest approximation, one can assume that an external charge will cause a response in the substrate as if an image charge has been induced at the opposite side of the surface plane. For this reason, the response function of a substrate is sometimes modelled by an *image point charge* model. Here, we derive the image-point-charge response, because it is easy and will help

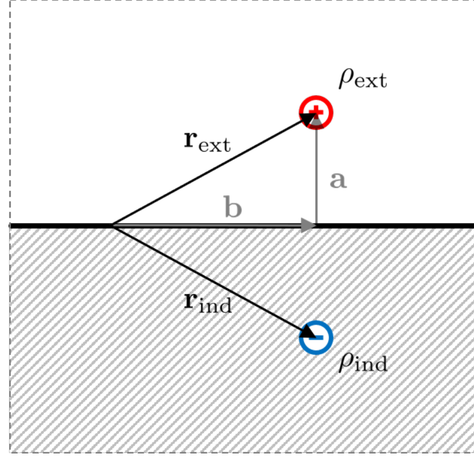

Figure 5.1: Image-point-charge model in a periodic supercell. In this model, the point charge $\rho_{\rm ext}$ induces an image charge $\rho_{\rm ind}$. In the limit where $\mathcal{V} \to \infty$, there will be no periodic images. In practical calculations, the periodic supercell has a finite volume. To avoid interactions between the periodic images, the Coulomb potential $v_c(\mathbf{q}+\mathbf{G})$ used to calculate the response function $\chi_{\mathbf{G}\mathbf{G}',\rm static}(\mathbf{q})$ is appropriately truncated in the out-of-plane direction [85].

the reader understand the derivation of the surface-charge response below that is physically more accurate.

We begin by defining a general position for the external point charge $\mathbf{r}_{\rm ext}$ such that,

$$\mathbf{r}_{\rm ext\parallel} = \mathbf{b},$$
$$\mathbf{r}_{\rm ext\perp} = \mathbf{a}.$$

Since the position of the induced charge $\mathbf{r}_{\rm ind}$ is,

$$\mathbf{r}_{\rm ind} = \mathbf{r}_{\rm ext} - 2\mathbf{a},$$

the particle density distributions of the external and induced charges in the real-space representation can both be written in terms of $\mathbf{r}_{\rm ext}$ as,

$$\rho_{\rm ext}(\mathbf{r};\mathbf{r}_{\rm ext}) = \delta(\mathbf{r}-\mathbf{r}_{\rm ext}), \tag{5.6}$$
$$\rho_{\rm ind}(\mathbf{r};\mathbf{r}_{\rm ext}) = -\delta[\mathbf{r}-(\mathbf{r}_{\rm ext}-2\mathbf{a})], \tag{5.7}$$

and their Fourier transforms to the reciprocal-space representation become,

$$\rho_{\rm ext}(\mathbf{q}+\mathbf{G};\mathbf{r}_{\rm ext}) = e^{-i(\mathbf{q}+\mathbf{G})\cdot\mathbf{r}_{\rm ext}}, \tag{5.8}$$
$$\rho_{\rm ind}(\mathbf{q}+\mathbf{G};\mathbf{r}_{\rm ext}) = -e^{-i(\mathbf{q}+\mathbf{G})\cdot(\mathbf{r}_{\rm ext}-2\mathbf{a})}. \tag{5.9}$$

Finally, substituting Eqs. (5.8) and (5.9) into Eq. (5.5), we solve for $\chi_{\mathbf{GG}',\mathrm{static}}(\mathbf{q})$ using Eq. (5.5),

$$\begin{aligned}
-e^{-i(\mathbf{q}+\mathbf{G})\cdot(\mathbf{r}_{\mathrm{ext}}-2\mathbf{a})} &= \frac{1}{\mathcal{V}}\sum_{\mathbf{G}'}\chi_{\mathbf{GG}',\mathrm{static}}(\mathbf{q})v_c(\mathbf{q}+\mathbf{G}')e^{-i(\mathbf{q}+\mathbf{G}')\cdot\mathbf{r}_{\mathrm{ext}}},\\
-e^{-i\mathbf{G}\cdot(\mathbf{b}-\mathbf{a})} &= \frac{1}{\mathcal{V}}\sum_{\mathbf{G}'}\chi_{\mathbf{GG}',\mathrm{static}}(\mathbf{q})v_c(\mathbf{q}+\mathbf{G}')e^{-i\mathbf{G}'\cdot(\mathbf{b}+\mathbf{a})},\\
-\int_{\mathcal{V}}\mathrm{d}\mathbf{r}_{\mathrm{ext}}\,e^{-i\mathbf{G}\cdot(\mathbf{b}-\mathbf{a})}e^{i\tilde{\mathbf{G}}'\cdot(\mathbf{b}+\mathbf{a})} &= \frac{1}{\mathcal{V}}\sum_{\mathbf{G}'}\chi_{\mathbf{GG}',\mathrm{static}}(\mathbf{q})v_c(\mathbf{q}+\mathbf{G}')\int_{\mathcal{V}}\mathrm{d}\mathbf{r}_{\mathrm{ext}}\,e^{-i\mathbf{G}'\cdot(\mathbf{b}+\mathbf{a})}e^{i\tilde{\mathbf{G}}'\cdot(\mathbf{b}+\mathbf{a})},\\
-\int_{\mathcal{V}}\mathrm{d}\mathbf{b}\mathrm{d}a\,e^{i(-\mathbf{G}+\tilde{\mathbf{G}})\cdot\mathbf{b}}e^{i(\mathbf{G}+\tilde{\mathbf{G}})\cdot\mathbf{a}} &= \frac{1}{\mathcal{V}}\sum_{\mathbf{G}'}\chi_{\mathbf{GG}',\mathrm{static}}(\mathbf{q})v_c(\mathbf{q}+\mathbf{G}')\int_{\mathcal{V}}\mathrm{d}\mathbf{b}\mathrm{d}a\,e^{i(-\mathbf{G}'+\tilde{\mathbf{G}})\cdot\mathbf{b}}e^{i(-\mathbf{G}'+\tilde{\mathbf{G}})\cdot\mathbf{a}},\\
-\int_{\mathcal{V}}\mathrm{d}\mathbf{b}\mathrm{d}a\,e^{i(-\mathbf{G}_{\parallel}+\tilde{\mathbf{G}}_{\parallel})\cdot\mathbf{b}}e^{i(G_{\perp}+\tilde{G}_{\perp})a} &= \frac{1}{\mathcal{V}}\sum_{\mathbf{G}'}\chi_{\mathbf{GG}',\mathrm{static}}(\mathbf{q})v_c(\mathbf{q}+\mathbf{G}')\int_{\mathcal{V}}\mathrm{d}\mathbf{b}\mathrm{d}a\,e^{i(-\mathbf{G}'_{\parallel}+\tilde{\mathbf{G}}_{\parallel})\cdot\mathbf{b}}e^{i(-G'_{\perp}+\tilde{G}_{\perp})a},\\
-\delta_{\mathbf{G}_{\parallel}\tilde{\mathbf{G}}_{\parallel}}\delta_{G_{\perp},-\tilde{G}_{\perp}} &= \frac{1}{\mathcal{V}}\sum_{\mathbf{G}'}\chi_{\mathbf{GG}',\mathrm{static}}(\mathbf{q})v_c(\mathbf{q}+\mathbf{G}')\,\delta_{\mathbf{G}'\tilde{\mathbf{G}}},\\
-\delta_{\mathbf{G}_{\parallel}\mathbf{G}'_{\parallel}}\delta_{G_{\perp},-G'_{\perp}} &= \frac{1}{\mathcal{V}}\chi_{\mathbf{GG}',\mathrm{static}}(\mathbf{q})v_c(\mathbf{q}+\mathbf{G}'),\\
\chi_{\mathbf{GG}',\mathrm{static}}(\mathbf{q}) &= -\mathcal{V}\frac{\delta_{\mathbf{G}_{\parallel}\mathbf{G}'_{\parallel}}\delta_{G_{\perp},-G'_{\perp}}}{v_c(\mathbf{q}+\mathbf{G}')}. \qquad (5.10)
\end{aligned}$$

Diagonality of the response function $\chi_{\mathbf{GG}',\mathrm{static}}(\mathbf{q})$ in the in-plane directions in reciprocal space necessarily means that screening is translationally-invariant in the in-plane directions in real space. This comes from the infinitesimal translational invariance of the system along the in-plane directions. To understand this, suppose the external charge $\rho_{\mathrm{ext}}(\mathbf{r};\mathbf{r}_{\mathrm{ext}}+\Delta\mathbf{r}_{\mathrm{ext}\parallel})$ is displaced in real space by $\Delta\mathbf{r}_{\mathrm{ext}\parallel}$. In this model, we expect its induced charge $\rho_{\mathrm{ind}}(\mathbf{r};\mathbf{r}_{\mathrm{ext}}+\Delta\mathbf{r}_{\mathrm{ext}\parallel})$ to also be displaced by the same amount in real space, such that $\chi_{\mathbf{GG}',\mathrm{static}}(\mathbf{q})$ in reciprocal space will be phase-shifted accordingly,

$$e^{i(\mathbf{q}+\mathbf{G})\cdot\Delta\mathbf{r}_{\mathrm{ext}\parallel}}\chi(\mathbf{q}+\mathbf{G},\mathbf{q}+\mathbf{G}')e^{-i(\mathbf{q}+\mathbf{G}')\cdot\Delta\mathbf{r}_{\mathrm{ext}\parallel}}. \qquad (5.11)$$

If $\chi(\mathbf{q}+\mathbf{G},\mathbf{q}+\mathbf{G}')$ is non-zero for $\mathbf{G}_{\parallel}\neq\mathbf{G}'_{\parallel}$, then χ is not invariant under the translational displacement of $\rho_{\mathrm{ext}}(\mathbf{r};\mathbf{r}_{\mathrm{ext}}+\Delta\mathbf{r}_{\mathrm{ext}})$ in real space.

Note, however, that this image point charge model is not entirely correct, because even though an image charge reproduces the correct induced potential in the region above the substrate, it induces a mirrored potential within the substrate, when in fact the potential within the substrate is always zero for a metal. The physically-correct response should be one that induces a surface charge at the metal surface (See Fig. 5.2).

Surface-Charge Response

Here, we derive the quasi-2D ideal-metal model (IMM) substrate (Fig. 5.2). Classical electromagnetism dictates that at the interface between free space and the ideal-metal substrate,

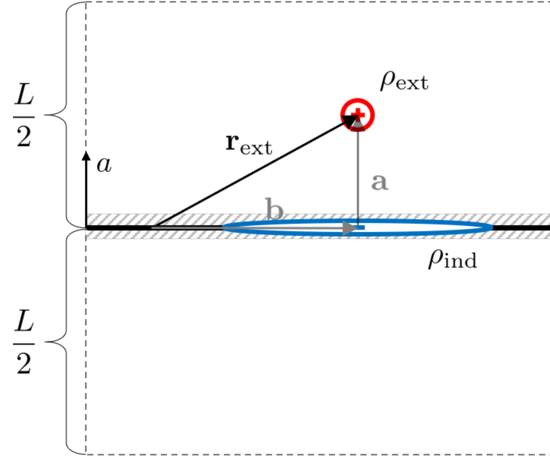

Figure 5.2: Surface-charge-inducing ideal metal model (IMM) in a periodic supercell of height L. In this model, the point charge $\rho_{\rm ext}$ induces a quasi-2D surface charge $\rho_{\rm ind}$. In the limit where $\mathcal{V} \to \infty$, there will be no periodic images. In practical calculations, the periodic supercell has a finite volume. To avoid interaction between the periodic images, the Coulomb potential $v_c(\mathbf{q}+\mathbf{G})$ used to calculate the response function $\chi_{\mathbf{G}\mathbf{G}',\rm static}(\mathbf{q})$ is appropriately truncated in the out-of-plane direction [85].

the normal derivative of the total potential $\phi_{\rm tot}$ is discontinuous. According to the Gauss's law, this corresponds to a collection of bound surface charges at the surface of the ideal-metal substrate. The particle density distributions of this external point charge $\rho_{\rm ext}(\mathbf{r};\mathbf{r}_{\rm ext})$ and induced surface charge $\rho_{\rm ind}(\mathbf{r};\mathbf{r}_{\rm ext})$ [70, 87, 63] can be given in terms of $\mathbf{r}_{\rm ext}$ by,

$$\begin{aligned}\rho_{\rm ext}(\mathbf{r};\mathbf{r}_{\rm ext}) &= \delta(\mathbf{r}-\mathbf{r}_{\rm ext}),\\ &= \delta(\mathbf{r}-\mathbf{a}),\end{aligned} \tag{5.12}$$

$$\begin{aligned}\rho_{\rm ind}(\mathbf{r};\mathbf{r}_{\rm ext}) &= \rho_{\rm ind}(s,\theta,z;\mathbf{r}_{\rm ext})\\ &= -\frac{|\mathbf{a}|}{2\pi}\frac{\delta(z)}{s^2+|\mathbf{a}|^2},\end{aligned} \tag{5.13}$$

in cylindrical coordinates in an analogy of Eqs. (5.6) and (5.7), where we use the same definitions, i.e., $\mathbf{r}_{\rm ext\parallel} = \mathbf{b}$ and $\mathbf{r}_{\rm ext\perp} = \mathbf{a}$, but set $\mathbf{b} = 0$ for simiplicity. Also analogous to Eqs. (5.8) and (5.9), the Fourier transform of $\rho_{\rm ext}(\mathbf{r};\mathbf{r}_{\rm ext})$ and $\rho_{\rm ind}(\mathbf{r};\mathbf{r}_{\rm ext})$ are given by,

$$\rho_{\rm ext}(\mathbf{q}+\mathbf{G};\mathbf{r}_{\rm ext}) = e^{-i(\mathbf{q}+\mathbf{G})\cdot\mathbf{a}}, \tag{5.14}$$

$$\begin{aligned}\rho_{\rm ind}(\mathbf{q}+\mathbf{G};\mathbf{r}_{\rm ext}) &= \int_{\mathcal{V}} \mathrm{d}\mathbf{r}\rho_{\rm ind}(\mathbf{r};\mathbf{r}_{\rm ext})e^{-i(\mathbf{q}+\mathbf{G})\cdot\mathbf{r}}\\ &= -\frac{|\mathbf{a}|}{2\pi}\int_{\mathcal{V}} \mathrm{d}\mathbf{r}\frac{\delta(z)}{s^2+|\mathbf{a}|^2}e^{-i(\mathbf{q}+\mathbf{G})\cdot\mathbf{r}}\end{aligned}$$

$$
\begin{aligned}
&= -\frac{|\mathbf{a}|}{2\pi}\int_{\mathcal{V}} s\,\mathrm{d}s\,\mathrm{d}\theta\,\mathrm{d}z\frac{\delta(z)}{s^2+|\mathbf{a}|^2}e^{-i(\mathbf{q}+\mathbf{G}_\parallel)\cdot\mathbf{s}}e^{-iG_\perp z}\\
&= -\frac{|\mathbf{a}|}{2\pi}\int_{\mathcal{S}} s\,\mathrm{d}s\,\mathrm{d}\theta\frac{1}{s^2+|\mathbf{a}|^2}e^{-i|\mathbf{q}+\mathbf{G}_\parallel||\mathbf{s}|\cos\theta}\\
&= -\frac{|\mathbf{a}|}{2\pi}\int_0^\infty \mathrm{d}s\int_0^{2\pi}\mathrm{d}\theta\frac{s}{s^2+|\mathbf{a}|^2}e^{-i|\mathbf{q}+\mathbf{G}_\parallel||\mathbf{s}|\cos\theta}\\
&= -\frac{|\mathbf{a}|}{2\pi}2\pi\int_0^\infty s\,\mathrm{d}s\frac{1}{(s^2+|\mathbf{a}|^2)^{\frac{3}{2}}}J_0(|\mathbf{q}+\mathbf{G}_\parallel|s)\\
&= -\frac{|\mathbf{a}|}{2\pi}2\pi\,\mathcal{H}_0\left\{\frac{1}{(s^2+|\mathbf{a}|^2)^{\frac{3}{2}}}\right\}\\
&= -\frac{|\mathbf{a}|}{2\pi}2\pi\frac{e^{-|\mathbf{q}+\mathbf{G}_\parallel||\mathbf{a}|}}{|\mathbf{a}|}\\
&= -e^{-|\mathbf{q}+\mathbf{G}_\parallel||\mathbf{a}|},
\end{aligned}
\tag{5.15}
$$

where $J_0(x)$ is the Bessel function of the first kind and zeroth order, $\mathcal{H}_0\{f(s)\}$ is the zeroth-order Hankel transform of $f(s)$. Eq. (5.15) can now be generalized to an arbitrary $\mathbf{b}$ using the Shift Theorem,

$$
\rho_{\mathrm{ind}}(\mathbf{q}+\mathbf{G};\mathbf{r}_{\mathrm{ext}}) = -e^{-|\mathbf{q}+\mathbf{G}_\parallel||\mathbf{a}|}e^{-i(\mathbf{q}+\mathbf{G}_\parallel)\cdot\mathbf{b}}. \tag{5.16}
$$

Finally, similar to our derivation of Eq. (5.10), $\chi_{\mathbf{GG}',\mathrm{static}}(\mathbf{q})$ can be solved by substituting Eqs. (5.14) and (5.16) into Eq. (5.5),

$$
\begin{aligned}
-e^{-|\mathbf{q}+\mathbf{G}_\parallel||\mathbf{a}|}e^{-i(\mathbf{q}+\mathbf{G}_\parallel)\cdot\mathbf{b}} &= \frac{1}{\mathcal{V}}\sum_{\mathbf{G}'}\chi_{\mathbf{GG}',\mathrm{static}}(\mathbf{q})v_c(\mathbf{q}+\mathbf{G}')e^{-i(\mathbf{q}+\mathbf{G}')\cdot\mathbf{r}_{\mathrm{ext}}},\\
-e^{-|\mathbf{q}+\mathbf{G}_\parallel||\mathbf{a}|}e^{-i(\mathbf{q}+\mathbf{G}_\parallel)\cdot\mathbf{b}} &= \frac{1}{\mathcal{V}}\sum_{\mathbf{G}'}\chi_{\mathbf{GG}',\mathrm{static}}(\mathbf{q})v_c(\mathbf{q}+\mathbf{G}')e^{-i(\mathbf{q}+\mathbf{G}')\cdot(\mathbf{b}+\mathbf{a})},\\
-e^{-|\mathbf{q}+\mathbf{G}_\parallel||\mathbf{a}|}e^{-i\mathbf{G}_\parallel\cdot\mathbf{b}} &= \frac{1}{\mathcal{V}}\sum_{\mathbf{G}'}\chi_{\mathbf{GG}',\mathrm{static}}(\mathbf{q})v_c(\mathbf{q}+\mathbf{G}')e^{-i\mathbf{G}'_\parallel\cdot\mathbf{b}}e^{-iG'_\perp a},\\
-e^{-|\mathbf{q}+\mathbf{G}_\parallel||\mathbf{a}|}\delta_{\mathbf{G}_\parallel\mathbf{G}'_\parallel} &= \frac{1}{\mathcal{V}}\sum_{G'_\perp}\chi_{\mathbf{GG}',\mathrm{static}}(\mathbf{q})v_c(\mathbf{q}+\mathbf{G}')e^{-iG'_\perp a},\\
-\left(\int_{-\frac{L}{2}}^{\frac{L}{2}}\mathrm{d}a\,e^{-|\mathbf{q}+\mathbf{G}_\parallel||\mathbf{a}|}e^{i\tilde{G}_\perp a}\right)\delta_{\mathbf{G}_\parallel\mathbf{G}'_\parallel} &= \frac{1}{\mathcal{V}}\sum_{G'_\perp}\chi_{\mathbf{GG}',\mathrm{static}}(\mathbf{q})v_c(\mathbf{q}+\mathbf{G}')\left(\int_{-\frac{L}{2}}^{\frac{L}{2}}\mathrm{d}a\,e^{i(-G'_\perp+\tilde{G}_\perp)a}\right),\\
-\left(\int_{-\frac{L}{2}}^{\frac{L}{2}}\mathrm{d}a\,e^{-|\mathbf{q}+\mathbf{G}_\parallel||\mathbf{a}|}e^{i\tilde{G}_\perp a}\right)\delta_{\mathbf{G}_\parallel\mathbf{G}'_\parallel} &= \frac{1}{\mathcal{V}}\sum_{G'_\perp}\chi_{\mathbf{GG}',\mathrm{static}}(\mathbf{q})v_c(\mathbf{q}+\mathbf{G}')L\,\delta_{G'_\perp\tilde{G}_\perp},\\
-\left(\frac{1}{L}\int_{-\frac{L}{2}}^{\frac{L}{2}}\mathrm{d}a\,e^{-|\mathbf{q}+\mathbf{G}_\parallel||\mathbf{a}|}e^{iG'_\perp a}\right)\delta_{\mathbf{G}_\parallel\mathbf{G}'_\parallel} &= \frac{1}{\mathcal{V}}\chi_{\mathbf{GG}',\mathrm{static}}(\mathbf{q})v_c(\mathbf{q}+\mathbf{G}'),
\end{aligned}
$$

$$\chi_{\mathbf{G}\mathbf{G}',\mathrm{static}}(\mathbf{q}) = -\mathcal{V}\frac{\delta_{\mathbf{G}_\parallel \mathbf{G}'_\parallel}}{v_c(\mathbf{q}+\mathbf{G}')} \underbrace{\left(\frac{1}{L}\int_{-\frac{L}{2}}^{\frac{L}{2}} \mathrm{d}a\, e^{-|\mathbf{q}+\mathbf{G}_\parallel||\mathbf{a}|} e^{iG'_\perp a}\right)}_{I(\mathbf{q},\mathbf{G}_\parallel,G'_\perp)},$$

$$\chi_{\mathbf{G}\mathbf{G}',\mathrm{static}}(\mathbf{q}) = -\mathcal{V}\frac{\delta_{\mathbf{G}_\parallel \mathbf{G}'_\parallel} I(\mathbf{q},\mathbf{G}_\parallel,G'_\perp)}{v_c(\mathbf{q}+\mathbf{G}')}. \tag{5.17}$$

Note that function $I(\mathbf{q},\mathbf{G}_\parallel,G'_\perp)$ peaks at $\mathbf{q}+\mathbf{G}_\parallel = 0$ and $G'_\perp = 0$. In the limit of $L \to \infty$, $I(\mathbf{q},\mathbf{G}_\parallel,G'_\perp) \to \delta_{\mathbf{q}+\mathbf{G}_\parallel,0}\delta_{G'_\perp,0}$. Similar to the image-point-charge response function in Eq. (5.10), $\chi_{\mathbf{G}\mathbf{G}',\mathrm{static}}(\mathbf{q})$ for a surface-charge response is also diagonal in $\mathbf{G}_\parallel$ and $\mathbf{G'}_\parallel$. Unlike the image-point-charge response function, however, the surface-charge response function is a constant for all $G_\perp$ (since the induced charge is a delta function in the z-direction). Now, we will proceed to evaluate $I(\mathbf{q},\mathbf{G}_\parallel,G'_\perp)$. For a general $G'_\perp$ and noting that $G'_\perp$ is discrete, we get

$$\begin{aligned}
I(\mathbf{q},\mathbf{G}_\parallel,G'_\perp) &= \frac{1}{L}\int_{-\frac{L}{2}}^{\frac{L}{2}} \mathrm{d}a\, e^{-|\mathbf{q}+\mathbf{G}_\parallel||\mathbf{a}|} e^{iG'_\perp a} \\
&= \frac{e^{-\frac{L}{2}(iG'_\perp + |\mathbf{q}+\mathbf{G}_\parallel|)}\left[-iG'_\perp(-1+e^{iG'_\perp L}) - (1+e^{iG'_\perp L} - 2e^{\frac{L}{2}(iG'_\perp+|\mathbf{q}+\mathbf{G}_\parallel|)})|\mathbf{q}+\mathbf{G}_\parallel|\right]}{L\,(G'^2_\perp + |\mathbf{q}+\mathbf{G}_\parallel|^2)} \\
&= \frac{e^{-\frac{L}{2}|\mathbf{q}+\mathbf{G}_\parallel|}}{\frac{L}{2}(G'^2_\perp + |\mathbf{q}+\mathbf{G}_\parallel|^2)}\left[G'_\perp \sin(\frac{L}{2}G'_\perp) - |\mathbf{q}+\mathbf{G}_\parallel|\cos(\frac{L}{2}G'_\perp)\right] + \frac{|\mathbf{q}+\mathbf{G}_\parallel|}{\frac{L}{2}(G'^2_\perp + |\mathbf{q}+\mathbf{G}_\parallel|^2)} \\
&= \frac{|\mathbf{q}+\mathbf{G}_\parallel|\left[1 - e^{-\frac{L}{2}|\mathbf{q}+\mathbf{G}_\parallel|}\cos(\frac{L}{2}G'_\perp)\right]}{\frac{L}{2}(G'^2_\perp + |\mathbf{q}+\mathbf{G}_\parallel|^2)}.
\end{aligned} \tag{5.18}$$

With Eqs. (5.17) and (5.18), we have derived a static perfectly-screening surface-charge response. According to the Uniqueness Theorem of electrostatics, this response by a quasi-2D metal is equivalent to the screening by a semi-infinite metal (Fig. 5.3). We also showed numerically that this response function $\chi_{\mathbf{G}\mathbf{G}',\mathrm{static}}(\mathbf{q})$ also reproduces the calculated $|\mathbf{q}+\mathbf{G}|$-dependence of $\epsilon^{-1}_{\mathbf{G}=\mathbf{G}'}(\mathbf{q})$ of doped monolayer graphene, unlike its image-point-charge counterpart.

Semi-classical Full Frequency-Dependent Response

Since our static surface-charge response (Eq. (5.17)) is derived using a classical model, we also derive the time-dependence of its dynamical response using a classical starting point. In this subsection, we will show that even though we begin our derivation using the semiclassical Boltzmann transport equation, we will arrive at similar result as the Lindhard equation.

Frequency-dependence of the dynamical response of the induced surface charge can be understood from the time-dependence of its motion in the in-plane directions. In the classical

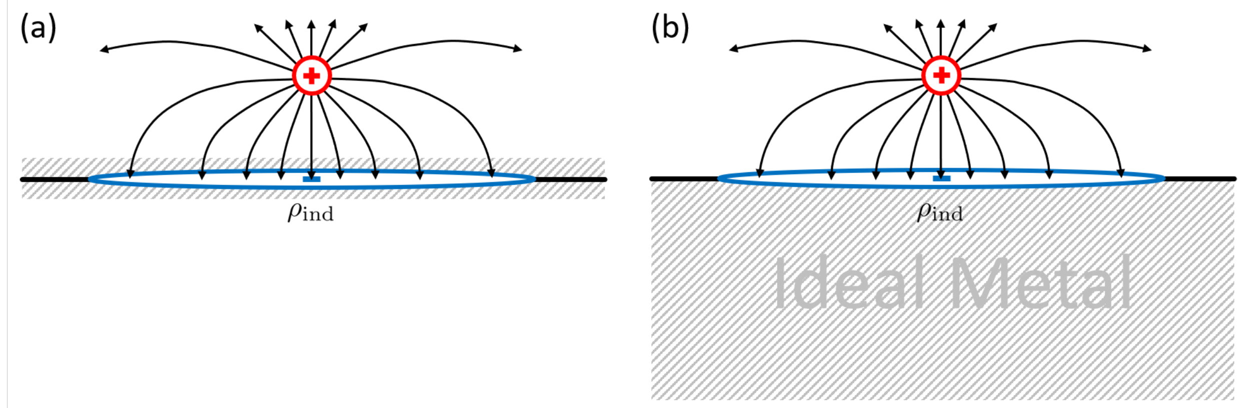

Figure 5.3: Perfect screening by a surface-charge-inducing quasi-2D ideal-metal model (IMM) (a) is equivalent to screening by a semi-infinite metal (b) according to the Uniqueness Theorem.

picture, this motion is constrained by particle conservation and the rate of change of its momentum. The induced particle density, $\rho_{\mathbf{k}}^{\text{ind}} = \rho_{\mathbf{k}}^{\text{ind}}(\mathbf{r}, t)$, changes with time according to the semiclassical Boltzmann transport equation [22],

$$\frac{d\rho_{\mathbf{k}}^{\text{ind}}}{dt} = \left(\frac{\partial \rho_{\mathbf{k}}^{\text{ind}}}{\partial t}\right)_{\text{collision}}, \tag{5.19}$$

where on the LHS, its total derivative describes the dynamics of a single particle,

$$\frac{d\rho_{\mathbf{k}}^{\text{ind}}}{dt} = \frac{\partial \rho_{\mathbf{k}}^{\text{ind}}}{\partial t} + \frac{\partial \mathbf{k}}{\partial t} \cdot \boldsymbol{\nabla}_{\mathbf{k}} \rho_{\mathbf{k}}^{\text{ind}} + \frac{\partial \mathbf{r}}{\partial t} \cdot \boldsymbol{\nabla}_{\mathbf{r}} \rho_{\mathbf{k}}^{\text{ind}}, \tag{5.20}$$

with the effects of the total (single-particle) potential $\phi_{\text{tot}}(\mathbf{r}, t)$ showing up through the force it exerts on the particle,

$$\frac{\partial \mathbf{k}}{\partial t} = -\boldsymbol{\nabla}_{\mathbf{r}} \phi_{\text{tot}}(\mathbf{r}, t). \tag{5.21}$$

Collisions scatter electrons between different **k**-states and the change in number of electrons in a given **k**-state is described by the collision term on the RHS of Eq. (5.19). Without interparticle collisions, the number of electrons in a given **k**-state is conserved and collision term on the RHS of Eq. (5.19) will be zero. Using the Relaxation Time Approximation, the collision term in the Boltzmann equation is replaced using an infinitesimal imaginary shift of ω (i.e., $\omega \to \omega + i\eta$), where η is a real finite positive number.

Finally, substituting Eqs. (5.20) and (5.21) into Eq. (5.19) and performing a Fourier transform from the $(\mathbf{r}$,$t)$-space to $(\mathbf{q}$,$\omega)$-space, we get,

$$-i(\omega + i\eta)\rho_{\mathbf{k}}^{\text{ind}} - i\phi_{\text{tot}}(\mathbf{q}, \omega)\mathbf{q} \cdot \boldsymbol{\nabla}_{\mathbf{k}} \rho_{\mathbf{k}}^{\text{ind}} + i\rho_{\mathbf{k}}^{\text{ind}} \mathbf{v}_{\mathbf{k}} \cdot \mathbf{q} = 0, \tag{5.22}$$

where now, $\rho^{\text{ind}}_{\mathbf{k}} = \rho^{\text{ind}}_{\mathbf{k}}(\mathbf{q},\omega)$, and $\mathbf{q}$ is the momentum wavevector that spans the whole reciprocal space. Using Eq. (5.22), the total induced particle density $\rho^{\text{ind}}(\mathbf{q},\omega)$ can be expressed as the linear response to the total potential $\phi_{\text{tot}}(\mathbf{q},\omega)$,

$$\begin{aligned}\rho^{\text{ind}}(\mathbf{q},\omega) &= \frac{2}{\mathcal{V}}\sum_{\mathbf{k}} \rho^{\text{ind}}_{\mathbf{k}}(\mathbf{q},\omega) \\ &= \frac{2}{\mathcal{V}}\sum_{\mathbf{k}} \frac{\mathbf{q}\cdot\boldsymbol{\nabla}_{\mathbf{k}}\rho^{\text{ind}}_{\mathbf{k}}}{-\omega - i\eta + \mathbf{v}_{\mathbf{k}}\cdot\mathbf{q}}\phi_{\text{tot}}(\mathbf{q},\omega) \\ &= \frac{2}{\mathcal{V}}\sum_{\mathbf{k}} \frac{\mathbf{v}_{\mathbf{k}}\cdot\mathbf{q}\big(-\frac{\partial\rho_{\mathbf{k}}}{\partial E_{\mathbf{k}}}\big)}{-\mathbf{v}_{\mathbf{k}}\cdot\mathbf{q}+\omega+i\eta}\phi_{\text{tot}}(\mathbf{q},\omega) \\ &= \frac{2}{\mathcal{V}}\sum_{\mathbf{k}} \frac{(E_{\mathbf{k}+\mathbf{q}}-E_{\mathbf{k}})\big(-\frac{\partial\rho_F}{\partial E_{\mathbf{k}}}\big)}{-E_{\mathbf{k}+\mathbf{q}}+E_{\mathbf{k}}+\omega+i\eta}\phi_{\text{tot}}(\mathbf{q},\omega) \\ &= \underbrace{\frac{2}{\mathcal{V}}\sum_{\mathbf{k}} \frac{\rho_F(E_{\mathbf{k}})-\rho_F(E_{\mathbf{k}+\mathbf{q}})}{-E_{\mathbf{k}+\mathbf{q}}+E_{\mathbf{k}}+\omega+i\eta}}_{\chi^0_{\text{L}}(\mathbf{q},\omega)}\phi_{\text{tot}}(\mathbf{q},\omega),\end{aligned} \tag{5.23}$$

where $\chi^0_{\text{L}}(\mathbf{q},\omega)$ is the response function. The factor of 2 comes from spin degeneracy. In the fourth line, we consider the low-energy linear response limit, in which $\rho_{\mathbf{k}}$ is replaced by the equilibrium Fermi-Dirac distribution $\rho^0_{\mathbf{k}}(E) = \rho_F(E)$, and that $\mathbf{v}_{\mathbf{k}} = \frac{dE_{\mathbf{k}}}{d\mathbf{k}}$ and $\frac{\partial\rho_F}{\partial E_{\mathbf{k}}}$ are both constants to first order.

Interestingly, starting from a semiclassical origin, we arrive at the Lindhard response function $\chi^0_{\text{L}}(\mathbf{q},\omega)$ in the limit $\eta \to 0^+$, which has the exact same form as Eq. (5.23). For the Lindhard function, time-dependence is governed by the (time-dependent) Schrödinger Equation, $\phi_{\text{ext}}(\mathbf{r}',t')$ is a small perturbation and $\rho^{\text{ind}}(\mathbf{q},\omega)$ is the change in the expectation value of the particle density operator to linear order.

The Lindhard function can be decomposed into a static part $\chi^0_{\text{L,static}}$ and the frequency-dependent part $f^0_{\text{L}}(\mathbf{q},\omega)$ through the following defining equation,

$$\chi^0_{\text{L}}(\mathbf{q},\omega) \equiv \chi^0_{\text{L,static}} f^0_{\text{L}}(\mathbf{q},\omega). \tag{5.24}$$

On the RHS, the first factor $\chi^0_{\text{L,static}} = \lim_{q\to 0}\chi^0_{\text{L}}(q,0) = -D(E_F)$ is the static limit of the Lindhard function, and is equal to the negative of the density of states $D(E)$ at the Fermi Level E_F. It is a measure of the number of excited states available to the system at vanishing excitation energy and may be identified as having similar meaning as Eq. (5.17). Eq. (5.17), however, depends on $\mathbf{q}$ and $\mathbf{G}$. The second factor $f^0_{\text{L}}(\mathbf{q},\omega)$ contains the (time- or frequency-dependence) of the charge response.

Motivated by the similarity between our equation (Eq. (5.17)) and the 2D Lindhard function (Eq. (5.24)) and that Eq. (5.17) is diagonal in $(\mathbf{G}_\parallel, \mathbf{G'}_\parallel)$, we extend our static response function (Eq. (5.17)) to finite frequencies by expressing it using the following ansatz,

$$\chi^0_{\mathbf{GG'},\text{IMM}}(\mathbf{q},\omega) \equiv \chi^0_{\mathbf{GG'},\text{static}}(\mathbf{q}) f^0_{\text{L}}(\mathbf{q}+\mathbf{G}_\parallel,\omega)\delta_{\mathbf{G}_\parallel,\mathbf{G'}_\parallel}, \tag{5.25}$$

where we make the drastic but physically-motivated assumption that the frequency response in the in-plane directions is independent of the $G_\perp$ and $G'_\perp$ components. Here, $\mathbf{q}$ is again restricted to the First Brillouin Zone, as in Eq. (5.4). The first term on the RHS $\chi^0_{\mathbf{GG'},\mathrm{static}}(\mathbf{q})$ is the (noninteracting) response function of a static ideal metal ($\omega = 0$), and the second term $f^0_{\mathrm{L}}(\mathbf{q}+\mathbf{G}_\parallel,\omega)$ describes its Lindhard-like frequency- and phase-space-dependences. The delta function $\delta_{\mathbf{G}_\parallel,\mathbf{G'}_\parallel}$ emphasizes the fact that $\mathbf{G}$ and $\mathbf{G'}$ components of $\chi^0_{\mathbf{GG'},\mathrm{static}}(\mathbf{q})$, $f^0_{\mathrm{L}}(\mathbf{q}+\mathbf{G}_\parallel,\omega)$ and therefore $\chi^0_{\mathbf{GG'},\mathrm{IMM}}(\mathbf{q},\omega)$ are diagonal in the in-plane directions, due to the translational invariance of this model and the homogeneous 2D electron gas in the in-plane directions.

Unlike the original Lindhard function for 2D metals (Eq. (5.24)), however, our model (Eqs. (5.25) and (5.17)) is a function of $G_\perp$ and implicitly includes the distance-dependence between the metallic substrate and the quasi-2D material. In this work, the ideal-metal substrate is positioned at a distance from the quasi-2D material that is the same as the distance the charge center of the closest p_z orbital of the doped 14-layer graphene substrate is from the quasi-2D material. The charge centers are defined using the peaks in the calculated *ab initio* noninteracting polarizability $\chi^0(z = z')$ of a doped 14-layer graphene substrate for $q \to 0$. In addition, $f^0_{\mathrm{L}}(\mathbf{q}+\mathbf{G}_\parallel,\omega)$ depends on the Fermi wavevector k_F. Since the electron density determines k_F and is different for different metals, k_F represents a fitting parameter that our model requires. We set k_F to 0.72 Å^{-1} using the calculated Fermi surface of a doped 14-layer graphene substrate and can be regarded as a highly screening metallic substrate.

Note that both the 2D Lindhard function $\chi^0_{\mathrm{L}}(\mathbf{q},\omega)$ and our dynamical response function $\chi^0_{\mathbf{GG'},\mathrm{IMM}}(\mathbf{q},\omega)$ are derived as responses of non-interacting electrons to effective (single-particle) total potentials ϕ_{tot} (Eqs. (5.21) and (5.22)). In the language of Feynman diagrammatic analysis, this is also known as the noninteracting polarizability. The static response function (Eq. (5.17)) that we have derived in Sec. 5.3 is for the response to an external potential ϕ_{ext} (Eqs. (5.3) and (5.12)), and is also known as the interacting polarizability. The noninteracting polarizability and the interacting polarizability are related by the Dyson equation,

$$\chi_{\mathbf{GG'},\mathrm{static}}(\mathbf{q}) = \frac{\chi^0_{\mathbf{GG'},\mathrm{static}}(\mathbf{q})}{1 - v_c(\mathbf{q}+\mathbf{G})\chi^0_{\mathbf{GG'},\mathrm{static}}(\mathbf{q})}, \tag{5.26}$$

where $v_c(\mathbf{q}+\mathbf{G})$ is the Coulomb potential truncated [85] in the out-of-plane direction to avoid interactions between the periodic images (Figs. 5.1 and 5.2).

5.4 Singularity in Electron-Hole Continuum of a 2D metal

The dielectric screening $\epsilon_{\mathbf{G},\mathbf{G'}}(\mathbf{q},\omega)$ of a metal changes drastically in the small-ω and small-q regime (Fig. 5.4). This is the same energy and length scales as those of a bound Wannier exciton, which has binding energies (E_b) that can be hundreds of meV or smaller and wavefunctions that span several nm in real space (corresponding to tenths of Å^{-1} in reciprocal

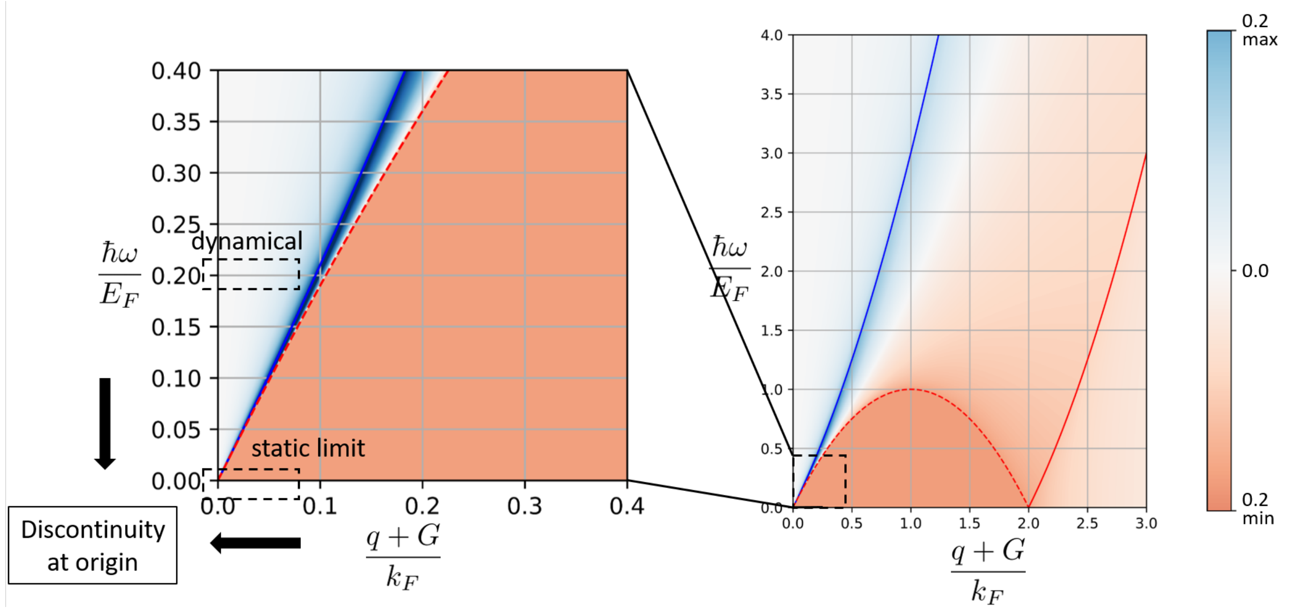

Figure 5.4: The right panel show the plot of $\mathrm{Re}[\chi^0(q+G,\omega)]$ for a 2D electron gas in color scale. The region of the $(q+G,\omega)$-plane in which $\mathrm{Im}[\chi^0(q+G,\omega)]$ differs from zero is known as the electron-hole continuum. The left panel shows the zoomed-in region for small-q and small-ω, which is the relevant length and energy scales of a Wannier exciton. Here, q is the momentum wavevector restricted to the First Brillouin Zone.

space) (Table 4.3). In this regime, the noninteracting polarizability function $\chi^0_{\mathbf{GG'}}(\mathbf{q},\omega)$ (and therefore the dielectric function $\epsilon_{\mathbf{G},\mathbf{G'}}$) is a singular function in the limit of $q \to 0$ and $\omega \to 0$ and its limit depends strongly on the direction along which the singularity is approached. In the dynamical long-wavelength limit, the origin is approached along the ω-axis at $q = 0$. Here, $\chi^0_{00}(\mathbf{q},\omega)$ always approaches 0, $1/\epsilon^{-1}_{00}(\mathbf{q},\omega)$ always approaches 1 and is insensitive to the exact value of ω. It is also the limit one should use to calculate the exciton energy level because E_b is always small but finite. In the static limit, the origin is approached along the $\mathbf{q}$-axis at $\omega = 0$ and $\lim_{q\to 0}\chi^0_{00}(\mathbf{q},0)$ approaches a constant that is equal to $-D(E_F)$ and $\lim_{q\to 0} 1/\epsilon^{-1}_{00}(\mathbf{q},0)$ diverges like $1/q$ for a 2D metal. This means that for a properly-converged calculation, static screening always dramatically overscreens at small q and that E_b calculated using static screening will be severely underestimated. In Table 4.3, we see that static screening overscreens by so much that the 1s exciton becomes its only bound state.

The above discussion can also be seen graphically from Fig. 5.5, where the BSE of WSe_2 on ideal metal is solved at different screening frequencies ω. The increase in the calculated binding energies E_b for the 1s, 2p and 2s excitons from a static calculation to a finite-frequency calculation at 0.05 eV is almost 0.2 eV. However, for screenings at finite frequencies ranging 0.05 to 0.40 eV, the binding energies vary by a maximum of only 0.01 eV and is

comparatively insensitive to the exact value of ω.

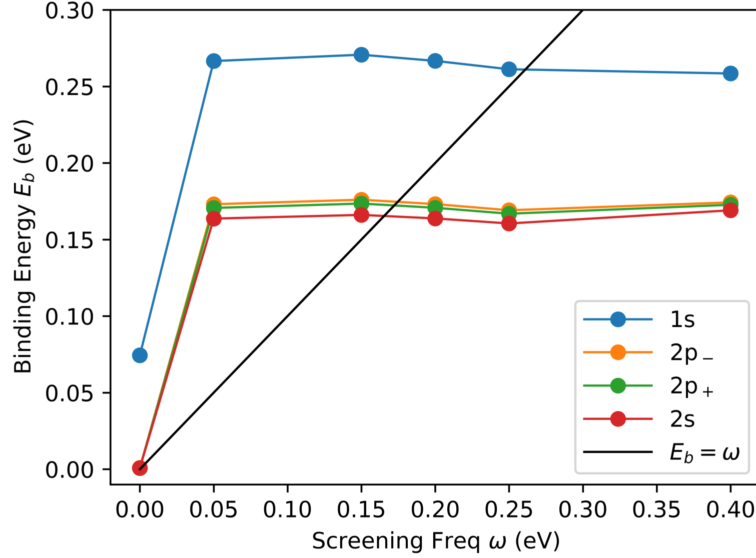

Figure 5.5: Calculated binding energies E_b at different screening frequencies ω.

5.5 QP Bandgap Renormalization due to Substrate and Encapsulation

In this section, for notational simplicity, we will assume that the interacting polarizability χ is translationally-invariant in time and space, i.e. $\chi(\mathbf{r}t, \mathbf{r}'t') = \chi(\mathbf{r} - \mathbf{r}'; t - t')$, such that it can be written as a product in the momentum and frequency space. With this simplification, the total potential $\phi_{\text{tot}}(\mathbf{q}, \omega)$ and the inverse dielectric function $\epsilon^{-1}(\mathbf{q}, \omega)$ can be written in terms of the interacting polarizability $\chi(\mathbf{q}, \omega)$ as,

$$
\begin{aligned}
\phi_{\text{tot}}(\mathbf{q}, \omega) &= \phi_{\text{ext}}(\mathbf{q}, \omega) + \phi_{\text{ind}}(\mathbf{q}, \omega) \\
&= \phi_{\text{ext}}(\mathbf{q}, \omega) + v_c(\mathbf{q})\chi(\mathbf{q}, \omega)\phi_{\text{ext}}(\mathbf{q}, \omega) \\
&= [1 + v_c(\mathbf{q})\chi(\mathbf{q}, \omega)]\phi_{\text{ext}}(\mathbf{q}, \omega), \\
\epsilon^{-1}(\mathbf{q}, \omega) &= \frac{\delta\phi_{\text{tot}}(\mathbf{q}, \omega)}{\delta\phi_{\text{ext}}(\mathbf{q}, \omega)} \\
&= 1 + v_c(\mathbf{q})\chi(\mathbf{q}, \omega).
\end{aligned}
$$

Defining $\Delta W(\mathbf{q},\omega)$ as the change in screening within the quasi-2D material due to the addition of a substrate, we get

$$\begin{aligned}\Delta W(\mathbf{q},\omega) &= \Delta\epsilon^{-1}(\mathbf{q},\omega)v_c \\ &= [v_c(\mathbf{q})\Delta\chi(\mathbf{q},\omega)]v_c(\mathbf{q}).\end{aligned} \tag{5.27}$$

The change in screening $\Delta W(\mathbf{q},\omega)$ is related to the QP bandgap renormalization of the quasi-2D material, $\Delta\Sigma = iG\Delta W$. From Eq. (5.1), we know that with the addition of a substrate, the induced potential within the quasi-2D material $\phi_{\text{ind}}(\mathbf{q},\omega)$ in response to the same external potential $\phi_{\text{ext}}(\mathbf{q},\omega)$ is modified by,

$$\Delta\phi_{\text{ind,sub}}(\mathbf{q},\omega) = v_c(\mathbf{q})\Delta\chi(\mathbf{q},\omega)\phi_{\text{ext}}(\mathbf{q},\omega), \tag{5.28}$$

Comparing Eqs. (5.27) and (5.28), we see that $\Delta\phi_{\text{ind,sub}}$ is proportional to the QP bandgap renormalization $\Delta\Sigma$ brought about by the substrate.

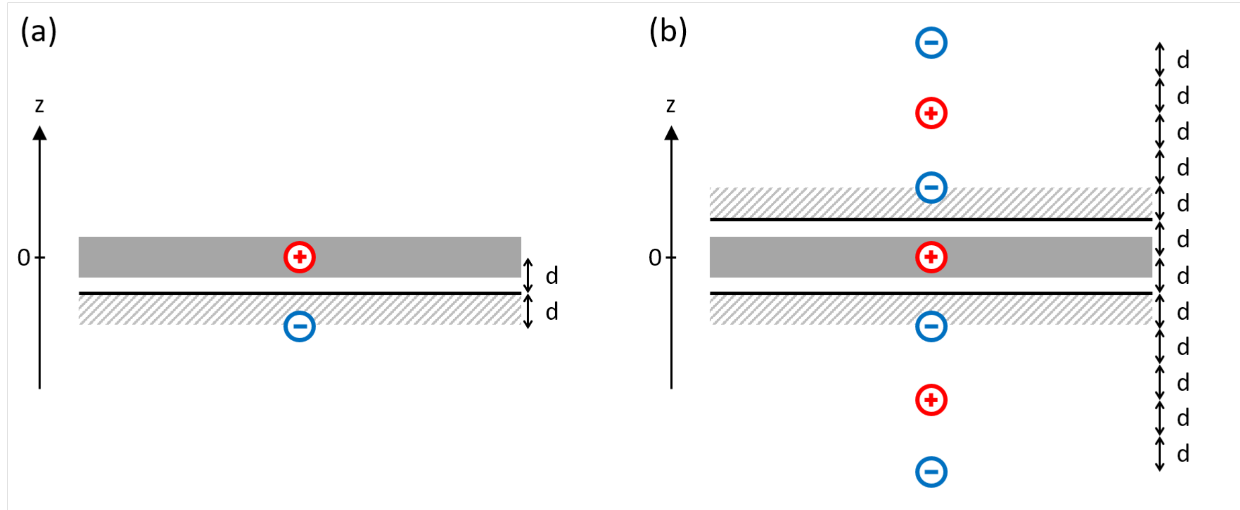

Figure 5.6: Image charges due to substrate (a) and encapsulation (b)

In this discussion of estimating band gap renormalization, we revert to the image charge model because we are only interested in the change in potential induced within the quasi-2D material in response to its own charged particles $\Delta\phi_{\text{ind,sub}}$. When a substrate is added below a free-standing quasi-2D material, a charged particle ρ_{ext} in the quasi-2D material at $z = 0$ (Fig. 5.6a) induces an image charged particle ρ_{ind} in the substrate at $z = -2d$. Through the Coulomb interaction, this corresponds to inducing a potential of $\Delta\phi_{\text{ind}}$ within the quasi-2D material at $z = 0$,

$$\Delta\phi_{\text{ind,sub}} = -\frac{1}{2d}.$$

Now, if the quasi-2D material is not only screened by a substrate but also an encapsulating capping layer, the charged particle ρ_{ext} in the quasi-2D material at $z = 0$ does not just induce image charged particles ρ_{ind} in the substrate at $z = -2d$ and the capping layer at $z = +2d$ because they alone do not preserve the original boundary conditions. Instead, an infinite series of image charges is needed. Through the Coulomb interaction, this corresponds to inducing a potential of $\Delta\phi_{\text{ind,enc}}$ in the quasi-2D material at $z = 0$ (Fig. 5.6b),

$$\begin{aligned}\Delta\phi_{\text{ind,enc}} &= -\frac{1}{d} + \frac{1}{2d} - \frac{1}{3d} + \frac{1}{4d} - \dots \\ &= -2\ln(2) \times \frac{1}{2d} \\ &= 1.4 \times \Delta\phi_{\text{ind,sub}}.\end{aligned}$$

In other words, every image charge generates a new one, continuing indefinitely and leading to an infinite number of images.

5.6 Wavefunction Hybridization between the Substrate and Quasi-2D Material

In this section, we use monolayer MoS_2 as the prototypical quasi-2D material. The left column of Fig. (5.7) shows the DFT bandstructures of monolayer MoS_2 in a supercell without substrates. The right column of Fig. (5.7) shows the bandstructures of supercells of monolayer MoS_2 with three separate commensurate substrates, namely, monolayer undoped graphene, bilayer hBN and three layers of (001)-terminated gold, which are projected onto the atomic orbitals of monolayer MoS_2. We see that when monolayer MoS_2 is on graphene, wavefunction hybridization is minimal and the original wavefunction of monolayer MoS_2 is preserved. For monolayer MoS_2 on hBN, even though there is some wavefunction hybridization between monolayer MoS_2 and hBN, the main features of the MoS_2 bandstructure is preserved. When monolayer MoS_2 is grown on Au, wavefunction hybridization is larger. Except for the preservation of the conduction band minimum and valence band maximum at the K-valley, much of monolayer MoS_2's wavefunctions has changed, hybridizing with Au to some extent. In these three calculation, the supercell geometry containing both the quasi-2D material and the substrate is determined by minimizing the strain to no more than 4%.

5.7 Conventions for Fourier Series Expansion

Following the conventions used by Bruus and Flensberg [22], we consider a function $f(\mathbf{r})$ that is periodic and continuous. For simplicity, we will assume that the repeat unit is a three-dimensional orthorhombic (i.e. rectangular) box of side lengths L_x, L_y and L_z and a volume of $\mathcal{V} = L_x L_y L_z$. Each repeat unit has N_x, N_y and N_z identical lattices in the $\mathbf{e}_x$, $\mathbf{e}_y$ and $\mathbf{e}_z$ directions. The lattice constants for each (direct) lattice is a_x, a_y and a_z.

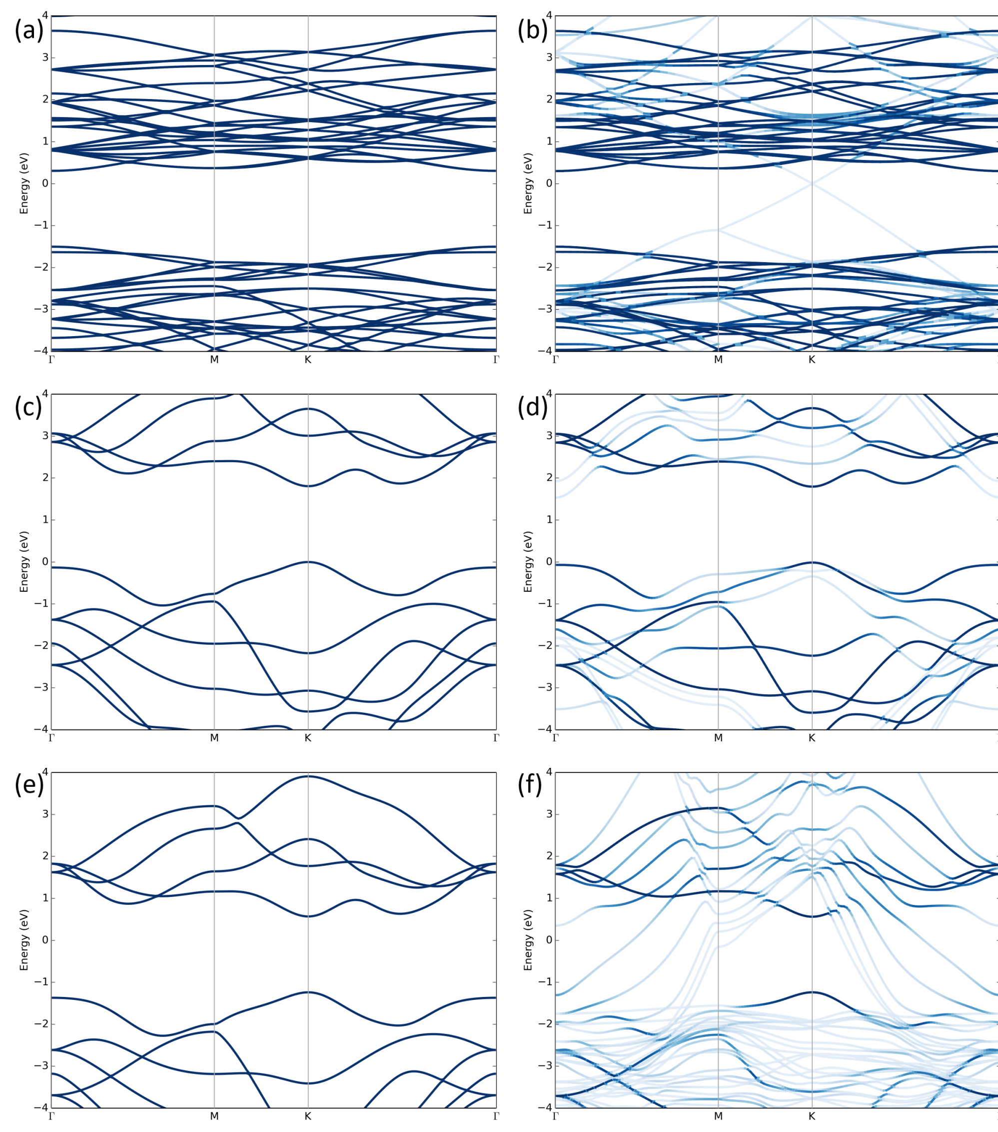

Figure 5.7: DFT bandstructures of monolayer MoS_2 (a,c,e) and MoS_2 on monolayer undoped graphene (b), bilayer hBN (d) and three layers of (001)-terminated gold (e).

For a periodic function such as $f(\mathbf{r})$,

$$f(\mathbf{r}) = f(\mathbf{r} + L_x\mathbf{e}_x) = f(\mathbf{r} + L_y\mathbf{e}_y) = f(\mathbf{r} + L_z\mathbf{e}_z) \tag{5.29}$$

$$= f(\mathbf{r} + a_xN_x\mathbf{e}_x) = f(\mathbf{r} + a_yN_y\mathbf{e}_y) = f(\mathbf{r} + a_zN_z\mathbf{e}_z), \tag{5.30}$$

it can be written as a Fourier series. In our convention, the prefactor of $\frac{1}{\mathcal{V}}$ is included in the

expansion, such that

$$f(\mathbf{r}) = \frac{1}{\mathcal{V}} \sum_{k} f_{\mathbf{k}} e^{i\mathbf{k}\cdot\mathbf{r}}, \tag{5.31}$$

where

$$k_x = \frac{2\pi n_x}{L_x} = \frac{2\pi}{a_x}\frac{n_x}{N_x} = b_x \frac{n_x}{N_x}, n_x = 0, 1, \cdots, N_x - 1, \tag{5.32}$$

$$k_y = \frac{2\pi n_y}{L_y} = \frac{2\pi}{a_y}\frac{n_y}{N_y} = b_y \frac{n_y}{N_y}, n_y = 0, 1, \cdots, N_y - 1, \tag{5.33}$$

$$k_z = \frac{2\pi n_z}{L_z} = \frac{2\pi}{a_z}\frac{n_z}{N_z} = b_z \frac{n_z}{N_z}, n_z = 0, 1, \cdots, N_z - 1. \tag{5.34}$$

Here, b_x, b_y and b_z are the lattice constants of the reciprocal lattice.

In this convention, the Fourier coefficient, $f_{\mathbf{k}}$, is given by

$$f_{\mathbf{k}} = \int_{\mathcal{V}} \mathrm{d}\mathbf{r} f(\mathbf{r}) e^{-i\mathbf{k}\cdot\mathbf{r}}, \tag{5.35}$$

and does not contain the prefactor of $\frac{1}{\mathcal{V}}$. Eqs. (5.31) and (5.35) define the conventions we are using for our Fourier series expansion. Note that prefactor of $\frac{1}{\mathcal{V}}$ is found in the former but not the latter.

This discussion can be generalized from an orthorhombic lattice to any Bravais lattice, which is a three-dimensional parallelpiped defined by three noncoplanar lattice vectors ($\mathbf{a_1}$, $\mathbf{a_2}$ and $\mathbf{a_3}$) In the more general case, $\mathbf{a_x}$, $\mathbf{a_y}$ and $\mathbf{a_z}$ generalizes to $\mathbf{a_1}$, $\mathbf{a_2}$ and $\mathbf{a_3}$, which are the primitive vectors of the crystal lattice, while $\mathbf{b_x}$, $\mathbf{b_y}$ and $\mathbf{b_z}$ generalizes to $\mathbf{b_1}$, $\mathbf{b_2}$ and $\mathbf{b_3}$, which are the primitive vectors of the reciprocal lattice, such that

$$\mathbf{b_i} \cdot \mathbf{a_j} = 2\pi\delta_{ij}. \tag{5.36}$$

Note also that in the limit where $\mathcal{V} \to \infty$, the summation over $\mathbf{k}$ will be replaced by integral over $\mathbf{k}$, i.e.

$$\sum_{\mathbf{k}} \to \frac{\mathcal{V}}{(2\pi)^3} \int \mathrm{d}\mathbf{k}. \tag{5.37}$$

Chapter 6

A Dielectric-Defined Lateral Heterojunction in a Monolayer Semiconductor

6.1 Introduction

Atomically thin semiconductors, such as monolayer transition metal dichalcogenides (TMDs) [217, 23, 226], provide a platform for investigating nanoscale quantum phenomena [172, 130, 42] and have a range of potential applications in nanoelectronics [55, 90, 35]. A freestanding monolayer of a transition metal dichalcogenide experiences a reduced dielectric screening and an enhanced Coulomb interaction by virtue of its atomically thin structure. In contrast to bulk materials, electric field lines between charges inside a monolayer can extend substantially outside of the layer [168, 33, 169]. This leads to an ineffective intrinsic screening that enhances electronic interaction and leads to large exciton binding energies between 0.2 to 0.7 eV in these materials [168, 33, 169, 211, 238, 246, 253, 79, 248]. Furthermore, the electronic band structure of atomically thin 2D layers is not completely intrinsic to the material and can be strongly affected by the surrounding environment [211, 103, 199, 180, 173, 36]. With both electron and hole experiencing the screening, the conduction and valence band edges shift in the opposite direction [169, 211, 180, 36]. *Ab initio* calculations predict that there is a monotonic decrease of electronic bandgap energy with increasing dielectric screening, where the reduction of bandgap can reach the order of hundreds of meV relative to the bandgap of a freestanding monolayer [211, 199, 173, 20, 6, 106, 156]. Recent scanning tunnelling spectroscopy and optical spectroscopy [199, 173] studies provided evidence that the bandgap renormalization phenomenon in atomically thin 2D semiconductors can indeed be significant. Such bandgap renormalization may have a profound effect on electrical transport in atomically thin 2D semiconductors; yet, the effect has not been investigated thoroughly and its implications in the development of applications based on 2D materials remains unclear.

In this chapter, we design lateral heterojunctions within a homogeneous MoS_2 monolayer exploiting the dielectric-dependent bandgap renormalization and explore its influence on electrical transport. We prepared a continuous monolayer MoS_2 which has a segment on a high-ϵ substrate and an adjacent segment on a low-ϵ substrate (Fig. 6.1a). Due to the different degree of renormalization of the electronic bandgap introduced by the two substrates on each segment, the monolayer MoS_2 forms an in-plane type-I heterojunction above the boundary of the two substrates (Fig. 6.1b,c). We used this sample configuration to perform Kelvin Probe Force Microscopy (KPFM) and electrical transport measurements across the heterojunction. KPFM [151, 141] examines the local variation of surface potential across the device channel [207] and provides a direct determination of the band offset of the MoS_2 heterojunction from the dielectric engineering. Electrical measurements show that the presence of the heterostructure has a significant effect on electrical transport through the device, leading to a strong asymmetric rectification behavior. The experimentally observed transport phenomena can also be qualitatively reproduced in a numerical simulation of the device, which exhibits several unique aspects arising from the atomically thin layers. Such dielectric-defined heterostructure behavior can be important for understanding electrical transport behavior in atomically thin 2D layers and provide a new approach for engineering 2D nanoelectronic devices [172, 57].

Theoretical calculations [180, 36, 113, 167] show that the change in the bandgap of the 2D layer due to dielectric screening effect by the substrate(s) is most dramatic when the 2D layer has a low intrinsic dielectric constant (ϵ). In addition, a high contrast from the dielectric screening environment involving a low-ϵ substrate and a high-ϵ substrate is desirable to introduce a significant change in the bandgap of the 2D layer at the heterojunction. We choose the fluoropolymer Cytop ($\epsilon = 2.0$ to 2.1) and hBN ($\epsilon(0) = 6.9$, $\epsilon(\infty) = 5.0$ normal to c-axis [64]) to serve as the and substrates respectively. The fluoropolymer Cytop substrate is one of the materials with the lowest dielectric constant that still allows ease of processing and device fabrication. Meanwhile, the straight edges of as-exfoliated thin hBN flake provide a boundary that is atomically sharp for a well-defined junction area. Moreover, both Cytop [118] and hBN [44] are known to be insulating layer with a low density of surface trap states.

6.2 Heterojunction device design and electrical measurement

We transferred a monolayer of MoS_2 atop the boundary of an hBN flake on a Cytop film and then fabricated electrical contacts onto the monolayer to form a device channel that is perpendicular to the Cytop/hBN substrate boundary (Fig. 6.2a). The electrical measurements are then performed in 4-terminal configuration to minimize the influence of contacts. Fig. 6.2b shows the I-V measurement of the device for different back gatesource voltages (which we shall refer to as "gate voltage" for brevity) $V_{gs} > 0$ V, which correspond to electron doping. With the MoS_2 segment on Cytop grounded, the device exhibited a rectifi-

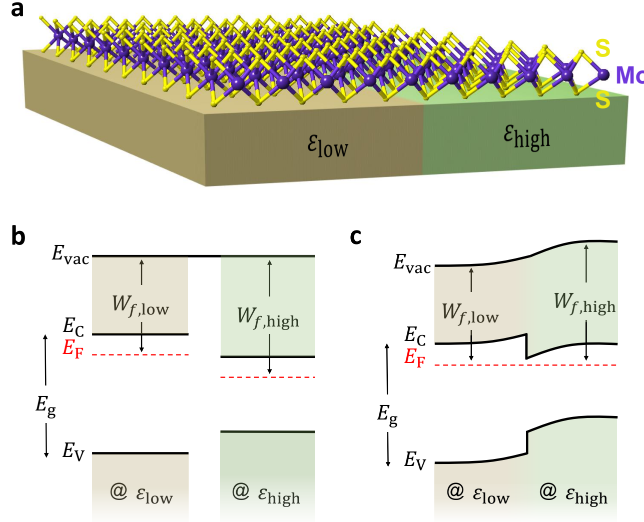

Figure 6.1: Engineering 2D heterojunctions through dielectric-dependent bandgap renormalization. a, Schematic illustration of the heterostructure. Two substrates with different dielectric constant ($\epsilon_{\text{low}} < \epsilon_{\text{high}}$) are used to locally vary the MoS_2 electronic bandgap. b, The expected band alignment of isolated monolayer MoS_2 situated on the low-ϵ substrate (Cytop) and on the high-ϵ substrate (hBN), respectively. The segments of MoS_2 monolayers on Cytop and on hBN are assumed to have the same electron doping density from the electrostatic gating. c, The band alignment from b if the MoS_2 segments on the two substrates are in contact and reach equilibrium following Anderson's rule. A type-I lateral heterojunction forms with an energy barrier for electron transport in the conduction band.

cation behavior that is reminiscent of a diode. This rectification behavior is consistent with the expected type-I heterojunction formation drawn in Fig. 6.1c, where the MoS_2 segments above the ϵ_{low} and ϵ_{high} substrates have different electronic bandgap due to dielectric screening. This behavior is similar to an n-n heterojunction with MoS_2 segment on Cytop (hBN) containing the depletion (accumulation) regime [203].

In comparison, the reference MoS_2 monolayer device on a uniform Cytop film exhibits linear Ohmic-like behavior (Fig. 6.2c), suggesting that the rectification arises from the presence of the heterojunction at the boundary between high-ϵ and low-ϵ substrates. Furthermore, we also conducted control experiments with MoS_2 monolayer on a step edge of an hBN flake that otherwise supports a uniform dielectric environment. Such control device shows symmetric output curves, which also substantiates that the rectification cannot be attributed only to the presence of step edge (e.g., strain-induced or otherwise) without introducing dielectric contrast.

A prominent feature of our MoS_2 heterojunction device behavior is that the I-V curve at forward bias that is higher than $V_{\text{ch}} \approx 0.1$ V is mostly linear. This behavior is commonly

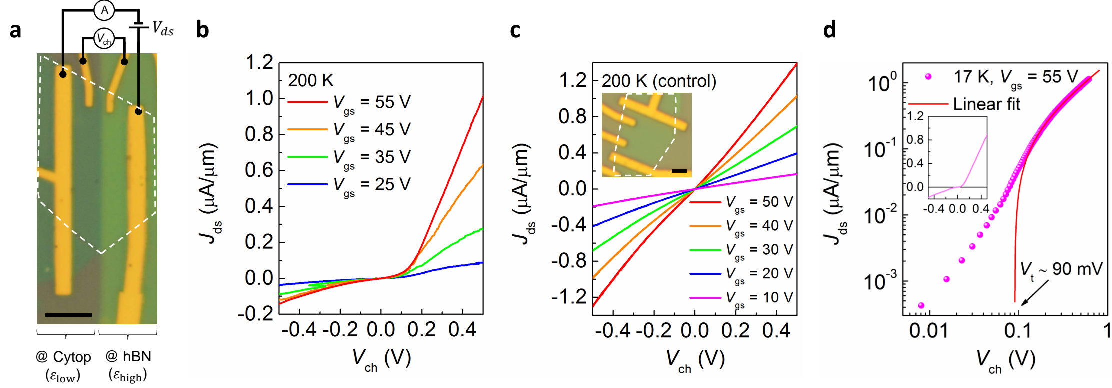

Figure 6.2: Current-voltage characteristics of a MoS_2 heterojunction device. a, Optical micrograph of a MoS_2 monolayer that is partially situated on Cytop and on hBN substrates. The white dashed line denotes the location of the monolayer that acts as the device channel. The MoS_2 segment on hBN received the high bias potential (drain). Scale bar: 2 μm. b, The output characteristics of the device with various back gating at a temperature of 200 K. c, The output characteristics of a reference MoS_2 monolayer device on a uniform Cytop substrate measured at 200 K. Inset: The micrograph of the reference device. Scale bar: 2 μm. d, The output characteristics of the heterojunction device at 17 K on a log-log scale. The forward bias current is fitted with a straight line that extrapolates to a turn-on voltage of 90 mV. Inset: the same data on a linear scale.

found in a real diode, which can be described by a piecewise linear model with a "turn-on" voltage (V_t) before the device appears to be Ohmic-like [186]. The turn-on voltage is often correlated to the potential landscape of the diode (e.g., built-in voltage in Si p-n diode), and it provides an estimate of conduction band offset across the heterojunction. Our low-temperature transport measurements yield a turn-on voltage $V_t \sim 90$ mV in the device (17 K, Fig. 6.2d).

6.3 KPFM characterization

Fig. 6.3a illustrates the KPFM measurement configuration, where lift mode with a constant tip height (h = 30 nm) is used and the DC component of bias voltage (V_{bias}) is applied to the sample. Fig. 6.3b displays the topography scan of atomic force microscope (AFM) from the MoS_2 heterojunction area at the Cytop/hBN substrate boundary. The averaged height profile (Fig. 6.3c) shows that the thickness of the hBN is around 10 nm. The exposed top surface in our devices allows for direct KPFM characterization.

As KPFM typically requires the sample to be sufficiently conducting, we performed KPFM on the MoS_2 when it is electrostatically gated to its on-state (electron accumulation)

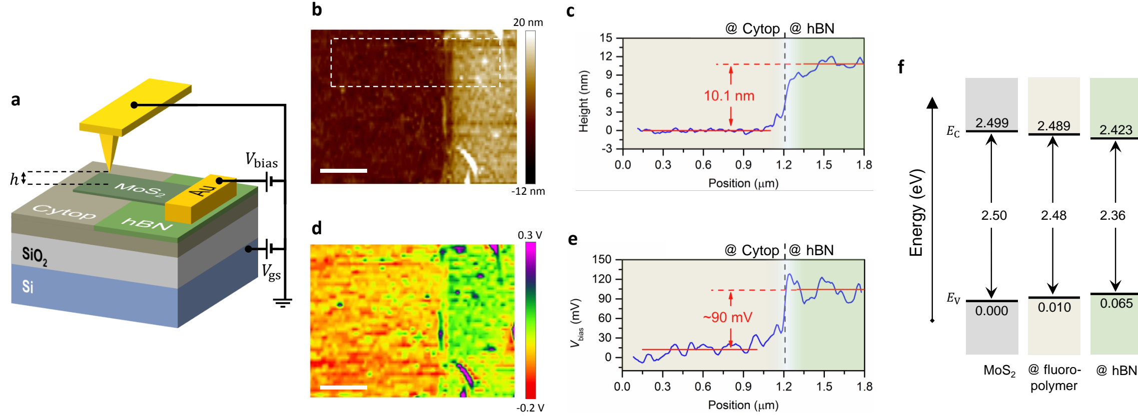

Figure 6.3: KPFM characterization of the MoS_2 heterojunction formation from differences in the degree of local dielectric screening. a, Schematic of the KPFM set-up with V_{bias} applied to the sample. For the measurements herein, the device is back gated to $V_{\text{gs}} = 50$ V and the lift height of the tip is set to h = 30 nm. b, The topography image recorded in tapping mode AFM. c, The height profile, averaged from the area inside the white dashed rectangle in b. d, The spatially mapped V_{bias} from the same area as in b. e, The V_{bias} profile from d, also averaged similarly from the same area as in c. Given that $\Delta E_{\text{c}} = -e\Delta V_{\text{bias}}$ in the measurement configuration, the KPFM result demonstrates that the conduction band edge of MoS_2 on the Cytop substrate is higher by 90 meV than that of MoS_2 on hBN. f, Results from GW calculations of the bandgap and band alignment of monolayer MoS_2 that is freestanding without a substrate screening effect (left), placed on a surface of a fluoropolymer (middle), and placed on a hBN substrate (right). Scale bars in b and d correspond to 500 nm.

at high gate voltage. Figure 6.3d shows the map of V_{bias} that was applied to the sample to cancel the electrostatic force between the tip and the sample, which is imaged at $V_{\text{gs}} = 50$ V. Meanwhile, Fig. 6.3e shows the corresponding averaged V_{bias} profile. The V_{bias} magnitude is related to the work function of the sample and that of the tip by $W_{f,\text{sample}} = eV_{\text{bias}} + W_{f,\text{tip}}$. Therefore, the difference in local work function between two segments of the sample that are imaged by the same tip is given by:

$$\Delta W_{f,\text{sample}} = eV_{\text{bias}} \tag{6.1}$$

Two distinct areal regions of V_{bias} are seen in Fig. 6.3d that correlates well with the two segments of MoS_2 on Cytop and hBN from the topographic image (Fig. 6.3b). By using the averaged line profile in Fig. 6.3e, we therefore conclude that the work function difference ($\Delta W_f = \Delta W_{f,\text{low}} - \Delta W_{f.\text{high}}$) of MoS_2 on the Cytop and hBN substrate is -90 ± 20 meV at $V_{\text{gs}} = 50$ V. Here, the negative sign means that the vacuum level of MoS_2 on Cytop is lower than that on hBN.

The conduction band offset can be obtained from the work function difference by

$$\Delta E_{\mathrm{c}} = -\Delta W_f - kT \ln \left[\frac{\exp(\frac{\pi\hbar^2 n_{\mathrm{low}}}{m^* kT}) - 1}{\exp(\frac{\pi\hbar^2 n_{\mathrm{high}}}{m^* kT}) - 1} \right] \tag{6.2}$$

with the carrier density $n = C_{\mathrm{g}}(V_{\mathrm{gs}} - V_{\mathrm{th}})/e$, where V_{th} is the gate threshold voltage, and m^* is the effective mass of electrons. Because the serial gate capacitance (C_{g}) at ϵ_{high} and ϵ_{low} side of the device does not differ significantly (the geometric capacitance of the 285 nm SiO_2 substrate dominates the serial capacitance), the ratio $n_{\mathrm{low}}/n_{\mathrm{high}}$ becomes closer to unity at high gate voltage. Applying these considerations to equation Eq. 6.2 in combination with Eq. 6.1 suggests that performing the measurement at the high gate voltage provides two major benefits: first, it counters the doping contribution from the environment to allow the relative carrier density on both sides of the junction to be more balanced since the charge density is dominated by that induced by the gate. Secondly, as the consequence of $n_{\mathrm{low}}/n_{\mathrm{high}} \approx 1$, KPFM measurements at high gate voltage allow direct interpretation of the conduction band offset from the V_{bias} contrast. Figure 6.3e therefore implies that $\Delta E_{\mathrm{c}} \approx -e\Delta V_{\mathrm{bias}} \sim 90$ meV for our experimental condition, i.e., E_{c} for MoS_2 on Cytop is positioned higher than that on hBN.

The heterojunction measured by KPFM is consistent with the electrical transport data. It suggests that dielectric engineered bandgap difference is around $\Delta E_{\mathrm{g}} \approx 2\Delta E_{\mathrm{c}} = -180 \pm 40$ meV (illustrated in Fig. 6.1c), assuming electron-hole symmetry. We compare this experimental result with the theoretical calculation of the electronic bandgap of MoS_2 within the *ab initio* GW_0 approach as implemented in the BerkeleyGW package [83, 178, 46] and account for the dielectric screening effect from the substrates using the in-plane substrate averaging approach (details regarding the GW_0 calculation is in Sec. 6.7) [211, 167]. The GW_0 calculation shows that the bandgap of MoS_2 on a similar dielectric fluoropolymer as Cytop, after accounting of surface roughness (Fig. 6.5), is larger than that of MoS_2 on hBN by 120±40 meV, of which the CBM offset is $\sim 70 \pm 20$ meV (Fig. 6.3f). Our calculations reveal that the roughness of the Cytop surface decreases the effective dielectric screening experienced by MoS_2; the same calculation performed on a perfectly smooth Cytop-like substrate results in a CBM offset of ~ 40 meV. The calculated bandgap and CBM offset agree well with the experimental results, with overlapping error bars. The CBM and VBM offsets are also approximately symmetric.

6.4 Energy band modelling

We model the electrical potential and charge transport through the junction numerically to understand the unusual electrical transport from an atomically thin 2D heterojunction. While the rectification behavior of the heterojunction is consistent with the predicted band alignment in Fig. 6.1c, the transport data cannot be aptly modelled with a thermionic emission theory commonly used to describe a Schottky diode, in which the current level

predicted from a thermionic emission mechanism is several orders of magnitude larger than that measured herein. The thermionic emission model fails in atomically thin 2D layers because these 2D materials tend to have rather low mobility, and the drift-diffusion behavior of charge carriers plays a dominant role in the transport across the heterojunction [203]. To accurately model the device behavior, we introduce a carrier density dependent electron mobility in MoS_2 by $\mu(n) = \mu_0/[1+\exp(\alpha^{-n+n_0})]$. Here, the mobility has a constant value of μ_0 at high doping but drops significantly at low doping. This functional form is reminiscent to an activated behavior with a certain density of trap states, and the relevant parameters are obtained through gate-dependent transport data from a homogeneous MoS_2 monolayer. The density-dependent mobility is especially relevant at the depletion region, which would experience increased local electrical resistance due to lowered carrier density (Fig. 6.4d).

Fig. 6.4 shows the calculated band diagram and the associated band bending of MoS_2 around the Cytop and hBN substrates for the conduction band edges at zero, forward, and reverse applied bias. The electron density n_0 at $x < 0$ (at Cytop) is assumed to be $\sim 2 \times 10^{12}$ cm^{-2}. The zero bias calculation result (Fig. 6.4a) captures the built-in potential on each side of the junction (ψ_1 and ψ_2 for MoS_2 on hBN and Cytop, respectively) because of the work function differences between the two segments of MoS_2. In the case of a biased channel, the current flow is a response of a voltage drop over the whole channel: $V_{\mathrm{ch}} = E_F(z = -L) - E_F(z = L)$ that shifts the Fermi level out of equilibrium. However, we see from both Figs. 6.4b and 6.4c that the voltage drop primarily transpires at the heterojunction, ensuring that the heterojunction property to define the I-V behavior of the device.

In the forward bias (Fig. 6.4b), the voltage drop across the heterojunction reduces the net built-in potential into $\psi_1 - V_1$ and $\psi_2 - V_2$, respectively. A net current will flow with the electrons moving from the segment on Cytop to that on hBN. At a finite temperature, electrons moving in this direction will see an energy barrier for transport across the heterojunction. However, this energy barrier becomes negligible at a sufficiently large applied bias $V_{\mathrm{ch}} > V_{\mathrm{t}}$, as illustrated in Fig. 6.4b. In other words, $\psi_2 - V_2 \approx 0$ and the transport across the junction should be mostly dominated by the sheet resistance of MoS_2 away from the junction and appears Ohmic-like. As an approximation, the $\psi_2 - V_2 \approx 0$ condition is achieved when the total built-in voltage across the junction: $\psi_i = \psi_1 + \psi_2 \approx V_{\mathrm{t}}$. We believe that this picture might explain the I-V behavior for the heterojunction as discussed in Fig. 6.2. An equivalent diode circuit for the junction is shown in the inset of Fig. 6.4b: the heterojunction is comprised of an internal built-in potential V_{t} that needs to be compensated by applying an external potential, following which the current-voltage behavior is dictated by a resistance R_S in series due to the MoS_2 segment away from the junction. Our simulated I-V plot (Fig. 6.4e) reproduces the threshold-like behavior of the device.

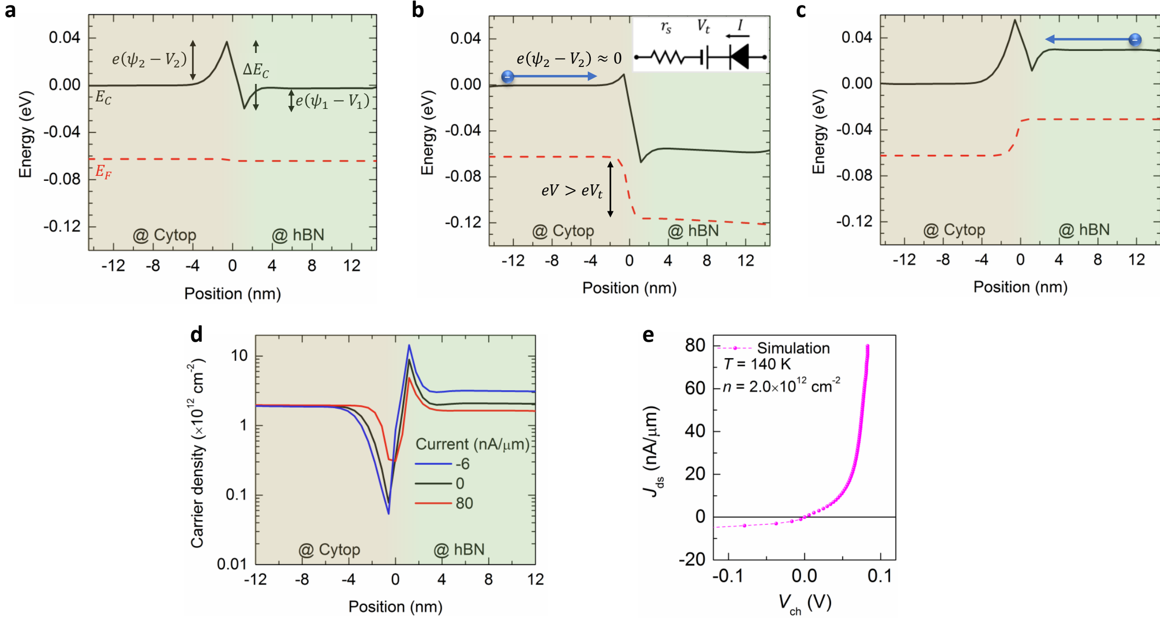

Figure 6.4: Simulation results of the energy band bending at the 2D heterojunction. a-c, The conduction band edges and Fermi levels are calculated at zero bias (a), forward bias (current: 80 nA μm^{-1}) (b) and reverse bias (current: -6 nA μm^{-1}) (c) conditions. In the three cases, the MoS_2 segment on Cytop is assigned to be electrically grounded. Under a small forward bias ($V_{\mathrm{ch}} = V_1 + V_2$), an electron traversing the heterojunction from the segment on Cytop to that on hBN experiences an energy barrier due to the built-in voltage. However, for large enough bias beyond the turn-on voltage ($V_{\mathrm{ch}} > V_{\mathrm{t}}$), electrons traversing the heterojunction (blue circle) do not experience a significant energy barrier and the current-voltage characteristic is determined by the resistance of the channel instead of the junction. Inset in b, a schematic of the diode modelling according to piecewise linear model. d, Carrier density distribution across the junction under different bias conditions. e, Simulated current-voltage characteristics with a carrier-density-dependent mobility. All calculations are performed using a carrier density of 2.0×10^{12} cm^{-2} at 140 K.

6.5 Conclusions

We have reported an operational device application of bandgap renormalization in 2D materials via dielectric screening, and shown that a dielectric-engineered lateral heterojunction can strongly modify electrical transport in monolayer MoS_2. Since heterostructures are fundamental building blocks in electronics, such dielectric engineering can provide a powerful new route for realizing more complex device architecture. Our findings also have implications for the efforts to incorporate 2D materials in optoelectronics, in order to improve functionality (for example, spin-valley current for information encoding [93]) and drive miniaturization [3,

45].

In practical applications, all aspects of manufacturing must be considered. For instance, the monolithic integration of 2D materials in circuitry requires interfacing with other components, such as substrate, electrodes, and interconnections. Each component may screen the 2D materials, resulting in different degree of bandgap renormalization across the channel. Notably, the bandgap of MX_2 should decrease significantly upon interfacing with electrodes due to the high permittivity of metals and thus a heterojunction is expected to form at each border between the MX_2 segments with and without metal contact. Although the behavior of metal-MX_2 junction is dominated by other mechanisms such as Fermi-level pinning [43, 65], recent work suggests the possibility to prevent pinning by minimizing disorders and interface states at the metal-MX_2 junction [41, 120]. At such limit, accounting for bandgap renormalization is essential to fully understand the physics of electrical contact to MX_2 monolayers.

Although we have used Cytop and hBN substrates in order to simplify fabrication, the bandgap renormalization is a general phenomenon in 2D semiconductors and the heterojunction should form with other combinations of dielectrics. The constraint for low-ϵ substrate may be satisfied by other established materials in industry, such as electronic-grade plastic substrates [128, 200] with well-developed scalability and processability. Additionally, an advantage of such polymeric surfaces is the absence of dangling bonds, leading to a low density of surface trap sites. If conventional high-ϵ dielectrics are used, an abrupt heterojunction is affordable by patterning with state-of-the-art microfabrication technology. Another scalable approach also includes using CVD-grown 2D lateral heterojunction as the substrate if the material combination has a significant dielectric contrast [111, 122]. We also believe that the influence from interface trapping and substrate doping for non-optimized surface can be minimized if the heterojunction is operated at high carrier density as defined by the electrostatic gating, where the difference in the work functions between low- and high-ϵ channel segments are primarily due to the bandgap renormalization.

6.6 Methods

Device fabrication

Cytop (CYTOP CTL-809M, Asahi Glass Co.) is mixed into CTL180 (Asahi Glass Co.) in 2:7 v/v and spincoated at 1000 rpm for 1 min to a uniform thickness of ~70 nm on highly doped Si substrates with 285 nm SiO_2. The Cytop-coated substrate is then heated at a hotplate for 5 min at 100°C and then 5 min at 150°C. Crystal of hBN is then exfoliated on the Cytop surface. The hBN flakes with thickness of 5-15 nm that have a flat side edge are identified from optical microscopy and confirmed with AFM imaging. Monolayers of MoS_2 are exfoliated onto a PDMS stamp and dry-transferred [26, 107] to the flat edge of such hBN flake. For all devices, 100 nm Au film is deposited for the electrode of MoS_2 using a standard electron beam lithography (EBL) process with two layers of EBL resist (495PMMA A4 and

950PMMA A4, MicroChem). We found that exposing the Cytop film to a short, low power N_2 plasma (10 sccm, 5 W for 1 s) before the hBN exfoliation can help to produce better spincoating of the resists on Cytop.

KPFM

KPFM were performed using a Multimode AFM with grounded tip and biased sample. A blunted Si cantilever with ∼50 nm Au film coating was used for the imaging. The measurement was performed in surface potential mode with a lift-height of 30 nm and a drive amplitude of 2 V. The high lift-height was chosen to avoid interaction between the metal tip and the monolayer MoS_2 that can introduce additional screening effect. The AFM instrument is housed inside a home-made enclosure that is flushed with a constant flow of dry nitrogen to provide an inert atmosphere.

6.7 GW_0 calculations for the CBM offsets and change in bandgap of MoS_2 due to dielectric screening from the substrates

We first carry out density-functional theory (DFT) calculations as implemented in the Quantum ESPRESSO [66] package using a plane-wave basis set, norm-conserving pseudopotentials and the local density approximation (LDA) [27, 161] for electron exchange and correlation. With the Kohn-Sham wave functions, we then calculate the quasiparticle (QP) self-energies using the eigenvalue-self-consistent, full-frequency GW_0 approximation with the BerkeleyGW [46] package. To include substrate screening when calculating the quasiparticle energies, we adopt the in-plane substrate-averaging (IPSA) [211] approximation, in which the noninteracting polarizability of the substrate is added onto the full dielectric matrix of MoS_2, while neglecting only the in-plane local ($G_x \neq G_{x'}$ or $G_y \neq G_{y'}$) fields but explicitly including all out-of-plane local fields ($G_z \neq G_{z'}$). In all our GW_0 calculations, the c-axis of all supercells is defined as the out-of-plane direction, and the length of the supercell in this confined direction is always set to be $L_z = 120$ Å, unless otherwise stated. Also, for clarity, we will adopt the following nomenclature: the CBM of free-standing MoS_2 will be labeled as $\mathrm{CBM}_{\mathrm{fsMoS_2}}$ and the CBM of MoS_2 when screened by substrate A will be labeled as $\mathrm{CBM}_{\mathrm{A}}$. The same nomenclature will also be applied to the VBM.

We first compute the quasiparticle energies of monolayer MoS_2, using a structure with an in-plane lattice constant [242] of 3.16 Å and a thickness of 3.17 Å measured from the centers of the S atoms. The kinetic energy cutoff for the DFT calculation is set at 80 Ry for the plane-wave expansion of the wave functions. For the GW_0 calculations, the dielectric matrix is calculated on an effective [94] q grid of 1143 × 1143, expanded from a regular q grid of 6×6. When calculating the dielectric matrix, a total of 26450 bands is used and the energy cutoff used to calculate the screened exchange is set at 35 Ry.

To calculate $\mathrm{CBM_{Cytop}}$, we note that the interface between Cytop and $\mathrm{MoS_2}$ is very rough since Cytop is spin coated. According to the AFM data (Fig. 6.5), the height profile of Cytop fluctuates within a range of ±2 nm. Moreover, since Cytop has a very low dielectric constant ($\epsilon = 2.0 - 2.1$), one can consider $\mathrm{CBM_{fsMoS_2}}$ as the upper bound of $\mathrm{CBM_{Cytop}}$. To determine the lower bound of $\mathrm{CBM_{Cytop}}$, we approximate the screening environment of Cytop, which has an amorphous structure, as that of polytetrafluoroethylene (PTFE), which is crystalline. Apart from the crystal order, the two compounds have a very similar bulk dielectric constant ($\epsilon \sim 2$) and chemical composition (mainly C and F atoms), though PTFE is expected to have a slightly larger dielectric constant because it is more densely packed. In our model for PTFE, we use a supercell with an orthorhombic crystal lattice ($a = 2.66$ Å, $b = 5.55$ Å). The C-C bonds of the polymer chains are oriented parallel to the in-plane directions of $\mathrm{MoS_2}$. In our calculations, we use 7 layers of PTFE (3.3-nm thick) and position them such that F atom of the topmost layer of PTFE is 2 nm away from the nearest S of $\mathrm{MoS_2}$ in the out-of-plane direction. The DFT energy cutoff is set at 100 Ry, and 4700 bands and an energy cutoff of 8 Ry are used to calculate the substrate polarizability matrix. Our GW_0 calculation shows that $\mathrm{CBM_{Cytop}}$ is at most 10 meV lower than $\mathrm{CBM_{fsMoS_2}}$, while $\mathrm{VBM_{Cytop}}$ is at most 10 meV higher relative to $\mathrm{VBM_{fsMoS_2}}$. We note that it is very important to take into account the roughness of the fluoropolymer. If we place $\mathrm{MoS_2}$ right on top of PTFE with a relaxed distance of 2.9 Å between the adjacent layers of F and S atoms, we find that $\mathrm{CBM_{PTFE}}$ is 33 meV lower than $\mathrm{CBM_{fsMoS_2}}$, while $\mathrm{VBM_{PTFE}}$ is 25 meV higher than $\mathrm{VBM_{fsMoS_2}}$.

For hBN, we will consider the upper bound of the CBM in the scenario where there is no electron doping of $\mathrm{MoS_2}$ due to the substrate. The $\mathrm{MoS_2}$-substrate distance is determined by minimizing the energy of the system in a separate DFT calculation that also incorporates van der Waals interactions (vdW-DF$^{\mathrm{C09x}}$) [39] and dipole corrections [14, 142]. Using a supercell of $L_z = 22.5$ Å that consists of 4×4 monolayer $\mathrm{MoS_2}$ unit cells stacked on top of 5×5 bilayer hBN unit cells, we relax the $\mathrm{MoS_2}$-substrate distance in the out-of-plane direction and determine the separation between the topmost BN layer and the nearest S layer of $\mathrm{MoS_2}$ to be 3.30 Å. To calculate the quasiparticle self-energies, we construct a slab consisting of 14 BN layers that is 4.3-nm thick and has an in-plane lattice constant [225] of 2.50 Å. The DFT energy cutoff is set at 60 Ry. An energy cutoff of 6 Ry and 1117 bands are used to calculate the substrate polarizability matrix. In the experiment, $\mathrm{MoS_2}$ is screened by hBN that is ∼10.1-nm thick, which is in turn situated on top of Cytop (Fig. 6.3a). Hence, we will extrapolate the substrate correction by hBN from 14 layers of substrate to a substrate of semi-infinite thickness. The extrapolation is carried out by also calculating the substrate corrections for 2-, 6- and 10-layer thick substrates and fitting the relation of substrate correction to substrate thickness with an exponential function. In the GW_0 calculation, we find that $\mathrm{CBM_{hBN}}$ is −76 meV relative to $\mathrm{CBM_{fsMoS_2}}$, and that $\mathrm{VBM_{hBN}}$ is 65 meV relative to $\mathrm{CBM_{fsMoS_2}}$.

Due to the proximity of hBN to $\mathrm{MoS_2}$, the segment of $\mathrm{MoS_2}$ above hBN is also susceptible to other contributions that close the band gap and lower the CBM, such as, (1) wave function hybridization between the orbitals of $\mathrm{MoS_2}$ and hBN and, (2) electron doping of $\mathrm{MoS_2}$ by hBN due to possible extrinsic effects like interfacial dipoles, electrostatic gating and vacancy

defects, that are not included in the IPSA approximation. From simpler model calculations, we estimate that the error from neglecting wave function hybridization is less than 10 meV. This, however, is a signed error, i.e., hybridization should decrease the $\mathrm{CBM}_{\mathrm{hBN}}$. The second contribution due to electron doping is experimentally constrained using a large back gate voltage V_{gs} and a thick SiO_2 substrate. Using Eq. 6.2, the maximum error can be determined also to be ∼10 meV, which is also a signed error that decreases $\mathrm{CBM}_{\mathrm{hBN}}$.

By taking the difference between the $\mathrm{CBM}_{\mathrm{hBN}}$ and $\mathrm{CBM}_{\mathrm{Cytop}}$, the CBM offset can be determined to be of the order of 70±20 meV; the VBM offset can be determined to be 60±20 meV by taking the difference of $\mathrm{VBM}_{\mathrm{hBN}}$ and $\mathrm{VBM}_{\mathrm{Cytop}}$. We stress that we do not include the doping effect into our calculations (which increases both the CBM and VBM offsets) but rather include them as error bars. In all, the QP band gap changes by $\sim 120 \pm 40$ meV. Finally, note that when calculating the quasiparticle energies of MoS_2 as screened by a substrate, the energy cutoff that is used to calculate the screened exchange (e.g. 6 Ry) can smaller than that used for MoS_2 (i.e. 35 Ry) because in the IPSA approximation, substrate correction to the self-energy is calculated as a perturbation. In hBN, for example, it is found that the QP gap is already converged to less than 4 meV with a cutoff of 6 Ry.

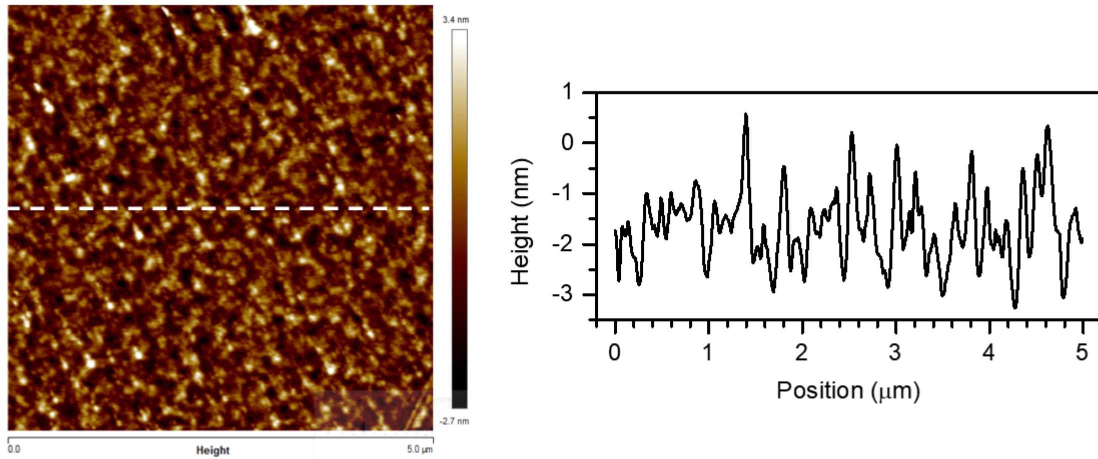

Figure 6.5: AFM height profile of a typical Cytop surface. a, AFM image. b, Height profile along the white dashed line in a

Chapter 7

Valley-dependent Exciton Fine Structure and Autler-Townes Doublets from Berry Phases in Monolayer $MoSe_2$

7.1 Introduction

In the momentum space of atomically-thin transition metal dichalcogenides (TMDs), a pair of degenerate exciton states are present at the K and K'-valleys, producing a valley degree of freedom that is analogous to the electron spin [233, 232, 25]. The electrons in the K and K'-valleys acquire a finite Berry phase when they traverse in a loop around the band extrema, with the phase equal in magnitude but opposite in sign at the K and K'-valleys, as required by the time-reversal symmetry [230, 233, 232, 25]. The Berry phase not only has close connections to the optical selection rules that allow optical generation and detection of the valley-polarized carriers by circularly polarized photons [233, 232, 25, 237, 129, 245], but also plays a central role in novel electron dynamics and transport phenomena in TMD and graphene layers, such as the valley Hall effect [249, 153, 130, 232, 231].

In principle the Berry phase, together with other effects from inversion symmetry breaking, can have profound consequences for the wavefunction and energy spectrum of the excited states in two-dimensional (2D) materials. TMD monolayers are known to host strongly bound excitons with a remarkably large exciton binding energy due to enhanced Coulomb interactions in 2D [211, 33, 238]. It was recently predicted that the Berry curvature of Bloch states can add an anomalous term to the group velocity of electrons and holes and creates an energy splitting between exciton states with opposite angular momentum [230, 32, 251, 198, 210, 15, 224], as illustrated in Fig. 7.1a. Figure 7.1b shows a simplified exciton energy spectrum illustrating the exciton fine structure based on our *ab initio* GW-Bethe-Salpeter equation (GW-BSE) calculations. The $2p_+$ and $2p_-$ exciton states are split in energy with

opposite order for the K and K' valleys due to the opposite chirality in the two valleys [251, 198, 210, 232]. Such novel exciton fine structure, which embodies important wavefunction properties arising from the Bloch band geometry, can strongly modify the intraexcitonic light-matter interactions. Experimental observation of this predicted exciton spectrum, however, has been challenging, because it requires new spectroscopic probe that can distinguish both the momentum valley and the exciton angular momentum.

Here, we report the first observation of the Berry-phase effect in the exciton energy spectrum of $MoSe_2$ monolayer using intraexciton optical Stark spectroscopy. We demonstrate that the degeneracy between the $2p_{\pm}$-exciton states is lifted by the Berry phase effect, and enabling a valley-dependent Autler-Townes doublet from strong intraexciton light-matter coupling. We coherently drive the intraexciton transitions using circularly-polarized infrared radiation, which couples the 1s exciton to the $2p_+$ or $2p_-$ states selectively through the pump photon polarization (solid arrowed lines in Fig. 7.1b). The pump-induced changes in the 1s exciton transition are detected by circularly polarized probes, which selectively measure the K or K'-valley excitons. Independent control of pump and probe photon polarization enables us to distinguish the exciton fine structures in the K and K'-valleys. We determine an energy splitting of 14 meV between the $2p_+$ and $2p_-$ exciton states within a single valley, and this energy splitting changes sign between K and K'-valleys. We determine the 1s-2p transition dipole moment to be 55$\pm$6 Debye. This leads to an optical Stark shift that is almost 40 times larger than the interband counterpart [239, 101, 192] under the same pump detuning and driving optical field strength. Such strong and valley-dependent intraexciton transitions open-up new pathways for the coherent manipulation of quantum states in 2D semiconducting materials using infrared radiation.

7.2 Results and Discussion

To investigate the fine structure of the excitonic p-manifold, we fabricated a high quality $MoSe_2$ monolayer that is encapsulated in hexagonal boron nitride (hBN) layers using mechanical exfoliation and stacking following Ref. [239]. The sandwiched hBN-$MoSe_2$-hBN heterostructure was then transferred to an alumina-coated silver surface (Fig. 7.1c). The device was kept in vacuum at 77 K for all optical measurements. Fig. 7.1d shows the reflection contrast spectrum of the $MoSe_2$ monolayer, which exhibits a prominent A-exciton absorption feature at energy $E_{1s} = 1.627$ eV with a full width half maximum (FWHM) of 9 meV. This A-exciton peak arises from the optical transition between the ground state and the lowest energy 1s exciton state in $MoSe_2$ monolayer, which is well-separated from the higher-lying exciton states due to strong Coulomb interactions in TMD monolayers [15, 224, 238, 216].

We use intraexciton optical Stark spectroscopy with helicity-defined pump and probe light to selectively access the $2p_+$ or $2p_-$ exciton states in the K and K'-valleys. As illustrated in Fig. 7.1b, we drive the 1s-$2p_+$ intraexciton transition coherently with a σ^+-polarized infrared pump and monitor the photoinduced changes in the 1s exciton absorption at K and K'-valleys with σ^+ and σ^--optical probes, respectively. Quantum-mechanical coupling between

the infrared photon field and the 1s-2p$_+$ electronic transition leads to an avoided-crossing behavior that modifies the 1s-exciton state systematically with the changing infrared photon energy, as illustrated in Fig. 7.1e. Specifically, the $|1s, n\hbar\omega\rangle$ and $|2p_+, (n-1)\hbar\omega\rangle$ states hybridize when driven by the infrared pump in the "dressed atom" picture, where n is the integer number of infrared pump photons at frequency ω. When the infrared photon energy is below (above) the 1s-2p$_+$ resonance, the non-resonant hybridization leads to a decreased (increased) energy for the 1s exciton state. When the infrared photons are resonant with the 1s-2p$_+$ transition, perfect hybridization between $|1s, n\hbar\omega\rangle$ and $|2p_+, (n-1)\hbar\omega\rangle$ states lead to an energy splitting in the 1s exciton absorption. The pump-induced optical Stark shift and splitting of 1s exciton in K and K'-valleys can be detected from the 1s exciton absorption spectrum by using σ^+ and σ^--polarized probe light, respectively. This allows us to explicitly identify the 1s-2p$_+$ intraexciton transition in each valley. Since the infrared pump photon energy is much lower than the transition energy of 1s exciton, our measurement scheme probes only the coherent optical Stark effects without non-coherent contribution from real carrier generation.

Figures 7.2a-c show the transient reflection signals for the σ^+-polarized probe, which measures the photoinduced changes of the K-valley exciton transition upon excitation with σ^+-infrared pump of different energies (E_p). The driving pump has an effective driving intensity (I_eff) of 7±1 MW/cm^2, which corresponds to a local optical field strength (E_eff) of 70±10 kV/cm. The colors in Fig. 7.2a-c represent the pump-induced change of the probe reflectivity ΔR , which is directly proportional to the change of absorption. The positive (negative) ΔR , is proportional to the decrease (increase) of absorption. The horizontal and vertical axes show the probe energy and pump-probe time delay τ, respectively. Strong transient signals are present for pump-probe delay closed to zero and they become negligible at pump probe delays larger than 500 fs. These instantaneous signals confirm the optical responses arise from coherent optical Stark effects. By changing the driving energy of the σ^+-pump, the optical response varies significantly. Figures 7.2d-e display the corresponding transient spectra of the K-valley exciton at $\tau = 0$ ps. At $E_\text{p} = 120$ meV, the absorption of K-valley exciton exhibits a decrease above E_1s and an increase below E_1s, corresponding to a red-shift of the 1s exciton resonance due to the optical Stark effect. The photoinduced responses is opposite for $E_\text{p} = 170$ meV, which is dominated by transition energy blue-shift. The spectrum at $E_\text{p} = 142$ meV, on the other hand, shows an increase of absorption at energies both above and below E_1s and a reduction of absorption at E_1s, which is consistent with an energy splitting of the 1s exciton peak.

The evolution of the 1s exciton absorption in monolayer $MoSe_2$ under coherent infrared driving can be better visualized directly from the optical absorption spectra characterized by the imaginary part of optical susceptibility (χ_im) [114]. Figure 7.3a displays the absorption spectra of the 1s exciton at $\tau = 0$ ps for both K and K'-valleys driven by σ^+-polarized infrared radiation of different photon energies. It shows clearly that the 1s exciton transition exhibits avoided-crossing behavior in both valleys, which evolves gradually from energy blueshift to splitting and then to redshift as the pump photon energy is decreased. However, there is an important distinction between the K and K' valley spectra: the resonant coupling between

the σ^+-infrared photons and the 1s-2p$_+$ intraexciton transition, which splits the 1s exciton resonance, occurs at driving photon energy of 142 meV and 128 meV in K and K'-valleys, respectively. It shows that the 1s-2p$_+$ intraexciton transition energy differs by 14 meV for the K and K' valleys. Due to the time-reversal symmetry between K and K'-valleys in $MoSe_2$ monolayer, this observation also indicates that the 2p$_+$ and 2p$_-$ exciton states are non-degenerate and has an energy difference of 14 meV in a single valley. (See Fig. 7.1b)

We further plot the blue- and red-shifted 1s resonance as a function of the infrared pump photon energy in Fig. 7.3b. We find that the energy shifts induced by the intraexciton optical Stark effect are almost 40 times larger than its interband counterpart at the same pump intensity and resonance detuning [239, 101, 192].

Since the driving photon energy is closed to the 1s-2p$_+$ transition and strongly off-resonant from the interband transition, our observation can be qualitatively understood using a model describing a driven three-state system as illustrated in Fig. 7.1b and Fig. 7.1e. Under σ^+-pump radiation, $|1s, n\hbar\omega\rangle$ hybridizes with $|2p_+, (n-1)\hbar\omega\rangle$, which can be described by the effective Hamiltonian

$$H_{\text{eff}} = \begin{pmatrix} E_{1\text{s}} + i\gamma_{1s} & \frac{V_1}{2} \\ \frac{V_1}{2} & E_{1\text{s}} + |E_{1s-2p_+}| - E_p + i\gamma_2 p_+ \end{pmatrix} \tag{7.1}$$

Here V_1 is proportional to the 1s-2p$_+$ intraexciton transition dipole moment μ_{1s-2p_+} via $V_1 = \mu_{1s-2p_+} E_{\text{eff}}$, where E_{eff} is the local optical field strength on the sample. E_{p}, $E_{1\text{s}}$ and E_{1s-2p_+} denote the pump photon energy, the 1s exciton energy and the 1s-2p$_+$ intra-exciton transition energy, respectively. γ_{1s} and γ_{2p_+} are the half width at half maximum of the 1s and 2p$_+$ exciton modes, respectively. Direct diagonalization of the effective Hamiltonian yields two new eigenstates $|\alpha\rangle$ and $|\beta\rangle$, which are energetically separated by $\sqrt{V_1^2 + (\Delta + i\gamma_{2p_+} - i\gamma_{1s})^2}$, where $\Delta \equiv E_p - |E_{1s-2p_+}|$ is the detuning energy. The optical absorption of the probe photon to the new eigenstates can then be computed.

Fig. 7.3b displays the calculated absorption spectra at different driving energy. The E_{1s-2p_+} used in the fitting is 142 meV and 128 meV for K and K' valleys, respectively. From the fitting to the experimental data, we extract the exciton-photon coupling constant V_1 of 8 meV, which corresponds to a 1s-2p$_+$ intraexciton transition dipole moment μ_{1s-2p_+} of 55±6 Debye. The μ_{1s-2p_+} is almost 6 times larger than that effective dipole moment in the interband exciton optical Stark effect [239, 101, 192], and it leads to a nearly 40 times larger optical Stark shift under the same driving intensity and detuning.

To better understand the experimental results, we performed *ab initio GW*-BSE calculations using the BerkeleyGW[178, 46, 83] package to determine the exciton energy levels and optical selection rules of exciton and intraexciton transitions in monolayer $MoSe_2$. In these calculations, environmental screening effects from the hexagonal boron nitride (hBN) encapsulation layers are included19 from first-principles (see Sec. 7.4). The simulation confirms the energy level diagram of the 1s, 2p$_+$, and 2p$_-$ excitons and the optical selection rules in K and K'-valleys in Fig. 7.1b. Our calculations find that the energies of the 1s and 2p$_-$ exciton states are separated by 117 meV, with 2p$_+$ exciton states further separated by 7 meV in K-valley. The energetic order of 2p$_+$, and 2p$_-$ excitons states is opposite in the K'-valley, as

a result of time-reversal symmetry. Although the $2p_\pm$ excitons are dark in linear optics, they are optically active when coupled to the 1s exciton with circularly-polarized light (Fig. 7.1b). For example, our calculations show that the 1s-$2p_+$ intraexciton transition couple exclusively to the left-handed circularly polarized (denoted as σ^+) light with a transition dipole moment of 42 Debye. The 1s-$2p_-$ intraexciton transition, on the other hand, coupled exclusively to the right-handed circularly polarized (denoted as σ^-) light. The experimentally observed intraexciton dipole moment and valley-dependent exciton fine structure match reasonably well with the *ab initio* GW-BSE calculations.

The combination of $2p_\pm$-exciton splitting and extremely strong intraexcitonic light-matter interaction allow us to observe valley-dependent Autler-Townes doublets at higher pump intensity in $MoSe_2$ monolayer. Towards this goal, we fabricated a hBN-encapsulated $MoSe_2$ heterostructure on a zinc-sulphide (ZnS) substrate, where the local field factor on the sample for the infrared pump light is more favorable than that for $MoSe_2$ on alumina coated silver substrate. In this device the 1s-$2p_+$ intraexciton transition energies for the K and K'-valleys are determined to be 150 meV and 138 meV, respectively. Figure 7.4a shows the absorption spectra of the 1s exciton at $\tau = 0$ ps for K and K'-valleys under series of excitation intensity. The σ^+-pump driving energy is set to 150 meV, which is on resonant with the 1s-$2p_+$ transition in the K-valley but positively detuned from the 1s-$2p_+$ transition in the K'-valley. We observe contrasting coherent phenomena between the K and K'-valleys: 1s exciton transition exhibits a striking splitting into the Autler-Townes doublet in the K-valley, but shows a mostly blueshift in the K'-valley. On the other hand, when the σ^+-pump energy is tuned to 138 meV, which is negatively detuned from the 1s-$2p_+$ transition in the K-valley but on resonant with the 1s-$2p_+$ transition in K'-valley, the 1s exciton transition shows red shift in the K-valley but a clear Autler-Townes doublet in the K'-valley (Fig. 7.4b). Fig. 7.4c,d show the splitting energy in the Autler-Townes doublet at resonant excitation scales linearly with the excitation field strength, as expected from Eq. 7.2 [8, 9]. At an effective driving intensity of 50±10 MW/cm^2, which corresponds to a local optical field strength of 200±20 kV/cm, the Autler-Townes splitting can reach ∼24 meV in both valleys. This Autler-Townes doublet leads to a valley-dependent electromagnetically induced transparency in the 1s exciton transition, where the absorption at the 1s exciton resonance is reduced by more than 10-fold compared to the undriven exciton (Fig. 7.4a, b). Our findings offer a new and effective pathway to coherently manipulate the quantum states and excitonic excitations using infrared radiation coupled to the 1s-$2p_+$ intraexciton transition.

7.3 Materials and Methods

Sample Fabrication

The $MoSe_2$ monolayer encapsulated in hBN flakes were prepared with a polyethylene terephthalate (PET) stamp by a dry transfer method [239]. Monolayer $MoSe_2$ and hBN flakes were first exfoliated onto silicon substrate with a 90 nm oxide layer. We used PET stamp to pick-

up the top hBN flake, monolayer $MoSe_2$, and bottom hBN flake in sequence with accurate alignment based on an optical microscope. The hBN/$MoSe_2$/hBN heterostructure was then stamped on a silver substrate coated with a 85 nm alumina layer or on a zinc sulphide (ZnS) substrate. Polymer and samples were heated to 60°C for the pick-up and 130°C for the stamping process. Finally, the PET was dissolved in dichloromethane for 12 hours at room temperature. The sample temperature was kept at 77 K in a liquid-nitrogen cooled cryostat equipped with BaF_2 window during optical measurements.

Intraexciton Optical Stark Spectroscopy

Pump-probe spectroscopy study is based on a regenerative amplifier seed by a mode-locked oscillator (Light Conversion PHAROS). The regenerative amplifier delivers femotosecond pulses at a repetition rate of 150 kHz and a pulse duration of ∼250 fs, which were split into two beams. One beam was used to pump an optical parametric amplifier and the other beam was focused onto a sapphire crystal to generate supercontinuum light (500 to 1100 nm) for probe pulses. Femtosecond mid-infrared pump pulses with tunable photon energies were generated via difference frequency mixing of the idler pulses from the optical parametric amplifier and residual of fundamental output (1026 nm) from regenerative amplifier in a 1 mm thick silver gallium sulphide (AGS) crystal. The mid-infrared pulse duration is ∼400 fs. The pump-probe time delay was controlled by a motorized delay stage. The probe light was detected by high sensitivity CCD line camera operated at 1000 Hz. The helicity of pump and probe pulses was independently controlled using Fresnel rhomb and broadband quarter-waveplates, respectively. The experiment followed a reflection configuration with a normal incidence and collinear pump-probe geometry, where the absorption spectra are extracted from the reflectance contrast.

7.4 GW-BSE calculations of $MoSe_2$

Density-functional theory (DFT) calculation of monolayer $MoSe_2$ as implemented in the Quantum ESPRESSO[66] package is first carried out to obtain the Kohn-Sham wavefunctions. We use a plane-wave basis set, norm-conserving scalar-relativistic pseudopotentials and the local density approximation (LDA) for electron exchange and correlation [27, 161]. The Mo 4s and 4p semi-core states and the 4d and 5s valence states are included in the calculation to accurately capture the exchange contribution to the self-energy. The monolayer $MoSe_2$ crystal structure has a lattice constant4 of 3.29 Å and a thickness of 3.34 Å as measured from the centers of the Se atoms. The length of the supercell in the out-of-plane direction is set to be $L_z = 120$ Å. The kinetic energy cutoff for the DFT calculation is set at 80 Ry for the plane-wave expansion of the wavefunctions. Using the calculated Kohn-Sham wavefunctions, the GW quasiparticle (QP) self-energies and the GW-BSE exciton energy levels are then computed with the BerkeleyGW package [83, 178, 46]. In our GW-BSE calculations, the Coulomb interaction is always truncated6 in the out-of-plane direction.

The quasiparticle self-energies are calculated using the eigenvalue-self-consistent, full-frequency GW_0 approximation. The full frequency-dependent dielectric matrix is calculated on an effective [94] q-grid of 1100×1100, expanded from a regular q-grid of 6×6 using 10 subsampled points. When calculating the dielectric matrix, a total of 26450 bands is used and the energy cutoff used to calculate the screened exchange is set at 35 Ry.

To calculate the exciton energy levels, the Bethe-Salpeter Equation (BSE) is solved using the calculated QP energies. Static screening [178] is used as an approximation for dynamical screening since the $MoSe_2$ monolayer encapsulated in hBN layers is an intrinsic semiconductor with negligible doping. The screening behavior is therefore constant for frequencies of the order of the binding energy. The electron-hole interaction kernel of the BSE Hamiltonian HBSE is first calculated on a regular k-grid of 72×72, using a static dielectric matrix that is calculated on regular q-grid of 72×72 using 1400 bands and a 5 Ry energy cutoff for the screened exchange. To obtain the envelope function of the exciton wavefunctions, the BSE Hamiltonian is fully diagonalized using interaction kernel matrix elements that are interpolated [94, 178] from the regular 72×72 k-grid to a finer k-grid of 648×648. To calculate the energy levels of the first few exciton states, the kernel matrix elements are interpolated [94] onto an even finer k-grid of 1440×1440 by diagonalizing the BSE Hamiltonian using the Lanczos algorithm [190]. Since the exciton wavefunctions are localized in the reciprocal space [168], the kernel matrix elements are only interpolated onto a round patch of k-points centered at the K-valley of radius 0.181 Bohr^{-1}. Finally, the optical transition dipole moment between the initial exciton state $|S_i\rangle$ to the final exciton state $|S_f\rangle$, i.e. $\hat{\boldsymbol{\epsilon}} \cdot \langle S_f|\boldsymbol{\mu}|S_i\rangle$, is calculated as follows:

$$\begin{aligned} \hat{\boldsymbol{\epsilon}} \cdot \langle S_f|\boldsymbol{\mu}|S_i\rangle &= |q|\hat{\boldsymbol{\epsilon}} \cdot \langle S_f| - \boldsymbol{r_e} + \boldsymbol{r_h}|S_i\rangle \\ &= \frac{|q|\hat{\boldsymbol{\epsilon}}}{i(\Omega_f - \Omega_i)} \cdot \left(- \langle S_f|\boldsymbol{v_e}|S_i\rangle + \langle S_f|\boldsymbol{v_h}|S_i\rangle\right) \end{aligned} \tag{7.2}$$

where $\hat{\boldsymbol{\epsilon}}$ is the polarization of the light inducing the transition, $\boldsymbol{r}$ is the position operators, $\boldsymbol{v}$ is the velocity operator, Ω is the exciton energy and the subscripts e and h label the electron and hole of the exciton.

Screening due to hBN-encapsulation is included during the calculation of the quasiparticle energies and the energy levels of the excitons using the in-plane substrate-averaging (IPSA) [211] approximation. In this approximation, the substrate screening is assumed to be translationally invariant, i.e. averaged in the in-plane direction. Theoretically, this means that the non-interacting polarizability of the encapsulation is added onto the full dielectric matrix of $MoSe_2$, including explicitly all out-of-plane local fields ($G_z \neq G_{z'}$) and neglecting only the in-plane local ($G_x \neq G'_x$ or $G_y \neq G_{y'}$) fields. This IPSA approximation has been shown to accurately capture the substrate-screening effects on the quasiparticle band structures and excitonic energy levels of transition metal dichalcogenide monolayer4. The $MoSe_2$-hBN distance is determined in a separate DFT calculation by minimizing the energy of the system that also incorporates van der Waals interactions (vdW-DF$^{\mathrm{C09x}}$) [39] and dipole corrections [14, 142]. The separation between the Se layer of $MoSe_2$ and its nearest

BN layer of the encapsulation is found to be 3.4 Å in the out-of-plane direction. To calculate the screening by hBN within the IPSA approximation, we construct a slab consisting of 14 hBN layers that is 4.3-nm thick and has an in-plane lattice constant [225] of 2.50 Å. The DFT energy cutoff is set at 60 Ry. A screened energy cutoff of 6 Ry and 1117 bands are used to calculate the polarizability matrix of the encapsulation.

The solution of the BSE Hamiltonian $\mathrm{H}_{\mathrm{BSE}}$ gives the two-particle exciton wavefunction,

$$|S\rangle = \sum_{vc\mathbf{k}} A_{vc\mathbf{k}} \, |\psi_{c\mathbf{k}}\rangle \, |\psi^*_{v\mathbf{k}}\rangle \tag{7.3}$$

where $A_{vc\mathbf{k}}$ is the amplitude of the free electron-hole pair that is the direct product of an electron state $|\psi_{c\mathbf{k}}\rangle$ and a hole state $|\psi^*_{v\mathbf{k}}\rangle$. The coefficients $A_{vc\mathbf{k}}$ describes the envelope function of the exciton wavefunction in reciprocal space. Since light has a negligible momentum, we consider only excitons with zero center-of-mass momenta. Our calculated energy difference between the $|2p_-\rangle$ and $|2p_+\rangle$ states is 7 meV whereas the energy difference between the lower $|2p\rangle$ state and the $|1s\rangle$ state is 117 meV.

The first column in Fig. 7.5 shows the amplitude-squared real-space plot of the envelope function of the 1s and 2p states of a hydrogenic exciton. In such hydrogenic excitons, the 2p states of opposite angular momenta are degenerate, so linear combinations of their envelope functions can be chosen to be real, with well-defined axial directions (x and y), i.e.

$$|2p_x\rangle = \frac{1}{\sqrt{2}}(|2p_+\rangle + |2p_-\rangle) \tag{7.4}$$

$$|2p_y\rangle = \frac{1}{i\sqrt{2}}(|2p_+\rangle - |2p_-\rangle) \tag{7.5}$$

These states are still exciton eigenstates in a hydrogenic model. In Fig. 7.5, the $|2p_x\rangle$ and $|2p_y\rangle$ states are plotted by assuming that the $|2p_\pm\rangle$ states are degenerate and that $|2p_x\rangle$ and $|2p_y\rangle$ states are linear combinations of the $|2p_\pm\rangle$ states.

The second column of Fig. 7.5 shows the amplitude-squared envelope-functions of the$|2p_\pm\rangle$ states of $\mathrm{MoSe_2}$ monolayer in real-space obtained from the first-principles calculation. The two-fold degeneracy of the $|2p_\pm\rangle$ exciton states is broken and their linear combinations no longer define eigenstates, i.e. neither $|2p_x\rangle$ nor $|2p_y\rangle$ is an eigenfunction of the system. This can be understood from the fact that the $\mathrm{MoSe_2}$ monolayer does not have an inversion symmetry, the $|2p_x\rangle$ and $|2p_y\rangle$ states do not separately possess the three-fold rotational symmetry of the crystal, unlike the non-degenerate $|2p_\pm\rangle$ eigenstates.

In the third column of Fig. 7.5, we show the exciton envelope function of the $|2p_+\rangle$ and $|2p_-\rangle$ states in the reciprocal space at the K-valley. The ordering of the $|2p_\pm\rangle$ states is reversed at the K'-valley due to time-reversal symmetry. Here, we use a smooth gauge as defined in Ref. [168]. Under this hydrogenic gauge choice, the envelope function of $|1s\rangle$ is chosen to be entirely real while those of $|2p_+\rangle$ and $|2p_-\rangle$ states have complex phases, enabling optical coupling via σ^+ and σ^--polarized infrared radiation respectively. We further calculate the optical transition dipole moments between the $|1s\rangle$ and $|2p_\pm\rangle$ states using Eq. 7.2. The

calculation shows that a resonant σ^+-polarized light can strongly couple the 1s-2p_+ transition with a transition dipole moment of 41.5 Debye, while the coupling between the 1s-2p_- transition with σ^+-polarized light is negligibly weak. The coupling by σ^--polarized light shows the opposite behaviour, i.e., the transition dipole moment for the 1s-2p_+ transition under σ^--polarized light radiation is 45.2 Debye but negligibly weak for the 1s-2p_+ transition. Such selective coupling of 1s-2$p_\pm$ transition is consistent with the experimental findings shown above.

The point group of the TMD monolayer is D_{3h}. Considering the optical transitions, the symmetry element that is relevant to the intraexciton selection rules is the 3-fold rotational symmetry (C_3). We adopted the convention and notation used in Ref. [69], and labelled the quantum number (pseudo-angular momentum) of 1s, 2p$_+$, and 2p$_-$ states under the C_3 rotation in Fig. 7.5.

7.5 Convention Used for Circularly-Polarized Light

In the literature, two opposite conventions have been used to describe circularly-polarized light. Depending on the convention, a particular circularly-polarized light can be described as right-handed or left-handed, and clockwise or anti-clockwise. In this section, we will be describing the convention that we are using in this chapter.

Decomposition of Circularly-Polarized Light into Two Linearly-Polarized Light

A circularly polarized light can be decomposed into two orthogonal linearly-polarized light of equal amplitude. In this section, we will focus our discussion on the optical transition induced from one state to another upon the *absorption* of a photon. Hence the wave is represented by the sinusoidal function of $(kz-\omega t)$. For transitions that lead to the *emission* of a photon, the argument of the sinusoidal function should be replaced by $(\omega t - kz)$.

For a classical light wave travelling in the +z-direction that is circularly-polarized in a particular handedness, its constituent waves can be expressed as,

$$\begin{aligned}\mathbf{E}_x(z,t) &= \hat{\mathbf{x}}\frac{E_0}{\sqrt{2}}\cos(kz-\omega t)\\ \mathbf{E}_y(z,t) &= \hat{\mathbf{y}}\frac{E_0}{\sqrt{2}}\cos(kz-\omega t-\frac{\pi}{2})\\ &= \hat{\mathbf{y}}\frac{E_0}{\sqrt{2}}\sin(kz-\omega t),\end{aligned} \tag{7.6}$$

with the resultant circularly polarized light being,

$$\mathbf{E}_L(z,t) = \frac{E_0}{\sqrt{2}}[\hat{\mathbf{x}}\cos(kz-\omega t)+\hat{\mathbf{y}}\sin(kz-\omega t)], \tag{7.7}$$

where L labels the angular momentum of the light.

Re-writing Eqs. (7.6-7.7) using complex phasor notation, we get,

$$\begin{aligned}\mathbf{E}_x(z,t) &= \hat{\mathbf{x}}\frac{E_0}{\sqrt{2}}\exp[i(kz-\omega t)]\\ \mathbf{E}_y(z,t) &= \hat{\mathbf{y}}\frac{E_0}{\sqrt{2}}\exp[i(kz-\omega t-\frac{\pi}{2})]\\ &= \hat{\mathbf{y}}\frac{E_0}{\sqrt{2}}\exp[i(kz-\omega t)]e^{-i\frac{\pi}{2}}\\ &= \hat{\mathbf{y}}\frac{E_0}{\sqrt{2}}\exp[i(kz-\omega t)](-i),\end{aligned}$$

and the resultant circularly polarized light will become,

$$\mathbf{E}_L(z,t) = (\hat{\mathbf{x}}-i\hat{\mathbf{y}})\frac{E_0}{\sqrt{2}}\exp[i(kz-\omega t)].$$

Angular Momentum L of Circularly-Polarized Light

On some arbitrary plane $z=z_0$ and using Eq. 7.7, we see that when $t=0$, $\mathbf{E}=E_0(\hat{\mathbf{x}}\cos(kz_0)+\hat{\mathbf{y}}\sin(kz_0))$. When $t=\frac{+kz_0}{\omega}$, $\mathbf{E}=E_0(\hat{\mathbf{x}}\cos(0)+\hat{\mathbf{y}}\sin(0))=E_0\hat{\mathbf{x}}$. The phasor diagram is plotted out in Fig. 7.6. For a test charge on the $z=z_0$ plane, the photon will impart an angular momentum of $\mathbf{L}=-\hbar\hat{\mathbf{z}}$ to the test charge, where $\hat{\mathbf{z}}$ is the propagating direction of the light. Here, we define the direction of the angular momentum using the right-hand rule, in which a positive angular momentum will have the same direction as the propagating direction of the light.

Naming Convention of Circularly-Polarized Light: Left or Right, Clockwise or Anticlockwise

To name the polarization of light in Eq. (7.7), there are two different conventions. One convention is defined from the point of view of the source. In this convention, left- or right-handedness is determined by pointing the person's left or right thumb away from the source, in the same direction that the wave is propagating, and matching the curling of one's fingers to the direction of the spatial rotation of the field at a given point in space. In this source's point-of-view convention, the circularly-polarized light in Eq. (7.7) is left-handed.

The other convention is defined from the point of view of the receiver. In this convention, left- or right- handedness is determined by pointing the person's left or right thumb towards the source, against the direction of propagation, and then matching the curling of one's fingers to the temporal rotation of the field. Using the receiver's point-of-view instead, the circularly-polarized light in Eq. (7.7) is right-handed.

In both conventions, right-handedness corresponds to a clockwise rotation and left-handedness corresponds to an anti-clockwise rotation.

Summary

For light with $\mathbf{L} = -\hbar\hat{\mathbf{z}}$:

- $\mathbf{E}_{-}(z,t) = \frac{E_0}{\sqrt{2}}[\hat{\mathbf{x}}\cos(kz-\omega t) + \hat{\mathbf{y}}\sin(kz-\omega t)]$ or
- $\mathbf{E}_{-}(z,t) = (\hat{\mathbf{x}} - i\hat{\mathbf{y}})\frac{E_0}{\sqrt{2}}\exp[i(kz-\omega t)]$ in phasor notation
- Left-handed or anti-clockwise in the source's point-of-view convention.
- Right-handed or clockwise in the receiver's point-of-view convention.

For light with $\mathbf{L} = +\hbar\hat{\mathbf{z}}$:

- $\mathbf{E}_{+}(z,t) = \frac{E_0}{\sqrt{2}}[\hat{\mathbf{x}}\cos(kz-\omega t) - \hat{\mathbf{y}}\sin(kz-\omega t)]$ or
- $\mathbf{E}_{+}(z,t) = (\hat{\mathbf{x}} + i\hat{\mathbf{y}})\frac{E_0}{\sqrt{2}}\exp[i(kz-\omega t)]$ in phasor notation.
- Right-handed or clockwise in the source's point-of-view convention.
- Left-handed or anti-clockwise in the receiver's point-of-view convention.

To avoid confusion, in this chapter, we label the circular polarization of the light using its angular momentum. σ_+-polarized light has $\mathbf{L} = +\hbar\hat{\mathbf{z}}$ while σ_--polarized light has $\mathbf{L} = -\hbar\hat{\mathbf{z}}$.

7.6 Convention Used to Define the Angular Momentum of Exciton Wavefunction

The relative motion of the electron and the hole in an exciton is similar to that of the electron and the proton inside a hydrogen atom. As a result, the effective mass equation of an exciton resembles the Schrödinger Equation for a hydrogen atom. As a result, exciton states are often expressed as solutions of the hydrogen atom.

2D exciton states can be described using solutions of the Schrödinger Equation of a 2D hydrogen atom,15 in which a bound state is described by a radial quantum number nr and an azimuthal quantum number m, such that the principle quantum number is given by $n = n_r + |m|$. In this chapter, we define our exciton states using the principle quantum number n and the azimuthal quantum number m. It should also be noted that unlike the solutions for a 2D hydrogen atom, experimentally-observed 2D exciton states describe an interaction of spatially-confined electrons within a quasi-2D material in a three-dimensional space. As such, its screening is not completely two-dimensional and the resulting ordering of the exciton eigen-energies may not be exactly identical to that of a 2D hydrogen atom, in what is also known as the nonhydrogenic Rydberg series. [168, 224, 169]

The time-independent solution of the 2D hydrogen Schrodinger Equation in circular coordinates $\Psi^n_m(r,\varphi)$ admits separable solutions of the form $\Psi^n_m(r,\varphi) = R^n_{|m|}(r)\Phi_m(\varphi)$, where

$\Psi(r,\varphi)$ is the hydrogen wavefunction, $R^n_{|m|}$ is the radial function, Φ_m is the azimuthal function, r is the radial coordinate and ϕ is angular coordinate. The solution of the azimuthal function can be given as,

$$\langle\varphi|\Phi_m\rangle = \Phi_m(\varphi) = \frac{e^{im\varphi}}{\sqrt{2\pi}} \tag{7.8}$$

such that the exciton wavefunction of a specific azimuthal angular momentum m can be defined as

$$\begin{aligned}\langle\Phi_m|S^n\rangle &= \int_0^{2\pi} d\varphi\,\langle\Phi_m|\varphi\rangle\,\langle\varphi|S^n\rangle \\ &= \int_0^{2\pi} d\varphi\frac{e^{-im\varphi}}{\sqrt{2\pi}}\,\langle\varphi|S^n\rangle\end{aligned} \tag{7.9}$$

If the states of opposite angular momenta are degenerate, such as the unperturbed solutions of the 2D hydrogen Schrödinger equation, and since these states are complex conjugates of each other, linear combinations of the states give real wavefunctions that also eigen-solution of the Schrödinger equation that are easier to visualize and frequently used in literature. This is because linear combination of two degenerate eigenfunctions gives a new eigenfunction with the same eigenvalue.

Specifically for $|2p_\pm\rangle$ states (i.e. $n=2$ and $m=\pm1$), which are given by,

$$\begin{aligned}\langle r\varphi|2p_+\rangle &= \Psi^2_1(r,\varphi) \\ &= R^2_{|1|}(r)\Phi_1(\varphi) \\ \langle r\varphi|2p_-\rangle &= \Psi^2_{-1}(r,\varphi) \\ &= R^2_{|-1|}(r)\Phi_{-1}(\varphi),\end{aligned}$$

their linear combinations can be written in terms of the $|2p_x\rangle$ and $|2p_y\rangle$ states, i.e.

$$\begin{aligned}\langle r\varphi|2p_x\rangle &= \Psi_{2p_x}(r,\varphi) \\ &= \frac{1}{\sqrt{2}}(\Psi^2_1+\Psi^2_{-1})(r,\varphi) \\ &= \frac{1}{\sqrt{2}}R^2_{|1|}(r)(\Phi_1(\varphi)+\Phi_{-1}(\varphi)) \\ &= \frac{1}{2\sqrt{\pi}}R^2_{|1|}(r)\cos(\varphi) \\ &= \frac{1}{2\sqrt{\pi}}R^2_{|1|}(r)\frac{x}{r} \\ \langle r\varphi|2p_y\rangle &= \Psi_{2py}(r,\varphi) \\ &= \frac{1}{i\sqrt{2}}(\Psi^2_1-\Psi^2_{-1})(r,\varphi)\end{aligned}$$

$$
\begin{aligned}
&= \frac{1}{i\sqrt{2}} R^2_{|1|}(r)(\Phi_1(\varphi) - \Phi_{-1}(\varphi)) \\
&= \frac{1}{i2\sqrt{\pi}} R^2_{|1|}(r)\sin(\varphi) \\
&= \frac{1}{i2\sqrt{\pi}} R^2_{|1|}(r)\frac{y}{r}. \qquad (7.10)
\end{aligned}
$$

Reversely, $|2p_\pm\rangle$ states can also be written in terms of the $|2p_x\rangle$ and $|2p_y\rangle$ states as follows:

$$
\begin{aligned}
|2p_+\rangle &= \frac{1}{\sqrt{2}}(|2p_x\rangle + i\,|2p_y\rangle) \\
|2p_-\rangle &= \frac{1}{\sqrt{2}}(|2p_x\rangle - i\,|2p_y\rangle) \qquad (7.11)
\end{aligned}
$$

In conclusion, if we are to define the azimuthal angular momentum m of the exciton wavefunction as in Eqs. (7.8, 7.9), then it is equivalent to defining the wavefunctions as linear combinations of real wavefunctions as in Eq. (7.11). It is important to note that since the Berry curvature results in a perturbation of the BSE equation, 2p$_+$ and 2p$_-$ exciton states are not degenerate in a GW-BSE calculation and hence 2p$_x$ and 2p$_y$ are separately not good eigen-functions of the BSE Hamiltonian.

The above defines the convention that is used in our chapter. This definition for the angular momentum of the exciton state is consistent with our definition for the angular momentum of circularly-polarized light in Sec. 7.5 and is immediately obvious by comparing 7.11 with the phasor notation that is used for circularly-polarized light. Our definition for the angular momentum of the exciton state is the same that those used by Refs. [224, 198]. In Ref. [251], the radial quantum number n_r is used instead of the principle quantum number n. In addition, m in Ref. [251] is defined using a different convention from ours (See Eq. 14 in Ref. [251], and Eq. 7.9 of this Section), and hence has an opposite sign.

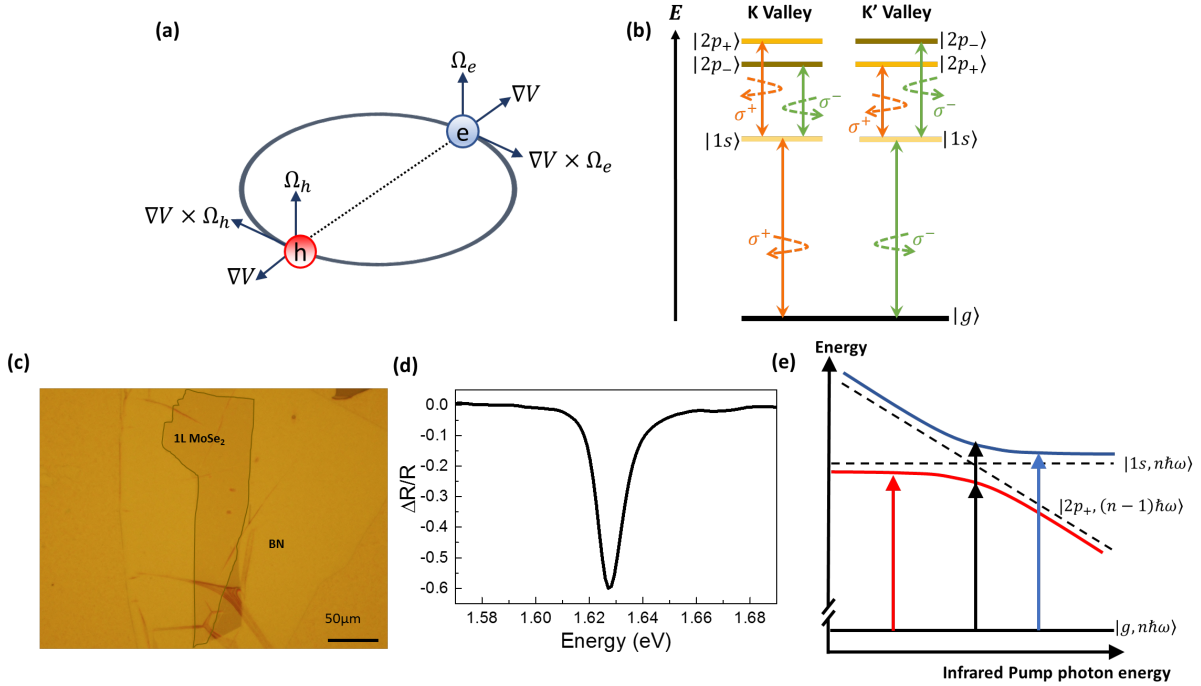

Figure 7.1: Schematics of exciton spectrum and optical transition in MoSe$_2$ monolayer. a. Diagram illustrating the effects of Berry curvature Ω_e and Ω_h on the energy of exciton. The electron and hole acquire an anomalous velocity $\nabla \times \Omega$ in a central potential V(r), resulting in a lift of the degeneracy between the exciton states with opposite angular momentum. b. Illustration of the optical transition and selection rules for one-photon and two-photon excitations in the K and K' valleys of MoSe$_2$ monolayer. $|g\rangle$, $|1s\rangle$, $|2p_-\rangle$, and $|2p_+\rangle$ denote the ground state, 1s, 2p$_-$, and 2p$_+$-exciton states, respectively. The symbol σ^+ and σ^- denotes left and right circular polarization state, respectively. c. Optical micrograph of monolayer MoSe$_2$ encapsulated by hBN layers on alumina coated silver substrate. The scale bar corresponds to 50 μm. d. The reflection contrast of hBN encapsulated MoSe$_2$ monolayer on alumina coated silver surface at 77 K. It shows prominent A-exciton resonance at 1.627 eV with a FWHM of ≈9 meV. e. Schematic diagram illustrating the avoided-crossing behavior due to quantum-mechanical coupling between the infrared photons field and the 1s-2p$_+$ electronic transition. The dashed lines show the energy difference between the $|g, n\hbar\omega\rangle$ and the unperturbed $|1s, n\hbar\omega\rangle$ and $|2p_+, (n-1)\hbar\omega\rangle$ states as a function of the infrared pump photon energy. The bare $|2p_+, (n-1)\hbar\omega\rangle$ state has one fewer pump photon than the bare $|1s, n\hbar\omega\rangle$ state, and will have a total energy decreasing linearly with the pump photon energy. The blue and red solid lines show the dressed exciton states from quantum hybridization. The arrows show the optical transitions from the ground state to the dressed 1s exciton state.

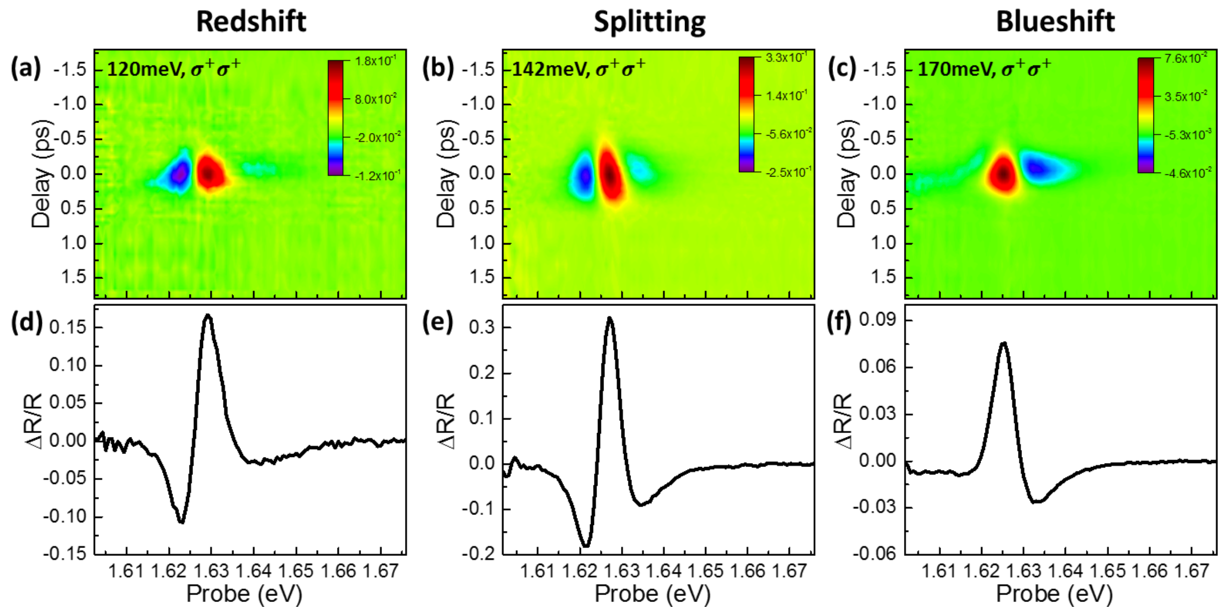

Figure 7.2: Transient reflection spectra of K-valley exciton transitions. a-c. Two-dimensional plot of transient reflection spectra of the K-valley 1s-exciton resonance of $MoSe_2$ at 77 K following photoexcitation with σ^+-polarized infrared pump at photon energy of (a) 120 meV, (b) 142 meV and (c) 170 meV. The color scale, vertical axis and horizontal axis represent the relative reflectivity change ΔR /R, the pump-probe time delay τ, and the probe photon energy, respectively. The positive (negative) ΔR /R represents decrease (increase) of absorption. The photoinduced absorption in the K-valley 1s-exciton is monitored by σ^+-polarized probes. The signals are finite only when the pump and probe pulses overlap in time, indicating an instantaneous coherent response and negligible excitation of real exciton population. d-f. At $\tau = 0$ ps, the coherent signals for σ^+-probes exhibit spectral responses that are characteristic of (d) energy redshift to (e) splitting and then to (f) energy blueshift as the driving photon energy is increased from 120 meV to 170 meV.

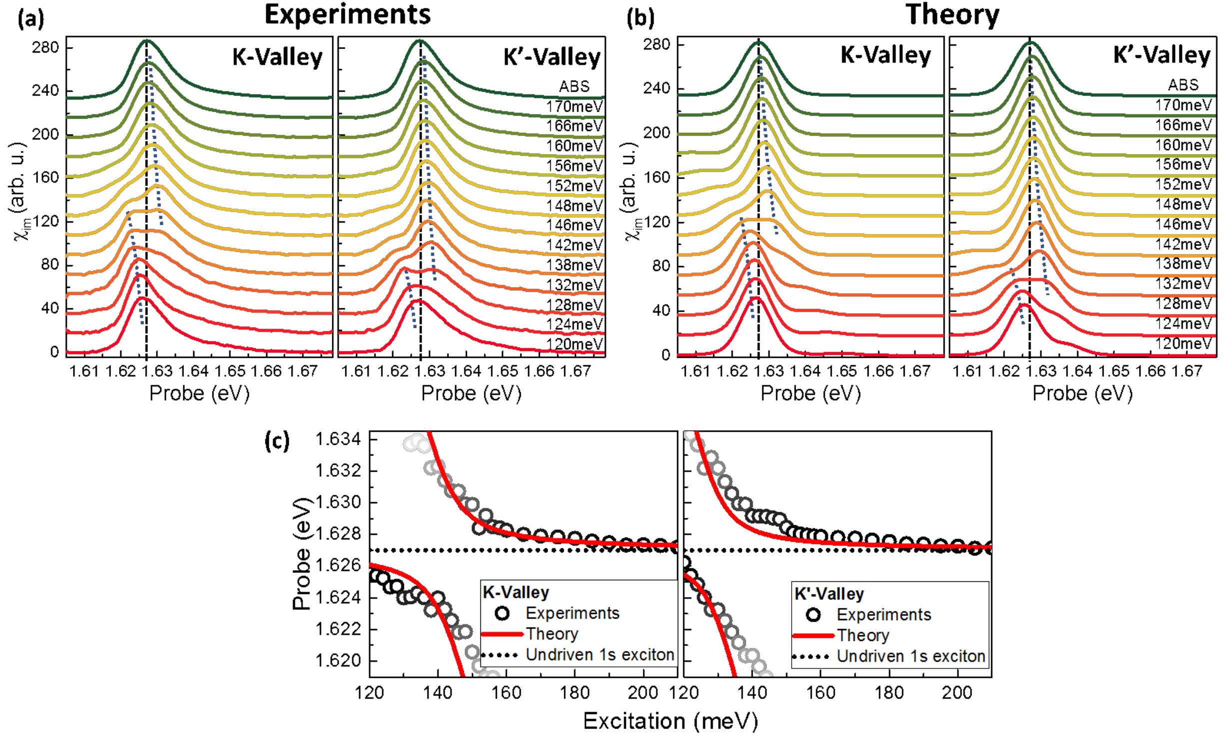

Figure 7.3: Valley-dependent intraexciton optical Stark effect. a-b. Experimentally observed (a) and calculated (b) photoinduced absorption spectra of $MoSe_2$ monolayer at $\tau =$ 0 ps under various σ^+- pump excitation energy for the K and K' valleys. The dashed-lines indicate the peak position of unperturbed A-exciton. The dotted lines are guides to the eyes for the peak position at different driving energies. The spectra are offset for clarity and labelled according to the excitation energy (meV). The spectra evolve from energy redshift to splitting and then to blueshift, as the driving energy is increased. The calculation is based on the Hamiltonian shown in Eq. 7.2. Exciton-photon coupling leads to avoided-crossing and the observed peak splitting at resonant coupling. This resonant coupling occurs at driving photon energy of 142 meV and 128 meV in the K and K' valleys, respectively. It corresponds to a Berry-phase induced 1s-2p$_+$ intraexciton transition energy difference of 14 meV. c. Measured 1s exciton peak position (circles) in the K and K' valleys as a function of σ^+-infrared pump photon energy for an effective driving intensity is 7±1 MW/cm^2. The greyscale shows the relative strength of optical transition. The solid lines show the calculated dressed-exciton states based on the Hamiltonian shown in Eq. 7.2.

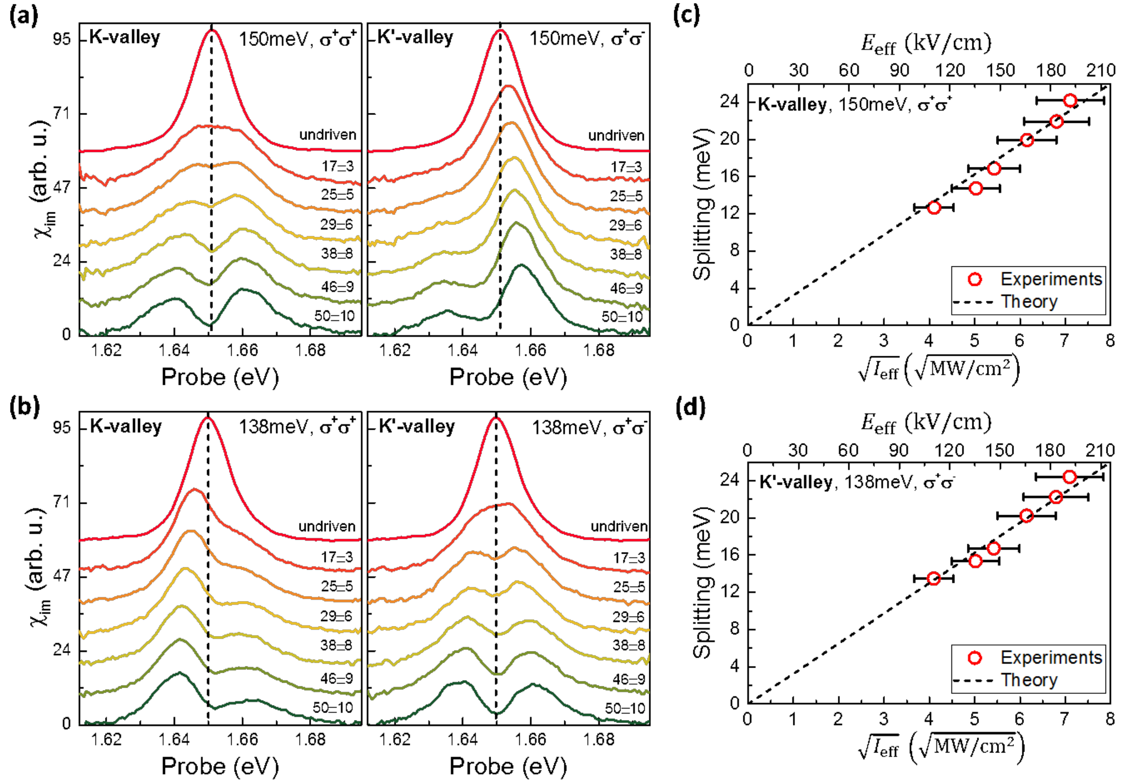

Figure 7.4: Valley-dependent Autler-Townes splitting. a-b. Photoinduced absorption spectra of $MoSe_2$ monolayer on ZnS substrate at $\tau = 0$ ps for a series of σ^+-pump intensity at driving energy of (a) 150 meV and (b) 138 meV for K and K'-valley. The dashed-lines indicate peak position of undriven A-exciton. The spectra are offset and labelled according to the effective driving intensity (MW/cm^2). c-d. The dependence of Autler-Townes splitting energy in K and K'-valley on the squared root of effective pump intensity ($\sqrt{I_{\text{eff}}}$)) for driving photon energy of (c) 150 meV and (d) 138 meV, respectively. The top axis shows the corresponding effective local optical field strength (E_{eff}). The splitting energies are obtained from fitting the photoinduced absorption lines with two Lorentzian lines. The dashed lines are fitting obtained from the Hamiltonian shown in Eq. 7.2.

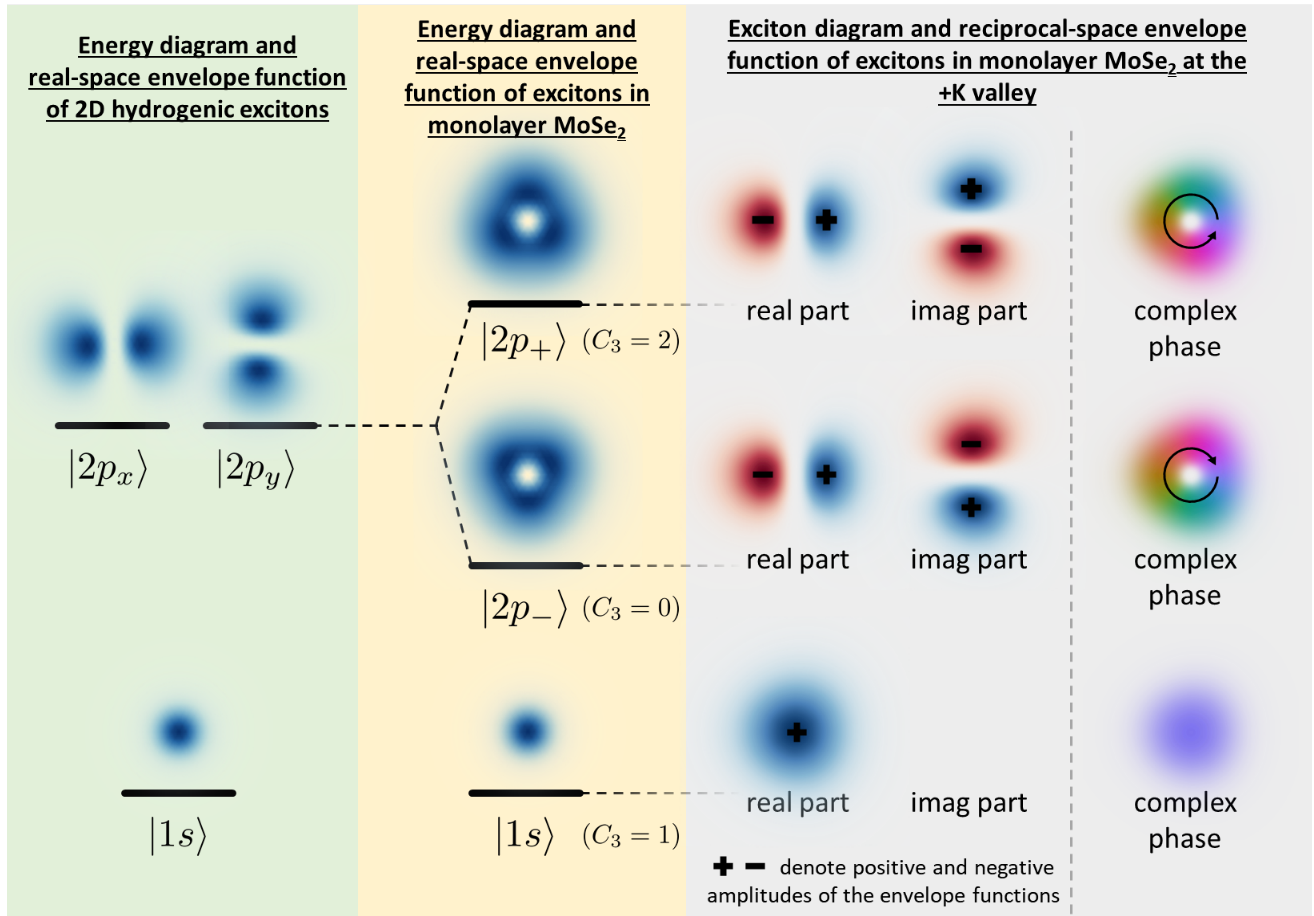

Figure 7.5: Plots of the exciton energy levels and their envelope functions in real and reciprocal space using a hydrogenic gauge.

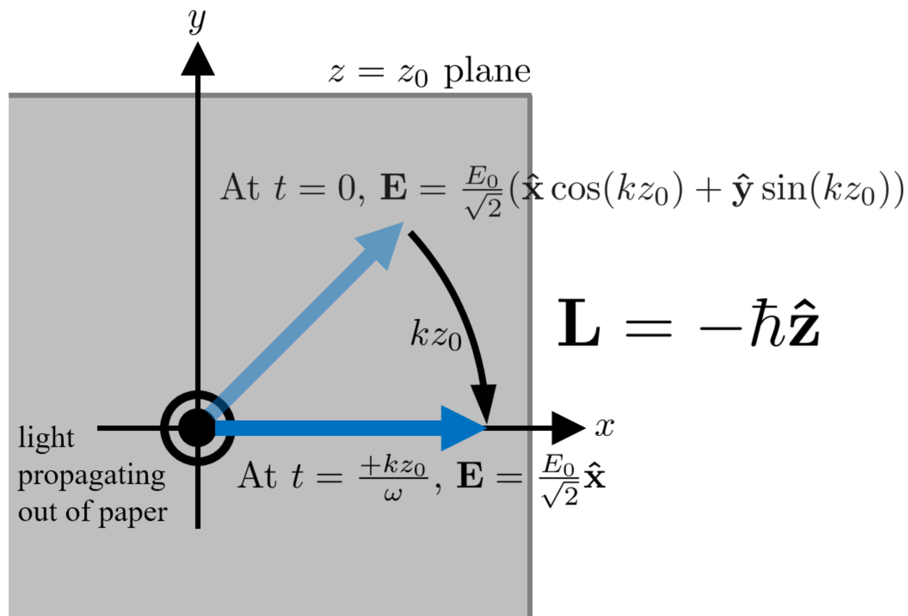

Figure 7.6: Angular momentum of circularly-polarized light.

Chapter 8

Dynamics of Symmetry-breaking Stacking Boundaries in Bilayer MoS_2

8.1 Introduction

Crystal symmetry in a material dictates its physical properties. Manipulating its symmetry provides a pathway to achieve novel and unusual functionalities. This is particularly relevant for two-dimensional (2D) materials, promising candidates for numerous applications, including next-generation flexible electronics. In bilayer graphene, for example, symmetry-inversion at a "soliton" stacking boundary between AB and BA stacked regions [4, 24] leads to robust, topologically protected 1D conducting channels at the domain walls [95, 247, 213]. In other 2D materials such as transition metal dichalcogenides (TMDs), the non-centrosymmetric crystal structure of the monolayer form leads to valley selectivity, and holds promise for applications in spintronics and valleytronics [232, 129, 245, 130].

One prototypical example of 2D TMDs is monolayer H-phase MoS_2. Monolayer H-phase MoS_2 is non-centrosymmetric and has a lattice constant of $a = 3.16$ Å (Fig. 8.1). The broken inversion symmetry, in addition to strong spin-orbit interactions, leads to the splitting of valence bands and spin-valley coupling [232], enabling valley selectivity when excited by circularly polarized light [129, 245, 130]. However, inversion symmetry is restored in bilayer 2H-phase MoS_2 - a phase that is naturally found and most commonly observed (also known to adopt AA' stacking sequence in Fig. 8.1). To break the inversion symmetry in bilayer MoS_2, a vertical electrical field can be applied [110]. Another way to introduce asymmetry in bilayer and multilayer MoS_2 is to engineer the stacking sequence by folding [92] or transferring [244, 81] exfoliated single-layer MoS_2, or by using chemical synthesis methods such as chemical vapor transport (CVT) [202] and chemical vapor deposition (CVD) [235, 124, 119, 227]. Two commonly observed stacking sequences in CVD/CVT grown MoS_2 are AA' stacking and AB stacking (a representative schematic of AB stacking is shown in Fig. 8.1), which are nearly energetically degenerate [235, 77]. Repeated AB stacking forms the 3R phase of MoS_2, in which centro-symmetry is broken throughout the bulk. A recent study shows that

valley-dependent spin-polarization is realized in CVT synthesized 3R-phase bulk MoS_2 [202].

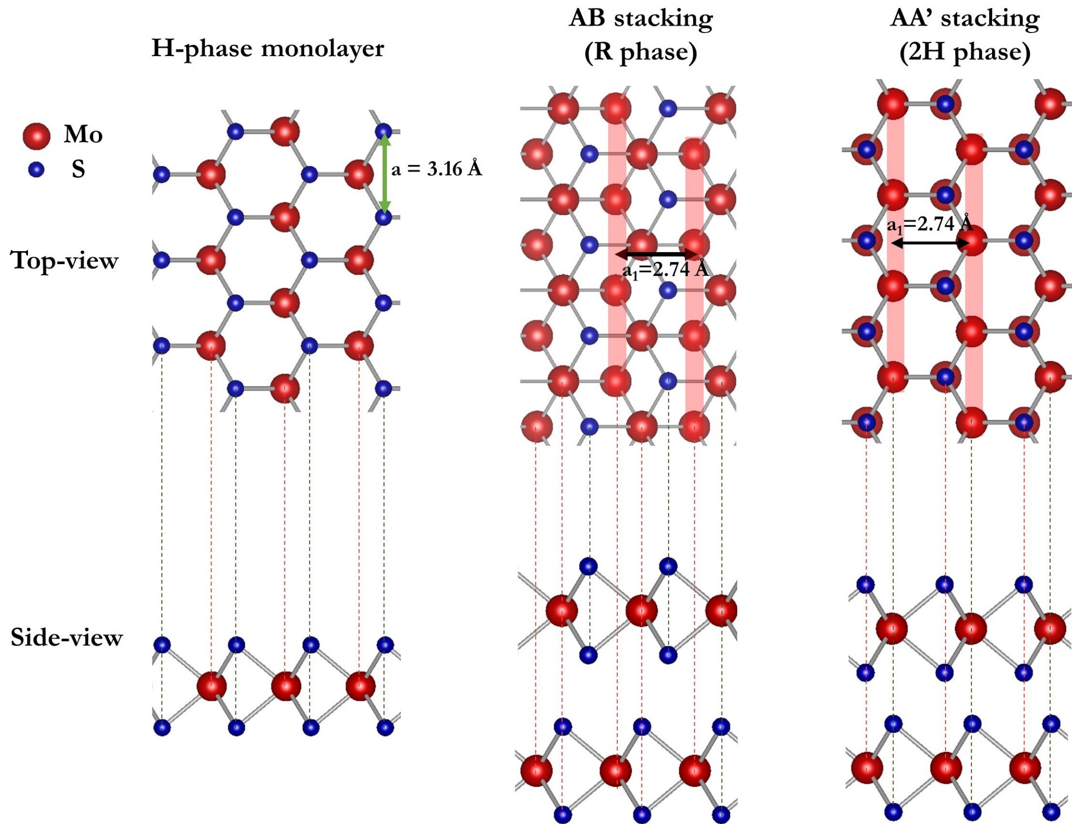

Figure 8.1: Ball-and-stick models for monolayer H-phase MoS_2, and AB (R phase) and AA' (2H-phase) stacked bilayer MoS_2, viewed from the top and the side, with red balls representing Mo atoms and blue balls representing S atoms. The lattice constant ($\mathbf{a}$) for monolayer H phase MoS_2 is 3.16 Å, and the Mo lattice distance in one layer MoS_2 ($\mathbf{a_1}$) is 2.74 Å, as indicated by red shadings in the schematics for both AB and AA' bilayers.

In this work, we demonstrate a novel way in which the symmetry of bilayer MoS_2 can be engineered via the creation of nanoscale stacking boundaries that separate domains with different inversion symmetries. We show that in bilayer MoS_2 the transition from AB to AA' stacking or from AA' to AB stacking can be realized by heating and electron-irradiating the AA' or AB stacked bilayer MoS_2 inside an aberration-corrected scanning transmission electron microscope (STEM). By using in-situ atomic-resolution STEM annular-dark field (ADF) imaging, we identify atomically sharp stacking boundaries between these two differently stacked domains. Combined with first-principles density functional theory (DFT) calculations, we investigate the atomic-scale dynamics of the domain nucleation and growth.

DFT calculation also reveals the existence of highly localized metallic states at the domain boundaries.

8.2 Results and Discussion

Bilayer MoS_2 studied here is grown on SiO_2/Si substrates via a modified CVD method based on Refs. [243, 147]. The as-grown MoS_2 flakes are then transferred to a Protochip heating TEM grid via the PMMA transfer method [201]. The Protochip TEM grid holder has the ability to heat the sample up to 1000°C with minimal local temperature variation. We use atomic-resolution STEM ADF imaging operated at 80 keV to track the stacking sequence change in bilayer MoS_2. STEM ADF images show the 2D projection of atomic positions of the layered material, and the intensity in STEM ADF images is closely related to the atomic number and thickness of the material. Since Mo and S have significantly different atomic numbers (Mo: 42 and S: 16), STEM ADF imaging is an ideal tool to identify the atomic species at different lattice positions and thus revealing the atomic structure of single- and few-layer MoS_2. High-resolution STEM ADF imaging has been used to visualize the atomic arrangement in single- and few-layer MoS_2, including stacking sequences, grain boundaries, point defects, edge sites and even phase transformation [235, 243, 147, 252, 115]. In our study, the electron beam serves two functions: (1) it facilitates in-situ imaging of local atomic structure and changes thereof in bilayer MoS_2; (2) it provides energy (in addition to the high temperature thermal bath) to stimulate local atomic movement. To make this atomic movement slow enough for real-time STEM tracking, an electron dose as low as 7×10^6 electrons/nm^2 s is applied. Although the electron energy of 80 keV is close to the threshold for S vacancy formation in monolayer MoS_2 [105], we are still able to image the regions of interest in bilayer samples for over 3 minutes. Movies composed of continuous STEM ADF imaging allows the transition between different stacking sequences to be recorded.

In our in-situ STEM study, we start from a CVD-grown pristine MoS_2 bilayer with a uniform stacking sequence of AB or AA'. Transitions between different stacking sequences are observed at 350°C and 400°C. Below, we focus on the representative case where the AB stacking is locally transformed into AA' stacking at 400°C. Different stacking sequences are identified by comparing the experimental STEM ADF image with multi-slice simulation results, as shown in Figs. 8.2d and 8.2e. There are three distinct lattice points in the original AB stacked bilayer MoS_2 (Fig. 8.1): (1) the highest intensity corresponds to the 2D projection of the Mo-S-S column (with Mo from the top layer and S-S from the bottom layer); (2) the second highest intensity corresponds to the Mo column from the bottom layer; and (3) the weakest intensity corresponds to the S-S column projected from the top layer. When viewed from the top (Fig. 8.1), the Mo-S-S columns and Mo columns are configured in a hexagonal lattice with three-fold symmetry, while the hollow centers of the hexagonal lattice are occupied by the S-S columns. As the electron beam scans in the AB stacked region (as shown in Figs. 8.2a and 8.2d) for 14 seconds, local atomic rearrangement occurs (marked by an orange ellipse in Fig. 8.2b). Strikingly, after another 14 seconds of scanning

in the same area, a triangular region with AA' stacking appears as shown in Figs. 8.2c and 8.2e. In this case, the three stacking boundaries between AA' and AB stacked regions form extremely rapidly and stay stationary as the scan continues.

In contrast, stacking boundaries can also be induced more gradually by using a lower electron beam intensity. Here, to study the dynamics of the transition between stacking sequences, continuous STEM ADF images are recorded as shown in Fig. 8.3. Figures 8.3a to 8.3d show the evolution of a fixed area in the bilayer MoS_2 sample in increments of 7 seconds. As a position reference between frames, red dotted circles mark the same atom from Fig. 8.3a to 8.3d, while dashed red triangles connect the same three lattice points from Fig. 8.3a to 3h. It is instructive to consider the nucleation of the stacking boundaries. Figures 3a and 3e (Fig. 8.3e is an enlarged image of the purple-squared area in Fig. 8.3a) show the original AB stacked bilayer MoS_2 at $t = 0$ s. At $t = 7$ s, local atomic rearrangement and a relative shift between the two MoS_2 layers are observed (Figs. 8.3b and 8.3f). The shift leads to the linear features as seen at the lower left corner of Fig. 8.3b (enclosed in a pink box). The separation between these linear features (orange lines in Fig. 8.3f) is 2.7 ± 0.05 Å, which is equivalent to the single-layer Mo lattice periodicity $\mathbf{a_1}$ ($= \frac{\sqrt{2}}{2}\mathbf{a}$, Fig. 8.1). Simulated STEM ADF image shows that a relative in-plane displacement [4] $\mathbf{u} = \frac{1}{3}\mathbf{a_1}$ agrees well with the experiment. The lateral shift between layers can be a source of large local strain, which may trigger other structural rearrangement or defects. For example, for a local region we observe obvious shrinkage of the projected Mo-Mo distance (green lines in Fig. 8.3f). This lattice distortion is most likely caused by S vacancy line defects which have also been observed in single-layer MoS_2 samples under TEM [219, 104] due to the "knock-on" effect by the electron beam, as the electron beam's energy (80 keV) is close to the threshold for S vacancy formation in single-layer MoS_2. Interstitial atoms and missing S-S columns are also observed in Fig. 8.3f, as indicated by white arrows and blue arrows respectively. These interstitial atoms and vacancies are highly mobile under combined electron irradiation and thermal heating, and eventually lead to the nucleation of AA' stacked region shown in Fig. 8.3g (blue hexagons). A straight stacking boundary (the orange line in Fig. 8.3g) is formed between AA' and AB stacked regions. We also notice that once the AA' stacked domain nucleates the interlayer shift (which originally concentrates at the lower left corner in Fig. 8.3b) significantly reduces. Therefore, it is likely that the nucleation and formation of the AA' stacked region release the strain caused by the interlayer shift, and the decrease in elastic energy compensates for the energy gain due to the newly formed stacking boundaries.

The AA' stacked region grows under continuous electron beam irradiation, from $\sim$2.88 nm^2 in Fig. 8.3c to $\sim$4.75 nm^2 in Fig. 8.3d after 7 seconds. At this point, a second straight stacking boundary on the right (Fig. 8.3h) forms at 60° with respect to the left boundary. Since the corner where these two boundaries meet is pinned by some defects, the AA' stacked region cannot expand upwards and has to grow downwards in the direction indicated by vector $\mathbf{W}$. It is worth noting that when we image and heat the as-grown AA' stacked bilayer MoS_2 under the same conditions, triangular AB stacked domains can also nucleate and grow from the originally AA' stacked region. This two-way transition between AA' and AB stacked

bilayer MoS_2 suggests that the difference in total energy between AA' and AB stacked bilayer MoS_2 is very small, and excitations such as thermal energy and electron irradiation can overcome the energy barrier to allow the transition between these two stacking sequences. It is worth noting that we did not observe stacking boundary formation at a lower temperature such as 300°C or a higher temperature (> 400°C, where Mo and S atoms can be knocked out by the electron beam easily). This indicates the thermal annealing at a certain temperature provides the right amount of energy to assist the motion of S atoms (which is the key step for the stacking sequence transition) while maintaining the crystal framework. In addition, we always observe stacking sequence transition seconds or tens of seconds after we start imaging an area, although we have let the sample stay at a certain temperature for a while (> 30 minutes) before the imaging. This indicates the local interaction between the electron beam and the sample during the STEM imaging is the trigger for the stacking sequence transition.

We now examine the atomic structure of the stacking boundaries between the AB and AA' stacked regions (Fig. 8.4a). The atomic structure shown in the STEM images of these boundaries has three main characteristics: (1) Mo lattices are continuous from the AA' stacked region to the AB stacked region, which means that the Mo atoms in both regions remain roughly at their original positions; (2) The hollow centers of the hexagonal lattices at the boundary are occupied by fewer S atoms compared to the original AB stacked bilayer MoS_2, as shown in the experimental STEM ADF image in Fig. 8.4d (top panel); (3) the Mo-Mo distance near the boundary has decreased. These observations are possible because Mo-S-S columns and Mo columns in AB stacked bilayer MoS_2 show different intensities in ADF images. We then can differentiate the Mo atoms in the top layer from those in the bottom layer based on this intensity difference. In Fig. 8.4a, three solid lines connect the Mo lattice points at the boundaries in the top layer (labeled as B1, B2 and B3 respectively), while the dashed lines connect the Mo lattice points at the boundaries in the bottom layer. The Mo-Mo distances of both layers at these boundaries are shorter than that of bulk MoS_2, which has also been observed in monolayer MoS_2 with S line defects [219, 104]. Averaged over six boundaries, the average Mo lattice distance at the stacking boundaries is $\sim$2.3 Å in the top layer, and $\sim$2.5 Å in the bottom layer (Fig. 8.4b). This indicates the top layer and bottom layer may experience different energetics due to electron-matter interaction.

To further quantify and understand the exact atomic structure at the stacking boundaries, we perform first-principles DFT calculations [66] on different boundary structures (see Sec. 8.4 for computational details). The boundary structure in Fig. 8.4c best satisfies the three experimentally observed characteristics mentioned above, and is stabilized by having a T-phase-like structure. The simulated STEM ADF image of this boundary structure agrees very well with the experimental results (Fig. 8.4d). Moreover, our calculations show that compressive strain due to Mo-Mo distance shrinkage favors the formation of S vacancies (see Sec. 8.4). This indicates that the nucleation of this T-phase-like boundary probably originates from the formation of S line-defects, which are commonly observed in single-layer MoS_2 under extensive electron beam irradiation [219, 104]. To understand each step of this boundary formation, we rely on DFT calculations to identify the minimum-energy path for

the nucleation and growth of AA' stacked region from the original AB stacking (Fig. 8.4f, only top MoS_2 layer is shown in color). Here, we use r to represent the reaction coordinate of domain growth, and the energy change associated with each step is plotted in Fig. 8.4e. At $r = 0.0$, a domain wall (shaded orange in Fig. 8.4f) is formed by ejecting the top S atoms (blue balls) in the top MoS_2 layer. This leaves the bottom S atoms (black balls) exposed. Subsequent domain growth is achieved by the migration of the nearest S atoms in the top MoS_2 layer towards the domain wall. This process only involves S atoms in the top layer of bilayer MoS_2, because the energy absorbed by the bottom MoS_2 layer from the electron beam is significantly reduced due to the shielding effect by the top layer30. The minimum-energy path for the S migration in the top MoS_2 layer is composed of two steps: (1) the top S atoms of the top layer migrating first ($r = 0.25$); followed by (2) the bottom S atoms of the same layer migrating ($r = 0.5$), which is also a local energy minimum (Fig. 8.4e). At this point, a unit cell of AA' stacking is formed (Fig. 8.4f). Subsequent expansion of the AA' region involves the repetition of the above two S migration steps (Fig. 8.4f). Since the energy barrier for each migration step is small, ranging from 0.15 eV to 1.05 eV per atom (Fig. 8.4e), this domain growth process can be easily activated by the 80 keV electron beam used in the experiment. This S migrating process has also been previously reported for the H-to-H' transition in monolayer MoS_2 [115], which is also observed in our experiment. Notably, this inversion domain formation in monolayer MoS_2 alone cannot explain our experimentally obtained atomically sharp stacking boundaries, which require both domain inversion in the top layer via S migrating and bonding modification in the bottom layer at the boundaries (Fig. 8.4). This indicates a strong interlayer interaction is the key to forming atomically sharp stacking boundaries in bilayer MoS_2. We emphasize the novel integration of different inversion symmetries in the same bilayer MoS_2 sample via creation of atomically sharp stacking boundaries between different stacking sequences.

Finally, we calculate the electronic band structure of the boundary, and find in-gap states localized at the domain wall (see Sec. 8.4 for details). To identify states from the boundary, we project the band structure onto atomic wave functions of atoms near the stacking boundary (Fig. 8.5a). In the band structure (Fig. 8.5b), states with contributions from Mo and S atoms adjacent to the domain wall are colored red and blue respectively, while contributions from atoms in the bulk are colored gray. We see that, importantly, the presence of the domain wall introduces metallic in-gap states that are absent in either AA' or AB stacked MoS_2 bilayer. Similar in-gap states have also been observed at the edges23,31 and mirror twin boundaries [243, 252, 255] of monolayer MoS_2. The in-gap states in our case are composed primarily of 4d-states from Mo atoms bordering the domain wall. From the contour lines of the integrated charge density in Fig. 8.5a, we see that these in-gap states are exponentially localized at the domain wall. We note that DFT-LDA has a well-known tendency to underestimate bandgaps and overestimate occupied bandwidths [152]. Appropriate theory of higher levels such as the GW approximation [83, 168, 169] must be used to obtain quantitatively accurate quasiparticle band structures. Here, LDA already provides a good description of qualitative features and wave function character.

8.3 Conclusion

In summary, we have demonstrated a novel way to engineer domains with different inversion symmetries in bilayer MoS_2 through the synergy of thermal excitation and electron irradiation. Using our method, we are able to reversibly convert between regions of AA' and AB stacking, thus switching between stacking sequences that result in different valley polarization. Through a first-principles study, we find that there are highly localized metallic states at the atomically sharp stacking boundaries. We propose that this approach may be used to reversibly pattern regions of different inversion symmetries, as well as controllably embed defect lines with different transport properties, within 2D semiconductors. This method of domain and symmetry engineering can be generalized to other TMDs. We hope that this study will inspire greater interest in future studies of valleytronics control and defect state patterning in atomically thin MoS_2 and other TMDs via nanoscale symmetry engineering.

8.4 First-principle calculations

First-principles calculations in a supercell geometry containing the grain boundaries were carried out based on density functional theory (DFT) as implemented in the Quantum ESPRESSO [66] package using ultrasoft [214, 175] pseudopotentials for electron-ion interaction and the local density approximation (LDA) [161, 27] for electron exchange and correlation. When required, the atomic positions are relaxed by minimizing every force component on the ions to less than 10^{-4} Ry/Å. During relaxation, the kinetic energy cutoff is set to 80 Ry for the plane-wave expansion of the wave functions and 500 Ry for the charge densities. A Γ-centered Monkhorst-Pack [144] grid is used for integration over the Brillouin zone of the supercell. With these parameters and a k grid of $15 \times 15 \times 1$, the lattice parameter of a fully-relaxed AB-stacked MoS_2 bilayer is determined to be 3.13 Å which compares favorably to the experimental value of 3.16 Å. In our calculation, we also confirm that AA' and AB stackings are nearly degenerate in energy1, with a fully-relaxed AA'-stacked bilayer being only 0.0007 eV per MoS_2 lower in energy than a fully-relaxed AB-stacked bilayer.

There are several different types of stacking boundaries that can be formed between AA' and AB stacked domains in bilayer MoS_2. Here, we focus on those that are consistent with the experimental observations as discussed in Fig. 8.4. To find the most energetically stable boundary that matches the experimental observations, in our calculations the Mo-Mo distance in the bottom layer is fixed at 2.5 Å and the top layer is allowed to relax. As shown in Fig. 8.6, the Mo-Mo distance in the top layer is ∼2.55 Å at locations far away from the boundary, and changes gradually to ∼2.5 Å close to the boundary, and suddenly drops to 2.3 Å right at the boundary. This sudden shrinkage of Mo-Mo distance at the boundary is due to the S deficiency. This result agrees with the experimental observation.

For the band structure calculation, a periodic supercell that is made up of $13 \times 1 \times 1$ unit cells (Fig. 8.7) is constructed. It is 25 Å long in the **c** direction, which is also the out-of-plane direction of the bilayer. The bilayer and its periodic image are separated by a vacuum space

of at least 15 Å. The bottom layer of the MoS_2 bilayer is periodic in the **a** and **b** directions while the top layer is periodic in the **b** direction. In the STEM images, the bilayer is shown to be reasonably flat within at least a 100 nm × 100 nm region. Hence, the structure is relaxed by constraining the Mo atoms from both layers into two separate planes while allowing for the full relaxation of the S atoms and interlayer distance. In our band structure calculations, the kinetic energy cutoff is set to 55 Ry and 500 Ry for the wave functions and the charge densities respectively. It uses fully relativistic ultrasoft pseudopotentials and includes spin-orbit coupling10. The self-consistent calculation for the charge densities are performed on a $1 \times 15 \times 1$ k grid.

Due to the periodic nature of the supercell and the structure of MoS_2, an $N \times 1 \times 1$ supercell will always contain two inequivalent domain walls. The S-deficient domain wall 1 instead of S-absent domain wall 2 agrees with our experimental observation, so we project the band structure of the supercell onto atomic wave functions of atoms near the domain wall 1 to distinguish the contributions from these two stacking boundaries. As the model is periodic in the b direction, we plot the band structure (as shown in Fig. 8.5b) along a path in reciprocal space parallel to this direction.

We observe in-gap states in the calculated band structure at this domain wall as shown in Figs. 8.5b and 8.8c. These in-gap states are robust and exist in different domain wall structures. As an example, we here show the band structure of another domain wall labeled domain wall 3, which is different from both the experimentally observed domain wall 1 and domain wall 2 (Fig. 8.7). Separate band structure calculations for the domain walls 1 and 3 are shown in Figs. 8.8c and 8.8d, respectively. Even though the domain wall structures are different, the main features of the band structures remain the same. Domain wall 3, however, has three in-gap boundary states that form Dirac cones unperturbed by spin-orbit coupling. H passivation of the dangling bonds at the domain walls also does not change these main features (Figs. 8.8e and 8.8f). They, however, lower some of the high-energy valence states back into the bulk.

Formation Energy Calculation

The formation energy E_f needed to form one S vacancy in a neutral state is given by $E_f = E^d_{\text{tot}} - E^0_{\text{tot}} + n\mu_{\text{S}}$, where E^d_{tot} is the total energy of the supercell with defects, E^0_{tot} is the total energy of the supercell with no defects, n is the number of S atoms removed and μ_{S} is the chemical potential of the S atom(s) removed. The chemical potential μ_{S} of S depends on the experimental growth conditions but is theoretically bounded by two limits. The upper limit of μ_{S} is the energy of S in an S-rich environment. The lower limit of μ_{S} is constrained by $\mu_{\text{Mo}} + 2\mu_{\text{S}} = \mu_{\text{MoS}_2}$ (the thermodynamic equilibrium between the Mo and S particle reservoirs and MoS_2) and the upper limit of μ_{Mo}, which is the energy of Mo in a Mo-rich environment. In this chapter, we use the chemical potential of S in crystalline α-S_8 for μ_{S} in a S-rich environment, the chemical potential of Mo in crystalline bcc Mo metal for in a Mo-rich environment and the chemical potential of a strained AB-stacked bilayer for μ_{MoS_2}. This limits μ_{S} to an energy window of 1.11 eV.

To calculate the formation energy of 2 at% S vacancy, we use a $3 \times 3 \times 1$ supercell with 54 atoms and evaluate the energy needed to remove one S. In our calculation, we find that the energy needed to form 2 at% S vacancy is reduced by $\sim$1.51 eV under strain, from a theoretical range of 1.84 to 2.95 eV to a range of 0.33 to 1.44 eV (a reduction of more than 50%). To calculate the formation energy of a linear defect of S vacancy from a pristine AB-stacked bilayer (at $r = 0.0$) (Fig. 8.4f), we use a $9 \times 1 \times 1$ supercell. This is also the supercell used to calculate the migration barriers of domain wall propagation. We evaluate the energy needed to form a line of S vacancies in a pristine AB-stacked bilayer at $r = 0.0$ (Fig. 8.4f), where both the top and bottom S atoms are removed. We calculate that it costs 0.34 to 1.45 eV per atom to remove the top S. Once it is removed, it costs 0.4 eV less (-0.03 to 1.07 eV per atom) to remove the bottom S. In fact, the removal of the second S may even be spontaneous, given the negative formation energy. In all, the total nucleation energy of the domain wall ranges from 0.31 to 2.52 eV per atom (or 0.01 to 0.10 eV per nm of domain wall).

Interestingly, the presence of in-gap states is robust under strain, minor structural distortions, with and without H passivation and exist also for other kinds of domain wall structures. Similar in-gap states have also been observed at the edges [252, 160] and mirror twin boundaries [252, 243, 255] of monolayer MoS_2. Dangling bonds at the domain wall lead to p-type doping, since some valence electrons are not paired, causing states to increase in energy compared to pristine bilayer MoS_2. If these dangling bonds are passivated with H, the high-energy valence states will decrease in energy.

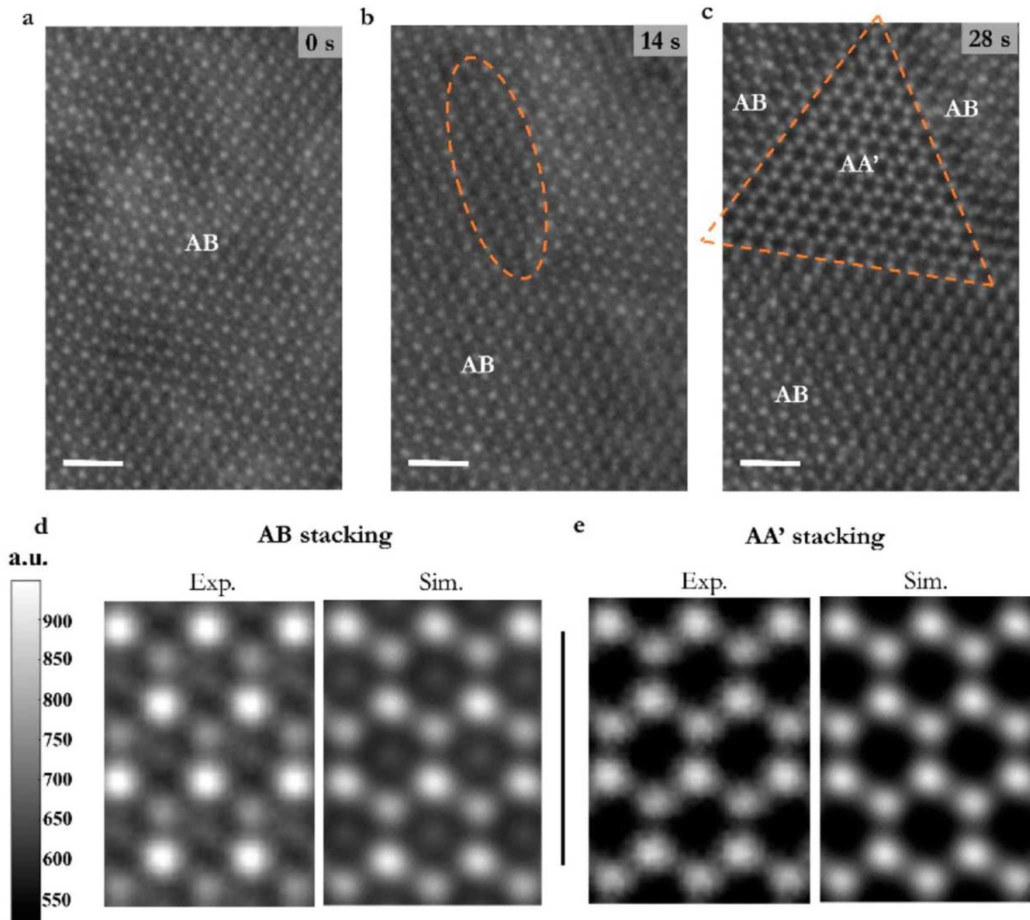

Figure 8.2: Stitching of AB and AA' stacked regions with sharp stacking boundaries in bilayer MoS_2. (a) High-resolution STEM ADF image taken at time 0s, showing AB stacked bilayer MoS_2. (b) After 14 s of scanning in the same area, rearrangement of atoms occurred, as highlighted by the orange ellipse. at the center of this AB stacked region, (c) High-resolution STEM ADF image showing a triangular AA' stacked region (highlighted by an orange circle) surrounded by AB stacked region. This image was taken 14 seconds after (b) and is from the same area as (b). (d) (e), STEM ADF images from AB stacked region in (a) and AA' stacked region in (c), respectively, with the intensity averaged over more than 10 unit cells of the same stacking sequence. The experimental results are compared to the multislice simulation [102] of STEM ADF images of AB and AA' stacked bilayer MoS_2 under the same experimental imaging condition in (d) and (e), respectively. All images in (d) and (e) are plotted on the same absolute scale. Scale bars in (a) (b) and (c) are 1 nm.

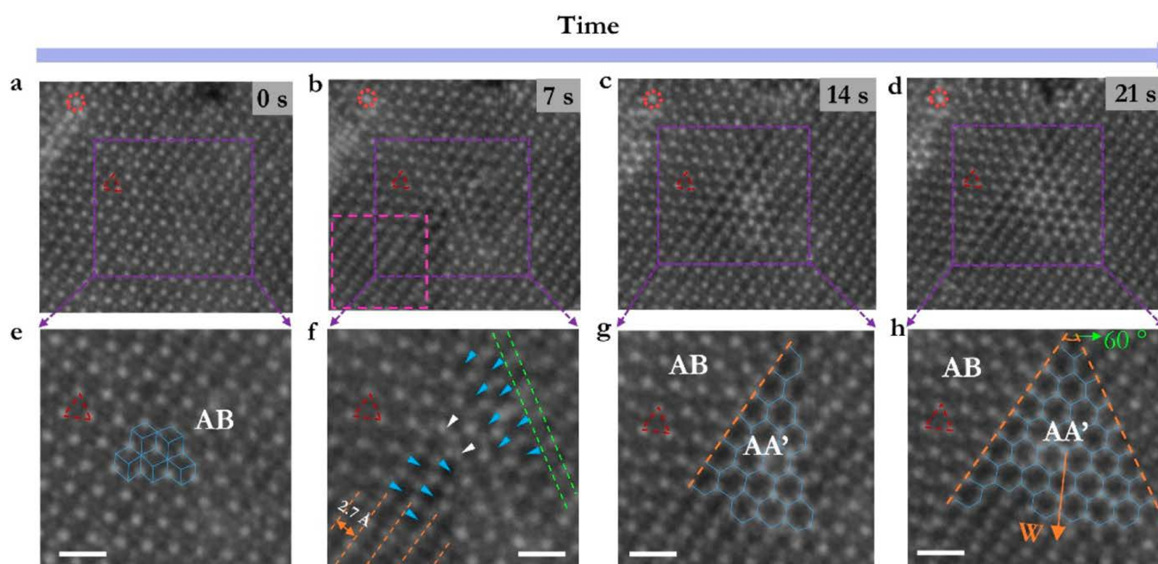

Figure 8.3: Nucleation and motion of the stacking boundaries in bilayer MoS_2 at 400°C. (a)-(d), STEM ADF image series of structural change in bilayer MoS_2 from the same area as time evolves from left to right. Red circles and triangles in these images highlight the same atoms and lattice points in this area. e-h, enlarged images of the area highlighted with purple squares in a-d respectively. e, At $t = 0$ s, AB stacked bilayer MoS_2 with the lattice points connected by blue lines. The S-S columns from the top layer occupy the hollow centers of the hexagonal lattices in this image. f, At $t = 7$ s, local atomic rearrangement starts to occur, which triggers the nucleation of AA' stacked domain. Large-area linear features with spacing 2.74 Å (orange lines) are due to the interlayer lateral shift between the top and bottom MoS_2 layers. Other structural changes are also observed, such as extra atoms (white arrowheads) and local shrinkage of projected Mo-Mo distance (green lines). g, At $t = 14$ s, AA' stacked region grows to $\sim$2.88 nm^2. h, At $t = 21$ s, AA' stacked region grows to 4.75 nm^2 as outlined by the blue hexagons. The angle between the two straight stacking boundaries is 60°. The growth direction for the AA' stacked region is now along vector $\mathbf{W}$. Scale bars in (e)-(h) are 5 Å.

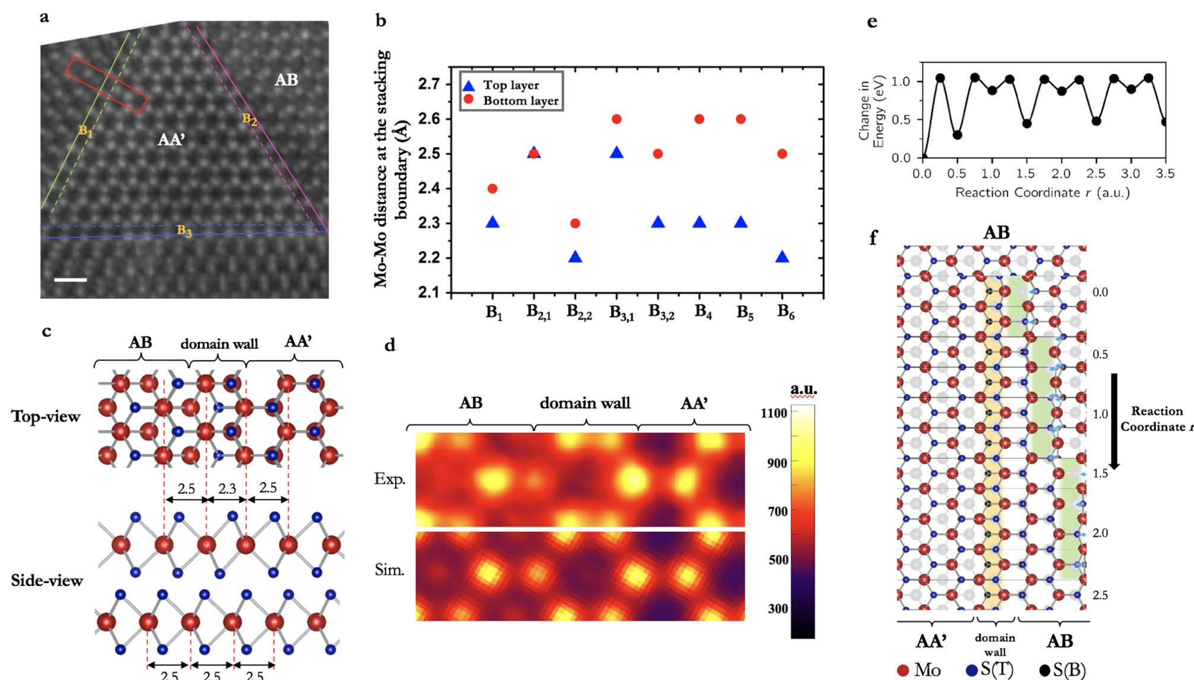

Figure 8.4: Atomic structure at the stacking boundaries. (a) A typical triangular AA' stacked domain is connected to the AB stacked domain by atomically sharp boundaries. At the three boundaries (labelled B_1, B_2, B_3), Mo lattices from the top layer are outlined by solid lines, and those from the bottom layer are outlined by dashed lines. Scale bar is 5 Å. (b) Summary of Mo lattice distances measured at six boundaries of two cases where AA' and AB domains are stitched together. Blue triangles represent the Mo lattice distances from the top layer, and red dots represent the Mo lattice distances from the bottom layer. The Mo lattice distances in the top layer at these boundaries shrink more than those in the bottom layer, indicating more severe structural change thus more energy injection from the electron beam into the top layer. (c) Schematic of the boundary structure obtained from DFT calculations. The dimensions of this boundary structure agree with the experimentally observed most dominant boundary structure. This boundary structure features a T-phase-like structure. (d) Experimental STEM ADF image at a typical stacking boundary, with the intensity averaged over 5 unit cells across the boundary, compared to the simulated STEM ADF image based on the atomic model in (c). The experimental and simulated STEM ADF images are plotted on the same color scale. (e) Energy barrier per atom as S migrates during domain wall propagation. (f) Schematic diagram of domain wall nucleation ($r = 0.0$) and domain growth ($r > 0.0$), starting from a pristine, strained AB-stacked bilayer.

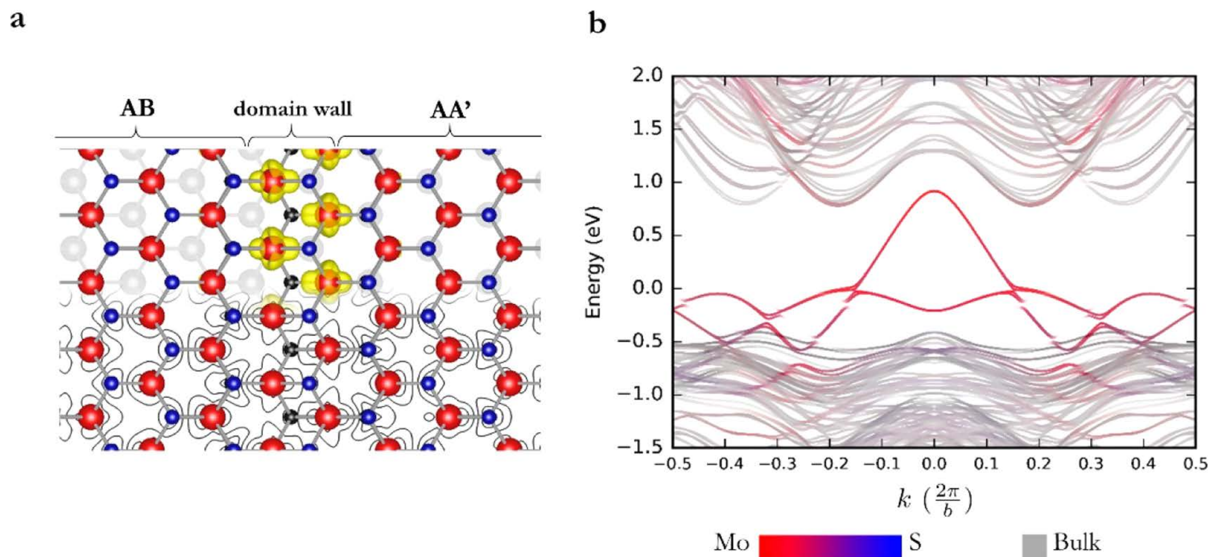

Figure 8.5: First-principles modelling of domain walls. (a) Atomic structure of the domain wall. The left side shows the AB domain while the right side shows the AA' domain, separated by the domain wall. The top half of the figure shows both the top and bottom layers of the bilayer, superposed with the 15% isosurface of the charge densities of the boundary states. The bottom half of the figure shows only the top layer, superposed with the contour lines of the same charge densities on a two-dimensional cut of the Mo plane. (b) Band structure of the domain wall within DFT in the local density approximation (LDA).

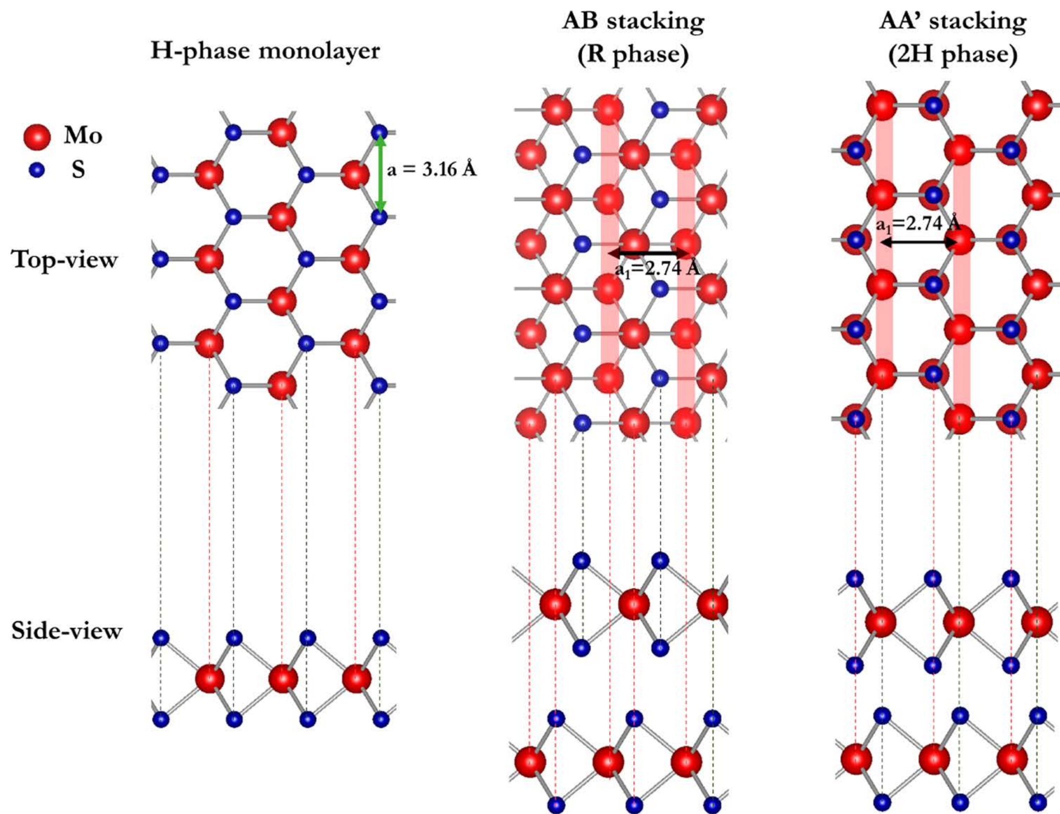

Figure 8.6: (a) Atomic structure of the domain wall separating AB and AA' domains. (b) shows the calculated change in the Mo-Mo distance of the top (red) and bottom (black) layers close to the domain wall in (a). In the top layer, S deficiency at the domain wall causes the Mo-Mo distance to narrow.

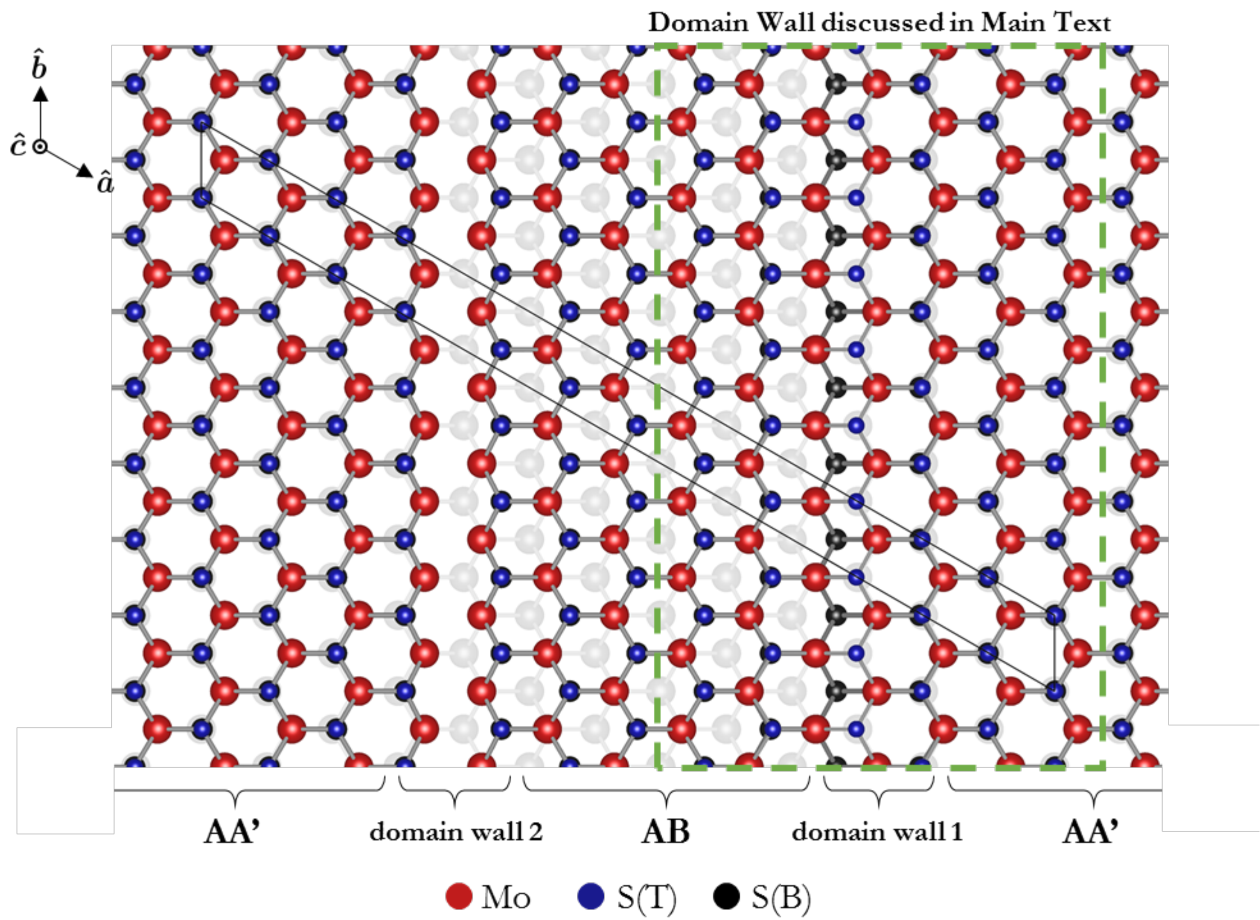

Figure 8.7: The $13 \times 1 \times 1$ supercell used for band structure calculation

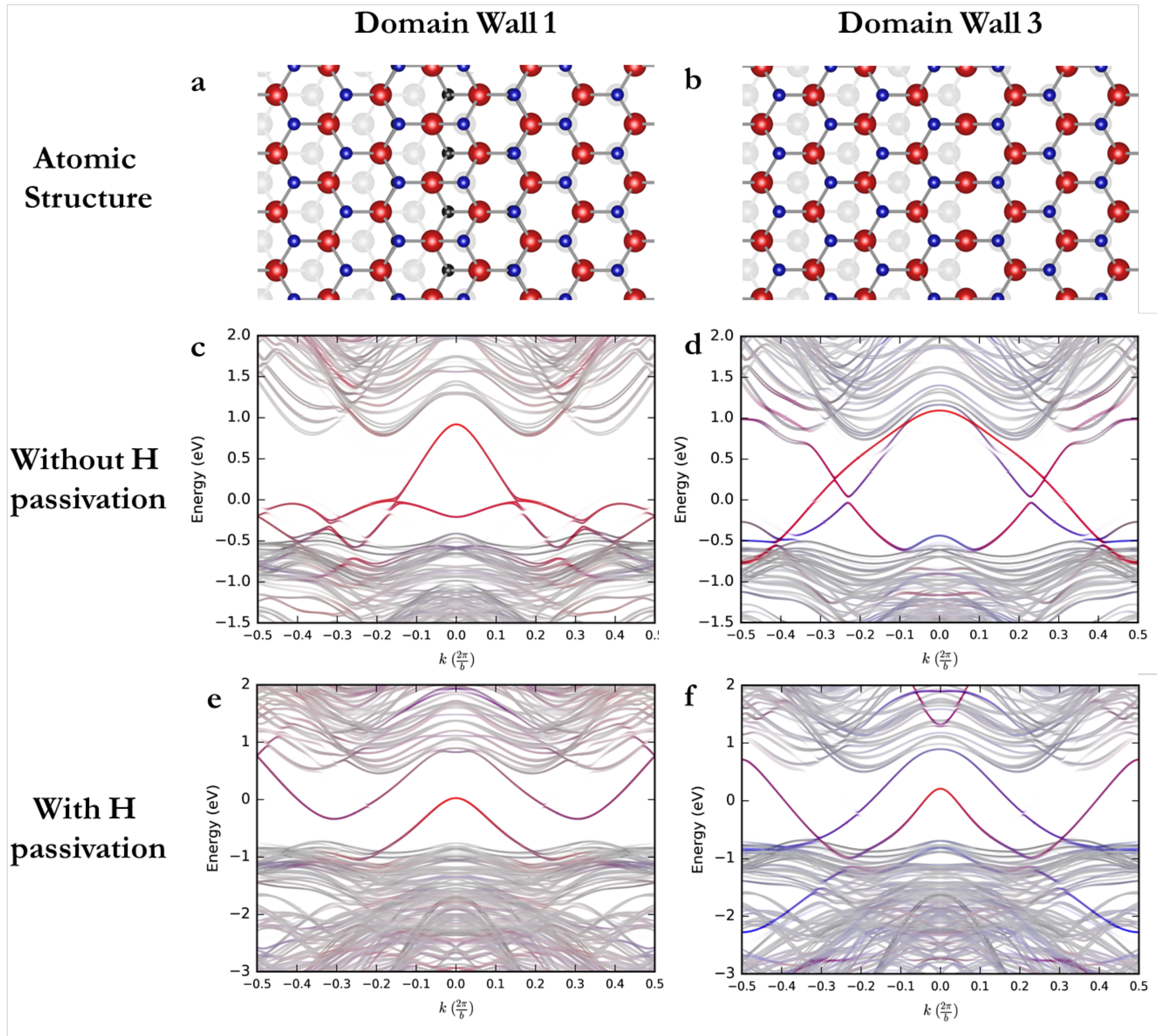

Figure 8.8: (a) and (b), Atomic structures of domain walls 1 and 3, respectively. Band structures of domain walls 1 and 3, without H passivation (c and d) and with H passivation (e and f).

Bibliography

[1] ASTM G173-03(2012) Standard Tables for Reference Solar Spectral Irradiances: Direct Normal and Hemispherical on 37° Tilted Surface, ASTM International, West Conshohocken, PA, 2012. DOI: 10.1520/G0173-03R12.

[2] Chin Shen Ong, Bradford A. Barker, Steven G. Louie, unpublished.

[3] Khairul Alam and Roger K. Lake. "Monolayer MoS_2 transistors beyond the technology road map". In: *IEEE Trans. Elect. Dev.* 59.12 (Dec. 2012), pp. 3250–3254. DOI: 10.1109/TED.2012.2218283.

[4] J. S. Alden et al. "Strain Solitons and Topological Defects in Bilayer Graphene". In: *Proceedings of the National Academy of Sciences* 110 (2013), pp. 11256–11260. DOI: 10.1073/pnas.1309394110.

[5] Maximilian Amsler et al. "Comment on "Towards Direct-Gap Silicon Phases by the Inverse Band Structure Design Approach"". In: *Physical Review Letters* 112 (19 May 2014), p. 199801. DOI: 10.1103/PhysRevLett.112.199801.

[6] K. Andersen, S. Latini, and K. S. Thygesen. "Dielectric genome of van der Waals heterostructures". In: *Nano Letters* 15.7 (2015), pp. 4616–4621. ISSN: 1530-6992. DOI: 10.1021/acs.nanolett.5b01251. arXiv: 1506.02463.

[7] D. E. Aspnes and A. A. Studna. "Dielectric functions and optical parameters of Si, Ge, GaP, GaAs, GaSb, InP, InAs, and InSb from 1.5 to 6.0 eV". In: *Physical Review B* 27 (2 Jan. 1983), pp. 985–1009. DOI: 10.1103/PhysRevB.27.985.

[8] S. H. Autler and C. H. Townes. "Stark Effect in Rapidly Varying Fields". In: *Physical Review* 100.2 (Oct. 1955), pp. 703–722. ISSN: 0031-899X. DOI: 10.1103/PhysRev.100.703.

[9] J. S. Bakos. "AC stark effect and multiphoton processes in atoms". In: *Physics Reports* 31.3 (July 1977), pp. 209–235. ISSN: 0370-1573. DOI: 10.1016/0370-1573(77)90016-3.

[10] John Bardeen and David Pines. "Electron-Phonon Interaction in Metals". In: *Physical Review* 99.4 (Aug. 1955), pp. 1140–1150. ISSN: 0031-899X. DOI: 10.1103/PhysRev.99.1140.

[11] Stefano Baroni et al. "Phonons and related crystal properties from density-functional perturbation theory". In: *Reviews of Modern Physics* 73.2 (July 2001), pp. 515–562. ISSN: 0034-6861. DOI: 10.1103/RevModPhys.73.515.

[12] Björn Baumeier, Michael Rohlfing, and Denis Andrienko. "Electronic excitations in push-pull oligomers and their complexes with fullerene from many-body Green's functions theory with polarizable embedding". In: *Journal of Chemical Theory and Computation* 10.8 (Aug. 2014), pp. 3104–3110. ISSN: 1549-9626. DOI: 10.1021/ct500479f.

[13] Friedhelm Bechstedt. "Many-Body Approach to Electronic Excitations". In: *Many-Body Approach to Electronic Excitations*. Springer-Verlag GmbH, Dec. 12, 2014. Chap. 19, pp. 439–457. ISBN: 9783662445921. DOI: 10.1007/978-3-662-44593-8_19.

[14] Lennart Bengtsson. "Dipole correction for surface supercell calculations". In: *Physical Review B* 59.19 (May 1999), pp. 12301–12304. ISSN: 0163-1829. DOI: 10.1103/PhysRevB.59.12301. arXiv: 0927-0256(96)00008 [10.1016].

[15] Timothy C. Berkelbach, Mark S. Hybertsen, and David R. Reichman. "Bright and dark singlet excitons via linear and two-photon spectroscopy in monolayer transition-metal dichalcogenides". In: *Physical Review B* 92 (8 Aug. 2015), p. 085413. DOI: 10.1103/PhysRevB.92.085413.

[16] Marco Bernardi, Maurizia Palummo, and Jeffrey C. Grossman. "Extraordinary Sunlight Absorption and 1 nm-Thick Photovoltaics using Two-Dimensional Monolayer Materials". In: *Nano Letters* (2013), p. 130610122620006. ISSN: 1530-6984. DOI: 10.1021/nl401544y.

[17] Marco Bernardi et al. "Ab initio study of hot electrons in GaAs". In: *Proceedings of the National Academy of Sciences* 112.17 (2015), pp. 5291–5296. ISSN: 0027-8424. DOI: 10.1073/pnas.1419446112.

[18] Michel Biron. *Thermoplastics and Thermoplastic Composites: Technical Information for Plastics Users*. Elsevier Science, 2007. ISBN: 9780080489803.

[19] Silvana Botti et al. "Low-energy silicon allotropes with strong absorption in the visible for photovoltaic applications". In: *Physical Review B* 86 (12 Sept. 2012), p. 121204. DOI: 10.1103/PhysRevB.86.121204.

[20] Aaron J. Bradley et al. "Probing the Role of Interlayer Coupling and Coulomb Interactions on Electronic Structure in Few-Layer $MoSe_2$ Nanostructures". In: *Nano Letters* 15.4 (Mar. 2015), pp. 2594–2599. ISSN: 1530-6992. DOI: 10.1021/acs.nanolett.5b00160.

[21] Christian Brouder et al. "Exponential Localization of Wannier Functions in Insulators". In: *Physical Review Letters* 98 (4 Jan. 2007), p. 046402. DOI: 10.1103/PhysRevLett.98.046402.

[22] H. Bruus and K. Flensberg. *Many-Body Quantum Theory in Condensed Matter Physics: An Introduction*. Oxford Graduate Texts. OUP Oxford, 2004. ISBN: 9780191057472.

[23] Sheneve Z. Butler et al. "Progress, challenges, and opportunities in two-dimensional materials beyond graphene". In: *ACS Nano* 7.4 (Mar. 2013), pp. 2898–2926. DOI: 10.1021/nn400280c.

[24] B. Butz et al. "Dislocations in Bilayer Graphene". In: *Nature* 505 (2014), p. 533.

[25] Ting Cao et al. "Valley-selective circular dichroism of monolayer molybdenum disulphide". In: *Nature Communications* 3.May (2012), pp. 885–887. ISSN: 2041-1723. DOI: 10.1038/ncomms1882. arXiv: 1112.4013.

[26] Andres Castellanos-Gomez et al. "Deterministic transfer of two-dimensional materials by all-dry viscoelastic stamping". In: *2D Materials* 1.1 (Apr. 2014), p. 011002. DOI: 10.1088/2053-1583/1/1/011002.

[27] D. M. Ceperley and B. J. Alder. "Ground state of the electron gas by a stochastic method". In: *Physical Review Letters* 45.7 (Aug. 1980), pp. 566–569. ISSN: 0031-9007. DOI: 10.1103/PhysRevLett.45.566.

[28] Tiago F. T. Cerqueira et al. "Materials Design On-the-Fly". In: *Journal of Chemical Theory and Computation* 11.8 (2015), pp. 3955–3960. DOI: 10.1021/acs.jctc.5b00212.

[29] Hamidreza Chalabi and Mark L. Brongersma. "Plasmonics: Harvest season for hot electrons." In: *Nature nanotechnology* 8.4 (Apr. 2013), pp. 229–30. ISSN: 1748-3395. DOI: 10.1038/nnano.2013.49.

[30] K. J. Chang and Marvin L. Cohen. "Structural and electronic properties of the high-pressure hexagonal phases of Si". In: *Physical Review B* 30.9 (9 Nov. 1984), pp. 5376–5378. DOI: 10.1103/PhysRevB.30.5376.

[31] K. J. Chang et al. "Superconductivity in High-Pressure Metallic Phases of Si". In: *Physical Review Letters* 54 (21 May 1985), pp. 2375–2378. DOI: 10.1103/PhysRevLett.54.2375.

[32] Ming-che Chang and Qian Niu. "Berry phase, hyperorbits, and the Hofstadter spectrum: Semiclassical dynamics in magnetic Bloch bands". In: *Physical Review Letters* 53.11 (1996), pp. 7010–7023.

[33] Alexey Chernikov et al. "Exciton Binding Energy and Nonhydrogenic Rydberg Series in Monolayer WS_2". In: *Physical Review Letters* 113.7 (Aug. 2014), p. 076802. ISSN: 0031-9007. DOI: 10.1103/PhysRevLett.113.076802. arXiv: 1403.4270.

[34] Alexey Chernikov et al. "Population inversion and giant bandgap renormalization in atomically thin WS_2 layers". In: *Nature Photonics* 9.7 (2015), pp. 466–470. ISSN: 1749-4893. DOI: 10.1038/nphoton.2015.104.

[35] M. Chhowalla, D. Jena, and H. Zhang. "Two-dimensional semiconductors for transistors". In: *Nature Reviews Materials* 1 (2016). DOI: 10.1038/natrevmats.2016.52.

[36] Y. Cho and T. C. Berkelbach. "Environmentally sensitive theory of electronic and optical transitions in atomically-thin semiconductors". In: *Physical Review B* 97 (2018). DOI: 10.1103/PhysRevB.97.041409.

[37] Marvin L. Cohen and Brad D. Malone. "Wave function engineering: Other phases of Si for photovoltaic applications". In: *Journal of Applied Physics* 109.10 (2011), p. 102402. ISSN: 0021-8979. DOI: 10.1063/1.3575641.

[38] G. Conibeer. "Progress on hot carrier cells". In: *Solar Energy Materials and Solar Cells* 93.6-7 (2009), pp. 713–719.

[39] Valentino R. Cooper. "Van der Waals density functional: An appropriate exchange functional". In: *Physical Review B* 81.16 (Apr. 2010), pp. 1–4. ISSN: 1098-0121. DOI: 10.1103/PhysRevB.81.161104. arXiv: 0910.1250.

[40] Pierluigi Cudazzo, Ilya V. Tokatly, and Angel Rubio. "Dielectric screening in two-dimensional insulators: Implications for excitonic and impurity states in graphane". In: *Physical Review B* 84.8 (Aug. 2011). ISSN: 10980121. DOI: 10.1103/PhysRevB.84.085406.

[41] Xu Cui et al. "Low-temperature Ohmic contact to monolayer MoS_2 by van der Waals bonded Co/h-BN electrodes". In: *Nano Letters* 17.8 (July 2017), pp. 4781–4786. DOI: 10.1021/acs.nanolett.7b01536.

[42] Xu Cui et al. "Multi-terminal transport measurements of MoS_2 using a van der Waals heterostructure device platform". In: *Nature Nanotechnology* 10.6 (Apr. 2015), pp. 534–540. DOI: 10.1038/nnano.2015.70.

[43] S. Das et al. "High performance multilayer MoS_2 transistors with scandium contacts". In: *Nano Letters* 13 (2013). DOI: 10.1021/nl303583v.

[44] C. R. Dean et al. "Boron nitride substrates for high-quality graphene electronics". In: *Nature Nanotechnology* 5.10 (Aug. 2010), pp. 722–726. DOI: 10.1038/nnano.2010.172.

[45] S. B. Desai et al. "MoS_2 transistors with 1-nanometer gate lengths". In: *Science* 354.6308 (Oct. 2016), pp. 99–102. DOI: 10.1126/science.aah4698.

[46] Jack Deslippe et al. "BerkeleyGW: A massively parallel computer package for the calculation of the quasiparticle and optical properties of materials and nanostructures". In: *Computer Physics Communications* 183.6 (June 2012), pp. 1269–1289. ISSN: 0010-4655. DOI: 10.1016/j.cpc.2011.12.006. arXiv: 1111.4429.

[47] Gary L. Doll. "Boron Nitride (BN)". In: *Handbook of Optical Constants of Solids*. Ed. by Edward D. Palik. Burlington: Academic Press, 1997, pp. 425–443. ISBN: 978-0-12-544415-6. DOI: 10.1016/B978-012544415-6.50110-2.

[48] Matthias Drüppel et al. "Diversity of trion states and substrate effects in the optical properties of an MoS_2 monolayer". In: *Nature Communications* 8.1 (2017), pp. 1–7. ISSN: 2041-1723. DOI: 10.1038/s41467-017-02286-6.

[49] Ivan Duchemin, Denis Jacquemin, and Xavier Blase. "Combining the GW formalism with the polarizable continuum model: A state-specific non-equilibrium approach". In: *Journal of Chemical Physics* 144.16 (Apr. 2016). ISSN: 0021-9606. DOI: 10.1063/1.4946778.

[50] Gordana Dukovic et al. "Structural dependence of excitonic optical transitions and band-gap energies in carbon nanotubes". In: *Nano Letters* 5.11 (2005), pp. 2314–2318. ISSN: 1530-6984. DOI: 10.1021/nl0518122.

[51] Sina Ebnesajjad. *Fluoroplastics, Volume 2: Melt Processible Fluoropolymers - The Definitive User's Guide and Data Book*. Plastics Design Library. Elsevier Science, 2015. ISBN: 9781455731985.

[52] David A. Egger et al. "Reliable Energy Level Alignment at Physisorbed Molecule-Metal Interfaces from Density Functional Theory". In: *Nano Letters* 15.4 (Apr. 2015), pp. 2448–2455. ISSN: 1530-6992. DOI: 10.1021/nl504863r.

[53] D. C. Elias et al. "Dirac cones reshaped by interaction effects in suspended graphene". In: *Nature Physics* 7.9 (2011), pp. 701–704. ISSN: 1745-2473. DOI: 10.1038/nphys2049. arXiv: 1104.1396.

[54] T. Elsaesser et al. "Initial thermalization of photoexcited carriers in GaAs studied by femtosecond luminescence spectroscopy." In: *Physical Review Letters* 66.13 (Apr. 1991), pp. 1757–1760. ISSN: 1079-7114. DOI: 10.1103/PhysRevLett.66.1757.

[55] Gianluca Fiori et al. "Electronics based on two-dimensional materials". In: *Nature Nanotechnology* 9.10 (Oct. 2014), pp. 768–779. DOI: 10.1038/nnano.2014.207.

[56] M. V. Fischetti and S. E. Laux. "Monte Carlo analysis of electron transport in small semiconductor devices including band-structure and space-charge effects." In: *Physical Review B* 38.14 (Nov. 1988), pp. 9721–9745. ISSN: 0163-1829. DOI: 10.1103/physrevb.38.9721.

[57] Carlos Forsythe et al. "Band structure engineering of 2D materials using patterned dielectric superlattices". In: *Nature Nanotechnology* 13.7 (2018), pp. 566–571. ISSN: 1748-3395. DOI: 10.1038/s41565-018-0138-7.

[58] Marcus Freitag et al. "Hot carrier electroluminescence from a single carbon nanotube". In: *Nano Letters* 4.6 (June 2004), pp. 1063–1066. ISSN: 1530-6984. DOI: 10.1021/nl049607u.

[59] H. Fröhlich. "Electrons in lattice fields". In: *Advances in Physics* 3.11 (July 1954), pp. 325–361. ISSN: 0001-8732. DOI: 10.1080/00018735400101213.

[60] Nathaniel M. Gabor et al. "Hot carrier-assisted intrinsic photoresponse in graphene." In: *Science* 334.6056 (Nov. 2011), pp. 648–52. ISSN: 1095-9203. DOI: 10.1126/science.1211384.

[61] Shiyuan Gao et al. "Dynamical Excitonic Effects in Doped Two-Dimensional Semiconductors". In: *Nano Letters* 16.9 (2016), pp. 5568–5573. ISSN: 1530-6992. DOI: 10.1021/acs.nanolett.6b02118.

[62] J. M. Garcia-Lastra et al. "Polarization-induced renormalization of molecular levels at metallic and semiconducting surfaces". In: *Physical Review B* 80.24 (Dec. 2009). ISSN: 1098-0121. DOI: 10.1103/PhysRevB.80.245427.

[63] A. Garg. *Classical Electromagnetism in a Nutshell*. In a Nutshell. Princeton University Press, 2012. ISBN: 9781400842759.

[64] R. Geick, C. H. Perry, and G. Rupprecht. "Normal modes in hexagonal boron nitride". In: *Physical Review* 146.2 (June 1966), pp. 543–547. DOI: 10.1103/PhysRev.146.543.

[65] F. Giannazzo et al. "Nanoscale inhomogeneity of the Schottky barrier and resistivity in MoS_2 multilayers". In: *Physical Review B* 92 (2015). DOI: 10.1103/PhysRevB.92.081307.

[66] Paolo Giannozzi et al. "QUANTUM ESPRESSO: A Modular and Open-Source Software Project for Quantum Simulations of Materials". In: *Journal of Physics: Condensed Matter* 21.39 (Sept. 2009), p. 395502. ISSN: 0953-8984. DOI: 10.1088/0953-8984/21/39/395502. arXiv: 0906.2569.

[67] Feliciano Giustino, Marvin L. Cohen, and Steven G. Louie. "Electron-phonon interaction using Wannier functions". In: *Physical Review B* 76.16 (2007), p. 165108. ISSN: 1098-0121. DOI: 10.1103/PhysRevB.76.165108.

[68] R. W. Godby and R. J. Needs. "Metal-insulator transition in Kohn-Sham theory and quasiparticle theory". In: *Physical Review Letters* 62.10 (Mar. 1989), pp. 1169–1172. ISSN: 0031-9007. DOI: 10.1103/PhysRevLett.62.1169.

[69] Pu Gong et al. "Optical selection rules for excitonic Rydberg series in the massive Dirac cones of hexagonal two-dimensional materials". In: *Physical Review B* 95.12 (2017), pp. 1–8. ISSN: 2469-9969. DOI: 10.1103/PhysRevB.95.125420.

[70] D.J. Griffiths. *Introduction to Electrodynamics*. Pearson international edition. Prentice Hall, 1999. ISBN: 9780139199608.

[71] J. B. Gunn. "Microwave oscillations of current in III-V semiconductors". In: *Solid State Communications* 1.4 (Sept. 1963), pp. 88–91. ISSN: 0038-1098. DOI: 10.1016/0038-1098(63)90041-3.

[72] Yaguang Guo et al. "A New Silicon Phase with Direct Band Gap and Novel Optoelectronic Properties". In: *Scientific Reports* 5 (2015). DOI: 10.1038/srep14342.

[73] S. J. Haigh et al. "Cross-sectional imaging of individual layers and buried interfaces of graphene-based heterostructures and superlattices". In: *Nature Materials* 11.9 (2012), pp. 764–767. ISSN: 1476-4660. DOI: 10.1038/nmat3386.

[74] D. R. Hamann. "Optimized norm-conserving Vanderbilt pseudopotentials". In: *Physical Review B* 88.8 (Aug. 2013), pp. 1–11. ISSN: 1098-0121. DOI: 10.1103/PhysRevB.88.085117.

[75] M. Hanfland et al. "Crystal Structure of the High-Pressure Phase Silicon VI". In: *Physical Review Letters* 82 (6 Feb. 1999), pp. 1197–1200. DOI: 10.1103/PhysRevLett.82.1197.

[76] R. M. Hazen et al. "High-pressure crystal chemistry and amorphization of α-quartz". In: *Solid State Communications* 72.5 (1989), pp. 507–511. ISSN: 0038-1098. DOI: 10.1016/0038-1098(89)90607-8.

[77] J. He, K. Hummer, and C. Franchini. "Stacking Effects on the Electronic and Optical Properties of Bilayer Transition Metal Dichalcogenides MoS_2, $MoSe_2$, WS_2, and WSe_2". In: *Physical Review B* 89 (2014), p. 75409.

[78] Lars Hedin. "New method for calculating the one-particle Green's function with application to the electron gas problem". In: *Physical Review* 139.3A (Aug. 1965), A796–A823. ISSN: 0031-899X. DOI: 10.1103/PhysRev.139.A796.

[79] Heather M. Hill et al. "Observation of excitonic Rydberg states in monolayer MoS_2 and WS_2 by photoluminescence excitation spectroscopy". In: *Nano Letters* 15.5 (Apr. 2015), pp. 2992–2997. DOI: 10.1021/nl504868p.

[80] J. Z. Hu and I. L. Spain. "Phases of silicon at high pressure". In: *Solid State Communications* 51.5 (1984), pp. 263–266. ISSN: 0038-1098. DOI: 10.1016/0038-1098(84)90683-5.

[81] S. Huang et al. "Probing the Interlayer Coupling of Twisted Bilayer MoS_2 Using Photoluminescence Spectroscopy". In: *Nano Letters* 14 (2014), p. 5500.

[82] Choongyu Hwang et al. "Fermi velocity engineering in graphene by substrate modification". In: *Scientific Reports* 2 (2012), pp. 2–5. ISSN: 2045-2322. DOI: 10.1038/srep00590. arXiv: 1208.0567.

[83] M. S. Hybertsen and S. G. Louie. "Electron correlation in semiconductors and insulators: band gaps and quasiparticle energies". In: *Physical Review B* 34.8 (1986), p. 5390. DOI: 10.1103/PhysRevB.34.5390.

[84] J. C. Inkson. "Many-body effects at metal-semiconductor junctions: Ii. the self energy and band structure distortion". In: *Journal of Physics C: Solid State Physics* 6.8 (Apr. 1973), pp. 1450–1460. ISSN: 0022-3719. DOI: 10.1088/0022-3719/6/8/004.

[85] Sohrab Ismail-Beigi. "Truncation of periodic image interactions for confined systems". In: *Physical Review B* 73.23 (June 2006), pp. 1–4. ISSN: 1098-0121. DOI: 10.1103/PhysRevB.73.233103. arXiv: 0603448 [cond-mat].

[86] Justin Iveland et al. “Direct measurement of auger electrons emitted from a semiconductor light-emitting diode under electrical injection: Identification of the dominant mechanism for efficiency droop”. In: *Physical Review Letters* 110.17 (Apr. 2013), pp. 1–5. ISSN: 0031-9007. DOI: 10.1103/PhysRevLett.110.177406.

[87] J.D. Jackson. *CLASSICAL ELECTRODYNAMICS, 3RD ED*. Wiley India Pvt. Limited, 2007. ISBN: 9788126510948.

[88] Carlo Jacoboni and Lino Reggiani. “The Monte Carlo method for the solution of charge transport in semiconductors with applications to covalent materials”. In: *Reviews of Modern Physics* 55.3 (July 1983), pp. 645–705. ISSN: 0034-6861. DOI: 10.1103/RevModPhys.55.645.

[89] J. C. Jamieson. “Crystal Structures at High Pressures of Metallic Modifications of Silicon and Germanium”. In: *Science* 139.3556 (Feb. 1963), pp. 762–764. ISSN: 0036-8075. DOI: 10.1126/science.139.3556.762.

[90] D. Jariwala et al. “Emerging device applications for semiconducting two-dimensional transition metal dichalcogenides”. In: *ACS Nano* 8 (2014). DOI: 10.1021/nn500064s.

[91] G. E. Jellison, J. D. Hunn, and Ho Nyung Lee. “Measurement of optical functions of highly oriented pyrolytic graphite in the visible”. In: *Physical Review B* 76.8 (2007), pp. 898–902. ISSN: 1098-0121. DOI: 10.1103/PhysRevB.76.085125.

[92] T. Jiang et al. “Valley and Band Structure Engineering of Folded MoS_2 Bilayers”. In: *Nature Nanotechnology* 9 (2014), p. 825.

[93] Chenhao Jin et al. “Imaging of pure spin-valley diffusion current in WS_2-WSe_2 heterostructures”. In: *Science* 360.6391 (May 2018), pp. 893–896. DOI: 10.1126/science.aao3503.

[94] F. H. Jornada, D. Y. Qiu, and S. G. Louie. “Nonuniform sampling schemes of the Brillouin zone for many-electron perturbation-theory calculations in reduced dimensionality”. In: *Physical Review B* 95.3 (2017), pp. 1–12. ISSN: 1550-235X. DOI: 10.1103/PhysRevB.95.035109. arXiv: 1610.06641.

[95] L. Ju et al. “Topological Valley Transport at Bilayer Graphene Domain Walls”. In: *Nature* 520 (2015), p. 650.

[96] H. Jung, K. Taniguchi, and C. Hamaguchi. “Impact ionization model for full band Monte Carlo simulation in GaAs”. In: *Journal of Applied Physics* 79.5 (2002), pp. 2473–2480.

[97] Leo P. Kadanoff and Gordon Baym. *Quantum statistical mechanics: Green’s function methods in equilibrium and nonequilibrium problems*. W.A. Benjamin Inc, New York, 1962. ISBN: 9780429961762. DOI: 10.1201/9780429493218.

[98] J. S. Kasper and S. M. Richards. “The crystal structures of new forms of silicon and germanium”. In: *Acta Crystallographica* 17.6 (1964), pp. 752–755.

[99] L. V. Keldysh. "Coulomb interaction in thin semiconductor and semimetal films". In: *Soviet Journal of Experimental and Theoretical Physics Letters* 29 (June 1979), p. 658.

[100] Duck Young Kim et al. "Synthesis of an open-framework allotrope of silicon". In: *Nature Materials* 14.2 (2014), pp. 169–173. ISSN: 1476-1122. DOI: 10.1038/nmat4140.

[101] Jonghwan Kim et al. "Ultrafast generation of pseudo-magnetic field for valley excitons in WSe_2 monolayers". In: *Science* 346.6214 (2014), pp. 1205–1208. ISSN: 0036-8075. DOI: 10.1126/science.1258122. eprint: https://science.sciencemag.org/content/346/6214/1205.full.pdf.

[102] Earl J. Kirkland. *Advanced computing in electron microscopy.* Springer, Aug. 12, 2010, p. 289. ISBN: 9781441965332.

[103] H. P. Komsa and A. V. Krasheninnikov. "Effects of confinement and environment on the electronic structure and exciton binding energy of MoS_2 from first principles". In: *Physical Review B* 86 (2012). DOI: 10.1103/PhysRevB.86.241201.

[104] H.-P. Komsa et al. "From Point to Extended Defects in Two-Dimensional MoS_2: Evolution of Atomic Structure under Electron Irradiation". In: *Physical Review B* 88 (2013), p. 35301.

[105] H.-P. Komsa et al. "Two-Dimensional Transition Metal Dichalcogenides under Electron Irradiation: Defect Production and Doping". In: *Physical Review Letters* 109 (2012), p. 35503.

[106] S. Latini, T. Olsen, and K. S. Thygesen. "Excitons in van der Waals heterostructures: the important role of dielectric screening". In: *Physical Review B* 92.24 (2015), pp. 1–13. ISSN: 1550-235X. DOI: 10.1103/PhysRevB.92.245123. arXiv: 1509.07972.

[107] Gwan-Hyoung Lee et al. "Flexible and transparent MoS_2 field-effect transistors on hexagonal boron nitride-graphene heterostructures". In: *ACS Nano* 7.9 (Aug. 2013), pp. 7931–7936. DOI: 10.1021/nn402954e.

[108] In-Ho Lee et al. "Ab initio materials design using conformational space annealing and its application to searching for direct band gap silicon crystals". In: *Computer Physics Communications* 203 (2016), pp. 110–121. ISSN: 0010-4655. DOI: 10.1016/j.cpc.2016.02.011.

[109] In-Ho Lee et al. "Computational search for direct band gap silicon crystals". In: *Physical Review B* 90 (11 Sept. 2014), p. 115209. DOI: 10.1103/PhysRevB.90.115209.

[110] J. Lee, K. F. Mak, and J. Shan. "Electrical Control of the Valley Hall Effect in Bilayer MoS_2 Transistors". In: *Nature Nanotechnology* 11 (2016), p. 421.

[111] Mark P. Levendorf et al. "Graphene and boron nitride lateral heterostructures for atomically thin circuitry". In: *Nature* 488.7413 (Aug. 2012), pp. 627–632. DOI: 10.1038/nature11408.

[112] Jing Li et al. "Accurate description of charged excitations in molecular solids from embedded many-body perturbation theory". In: *Physical Review B* 97.3 (2018), pp. 1–13. ISSN: 2469-9969. DOI: 10.1103/PhysRevB.97.035108.

[113] Likai Li et al. "Direct observation of the layer-dependent electronic structure in phosphorene". In: *Nature Nanotechnology* 12.1 (Sept. 2016), pp. 21–25. DOI: 10.1038/nnano.2016.171.

[114] Yilei Li et al. "Measurement of the optical dielectric function of monolayer transition-metal dichalcogenides: MoS_2, $MoSe_2$, WS_2, and WSe_2". In: *Physical Review B* 90 (20 Nov. 2014), p. 205422. DOI: 10.1103/PhysRevB.90.205422.

[115] Y.-C. Lin et al. "Atomic Mechanism of the Semiconducting-to-Metallic Phase Transition in Single-Layered MoS_2". In: *Nature Nanotechnology* 9 (2014), p. 391.

[116] Wolfgang von der Linden and Peter Horsch. "Precise quasiparticle energies and Hartree-Fock bands of semiconductors and insulators". In: *Physical Review B* 37.14 (May 1988), pp. 8351–8362. ISSN: 0163-1829. DOI: 10.1103/PhysRevB.37.8351.

[117] Johannes Lischner, Derek Vigil-Fowler, and Steven G. Louie. "Physical origin of satellites in photoemission of doped graphene: An Ab initio GW plus cumulant study". In: *Physical Review Letters* 110.14 (2013). ISSN: 0031-9007. DOI: 10.1103/PhysRevLett.110.146801. arXiv: arXiv:1302.3248v1.

[118] Bo Liu et al. "Engineering bandgaps of monolayer MoS_2 and WS_2 on fluoropolymer substrates by electrostatically tuned many-body effects". In: *Advanced Materials* 28.30 (May 2016), pp. 6457–6464. DOI: 10.1002/adma.201504876.

[119] K. Liu et al. "Evolution of Interlayer Coupling in Twisted Molybdenum Disulfide Bilayers". In: *Nature Communications* 5 (2014), p. 4966.

[120] Yuan Liu et al. "Approaching the Schottky-Mott limit in van der Waals metal-semiconductor junctions". In: *Nature* 557.7707 (May 2018), pp. 696–700. DOI: 10.1038/s41586-018-0129-8.

[121] Zhen-Fei Liu et al. " Accelerating GW-Based Energy Level Alignment Calculations for Molecule-Metal Interfaces Using a Substrate Screening Approach ". In: *Journal of Chemical Theory and Computation* (2019). ISSN: 1549-9618. DOI: 10.1021/acs.jctc.9b00326.

[122] Zheng Liu et al. "In-plane heterostructures of graphene and hexagonal boron nitride with controlled domain sizes". In: *Nature Nanotechnology* 8.2 (Jan. 2013), pp. 119–124. DOI: 10.1038/nnano.2012.256.

[123] Chih Pin Lu et al. "MoS_2: Choice substrate for accessing and tuning the electronic properties of graphene". In: *Physical Review Letters* 113.15 (Oct. 2014). ISSN: 1079-7114. DOI: 10.1103/PhysRevLett.113.156804.

[124] X. Lu et al. “Rapid and Nondestructive Identification of Polytypism and Stacking Sequences in Few-Layer Molybdenum Diselenide by Raman Spectroscopy”. In: *Advanced Materials* 27 (2015), p. 4502.

[125] G. G. Macfarlane et al. “Fine Structure in the Absorption-Edge Spectrum of Si”. In: *Physical Review* 111.5 (5 Sept. 1958), pp. 1245–1254. DOI: 10.1103/PhysRev.111.1245.

[126] O. Madelung. *Semiconductors - Basic Data*. Springer Berlin Heidelberg, 2012. ISBN: 9783642976759.

[127] G. D. Mahan. *Condensed Matter in a Nutshell*. In a Nutshell. Princeton University Press, 2011. ISBN: 9780691140162.

[128] G. Maier. “Low dielectric constant polymers for microelectronics”. In: *Prog. Polym. Sci.* 26.1 (Feb. 2001), pp. 3–65. DOI: 10.1016/S0079-6700(00)00043-5.

[129] K. F. Mak et al. “Control of Valley Polarization in Monolayer MoS_2 by Optical Helicity”. In: *Nature Nanotechnology* 7.8 (Aug. 2012), p. 494. ISSN: 1748-3387. DOI: 10.1038/nnano.2012.96. arXiv: 1205.1822.

[130] K. F. Mak et al. “The valley Hall effect in MoS_2 transistors.” In: *Science* 344.6191 (2014), pp. 1489–92. ISSN: 1095-9203. DOI: 10.1126/science.1250140. arXiv: 1403.5039.

[131] Kin Fai Mak, Jie Shan, and Tony F. Heinz. “Seeing many-body effects in single- and few-layer graphene: Observation of two-dimensional saddle-point excitons”. In: *Physical Review Letters* 106.4 (2011), pp. 1–4. ISSN: 0031-9007. DOI: 10.1103/PhysRevLett.106.046401.

[132] Kin Fai Mak et al. “Atomically thin MoS_2: A new direct-gap semiconductor”. In: *Physical Review Letters* 105.13 (2010), pp. 2–5. ISSN: 0031-9007. DOI: 10.1103/PhysRevLett.105.136805. arXiv: 1004.0546.

[133] Brad D. Malone, Steven G. Louie, and Marvin L. Cohen. “Electronic and optical properties of body-centered-tetragonal Si and Ge”. In: *Physical Review B* 81 (11 Mar. 2010), p. 115201. DOI: 10.1103/PhysRevB.81.115201.

[134] Brad D. Malone, Jay D. Sau, and Marvin L. Cohen. “*Ab initio* study of the optical properties of Si-XII”. In: *Physical Review B* 78 (16 Oct. 2008), p. 161202. DOI: 10.1103/PhysRevB.78.161202.

[135] Brad D. Malone, Jay D. Sau, and Marvin L. Cohen. “*Ab initio* survey of the electronic structure of tetrahedrally bonded phases of silicon”. In: *Physical Review B* 78 (3 July 2008), p. 035210. DOI: 10.1103/PhysRevB.78.035210.

[136] Andrea Marini and Rodolfo Del Sole. “Dynamical excitonic effects in metals and semiconductors”. In: *Physical Review Letters* 91.17 (2003), pp. 11–14. ISSN: 1079-7114. DOI: 10.1103/PhysRevLett.91.176402.

[137] R. M. Martin. *Electronic Structure: Basic Theory and Practical Methods*. Cambridge University Press, 2004. ISBN: 9780521782852.

[138] R. M. Martin, L. Reining, and D. M. Ceperley. *Interacting Electrons: Theory and Computational Approaches*. Cambridge University Press, 2016. ISBN: 9781316558560.

[139] Nicola Marzari and David Vanderbilt. "Maximally localized generalized Wannier functions for composite energy bands". In: *Physical Review B* 56 (20 Nov. 1997), pp. 12847–12865. DOI: 10.1103/PhysRevB.56.12847.

[140] M. I. McMahon et al. "Pressure dependence of the *Imma* phase of silicon". In: *Physical Review B* 50 (2 July 1994), pp. 739–743. DOI: 10.1103/PhysRevB.50.739.

[141] W. Melitz et al. "Kelvin probe force microscopy and its application". In: *Surf. Sci. Rep.* 66 (2011). DOI: 10.1016/j.surfrep.2010.10.001.

[142] B. Meyer and David Vanderbilt. "Ab initio study of BaTiO3 and PbTiO3 surfaces in external electric fields". In: *Physical Review B* 63.20 (2001), p. 205426. ISSN: 0163-1829. DOI: 10.1103/PhysRevB.63.205426. arXiv: 0009288 [cond-mat].

[143] S. Minomura and H. G. Drickamer. "Pressure induced phase transitions in silicon, germanium and some III-V compounds". In: *Journal of Physics and Chemistry of Solids* 23.5 (1962), pp. 451–456. ISSN: 0022-3697. DOI: 10.1016/0022-3697(62)90085-9.

[144] H. J. Monkhorst and J. D. Pack. "Special points for Brillouin-zone intergrations". In: *Physical Review B* 13.12 (1978), pp. 5897–5899. ISSN: 0717-6163. DOI: 10.1007/s13398-014-0173-7.2. arXiv: arXiv:1011.1669v3.

[145] Shaunak Mukherjee et al. "Hot electrons do the impossible: plasmon-induced dissociation of H2 on Au." In: *Nano Letters* 13.1 (Jan. 2013), pp. 240–7. ISSN: 1530-6992. DOI: 10.1021/nl303940z.

[146] Mit H. Naik and Manish Jain. "Substrate screening effects on the quasiparticle band gap and defect charge transition levels in MoS_2". In: *Physical Review Materials* 2.8 (8 Aug. 2018), p. 084002. DOI: 10.1103/PhysRevMaterials.2.084002.

[147] S. Najmaei et al. "Vapour Phase Growth and Grain Boundary Structure of Molybdenum Disulphide Atomic Layers". In: *Nature Materials* 12 (2013), p. 754.

[148] J. B. Neaton, Mark S. Hybertsen, and Steven G. Louie. "Renormalization of Molecular Electronic Levels at Metal-Molecule Interfaces". In: *Physical Review Letters* 97.21 (Nov. 2006), p. 216405. ISSN: 0031-9007. DOI: 10.1103/PhysRevLett.97.216405. arXiv: 0606640 [cond-mat].

[149] Jesse Noffsinger et al. "EPW: A program for calculating the electron-phonon coupling using maximally localized Wannier functions". In: *Computer Physics Communications* 181.12 (2010), pp. 2140–2148.

[150] Jesse Noffsinger et al. “Phonon-Assisted Optical Absorption in Silicon from First Principles”. In: *Physical Review Letters* 108.16 (16 Apr. 2012), p. 167402. DOI: 10.1103/PhysRevLett.108.167402.

[151] M. Nonnenmacher, M. P. O’Boyle, and H. K. Wickramasinghe. “Kelvin probe force microscopy”. In: *Applied Physics Letters* 58 (1991). DOI: 10.1063/1.105227.

[152] J. E. Northrup, M. S. Hybertsen, and S. G. Louie. “Theory of Quasiparticle Energies in Alkali Metals”. In: *Physical Review Letters* 59 (1987), p. 819.

[153] K. S. Novoselov et al. “Unconventional quantum Hall effect and Berry’s phase of 2 π in bilayer graphene”. In: *Nature Physics* 2.3 (2006), pp. 177–180. ISSN: 1745-2473. DOI: 10.1038/nphys245. arXiv: 0602565 [cond-mat].

[154] Young Jun Oh et al. “Dipole-allowed direct band gap silicon superlattices”. In: *Scientific Reports* 5 (2015), p. 18086. ISSN: 2045-2322. DOI: 10.1038/srep18086.

[155] H. Olijnyk, S. K. Sikka, and W. B. Holzapfel. “Structural phase transitions in Si and Ge under pressures up to 50 GPa”. In: *Physics Letters A* 103.3 (1984), pp. 137–140. ISSN: 0375-9601. DOI: 10.1016/0375-9601(84)90219-6.

[156] T. Olsen et al. “Simple Screened Hydrogen Model of Excitons in Two-Dimensional Materials”. In: *Physical Review Letters* 116.5 (2016), pp. 1–5. ISSN: 1079-7114. DOI: 10.1103/PhysRevLett.116.056401. arXiv: 1510.06777.

[157] Chin Shen Ong et al. “Real-space study of the optical absorption in alternative phases of silicon”. In: *Physical Review Materials* 1.7 (Dec. 2017), p. 075408. ISSN: 2475-9953. DOI: 10.1103/PhysRevMaterials.1.075408. arXiv: 1706.07382.

[158] Chin Shen Ong et al. “Substrate-Induced Dynamical Anti-Screening of Excitons in Quasi-2D Materials : A Study on the Substrate Renormalizations of Quasiparticle and Optical Excitations”. In: (2019). To be published.

[159] Edward D. Palik. “Silicon Dioxide (SiO2), Type α (Crystalline)”. In: *Handbook of Optical Constants of Solids*. Ed. by Edward D. Palik. Boston: Academic Press, 1985, pp. 719–747. ISBN: 978-0-08-054721-3. DOI: 10.1016/B978-0-08-054721-3.50039-3.

[160] H. Pan and Y.-W. Zhang. “Edge-Dependent Structural, Electronic and Magnetic Properties of MoS_2 Nanoribbons”. In: *J. Mater. Chem.* 22 (2012), p. 7280.

[161] J. P. Perdew and A. Zunger. “Self-interaction correction to density-functional approximations for many-electron systems”. In: *Physical Review B* 23.10 (1981), pp. 5048–5079. ISSN: 0163-1829. DOI: 10.1103/PhysRevB.23.5048. arXiv: 0706.3359.

[162] John P. Perdew, Kieron Burke, and Matthias Ernzerhof. “Generalized gradient approximation made simple”. In: *Physical Review Letters* 77.18 (1996), pp. 3865–3868. ISSN: 1079-7114. DOI: 10.1103/PhysRevLett.77.3865. arXiv: 0927-0256(96)00008 [10.1016].

[163] Chris J. Pickard and R. J. Needs. “High-Pressure Phases of Silane”. In: *Physical Review Letters* 97 (4 July 2006), p. 045504. DOI: 10.1103/PhysRevLett.97.045504.

[164] S. Picozzi et al. "Impact ionization in GaAs: A screened exchange density-functional approach". In: *Physical Review B* 65.11 (2002), p. 113206.

[165] R. O. Piltz et al. "Structure and properties of silicon XII: A complex tetrahedrally bonded phase". In: *Physical Review B* 52 (6 Aug. 1995), pp. 4072–4085. DOI: 10.1103/PhysRevB.52.4072.

[166] Albert Polman and Harry A. Atwater. "Photonic design principles for ultrahigh-efficiency photovoltaics." In: *Nature Materials* 11.3 (Feb. 2012), pp. 174–7. ISSN: 1476-1122. DOI: 10.1038/nmat3263.

[167] D. Y. Qiu, F. H. da Jornada, and S. G. Louie. "Environmental Screening Effects in 2D Materials: Renormalization of the Bandgap, Electronic Structure, and Optical Spectra of Few-Layer Black Phosphorus". In: *Nano Letters* 17.8 (July 2017), pp. 4706–4712. ISSN: 1530-6984. DOI: 10.1021/acs.nanolett.7b01365.

[168] D. Y. Qiu, F. H. Jornada, and S. G. Louie. "Optical spectrum of MoS_2: many-body effects and diversity of exciton states". In: *Physical Review Letters* 111.21 (2013), p. 216805. ISSN: 0031-9007. DOI: 10.1103/PhysRevLett.111.216805. arXiv: arXiv:1311.0963v1.

[169] D. Y. Qiu, F. H. Jornada, and S. G. Louie. "Screening and Many-Body Effects in Two-Dimensional Crystals: Monolayer MoS_2". In: *Physical Review B* 93.23 (May 2016), p. 235435. ISSN: 2469-9950. DOI: 10.1103/PhysRevB.93.235435. arXiv: 1605.08733.

[170] Hans J. Queisser. "Detailed balance limit for solar cell efficiency". In: *Materials Science and Engineering: B* 159 - 160 (2009), pp. 322–328. ISSN: 0921-5107. DOI: 10.1016/j.mseb.2008.06.033.

[171] Su Ying Quek et al. "Amine - Gold linked single-molecule circuits: Experiment and theory". In: *Nano Letters* 7.11 (Nov. 2007), pp. 3477–3482. ISSN: 1530-6984. DOI: 10.1021/nl072058i.

[172] B. Radisavljevic and A. Kis. "Mobility engineering and a metal-insulator transition in monolayer MoS_2". In: *Nature Materials* 12 (2013). DOI: 10.1038/nmat3687.

[173] Archana Raja et al. "Coulomb engineering of the bandgap and excitons in two-dimensional materials". In: *Nature Communications* 8 (May 2017), p. 15251. ISSN: 2041-1723. DOI: 10.1038/ncomms15251. arXiv: 1702.01204.

[174] Archana Raja et al. "Dielectric disorder in two-dimensional materials". In: *Nature Nanotechnology* (Aug. 2019). ISSN: 1748-3387. DOI: 10.1038/s41565-019-0520-0.

[175] Andrew M. Rappe et al. "Optimized pseudopotentials". In: *Physical Review B* 41.2 (1990), pp. 1227–1230. ISSN: 0163-1829. DOI: 10.1103/PhysRevB.41.1227.

[176] James P. Reed et al. "The effective fine-structure constant of freestanding graphene measured in graphite". In: *Science* 330.6005 (2010), pp. 805–808. ISSN: 0036-8075. DOI: 10.1126/science.1190920. arXiv: 1011.1590.

[177] Michael Rohlfing. "Electronic excitations from a perturbative LDA+GdW approach". In: *Physical Review B* 82.20 (Nov. 2010), pp. 1–10. ISSN: 1098-0121. DOI: 10.1103/PhysRevB.82.205127.

[178] Michael Rohlfing and Steven G. Louie. "Electron-hole excitations and optical spectra from first principles". In: *Physical Review B* 62.8 (2000), pp. 4927–4944. ISSN: 0163-1829. DOI: 10.1103/PhysRevB.62.4927. arXiv: 0406203v3 [arXiv:cond-mat].

[179] Sven Rühle. "Tabulated values of the Shockley-Queisser limit for single junction solar cells". In: *Solar Energy* 130 (June 2016), pp. 139–147. ISSN: 0038-092X. DOI: 10.1016/j.solener.2016.02.015.

[180] Junga Ryou et al. "Monolayer MoS_2 bandgap modulation by dielectric environments and tunable bandgap transistors". In: *Scientific Reports* 6.1 (July 2016). DOI: 10.1038/srep29184.

[181] N. S. Rytova. "The screened potential of a point charge in a thin film". In: *Moscow University Physics Bulletin* 3.3 (1967), p. 18.

[182] Elton J. G. Santos and Efthimios Kaxiras. "Electric-Field Dependence of the Effective Dielectric Constant in Graphene". In: *Nano Letters* 13.3 (Mar. 2013), pp. 898–902. ISSN: 1530-6984. DOI: 10.1021/nl303611v.

[183] Martin Schlipf and François Gygi. "Optimization algorithm for the generation of ONCV pseudopotentials". In: *Computer Physics Communications* 196 (Nov. 2015), pp. 36–44. ISSN: 0010-4655. DOI: 10.1016/j.cpc.2015.05.011. arXiv: arXiv:1502.00995v1.

[184] R. Schoenlein et al. "Femtosecond hot-carrier energy relaxation in GaAs". In: *Applied Physics Letters* 51.18 (1987), pp. 1442–1444.

[185] W. J. Schutte, J. L. De Boer, and F. Jellinek. "Crystal structures of tungsten disulfide and diselenide". In: *Journal of Solid State Chemistry* 70.2 (1987), pp. 207–209. ISSN: 1095-726X. DOI: 10.1016/0022-4596(87)90057-0.

[186] A. S. Sedra and K. C. Smith. *Microelectronic Circuits*. 5th. New York: Oxford Univ. Press, 2004.

[187] R. Seiwatz. "Possible structures for clean, annealed surfaces of germanium and silicon". In: *Surface Science* 2.Supplement C (Jan. 1964), pp. 473–483. ISSN: 0039-6028. DOI: 10.1016/0039-6028(64)90089-5.

[188] J. Shah. *Ultrafast Spectroscopy of Semiconductors and Semiconductor Nanostructures*. Springer Series in Solid-State Sciences. Springer Berlin Heidelberg, 2013. ISBN: 9783662037706.

[189] J. Shah et al. "Determination of intervalley scattering rates in GaAs by subpicosecond luminescence spectroscopy." In: *Physical Review Letters* 59.19 (Nov. 1987), pp. 2222–2225. ISSN: 1079-7114. DOI: 10.1103/PhysRevLett.59.2222.

[190] Meiyue Shao et al. “A structure preserving lanczos algorithm for computing the optical absorption spectrum”. In: *SIAM Journal on Matrix Analysis and Applications* 39.2 (2018), pp. 683–711. ISSN: 1095-7162. DOI: 10.1137/16M1102641. arXiv: 1611.02348.

[191] William Shockley and Hans J. Queisser. “Detailed Balance Limit of Efficiency of p-n Junction Solar Cells”. In: *Journal of Applied Physics* 32.3 (Mar. 1961), pp. 510–519. DOI: 10.1063/1.1736034.

[192] Edbert J. Sie et al. “Valley-selective optical Stark effect in monolayer WS_2”. In: *Nature Materials* 14.3 (2015), pp. 290–294. ISSN: 1476-4660. DOI: 10.1038/nmat4156. arXiv: 1407.1825.

[193] D. A. Siegel et al. “Many-body interactions in quasi-freestanding graphene”. In: *Proceedings of the National Academy of Sciences* 108.28 (2011), pp. 11365–11369. ISSN: 0027-8424. DOI: 10.1073/pnas.1100242108. arXiv: 1106.5822.

[194] Kristian Sommer Thygesen. “Calculating excitons, plasmons, and quasiparticles in 2D materials and van der Waals heterostructures”. In: *2D Materials* 4.2 (June 2017), p. 022004. ISSN: 2053-1583. DOI: 10.1088/2053-1583/aa6432.

[195] Ivo Souza, Nicola Marzari, and David Vanderbilt. “Maximally localized Wannier functions for entangled energy bands”. In: *Physical Review B* 65 (3 Dec. 2001), p. 035109. DOI: 10.1103/PhysRevB.65.035109.

[196] Catalin D. Spataru. “Electron excitations in solids and novel materials. PhD thesis”. PhD thesis. University of California, Berkeley, CA, 2004.

[197] Catalin D. Spataru. “Electronic and optical gap renormalization in carbon nanotubes near a metallic surface”. In: *Physical Review B* 88.12 (Sept. 2013), pp. 1–8. ISSN: 1098-0121. DOI: 10.1103/PhysRevB.88.125412.

[198] Ajit Srivastava and Ataç Imamoglu. “Signatures of Bloch-Band Geometry on Excitons: Nonhydrogenic Spectra in Transition-Metal Dichalcogenides”. In: *Physical Review Letters* 115.16 (2015), pp. 1–5. ISSN: 1079-7114. DOI: 10.1103/PhysRevLett.115.166802. arXiv: 1507.04040.

[199] A. V. Stier et al. “Probing the Influence of Dielectric Environment on Excitons in Monolayer WSe_2: Insight from High Magnetic Fields”. In: *Nano Letters* 16.11 (2016), pp. 7054–7060. ISSN: 1530-6992. DOI: 10.1021/acs.nanolett.6b03276. arXiv: 1608.05093.

[200] M. Stoppa and A. Chiolerio. “Wearable electronics and smart textiles: a critical review”. In: *Sensors* 14 (2014). DOI: 10.3390/s140711957.

[201] J. W. Suk et al. “Transfer of CVD-Grown Monolayer Graphene onto Arbitrary Substrates”. In: *ACS Nano* 5 (2011), p. 6916.

[202] R. Suzuki et al. “Valley-Dependent Spin Polarization in Bulk MoS_2 with Broken Inversion Symmetry”. In: *Nature Nanotechnology* 9 (2014), p. 611.

[203] S. M. Sze and K. K. Ng. *Physics of Semiconductor Devices*. Hoboken: Wiley, 2007.

[204] E. Takeda and N. Suzuki. "An empirical model for device degradation due to hot-carrier injection". In: *Electron Devices Lett IEEE* 4.4 (1983), pp. 111–113.

[205] Isaac Tamblyn et al. "Electronic energy level alignment at metal-molecule interfaces with a GW approach". In: *Rapid Communications Physical Review B* 84.4 (Nov. 2011), pp. 201402–201403. DOI: 10.1103/PhysRevB.84.201402.

[206] William A. Tisdale et al. "Hot-electron transfer from semiconductor nanocrystals." In: *Science* 328.5985 (June 2010), pp. 1543–7. ISSN: 1095-9203. DOI: 10.1126/science.1185509.

[207] Mahmut Tosun et al. "MoS_2 heterojunctions by thickness modulation". In: *Scientific Reports* 5.1 (June 2015). DOI: 10.1038/srep10990.

[208] N. Troullier and J. L. Martins. "Efficient pseudopotentials for plane-wave calculations." In: *Physical Review B* 43.3 (Jan. 1991), pp. 1993–2006. ISSN: 0163-1829. DOI: 10.1103/physrevb.43.1993.

[209] Peter Trucano and Ruey Chen. "Structure of graphite by neutron diffraction". In: *Nature* 258.5531 (1975), pp. 136–137. ISSN: 0028-0836. DOI: 10.1038/258136a0.

[210] Maxim Trushin, Mark Oliver Goerbig, and Wolfgang Belzig. "Model Prediction of Self-Rotating Excitons in Two-Dimensional Transition-Metal Dichalcogenides". In: *Physical Review Letters* 120 (18 May 2018), p. 187401. DOI: 10.1103/PhysRevLett.120.187401.

[211] Miguel M. Ugeda et al. "Giant bandgap renormalization and excitonic effects in a monolayer transition metal dichalcogenide semiconductor". In: *Nature Materials* 13.12 (Aug. 2014), pp. 1091–1095. ISSN: 1476-1122. DOI: 10.1038/nmat4061. arXiv: 1404.2331.

[212] M. Iqbal Bakti Utama et al. "A dielectric-defined lateral heterojunction in a monolayer semiconductor". In: *Nature Electronics* 2.2 (Feb. 2019), pp. 60–65. ISSN: 2520-1131. DOI: 10.1038/s41928-019-0207-4.

[213] A. Vaezi et al. "Topological Edge States at a Tilt Boundary in Gated Multilayer Graphene". In: *Physical Review X* 3 (2013), p. 21018.

[214] David Vanderbilt. "Soft self-consistent pseudopotentials in a generalized eigenvalue formalism". In: *Physical Review B* 41.11 (Apr. 1990), pp. 7892–7895. ISSN: 0163-1829. DOI: 10.1103/PhysRevB.41.7892.

[215] Lutz Waldecker et al. "Rigid band shifts in two-dimensional semiconductors through environmental screening". In: (July 12, 2019), pp. 1–6. arXiv: 1907.05535 [cond-mat.mes-hall].

[216] G. Wang et al. "Giant Enhancement of the Optical Second-Harmonic Emission of WSe_2 Monolayers by Laser Excitation at Exciton Resonances". In: *Physical Review Letters* 114.9 (2015), pp. 1–6. ISSN: 1079-7114. DOI: 10.1103/PhysRevLett.114.097403.

[217] Q. H. Wang et al. "Electronics and optoelectronics of two-dimensional transition metal dichalcogenides". In: *Nature Nanotechnology* 7 (2012). DOI: 10.1038/nnano.2012.193.

[218] Qianqian Wang et al. "Direct Band Gap Silicon Allotropes". In: *Journal of the American Chemical Society* 136.28 (2014), pp. 9826–9829. DOI: 10.1021/ja5035792.

[219] S. Wang et al. "Detailed Atomic Reconstruction of Extended Line Defects in Monolayer MoS_2". In: *ACS Nano* 10 (2016), p. 5419.

[220] Yanchao Wang et al. "Crystal structure prediction via particle-swarm optimization". In: *Physical Review B* 82 (9 Sept. 2010), p. 094116. DOI: 10.1103/PhysRevB.82.094116.

[221] R. H. Wentorf Jr. and J. S. Kasper. "Two New Forms of Silicon". In: *Science* 139 (Jan. 1963), pp. 338–339. DOI: 10.1126/science.139.3552.338-a.

[222] Kirsten T. Winther and Kristian S. Thygesen. "Band structure engineering in van der Waals heterostructures via dielectric screening: the GΔW method". In: *2D Materials* 4.2 (2017), p. 025059. DOI: 10.1088/2053-1583/aa6531.

[223] C. R. Woods et al. "Commensurate-incommensurate transition in graphene on hexagonal boron nitride". In: *Nature Physics* 10.6 (2014), pp. 451–456. ISSN: 1745-2481. DOI: 10.1038/nphys2954.

[224] Fengcheng Wu, Fanyao Qu, and A. H. Macdonald. "Exciton band structure of monolayer MoS_2". In: *Physical Review B* 91.7 (2015), pp. 1–8. ISSN: 1550-235X. DOI: 10.1103/PhysRevB.91.075310. arXiv: 1501.02273.

[225] R. Wyckoff. *Crystal Structures - Volume 1.* 2nd ed. New York: Interscience Publishers, 1963.

[226] F. Xia et al. "Two-dimensional material nanophotonics". In: *Nature Photonics* 8 (2014). DOI: 10.1038/nphoton.2014.271.

[227] M. Xia et al. "Spectroscopic Signatures of AA' and AB Stacking of Chemical Vapor Deposited Bilayer MoS_2". In: *ACS Nano* 9 (2015), p. 12246.

[228] H. J. Xiang et al. "Towards Direct-Gap Silicon Phases by the Inverse Band Structure Design Approach". In: *Physical Review Letters* 110 (11 Mar. 2013), p. 118702. DOI: 10.1103/PhysRevLett.110.118702.

[229] H. J. Xiang et al. "Xiang *et al.* Reply:" in: *Physical Review Letters* 112 (19 May 2014), p. 199802. DOI: 10.1103/PhysRevLett.112.199802.

[230] Di Xiao, Ming Che Chang, and Qian Niu. "Berry phase effects on electronic properties". In: *Reviews of Modern Physics* 82.3 (2010), pp. 1959–2007. ISSN: 0034-6861. DOI: 10.1103/RevModPhys.82.1959. arXiv: 0907.2021.

[231] Di Xiao, Wang Yao, and Qian Niu. "Valley-Contrasting Physics in Graphene: Magnetic Moment and Topological Transport". In: *Physical Review Letters* 99.23 (Dec. 2007), p. 236809. ISSN: 0031-9007. DOI: 10.1103/PhysRevLett.99.236809. arXiv: 0709.1274.

[232] Di Xiao et al. "Coupled Spin and Valley Physics in Monolayers of MoS 2 and Other Group-VI Dichalcogenides". In: *Physical Review Letters* 108.19 (2012), pp. 1–5. ISSN: 0031-9007. DOI: 10.1103/PhysRevLett.108.196802. arXiv: 1112.3144.

[233] Xiaodong Xu et al. "Spin and pseudospins in layered transition metal dichalcogenides". In: *Nature Physics* 10.5 (2014), pp. 343–350. ISSN: 1745-2473. DOI: 10.1038/nphys2942.

[234] Fengyuan Xuan, Yifeng Chen, and Su Ying Quek. "Quasiparticle Levels at Large Interface Systems from Many-Body Perturbation Theory: The XAF-GW Method". In: *Journal of Chemical Theory and Computation* 15.6 (June 2019), pp. 3824–3835. ISSN: 1549-9626. DOI: 10.1021/acs.jctc.9b00229.

[235] A. Yan et al. "Identifying Different Stacking Sequences in Few-Layer CVDGrown MoS_2 by Low-Energy Atomic-Resolution Scanning Transmission Electron Microscopy". In: *Physical Review B* 93 (2016), p. 41420.

[236] Aiming Yan et al. "Dynamics of Symmetry-Breaking Stacking Boundaries in Bilayer MoS 2". In: *The Journal of Physical Chemistry C* 121.40 (Oct. 2017), pp. 22559–22566. ISSN: 1932-7447. DOI: 10.1021/acs.jpcc.7b08398.

[237] Ziliang Ye, Dezheng Sun, and Tony F. Heinz. "Optical manipulation of valley pseudospin". In: *Nature Physics* (2017). ISSN: 1745-2481. DOI: 10.1038/nphys3891. arXiv: 1606.06806.

[238] Ziliang Ye et al. "Probing excitonic dark states in single-layer tungsten disulphide". In: *Nature* 513.7517 (2014), pp. 214–218. ISSN: 1476-4687. DOI: 10.1038/nature13734. arXiv: 1403.5568.

[239] Chaw Keong Yong et al. "Biexcitonic optical Stark effects in monolayer molybdenum diselenide". In: *Nature Physics* 14.11 (July 2018), pp. 1092–1096. ISSN: 1745-2481. DOI: 10.1038/s41567-018-0216-7.

[240] Chaw-Keong Yong et al. "Valley-dependent exciton fine structure and Autler-Townes doublets from Berry phases in monolayer $MoSe_2$". In: *Nature Materials* 18.10 (Oct. 2019), pp. 1065–1070. ISSN: 1476-1122. DOI: 10.1038/s41563-019-0447-8.

[241] J. F. Young et al. "Carrier-carrier scattering rates within nonequilibrium optically injected semiconductor plasmas." In: *Physical Review B* 50.4 (July 1994), pp. 2208–2215. ISSN: 0163-1829. DOI: 10.1103/physrevb.50.2208.

[242] P. A. Young. "Lattice parameter measurements on molybdenum disulphide". In: *Journal of Physics D: Applied Physics* 1.7 (July 2002), pp. 936–938. ISSN: 0022-3727. DOI: 10.1088/0022-3727/1/7/416.

[243] A. M. van der Zande et al. “Grains and Grain Boundaries in Highly Crystalline Monolayer Molybdenum Disulphide”. In: *Nature Materials* 12 (2013), p. 554.

[244] A. M. van der Zande et al. “Tailoring the Electronic Structure in Bilayer Molybdenum Disulfide via Interlayer Twist”. In: *Nano Letters* 14 (2014), p. 3869.

[245] H. Zeng et al. “Valley Polarization in MoS2Monolayers by Optical Pumping”. In: *Nature Nanotechnology* 7.8 (Aug. 2012), p. 490. ISSN: 1748-3387. DOI: 10.1038/nnano.2012.95. arXiv: 1202.1592 [cond-mat.mes-hall].

[246] C. Zhang et al. “Direct imaging of band profile in single layer MoS_2 on graphite: Quasiparticle energy gap, metallic edge states, and edge band bending”. In: *Nano Letters* 14 (2014). DOI: 10.1021/nl501133c.

[247] F. Zhang, A. H. MacDonald, and E. J. Mele. “Valley Chern Numbers and Boundary Modes in Gapped Bilayer Graphene”. In: *Proceedings of the National Academy of Sciences* 110 (2013), p. 10546.

[248] Yi Zhang et al. “Electronic structure, surface doping, and optical response in epitaxial WSe_2 thin films”. In: *Nano Letters* 16.4 (Mar. 2016), pp. 2485–2491. DOI: 10.1021/acs.nanolett.6b00059.

[249] Yuanbo Zhang et al. “Experimental observation of the quantum Hall effect and Berry’s phase in graphene”. In: *Nature* 438.7065 (2005), pp. 201–204. ISSN: 0028-0836. DOI: 10.1038/nature04235. arXiv: 0509355 [cond-mat].

[250] You-Xiang Zhao et al. “New metastable phases of silicon”. In: *Solid State Communications* 59.10 (1986), pp. 679–682. ISSN: 0038-1098. DOI: 10.1016/0038-1098(86)90372-8.

[251] Jianhui Zhou et al. “Berry Phase Modification to the Energy Spectrum of Excitons”. In: *Physical Review Letters* 115.16 (2015), pp. 1–5. ISSN: 1079-7114. DOI: 10.1103/PhysRevLett.115.166803. arXiv: arXiv:1507.08921v1.

[252] W. Zhou et al. “Intrinsic Structural Defects in Monolayer Molybdenum Disulfide”. In: *Nano Letters* 13 (2013), p. 2615.

[253] Bairen Zhu, Xi Chen, and Xiaodong Cui. “Exciton binding energy of monolayer WS_2”. In: *Scientific Reports* (2015). ISSN: 2045-2322. DOI: 10.1038/srep09218. arXiv: 1403.5108.

[254] J. M. Ziman. *Electrons and Phonons: The Theory of Transport Phenomena in Solids*. International series of monographs on physics. OUP Oxford, 2001. ISBN: 9780198507796.

[255] X. Zou, Y. Liu, and B. I. Yakobson. “Predicting Dislocations and Grain Boundaries in Two-Dimensional Metal-Disulfides from the First Principles”. In: *Nano Letters* 13 (2013), p. 253.